Investigations on the Structural and Kinetic Features of Amyloid Aggregation

Thesis Submitted for the Degree of

Doctor of Philosophy (Science)

of

Jadavpur University

By

Dibakar Sarkar

Department of Chemical Sciences

Bose Institute

Kolkata – 700091

India

संदर्भ सं, / Ref. No. :...............................   दिनांक / Date :

CERTIFICATE FROM THE SUPERVISOR

This is to certify that the thesis entitled *"Investigations on the Structural and Kinetic Features of Amyloid Aggregation"* submitted by Sri Dibakar Sarkar who got his name registered on 16ᵗʰ September 2019, for the award of Ph. D. (Science) degree of Jadavpur University, is absolutely based upon his own work under the supervision of Prof. Anirban Bhunia, Department of Chemical Sciences, Bose Institute Unified Campus, Kolkata - 700091 and that neither this thesis nor any part of it has been submitted for either any degree / diploma or any other academic award anywhere before.

29/02/24

....

(Signature of the Supervisor date with official seal)

डॉ. अनिर्बान भूनिया / Dr. Anirban Bhunia
प्रोफेसर / Professor
रासायनिक विज्ञान विभाग / Department of Chemical Sciences
बसु विज्ञान मंदिर / BOSE INSTITUTE
ई एन 80, सेक्टर V, विधाननगर / EN 80, Sector V, Bidhannagar
कोलकाता / Kolkata-700 091 (भारत / India)

To My Beloved Parents

Acknowledgements

As I stand on the threshold of realizing a lifelong aspiration, I find myself looking back on the twisted path of scientific exploration with a mix of nostalgia and gratitude. This journey has been filled with moments of extreme struggle, moments of nearly giving up, moments of strength, growth, and sheer joy. Each step, each setback and each small victory have not only shaped my academic journey but also enriched my understanding of the human capacity for resilience and the power of perseverance in the pursuit of scientific knowledge and passion.

*I would like to take this opportunity to convey my thanks and appreciation towards a great number of individuals. I will start by expressing my sincere gratitude to my Ph.D. supervisor, **Prof. Anirban Bhunia**, Department of Chemical Sciences, Bose Institute, for giving me the freedom and opportunity to explore exciting scientific challenges. Over the course of nearly seven years, he has consistently pushed me towards greater scientific achievement. His constant guidance and enthusiasm have always motivated me to move forward. It has been a remarkable experience to learn from him how to shape a scientific problem, from defining the problem to its experimental solution and scientific representation.*

*I am extremely grateful to the **Department of Science and Technology-Innovation in Science Pursuit for Inspired Research (DST-INSPIRE)** for providing fellowship. DST-INSPIRE has been a tremendous financial support throughout my academic journey, extending back to the days of my B.Sc. degree. I am thankful to Bose Institute and Jadavpur University for allowing me to pursue Ph.D. degree.*

*I am indebted to all my collaborators for their expert opinions and valuable contributions to various aspect of this research. I am thankful to all my international collaborators **Prof. Carmelo La Rosa** (Department of Chemical Sciences, University of Catania, Italy) and his student **Marcello Condorelli**; **Dr. Markus Weingarth** (Department of Chemistry, Utrecht University, The*

List of Abbreviations

- AD: Alzheimer's Disease
- Aβ: Amyloid β
- APP: Amyloid Precursor Protein
- WT: Wild Type
- hIAPP: Human Islet Amyloid Polypeptide
- TMD: Transmembrane Domain
- ThT: Thioflavin-T
- DPX: Dibutyl phthalate Polystyrene Xylene
- NMR: Nuclear Magnetic Resonance
- MD: Molecular Dynamics
- CD: Circular Dichroism
- FTIR: Fourier Transform Infrared
- SEM: Scanning Electron Microscopy
- AFM: Atomic Force Microscopy
- TEM: Transmission Electron Microscopy
- SERS: Surface Enhanced Raman Spectroscopy
- XRD: X-Ray Diffraction
- CMC: Critical Micelle Concentration
- CSP: Chemical Shift Perturbation
- CSI: Chemical Shift Index
- D_2O: Deuterium Oxide
- DLS: Dynamic Light Scattering
- DMF: Dimethyl Formamide
- DMSO: Dimethyl Sulfoxide
- DOPC: 1,2-Dioleoyl-sn-glycero-3 phosphocholine
- RT: Room Temperature
- INEPT: Insensitive Nuclei Enhanced by Polarization Transfer
- DOPG: 1, 2-dioleoyl-sn-glycero-3 phospho-(1'-racglycerol)
- LUV: Large Unilamellar Vesicles
- PBS: Phosphate Buffer Saline
- PRE: Paramagnetic Relaxation Enhancement
- DIPEA: N, N-Diisopropylethylamine
- HPLC: High Performance Liquid Chromatography
- PAGE: Polyacrylamide Gel Electrophoresis
- HSQC: Heteronuclear Single Quantum Coherence
- MTT: Methylthiazolyldiphenyl-tetrazolium
- NOE: Nuclear Overhauser Effect
- RMSD: Root Mean Square Deviation
- SDS: Sodium Dodecyl Sulfate
- TFA: Trifluoroacetic Acid
- TOCSY: Total Correlation Spectroscopy

- NOESY: transferred Nuclear Overhauser Effect Spectroscopy
- ROESY: Rotating frame Overhauser SpectroscopY
- TSP: 3-Trimethylsilyl propionic-2, 2, 3, 3-d4 acid
- Fmoc: Fluorenylmethyloxycarbonyl
- SEC: Size-Exclusion Chromatography
- SD: Standard Deviation
- h: Hour
- μM/mM: Micro/ Millimolar
- mg/mL: Milligram/milliliter
- 1D/2D: One/Two Dimensional
- ppm: Parts Per Million
- Å: Angstrom
- nm: Nanometer

- CPMG: Carr-Purcell-Meiboom-Gill
- DOSY: Diffusion Ordered SpectroscopY
- SVD: Singular Value Decomposition

Abstract

Title: Investigations on the Structural and Kinetic Features of Amyloid Aggregation

Index No.: 75/19/Life Sc./26

Amyloid aggregation is associated with a number of severe diseases, including Alzheimer's disease (AD), Parkinson's disease, and type 2 diabetes. Comprehensive understanding of the assembly process that leads to the generation of pathogenic aggregates is imperative for therapeutic interventions. For decades, researchers have been in pursuit of identifying novel structural motifs that dictates amyloidogenesis. On the other hand, self-assembled peptide materials have recently sparked the field of biomedicine and their implications may exceed far beyond amyloid disorder.

This thesis first provides a brief introduction to peptide self-assembly and its implications in disease association and functional biomaterials. Chapter I describes the implications of crucial sequence motifs in the self-assembly of amyloidogenic peptides. Chapter II demonstrates the role of GxxxG repeating motif in regulating the self-assembly and neurotoxicity in Amyloid-beta ($A\beta$) mediated AD pathogenesis. Our results suggest that the $G^{33}xxxG^{37}$ is the primary motif responsible for $A\beta$ neurotoxicity, providing a direct structure-function correlation. Subsequent experimental observations further provide unique insights into the regulatory role of G33 and G37 in membrane-mediated oligomerization of $A\beta40$. We illustrate how nanodiscs facilitate the formation of relatively stable oligomers, which are conformationally distinct from native $A\beta40$ and other minor states of free $A\beta40$ oligomers. Similar SxxxG/GxxxS motif is also present in the C-terminal region of human Islet Polypeptide (hIAPP). By employing different temperatures and sample agitation conditions, we show the significance of the C-terminal hIAPP fragment in generating structurally distinct oligomers. These oligomers could significantly accelerate the hIAPP aggregation, while potentially reducing the overall toxicity. Targeting these motifs, therefore, can be a promising strategy to prevent cell death associated with AD, type II diabetes and other related diseases. Next, we emphasize on how Singular Value Decomposition (SVD) can be employed to reveal hidden patterns and dominant modes of interaction that dictates the complex process of amyloidogenesis. We applied SVD to elucidate the interactions between amyloidogenic peptide and membrane mimic, as well as the complex process of peptide self-assembly, co-assembly, and seeded amyloid growth. Lastly, the unique ability of peptides to self-assemble into diverse nanostructures were investigated for biomedical applications. Three pentapeptide sequences derived from C-terminal of SARS CoV E protein with same amino acid residues but different sequence distributions were investigated. The relationship between peptide sequence arrangement and molecular assembly structure, and how these influence the mechanical properties of the hydrogel were also covered. Moreover, these hydrogels or micellar like supramolecular assemblies with tunable morphology and mechanical properties, are suitable for tissue engineering, injectable delivery, and 3D bio-printing applications.

Dibakar Sarkar
29/02/24

(Dibakar Sarkar)

29/2/24

(Sign of the Supervisor with Seal and Date)

DR. ANIRBAN BHUNIA
Professor
Dept. of Chemical Sciences
BOSE INSTITUTE (GOVT. OF INDIA)
EN 80, Sector-V, Bidhannagar
Kolkata-700091, India

Preface

*The thesis entitled **"Investigations on the Structural and Kinetic Features of Amyloid Aggregation"** is intended to be submitted by the investigator, **Dibakar Sarkar**, under the guidance of **Prof. Anirban Bhunia**, Department of Chemical Sciences, Bose Institute, 700091, India, for the Ph.D. (Sc.) degree at Jadavpur University. The summary of the thesis is presented below.*

Chapter I

Parts of this chapter have been adapted from the following publications:

(A) **Sarkar, D.** and Bhunia, A., 2021. Structural Insights Into the Amyloidogenic Aβ and Tau Species in Alzheimer's disease Pathophysiology: Defining Functional Motifs for Therapeutic Interventions. ***Royal Society of Chemistry Book Chapter.***

(B) **Sarkar, D.** and Bhunia, A., 2023. Delineating the Role of GxxxG Motif in Amyloidogenesis: A New Perspective in Targeting Amyloid-Beta Mediated AD Pathogenesis. ***ACS Bio & Med Chem Au.***

Chapter I covers a brief introduction of amyloid aggregation. Amyloid aggregation resulting from the protein/ peptide self-assembly has been linked with several neurodegenerative and metabolic disorders. The kinetic and structural features of amyloid species make it very intimidating to the interdisciplinary scientific community. Several amyloidogenic motif have been identified and extensively studied to uncover the complex mechanism of amyloid formation. The GxxxG motif present in the C-terminal region of amyloid beta (Aβ) peptide has emerged as one such crucial motif. The implications of this motif in Alzheimer's and related diseases have been discussed in this chapter. While amyloid formation closely associates with several diseases, the self-assembly of short peptides can lead to the development of nanostructured functional materials. These functional materials have emerged as highly promising in the field of biomedical applications. Overall, this chapter explains the background behind the work done in this thesis.

Chapter II

This chapter has been adapted from the following publication:

Chapter II describes the role of GxxxG motif in regulating the self-assembly and neurotoxicity of Aß. The three GxxxG repeating motifs from the C-terminal region of Aß peptide play a significant role in regulating the aggregation kinetics of the peptide. We showed that mutation of these Gly residues to Leu greatly accelerates the fibrillation process but generates a varied toxicity profile. Using an array of biophysical techniques, we demonstrated the uniqueness of the composite Gly residues in these structural repeats. We have employed solvent relaxation NMR technique to display the role played by the surrounding water molecules in determining the corresponding aggregation pathway. We found that the conformational changes induced by the Gly33 and Gly37 mutation resulted in a significantly reduced toxicity in a neuronal cell line. Our results indicate that the $G^{33}xxxG^{37}$ is the primary motif responsible for Aß neurotoxicity, hence providing a direct structure-function correlation. Targeting this motif, therefore, can be a promising strategy to prevent neuronal cell death associated with Alzheimer's and other related diseases, such as type II diabetes and Parkinson's.

Chapter III

In this chapter, we demonstrate the use of membrane scaffold protein (MSP) encased lipid nanodiscs (~8 nm) as a near-native model membrane mimic to investigate the role of G33 and G37 in membrane-mediated oligomerization of Aß40. By using a variety of spectroscopic and microscopic techniques we demonstrate that these Gly residues are highly significant in regulating both self-assembly and membrane-mediated oligomerization of Aß40. We report that the interaction with nanodiscs results in temporal evolution of structurally distinct oligomers. The direct involvement of G33/37 residues in membrane interaction is also reported.

(Nanodiscs preparation and characterization in this work has done by Ms. Dipanwita Roy.)

Chapter IV

This chapter has been adapted from the following publication:

Targeting amyloidosis requires high-resolution insight into the underlying mechanisms of amyloid aggregation. The sequence-specific intrinsic properties of a peptide or protein largely govern the amyloidogenic propensity. Thus, it is essential to delineate the structural motifs that define the subsequent downstream amyloidogenic cascade of events. Additionally, it is important to understand the role played by extrinsic factors, such as temperature or sample agitation, in modulating the overall energy barrier that prompts divergent nucleation events. Consequently, these changes can affect the fibrillation kinetics, resulting in structurally and functionally distinct amyloidogenic conformers associated with disease pathogenesis. In this chapter, we have focused on human Islet Polypeptide (hIAPP) amyloidogenesis for the full-length peptide along with its N- and C-terminal fragments, under different temperatures and sample agitation conditions. This helped us to gain a comprehensive understanding of the intrinsic role of specific functional epitopes in the primary structure of the peptide that regulates amyloidogenesis and subsequent cytotoxicity. Intriguingly, our study involving an array of biophysical experiments and ex vivo data suggests a direct influence of external changes on the C-terminal fibrillating sequence. Furthermore, the observations indicate a possible collaborative role of this segment in nucleating

hIAPP amyloidogenesis in a physiological scenario, thus making it a potential target for future therapeutic interventions.

Chapter V

This chapter has been adapted from the following publication:

(A) **Sarkar, D.**, Saha, S., Krishnamoorthy, J. and Bhunia, A., 2023. Application of singular value decomposition analysis: Insights into the complex mechanisms of amyloidogenesis. ***Biophysical Chemistry***, p.107157.

(B) Paul, A., Kumar, S., Kalita, S., Kalita, S., **Sarkar, D**., Bhunia, A., Bandyopadhyay, A., Mondal, A.C. and Mandal, B., 2021. An explicitly designed paratope of amyloid-β prevents neuronal apoptosis in vitro and hippocampal damage in rat brain. ***Chemical Science***, 12(8), pp.2853-2862.

Amyloidogenesis, with its multifaceted nature spanning from peptide self-assembly to membrane-mediated structural transitions, presents a significant challenge for the interdisciplinary scientific community. In this chapter, we emphasize on how Singular Value Decomposition (SVD) can be employed to reveal hidden patterns and dominant modes of interaction that govern the complex process of amyloidogenesis. We first utilize SVD analysis on Circular Dichroism (CD) spectral datasets to identify the intermediate structural species emerging during peptide-membrane interactions and to determine binding constants more precisely than conventional methods. We investigate the monomer loss kinetics associated with peptide self-assembly using Nuclear Magnetic Resonance (NMR) dataset and determine the global kinetic parameters through SVD. Furthermore, we explore the seeded growth of amyloid fibrils by analyzing a time-dependent NMR dataset, shedding light on the kinetic intricacies of this process. Our analysis uncovers two distinct states in the aggregation of Aβ40 and pinpoints key residues responsible for this seeded growth. To strengthen our findings and enhance their robustness, we validate those using simulated data, thereby highlighting the physical interpretations derived from SVD. Overall, SVD analysis offers a model-free, global kinetic perspective, enabling the selection of optimal kinetic models. This study not only

contributes valuable insights into the dynamics but also highlights the versatility of SVD in unravelling complex processes of amyloidogenesis.

Chapter VI

Short peptide-based supramolecular hydrogels hold enormous potential for a wide range of applications. However, gelation of these systems is very challenging to control. Minor changes in the peptide sequence can significantly influence the self-assembly mechanism and thereby the gelation propensity. The involvement of SARS CoV E protein in the assembly and release of the virus suggests that it may have inherent self-assembling properties that could contribute to the development of hydrogels. Here, we explored three pentapeptide sequences derived from C-terminal of SARS CoV E protein with same amino acid residues but different sequence distributions and discovered a drastic difference in the gelation propensity. By combining spectroscopic and microscopic techniques, we demonstrated the relationship between peptide sequence arrangement and molecular assembly structure, and how these influence the mechanical properties of the hydrogel. The present study expands the variety of secondary structures for generating supramolecular hydrogels by introducing the 3_{10}-helix as the primary building block for gelation, facilitated by a water-mediated structural transition in to β-sheet conformation. Moreover, these Fmoc-modified pentapeptide hydrogels/supramolecular assemblies with tunable morphology and mechanical properties are suitable for tissue engineering, injectable delivery, and 3D bio-printing applications.

('References' are given at the end of each chapter. Additionally, a list of publications has been appended at the end of the thesis.)

Contents

Chapter I

Peptide Self-Assembly and its Implications in Amyloid Disorder and Functional Biomaterials

Parts of this chapter have been adapted from the following publications:

(A) **Sarkar, D.** and Bhunia, A., 2021. Structural Insights Into the Amyloidogenic Aβ and Tau Species in Alzheimer's disease Pathophysiology: Defining Functional Motifs for Therapeutic Interventions.

(B) **Sarkar, D.** and Bhunia, A., 2023. Delineating the Role of GxxxG Motif in Amyloidogenesis: A New Perspective in Targeting Amyloid-Beta Mediated AD Pathogenesis. ***ACS Bio & Med Chem Au.***

1.1. Amyloid

The journey from the initial identification of amyloids to the near-atomic resolution structural elucidation has been nearly 400 years long.[1] A large number of proteins/peptides have been found to form amyloid that is associated with disease pathogenesis.[1-3] Despite the immense knowledge acquired on amyloid proteins and peptides, the detailed structural information is still inadequate. Typically, amyloid deposition involves the self-association of unfolded/partially folded protein/peptide into β-sheet rich mature fibrils via oligomeric intermediates.[3, 4] The characteristic fibrillar amyloid species share a common X-ray diffraction fingerprint,[5] in which the β-strands are stacked perpendicularly to the long axis of the fibril, separated by ~4.7-4.8 Å. Thus, amyloid fibrils adopt the canonical cross-β structure.[6] However, their molecular architectures are more complex and elaborate. In spite of the detailed amyloidogenic fibrillar structure well-described in literature, recent studies have shifted the focus to the pre-fibrillar species owing to their functional involvement in disease pathophysiology.[7, 8] The structural transition of amyloidogenic peptide and protein monomers involves a lag phase before forming oligomers.[9] The oligomeric intermediates are short-lived and quickly convert into proto-fibrillar species in an exponential/growth phase before maturing into the fibrillar structures, reaching the plateau/saturation phase.[10] Recent studies have shown the functional association of the dynamic intermediate oligomers and proto-fibrillar species in the disease etiology.[11] Oligomers are often found to be highly toxic compared to the monomer as well as the mature fibrils.[12] Thus, to adopt efficient therapeutic strategies, it is essential to gain structural insight into these rapidly changing landscapes of amyloidogenic intermediates, defining target motifs. Hence it is a tedious task to understand amyloid diseases because of the widespread structural variations of amyloid species, with different clinical expositions.

1.1.1. Factors influencing amyloid aggregation

Various intrinsic and extrinsic factors play a significant role in modulating the amyloidogenic propensity.[13-15] Intrinsic factors like the primary sequence of a protein are determinants of its aggregation propensity.[13] Mutation in the protein often leads to an increased/decreased fibrillation propensity.[16] Likewise, pH, temperature, and salt concentration are the major extrinsic factors influencing aggregation kinetics and fibril structure.[14, 17] Depending on the fibril growth conditions, a variety of fibrillar structures have been observed. Such differences in the structures may create a diverse level of toxicity. For example, amyloid β-40 (Aβ40) fibrils with different molecular structures have exhibited different toxicity levels in primary neuronal cell cultures.[18] Furthermore, solid-state NMR measurements of Aβ40 and Aβ42 fibrils prepared by seeded growth from the Alzheimer's disease (AD) brain cortex extracts showed a correlation between structural variation and AD phenotypes.[19] The use of repeated seeding steps to amplify early nucleating or fast-growing fibrils within a sample, for example, could result in a kinetically favored structure, which might differ from the most thermodynamically stable structure.[20] Moreover, the *in vivo* microenvironment is likely to differ significantly from environments accessible *in vitro* and may be affected by conditions promoted by AD.[21] Thus, understanding the molecular architecture of amyloid fibrils under disease-associated conditions may be an essential step towards developing therapeutic interventions based on targeting the fibrils themselves or the processes that generate them. Fortunately, recent developments in structural biology techniques, including solution- and solid-state NMR spectroscopy and cryo-electron microscopy, have finally paved the way for structural elucidation of amyloid fibrils.

1.1.2. Mechanistic insight into amyloidogenesis: defining the intermediate steps

Unfolded or partially folded monomeric precursors undergo structural transition, assemble into the oligomeric intermediates, typically seen for most amyloids.[22] The oligomers are transient in nature and eventually leads to fibril formation.[10, 23] The time dependence of fibril formation has been monitored by measuring the fluorescence intensity of the amyloid-sensitive dye thioflavin-T (ThT).[24] The molecular steps involved in the fibrillation process and the associated rate constants can be quantitatively analyzed from the ThT kinetics. The development of various mathematical models has improved our understanding of the kinetics and the mechanism of fibril formation.[25-27] One of the most exciting outcomes from such kinetic analysis has been the discovery of nucleation-dependent fibrillation of Aβ.[26] Monomeric species assemble into
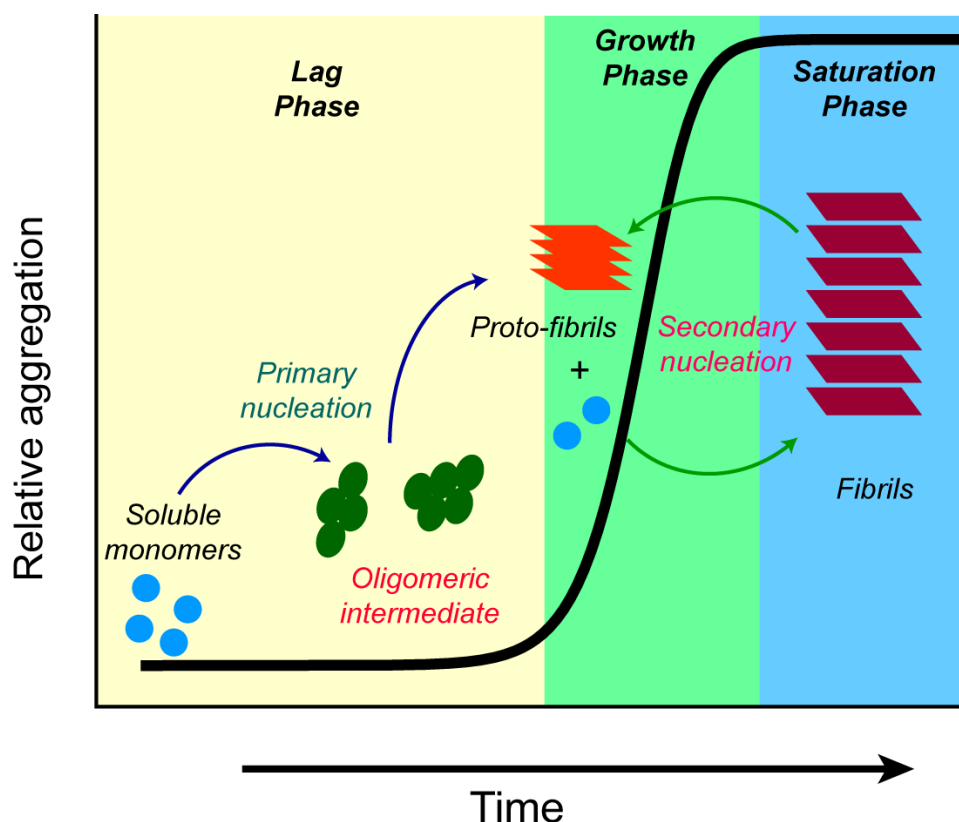
Figure 1.1. Schematic representation of a typical amyloid aggregation growth kinetics and the microscopic steps involved. The initial phase is the lag phase, where monomers self-assemble into oligomeric intermediates, followed by a rapid growth phase, ending in the saturation phase.

disordered oligomers through primary nucleation events, which then undergoes structural conversion into forms that can grow by elongation through the addition of more monomers (Figure 1.1).[28] During fibril formation, secondary nucleation may play a significant role, and in some cases, can dominate the overall aggregation behavior.[26] Secondary nucleation act as a positive-feedback loop that leads to an exponential increase in the proliferation of fibrils. It is important to understand each process and how they combine to determine the rate of fibril assembly, which is vital for the elucidation of the mechanism of fibril formation.

1.2. Structural correlation of Aβ pathological aggregates in AD etiology

AD is a severe neurodegenerative disorder, characterized by progressive impairment of cognitive function and memory loss. To date, there are over 45.0 million AD cases worldwide, enlisting it as the fifth most prevalent cause of death on a global scale and the number is growing

at an alarming rate.[29] By 2050, the number of individuals with dementia is expected to cross over 120 million.[30] On top of that, the emotional and financial burden on patients, their families, and communities are enormous. As of now, the accumulation of Aβ peptide into extracellular amyloid plaques is considered to be the distinct morphological hallmark of AD.[31] However, the in-depth molecular mechanism of Aβ pathway driving AD pathogenesis is still unclear. The pursuit for novel structural motif that can shed the light on the key functional attributes is a primary focus in the study of protein folding disorders, which includes AD as well. Decades of research on AD have centered on the Aβ pathway, highlighting its significance in understanding the disorder. The diversity in the Aβ pathway and the possible silent tracks which are yet to discover, makes it exceedingly intimidating to the inter-disciplinary scientific community. Over the course of AD research, Aβ has consistently been at the forefront of scientific inquiry and discussion. The revolutionary work of Glenner and Wong back in 1984 first publicized the primary structure of Aβ peptide.[32] The generation of various Aβ isoforms from the sequential processing of amyloid precursor protein (APP) by β-secretase and γ-secretase is well established through the amyloid hypothesis.[33] The sequences of Aβ40 and Aβ42 isoforms are identical except for the C-terminal amino acids I41 and A42, and yet they display dramatically different behaviors both *in vivo* and *in vitro*.[34] While the 40-residue peptide Aβ40 represents the most abundant Aβ isoform in the brain, Aβ42 is more aggregation-prone and toxic in nature.[34] Naturally, the sequence itself holds the key to its characteristic behavior. Various biophysical techniques, NMR spectroscopy, molecular dynamic (MD) techniques, and X-ray crystallography have provided extensive structural and kinetic information on both full-length Aβ peptide as well as different fragments of the Aβ peptide.[27, 35] Over the years, new findings on the proteolytic processing of amyloid precursor protein (APP),[36] potential evidence of highly toxic transient Aβ oligomers,[8, 37] and presence of high degree of polymorphism[38] in fibril structures have created an intricate scenario. In this rapidly evolving landscape, the conserved GxxxG motifs present in the C-terminus of Aβ appears to be a noteworthy target.

1.3. The "GxxxG" structural motif

The GxxxG motif stands out as the most prevalent sequence motif in naturally occurring transmembrane (TM) proteins and some soluble proteins that comprise at least one α-helix.[39] These TM motifs are essential for engaging in oligomeric interactions. Interestingly, Gly residues within a GxxxG motif exhibit a higher degree of conservation compared to random Gly residues.

(A)

Protein	Sequence

GPA: V_{62}QLAHHFSEPEITLIIFG_{79}VMAG_{83}VIGTILLISYGIRRLIKK$_{101}$

BNIP 3: R_{146}NTSVMKKGGIFSAEFLKVFLPSLLLSHLLAIGLG_{180}IYIG_{184}RRLTTS$_{190}$

(B) (C)
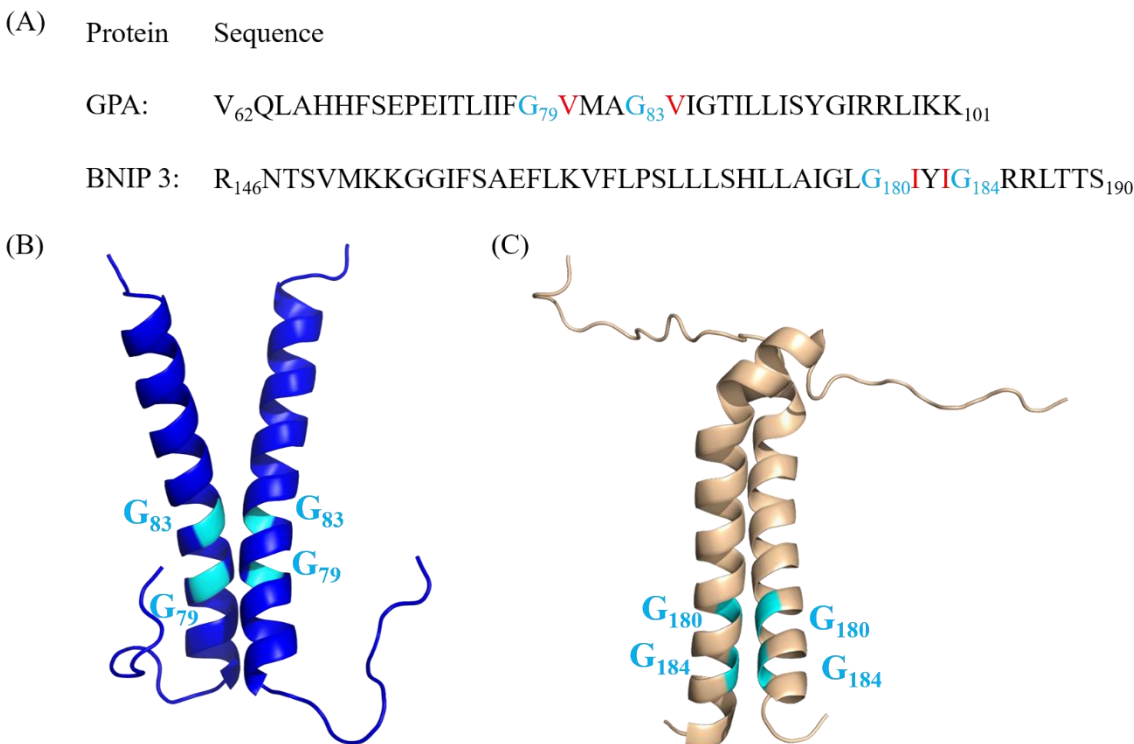
Figure 1.2. (A) Amino acid sequence of TM domain of GPA and BNIP3 containing GxxxG motif. The neighboring β-branched residues are highlighted (red). Helix-Helix association in (B) GPA (PDB file 1AFO), and (C) BNIP3 (PDB file: 2J5D) homodimer mediated by GxxxG motif. Gly residues within the GxxxG motif are highlighted with a cyan color.

The three residue spacing allows the Gly residues in a GxxxG motif to lie on one face of the helix.[39, 40] The lack of side chain in Gly allows the two helices to come into close proximity, thereby increasing van-der-Waals forces between adjacent helices, stabilizing the helix−helix association and thus forming a helical dimer. The flat surface provided by the Gly residues can offer a wide range of specific interactions that can manifest around the GxxxG motifs. The presence of β-branched amino acids such as Val, Ile, and Thr, often found at adjacent positions (as shown in Figure 1.2A), facilitates Gly to acts as a molecular notch, thereby strengthening the helix−helix interactionsinteractions.[41] The GxxxG motif therefore can be considered as a framework for the dimerization of TM α-helices.

Although the GxxxG motifs are abundant in human transmembrane domain (TMD) sequences, the extent to which these motifs participate in TMD interactions remains inconclusive. With the limited number of studies, one can only assume certain role in TM helix-helix dimerization. For example, a conserved GxxxG motif located in the unique membrane-spanning

segment of the mitochondrial ATP synthase is involved in the dimerization via inter- and intramolecular TMD interactions.[42] The glycophorin A (GPA) is one of the best characterized model protein to explore the conformation and behavior of intramembranous segments of single-pass TM proteins.[43] The TM domain largely consists of hydrophobic amino acid residues. By using solution NMR, MacKenzie et al.[44] showed that the interaction surface is composed of two ridges and their associated groove. The side chains of V80 and V84 form one ridge that packs against the groove created by G79 and G83 of the opposite monomer (Figure 1.2B). The combined results of site-directed mutagenesis and solution NMR spectroscopy suggest that these Gly residues stabilize dimerization by providing a surface for packing, allowing helix proximity and by entropic effects.[44, 45] The GxxxG element thus appears to be the most crucial part of the GPA interaction motif. Similarly, the pro-apoptotic protein BNIP3 (Bcl-2 Nineteen-kDa interacting protein 3) comprising a GxxxG motif, has also been found to form the right-handed parallel TM dimer.[46] Solution NMR study showed that the dimer is stabilized by hydrophobic side chain contacts of A176, I177, I181, and I183 and tight packing due to the presence of A176, G180, and G184 in the sequence spanning -A^{176}XXXG^{180}XXXG^{184}- residues (Figure 1.2C).[47] This motif also appears to be essential for the proper alignment of the side chains in the His-Ser node required for formation of hydrogen bonds. In addition, the aromatic residues F157, F161, and F165 forms a hydrophobic cluster which is stabilized by intra- and intermonomeric stacking interactions. Computational analysis has suggested that Gly residues are required at certain positions not only to act as hydrogen bonding donors but also for reducing the steric barrier for large side-chain amino acids at neighboring positions; Thus providing a rational structural understanding of the occurrence of GxxxG motifs in TM homodimers.[48]

A striking similarity between these segment and Alzheimer's Aβ peptide is that both can form helical dimer in presence of membrane mimicking detergent-micelle.[49, 50] The hydrophobic environment of a lipid bilayer, which facilitates hydrogen bonding is likely to promote dimerization. It is noteworthy to mention that many TM proteins have been identified to be dimeric in nature, with TM segments resembling those found in both GPA and APP. Therefore, it is reasonable to speculate that APP, which also possess analogous GxxxG segments within its TM domain, exists as a dimer in the lipid bilayer.[51] Studies have shown substantial evidence of SDS-stable dimeric configurations for both Aβ40 and Aβ42, suggesting that these Aβ dimers are linked with the lipid raft domains within the membrane.[49, 52] In this context, we can assume that when

APP is sequentially processed, its TM domains retain their association, forming dimeric Aβ peptides just as they existed in the intact APP molecules. However, the impacts of these intramembranous peptides are likely dependent on their site of generation and duration within the lipid bilayer, necessitating further investigation to fully comprehend their functional implications in Alzheimer's disease.

1.3.1. Influence on APP processing and subsequent Aβ production

From proteolytic generation to accumulation into amyloid, the Aβ pathway has been the center of attraction in AD pathophysiology (Figure 1.3). Typically, the proteolytic cleavage of APP by β- and γ-secretases within the lipid bilayer leads to the generation of Aβ peptides with predominant lengths of 40 (Aβ40) and 42 (Aβ42) amino acids.[53] The β-cleavage of APP first produces a 99 residue, membrane-anchored APP C-terminal fragment (βCTF or C99), which then further cleaved by the γ-secretase to generate Aβ. However, the escalating number of proteolytic enzymes with the ability to cleave APP and APP-like molecules suggest that Aβ peptides might be generated in ways other than through the coordinated actions of the β- and γ-secretases.[54] Nevertheless, a large number of the studies are focused on the γ-secretase complex, which mainly consist of: presenilins (PS), nicastrin (NCT), anterior pharynx defective 1 (APH-1), and presenilin enhancer 2 (PEN-2).[55] It is generally accepted that after the cleavage by γ-secretases, a large amount of Aβ peptides jump from membrane to the extracellular space The charged and polar amino acids at the N-terminus wield sufficient drag to pull the remaining hydrophobic region through the lipid bilayer and into the aqueous medium.[56]

In this context, the role played by the GxxxG motifs have been investigated by several groups.[57-59] Munter et al. showed that the γ-secretase cleavages of APP are intimately linked to the dimerization strength of the substrate TMS and these motifs are liable for facilitating the production of highly toxic Aβ42.[57] Mutation of the consecutive $G^{29}xxxG^{33}xxxG^{37}$ motifs by Leu or Ile was found to reduce the Aβ40 and Aβ42 production drastically.[60] Interestingly, the mammalian multipass membrane protein APH-1 also contains a conserved transmembrane $G^{122}xxxG^{126}xxxG^{130}$ motif that partake in helix-helix interaction and is essential for the stable association of APH-1 with presenilin, nicastrin, and PEN-2, forming the γ-secretase complex.[59] Thus, the interaction between APP and other proteins within the γ-secretase complex is likely to be influenced by the GxxxG motif.
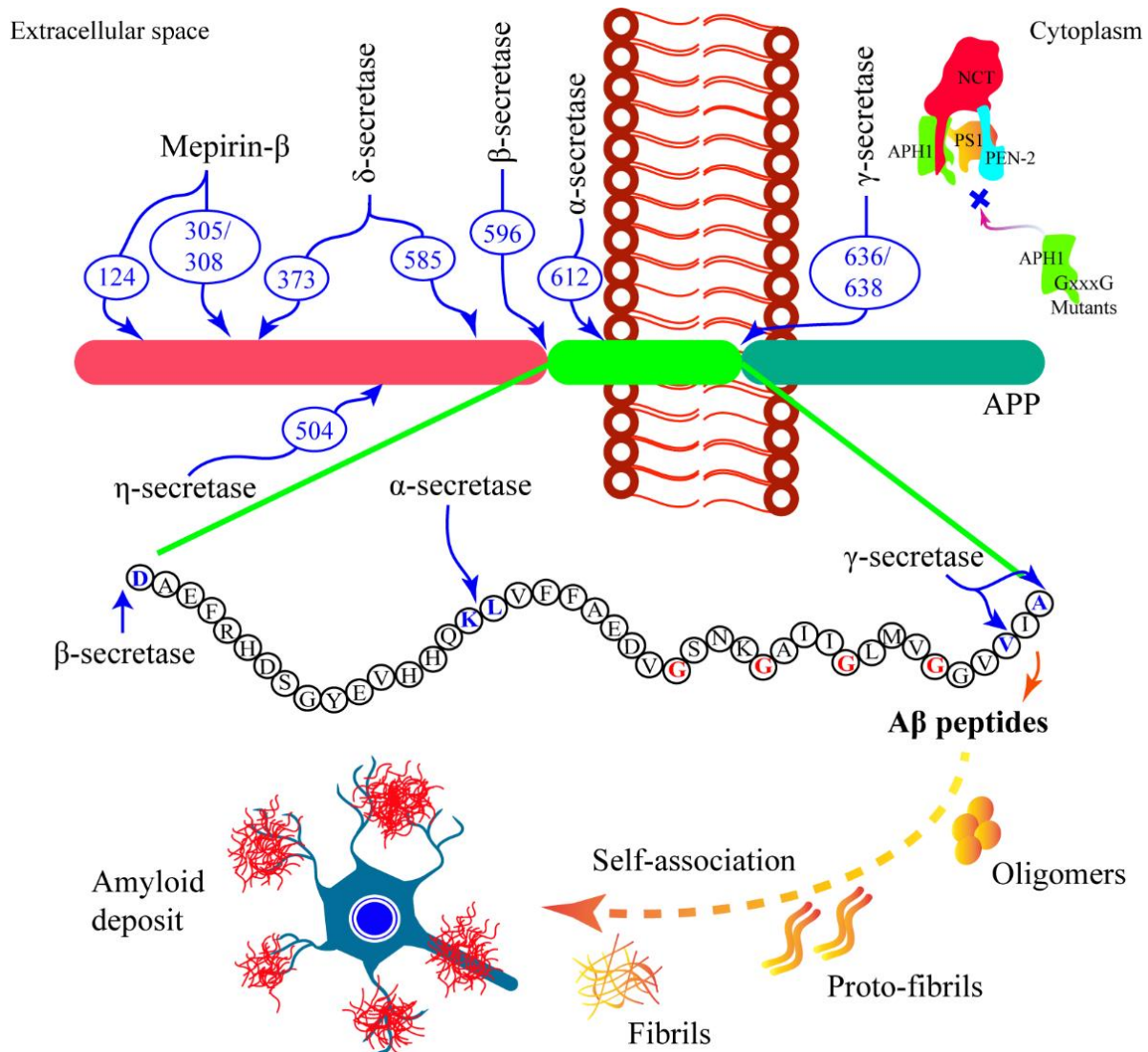
Figure 1.3. The Aβ pathway involving APP processing, generation of Aβ peptides of various length followed by amyloid deposition via multiple steps. APP cleavage sites of various proteolytic enzymes are indicated by blue arrows. Gly from the GxxxG motifs are in red. Numbering is according to the sequence of APP695.

Several familial mutations in APP such as A21G (Flemish), E22Q (Dutch), E22G (Arctic), E22K (Italian), and D23N (Iowa), have been found to influence the proteolytic processing of APP and associated with increased Aβ production.[61, 62] Among them, the A21G mutation appears to be particularly intriguing as A21G mutation generates a fourth consecutive upstream GxxxG motif. The A21G mutation was found to have a strong influence on intramembranous processing by the γ-secretase complex and increases the Aβ production by approximately 2-fold.[62] A recent study by Tzu-Chun Tang et al. revealed that A21G mutation induce conformational changes in the

structure of C55, the first 55 residues of the β-CTF which subsequently leads to an increased Aβ production.[63] They showed that the A21 residue resides at a breakpoint between a well-defined β-strand and the TM helix of β-CTF. The introduction of an additional GxxxG motif by A21G mutation destabilizes the β-sheet structure and increases the α-helical structure of the $G^{25}xxxG^{29}$ sequence, thereby stabilizing the TM dimers through GxxxG motifs.[63, 64] Conversely, alanine substitutions in the GxxxG motif of β-CTF causes decrease in the level of long Aβ species such as Aβ42 and Aβ43 and a concomitant increase in short Aβ (i.e., Aβ34, Aβ35, Aβ37, and Aβ38) production.[57, 65]

1.3.2. Regulation of Aβ aggregation and subsequent neurotoxicity

The GxxxG repeated motif from the C-terminus represent a unique feature of APP as well as of Aβ peptides. Structurally, this motif plays an important role in stabilizing both helix-helix association and sheet-to-sheet packing. Typically, the two Gly residues in a GxxxG motif are placed on the same side of a transmembrane helix or on the same face of a β-sheet. The non-chiral nature and small side-chain of Gly offer flexibility, contributing to peptide dynamism and facilitating membrane insertion through pore formation. Recent studies have shown that several amyloid fibrils, including those linked with AD take parallel in-register β-sheet, where Gly can create molecular notches or grooves on the surface of the β-sheet, extending along the length of the amyloid fibril.[66] The secondary conformation of the GxxxG motifs are thought to be highly dependent on the surrounding residues (i.e. hydrophobic or polar). Solid state NMR analysis of Aβ40 and Aβ42 peptides has revealed that the $G^{25}xxxG^{29}$ motif, containing polar amino acids in its sequence to be part of a β-hairpin structure.[67] Whereas the second and third GxxxG motifs in the Aβ peptides surrounded by hydrophobic β-branched residues adopt β-strand or β-sheet secondary structure.[68] Ahmed *et al.* showed that the solvent accessible turns at H13-Q15, G25-G29 and G37-G38 facilitate the compact folding of the peptide, by placing F19 in contact with L34.[69] NMR derived structural models have shown that in both Aβ40 and Aβ42, the surface grooves created by Gly33 and Gly37 can stabilize sheet-to-sheet packing by providing space for large amino acid side chains.[70] Moreover, computational studies have revealed that Gly to Leu substitutions at positions 33 and 37 within Aβ42 leads to a notable increase in the conformational instability.[71]

Interestingly, the three consecutive GxxxG motifs present in the transmembrane sequence of prion protein (PrP) have significant role in organization of transmembrane helixes and packaging of amyloidal fibers.[40, 72] Both toxic Aβ peptides and PrP peptides have been found to form ion channels that ultimately leads to neuronal cell death, suggests a possible common pathological role for these motifs.[73, 74] Notably the incidence of such structural motif in a number of bacterial channel proteins that induce ion channel formation further support the ion channel hypothesis.[75, 76] By G→L substitution in Aβ (particularly the G37L substitution), Kim et al.[77] demonstrated the significance of the Gly residues of the consecutive GxxxG motif, particularly the G37 in pore formation in synthetic membranes and inducing toxicity in cultured Neuro 2a neuroblastoma cells. Later Hung et al.[78] reported that the GxxxG repeat motif significantly modulate the formation of toxic Aβ oligomers. G→L mutants of Aβ42, generally termed as GSL peptides (G25L, G29L, G33L or G37L) showed increased rate in amyloid formation and a decrease in the formation of toxic oligomeric species. When treated against primary mouse cortical neurons, all mutants were found to be less toxic than wild type Aβ with the G33L and G37L substitutions having the greatest reduction in toxicity, suggesting a direct correlation with oligomer formation. Harmeier et al. reported that substitutions at G33 of Aβ42 by Ala or Ile dramatically reduced toxicity in neuroblastoma cells and while generating higher molecular weight oligomers *in vitro*.[79] They showed that unlike wild type Aβ, G33-substituted Aβ could not inhibit hippocampal LTP or disrupt eye formation in a Drosophila transgenic Aβ expression model. In addition to various models such as cell dysfunction, cell death, synaptic alteration, or tau phosphorylation the G37L substitution was further tested in a transgenic *C. elegans* model.[80] The Aβ G37L was actually found anti-toxic, thereby supporting the GxxxG-mediated Aβ oligomer formation hypothesis.

The highly amyloidogenic core (residues 60–85) of α-synuclein, the protein associated with Parkinson's disease also contain several glycine residues including a AxxxG sequence which would result in a similar molecular surface. In a recent study, Sakagashira et al. reported that S→G missense mutation at position 20 of the hIAPP has been associated 4.1% of Japanese patients with type 2 diabetes and 10% of those with early-onset type 2 diabetes.[81] Later the S20G substitution in hIAPP was found to be more amyloidogenic and cytotoxic.[82] This is interesting because such mutation will lead to the occurrence of a GxxxG motif.

1.3.3. GxxxG motif stabilizes Ion channel like pores through Cα—H···O interaction

Several TM protein and microbial peptides have been found to actively form membrane channels, with GxxxG motifs recurring in their sequences, emphasizing their significant role in ion channel formation. For instance, the VacA protein from *Helicobacter pylori* contains three tandem GxxxG motifs within its N-terminal hydrophobic region, which are crucial for oligomerization and subsequent channel formation.[75] Mutations in the Gly residues within these motifs, particularly G14 and G18, have been shown to disrupt oligomerization and reduce the protein's ability to form channels, leading to decreased cytotoxicity. Interestingly, ion channel-like pore formation is also a critical step in amyloid-mediated toxicity. Amyloid-forming peptides like Aβ, α-synuclein, and hIAPP have demonstrated the ability to form ion channel-like pores in various membrane mimics.[73, 83] Studies have suggested that the Aβ-membrane interaction can significantly impact the aggregation pathway, although the precise molecular mechanism of this association remains unclear. The Aβ-membrane interaction has been found to induce conformational changes in the peptide secondary structure, thereby regulating the fibrillation process.[84] In addition to membrane-assisted structural transition, cell membrane disruption is also a significant factor contributing to Aβ neurotoxicity.[85] In fact, it has been proposed that during fibrillation, Aβ monomers forms ion selective pores by aggregating on to the membrane, followed by nonspecific fragmentation of the lipid membrane in a detergent-like mode.[86] Moreover, Aβ-membrane binding is greatly influenced by several factors like membrane composition, charge, fluidity, and curvature.[87] For example, the negatively charged phospholipid DMPG has been identified to accelerate the fibrillation of Aβ.[88] Studies by Matsuzaki and co-workers revealed that Aβ40 specifically interacts with GM1 and undergo conformational transition into an anti-parallel β-sheet structure with higher toxicity than that of fibrils formed under aqueous solution.[89] Our group has recently demonstrated the impact of different membrane compositions on Aβ40 aggregation at an atomic resolution.[90] Through a comparison between a simplified blood-brain barrier (BBB) mimic, POPC/POPG/cholesterol/GM1 (PPCG), and the native BBB composed of total brain lipid extract, we have described the molecular events underlying membrane-induced amyloid aggregation. Specifically, we have highlighted the crucial role of hydrophobic interactions between the acyl chains of lipid and amino acid residues spanning K16-K28 and I31-V36 in forming transient conformations during peptide aggregation, thereby modulating the overall
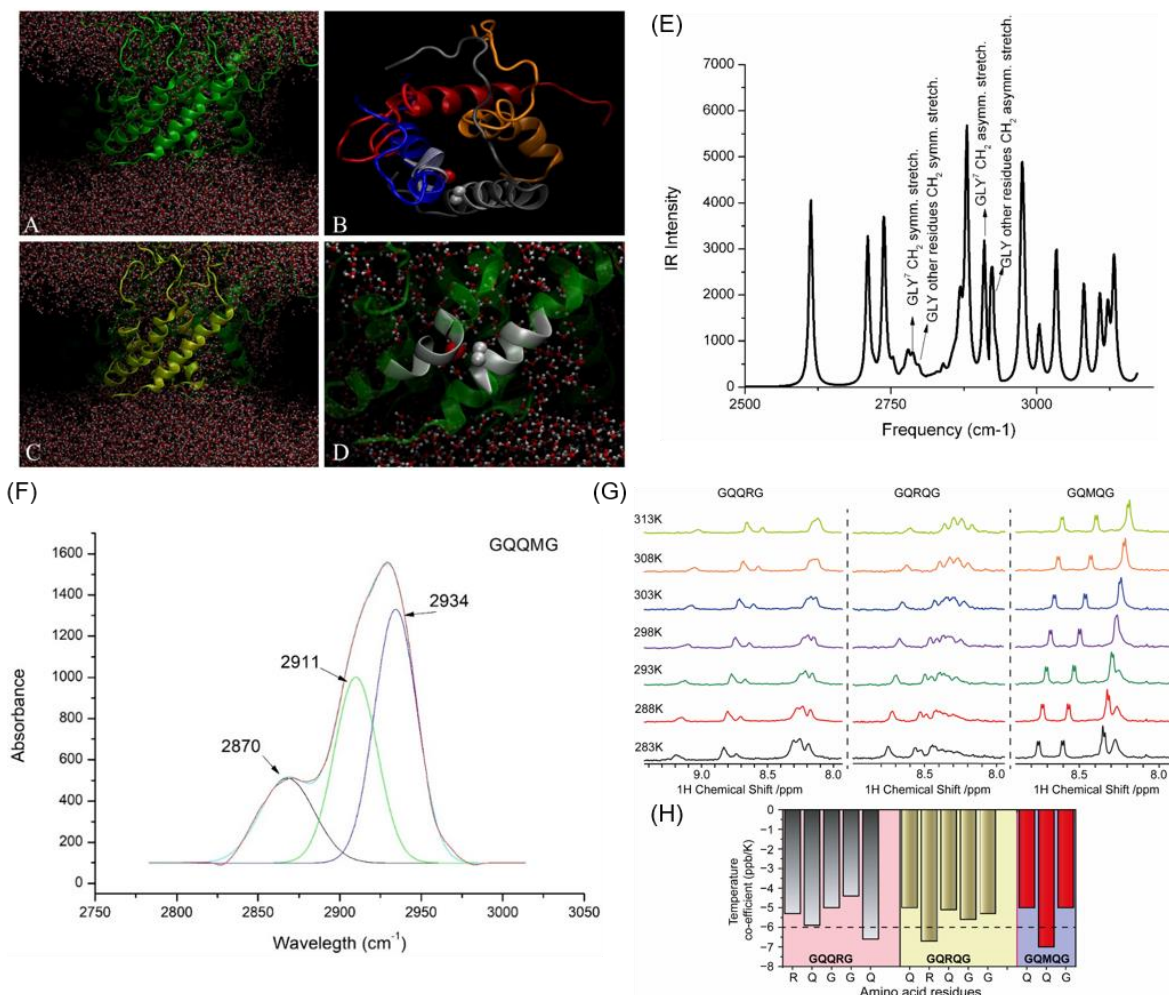
Figure 1.4. (A) An ion-channel-like pore is formed by a 24-mer of Aβ (1-40) embedded within a POPC bilayer, allowing water to cross the bilayer. (B) A top-down of the tetramer ion-channel-like pore. (C) The tetramer organizes into a structured pore. (D) Two intersecting α-helices within the tetramer create an angle of 39 ± 5 degrees, with gray spheres symbolizing the two Cα-hydrogens of Gly and the red sphere representing the C=O carbonyl oxygen. (E) The QM-simulated IR spectrum of a tetramer ion-channel pore, displaying the vibrational behavior of two neighboring Aβ40 helices. (F) Deconvoluted ATR-IR spectrum of pentapeptides indicating Cα—H···O hydrogen bond. (G) Temperature-dependent NMR spectra of pentapeptide in CD_3OD. (H) Bar diagram plot of the temperature coefficients for amino acid residues of individual pentapeptides. Reproduced from ref. 92 under Creative Commons Attribution (CC BY) license.

aggregation dynamics. Now, the question that arises is: how does the involvement of the GxxxG motif contribute to it?

According to liquid-chaperone model, amyloidogenic proteins are transported into the hydrophobic membrane core if a stable complex is formed between the polypeptide and free lipids

in the aqueous phase.[91] This complex, due to its higher hydrophobicity compared to the individual polypeptide, can then insert into the membrane. Interestingly, the GxxxG motif plays a crucial role throughout the process. Studies have shown that the presence of the GxxxG sequence on GPA and Intrinsically disorder proteins (IDPs) play a significant role in stabilizing ion-channel-like pores through weak hydrogen bonds between Cα—H of an α-helix and C=O of the neighboring helix. However, conflicting viewpoints exist in the literature regarding the stabilizing function of the GxxxG motif. Multi-scale molecular dynamics simulations of Aβ40 inserted into a POPC membrane revealed that the peptide self-assemble into a truncated cone-shape aggregate, causing a change in membrane curvature.[92] These aggregate exhibited ion-channel-like pores, facilitating the passage of water and ions across the bilayer (Figure 1.4A). This phenomenon is explicable through the frustrated-helix model, which attributes the change in bending radius to electrostatic repulsions among exposed hydrophilic amino acids.[93] Furthermore, the Aβ40 peptides predominantly adopted α-helix conformation, forming twisted dimers and trimers at an average angle of 39 ± 5 degrees. The aggregate within the membrane consisted of small transmembrane subunits composed of four Aβ molecules, resembling ion channels (Figure 1.4B). Quantum mechanics (QM) calculations revealed an inter-chain interaction between residues G29 and D23, where the Hα—O=C distance was 3.32 Å. (Figure 1.4E). Intra-chain interactions between Gly and other residues were also observed. Moreover, the formation of a lock between two neighboring α-helices facilitated by a GxxxG motif was suggested by molecular dynamics and QM calculations.

Several pentapeptides encompassing the GxxxG motif was investigated in order to evaluate the effect of hydrophobic environment. As depicted in Figure 1.4F, the ATR-IR spectra exhibited a band approximately at 2910 cm^{-1} across all investigated pentapeptides, indicating intermolecular interaction between the Gly of a pentapeptide with its neighboring C=O group. Temperature-dependent solution NMR study further confirmed the formation of weak hydrogen bonding in hydrophobic environment as opposed to water. The temperature coefficients for the backbone amide protons ranged from -4 to -6 ppb/K in CD_3OD, which can be attributed to some degree of conformation inclination resulting from the close proximity of the Gly amide proton to Cα—H⋯O hydrogen bonding (Figure 1.4G). Hence, the GxxxG motif can induce hydrogen bonding under hydrophobic environments, regardless of the intermediary residues between these Gly. This phenomenon could be an intrinsic trait of the motif, arising from the lack of steric hindrance in the Gly residue.

1.3.4. GxxxG motif targeted inhibitors

The aggregation of Aβ peptides into amyloid fibrils and prefibrillar intermediates is widely recognized as a key factor in AD pathogenesis. However, inhibiting Aβ aggregation have been extremely challenging. The intricate nature of Aβ aggregation, characterized by diverse intermediate forms and pathways, complicates therapeutic intervention. The persistence of polymorphism in Aβ structures, from oligomers to fibrils, correlating different phenotypes, hinders efficient drug design strategies.[19] Even a single amino acid substitution can alter fibrillation kinetics and toxicity significantly. The synergy between diverse oligomers and fibrils, alongside interactions with metal ions and cellular partners, further complicates matters.[94] Targeting oligomer formation may hold promise, but a lack of high-resolution structures and the dynamic nature of these species pose significant challenges. Furthermore, the formidable blood-brain barrier impedes effective drug delivery. Efforts to develop small molecules for Aβ inhibition have been stymied, as protein-protein interaction interfaces, crucial for inhibiting Aβ aggregation, are notably intricate.[95] Protein-protein interaction regions encompass substantial surface areas, while traditional small molecule interaction regions fall short.[96] Additionally, these interaction surfaces lack well-defined features for small molecules to dock favorably, and the plasticity of protein surfaces can thwart inhibition.[97] These formidable obstacles limit the development of Aβ aggregation inhibitors, rendering the task exceedingly challenging.

Nonetheless, a great number of inhibitors have been identified, designed and applied in order to prevent Aβ-amyloidogenesis.[98, 99] However, due to the lack of high-resolution oligomeric structures, developing specific inhibitors targeting oligomer or fibril formation have been very challenging. Some of the potent peptide-based designed inhibitors of Aβ fibrillation are listed in Table 1.1. So far, most of the design strategies include short peptide sequence analogous to part of the native sequence of the protein or peptide responsible for fibril formation.[100, 101] This approach is based on the fact that the short peptide fragments would self-recognize and thereby should bind to the homologous sequence in the native protein. The most popular approach for the inhibition of Aβ amyloidogenesis have been the design of peptides derived from the central hydrophobic cluster (L17-A21) of Aβ.[102, 103] Since, amyloid fibrils usually adopt a cross β-structure, structure-based agents such as β-sheet breakers have also been formulated to inhibit fibril formation.[104, 105] These inhibitory peptides are targeted to disrupt β-sheets by blocking the hydrogen bond formation between β-strands. In addition to peptide mimics, alterations in short peptides such as N-

methylation and peptide cyclization have shown enhanced conformational stability with significantly increased inhibitory effect on amyloid aggregation.[106]

The C-terminal segment of Aβ, which contains GxxxG motifs, has recently been discovered to have a significant impact on amyloidosis and demonstrate toxicity. Targeting this region has emerged as a promising strategy to prevent fibril formation. Peptide-based inhibitors that specifically target the GxxxG motif have been recently developed and tested in *in vitro* and *in vivo*. Interestingly, while GPA transmembrane sequence adopts an α-helical conformation, the truncated GPA (70-86) peptide was found to form β-sheet fibrils resembling those of Aβ42.[107] Liu et al. identified the Gly residues G79 and G83 as key components that stabilize the sheet-to-sheet packing in the fibril structure. To disrupt this packing, they developed an 8-residue peptide, RGTFEGKF-NH$_2$, which specifically interact with the Gly grooves on the fibril surface. The inhibitor was strategically designed to bind to the G-M-G face of GPA (70-86), with the bulky Phe side chains of the inhibitor interacting with the Gly backbone of the peptide. On the opposite face of the inhibitor, it carries charged and polar residues (R-T-E-K), intended to improve the solubility of the peptide. Later, Steven O. Smith and coworkers designed a series of peptides having alternating small and bulky residues on one face of a β-strand complementary to the GxMxG sequence in the C-terminus of Aβ peptides.[70] Solid-state NMR spectroscopy confirmed that these designed inhibitors effectively disrupted the packing between the M35 residue and various Gly residues within the GxxxG motifs. Some of these inhibitor peptides demonstrated significant reduction in the Aβ42 induced toxicity on cultured rat cortical neurons, highlighting their potential therapeutic value.

Studies involving curcumin (diferulomethane) as an amyloid inhibitor have revealed its efficacy in combating both Aβ oligomers and fibrils.[108] Of note, the curcumin molecule possesses two aromatic groups that are separated by a ~13 Å linker, a distance that closely aligns with the spacing between G33 and G37 of the Aβ peptides. This also holds true for several other natural products, providing possible explanations as how they act as amyloid fibril inhibitors.[109] Similarly, fullerene derivatives have shown remarkable potential as anti-amyloidogenic agents.[110] MD simulation studies have provided insights into the inhibitory mechanism, highlighting their interaction with crucial regions including the central hydrophobic cluster (CHC) represented by the LVFFA sequence, as well as the two GxxxG motifs ($G^{29}xxxG^{33}$ and $G^{33}xxxG^{37}$).[111] Since the

amyloidogenic regions of prion proteins and α-synuclein contains GxxxG or AxxxG sequences that hydrogen bond in a parallel and in-register orientation, it strongly suggests that these inhibitors are likely to have broad effectiveness. Furthermore, their ability to interfere and disrupt β-sheet packing should complement the previously designed inhibitors that block β-sheet hydrogen bonding.

Recent studies have elucidated the dock-lock mechanism of fibril formation, where unstructured Aβ monomers transiently associate with the fibril surface before undergoing a slower conformational rearrangement and incorporating into the primary fibril lattice.[112] This process, involving the central K16-A21 and C-terminal M35-V40 regions, plays a critical role in fibrillation and presents a potential avenue for inhibiting amyloidosis. Remarkably, our recent investigation employing a synthetic paratope, SP1, has demonstrated selective binding to the LVFFA epitope, a crucial amyloidogenic region of Aβ peptide.[102] Furthermore, SP1 effectively disaggregated preformed fibrils of Aβ40, leading to the formation of non-toxic species. Solution NMR analysis revealed that SP1 disrupts the essential dock-lock interactions of monomeric Aβ, suggesting molecular interference in the critical domain. Earlier studies have identified a mimotope (B6-C15) with limited resemblance to the C-terminus of Aβ42, which includes GxxxG dimerization motifs.[113] This mimotope was combined with biotinylated TAT at the N-terminus (TAT-B6-C15), resulting in significant inhibition of Aβ42 fibrillation. TAT-B6-C15 also exhibited selective binding to prefibrillar Aβ42 oligomers, displaying no affinity for monomers, trimers, tetramers, fibrils, or ultra-sonicated fragments. Moreover, it effectively countered Aβ42-induced cytotoxicity in human SH-SY5Y neuroblastoma cells. Strategically engineered multifunctional peptide inhibitors have been developed by combining a metal-chelating unit with an anti-aggregating peptidomimetic analog.[114] These inhibitory agents not only impede Aβ aggregation but also possess the capability to chelate metal ions, offering functional prospect against Aβ-metal complex formation and consequently inhibiting diverse forms of Aβ aggregation pathway. Overall, these findings underscore the potential of smartly designed inhibitors as a promising therapeutic candidate against AD and other amyloidosis by selectively targeting key segments involved in amyloidogenesis.

Table 1.1. Designed Peptide Inhibitors Based on Crucial Sequence Motifs in Aβ.

S. No.	Peptide inhibitors	Target motif/structure	Ref
1.	Ac-QKLVFF-NH$_2$	Designed based on CHC and acts as β-sheet breaker	[100]
2.	KLVFFKKKK, KLVFFEEEE	Designed based on CHC and acts as β-sheet breaker	[115]
3.	RYYAAFFARR	Target an extended region (Aβ (11-23)) mainly through hydrophobic and electrostatic interactions and hydrogen bonding interactions.	[116]
4.	iAβ5 (LPFFD), iAβ11 (RDLPFFPVRID)	Act as β- sheet breaker and disassembles preformed fibrils	[105, 117]
5.	Ac-LPFFN-NH$_2$	Acts as a stabilizer of the native and non-aggregative α-helical conformation of Aβ40	[118]
6.	NAP (NAPVSIPQ)	Disassembles preformed fibrils	[119]
7.	RG-KLVFF-GR-NH$_2$, rG-klvff-Gr-Ac	Prevent oligomerization	[120]
8.	NF11 (NAVRWSLMRPF)	Targets both N-terminus and CHC, disaggregates the preformed oligomers and mature Aβ fibrils	[98]
9.	MLRTKDLIWTLFFLGTAVSKKRPKP-NH$_2$, MLRTKDLIWTLFFLGTAVSKKLVFF-NH$_2$	Designed cell-penetrating peptide derived from polycationic sequence of the PrP protein that inhibits Aβ fibrillation and toxicity	[121]
10.	cyclo(17,21)-[Lys17,Asp21]Aβ(1−28)	Cyclic peptide based on CHC that disrupt Aβ fibrils into nontoxic short fibrils and amorphous aggregates	[122]
11.	H$_2$N-A(N-Me)FF(N-Me)VLG-Succinyl-(PEG)$_3$-Adipoyl-G(N-Me)LV(NMe)FFA-NH$_2$	Designed hairpin-like synthetic paratope that prevents Aβ fibrillation by interfering with the dock-lock mechanism	[102]

12.	IIGLMVGGVVIA, VVIA	Based on the C-terminal Aβ sequence and promotes formation of nontoxic amorphous oligomer	[123]
13.	GVVIA-NH$_2$, RVVIA-NH$_2$	Based on the C-terminal Aβ sequence and hinders fibril formation by complex formation	[124]
14.	RGTFEGKF-NH$_2$, RGTWEGKW-NH$_2$	Targets the GxxxG motif	[70, 107]
15.	IGLMVG-NH$_2$	Designed based on the C-terminal Aβ sequence, completely attenuates fibrillation and toxicity	[125]
16.	Pr-IIGL-NH$_2$, RIIGL-NH$_2$	Designed based on the C-terminal Aβ sequence, inhibits Aβ42 fibrillation and toxicity	[126]
17.	WWW, WWP, WPW, PWW	Tripeptides containing Trp and Pro that tightly binds to Aβ fibrils and depolymerize preformed fibrils	[127]

1.3.5. Implications of the GxxxG motif in AD pathogenesis and therapeutic strategies

If we consider that Aβ peptides or fragments of them are the main culprit in AD pathogenesis, a comprehensive road map of Aβ pathway is very much prerequisite before going for clinical trials. While recent updates on APP processing and subsequent amyloid aggregation of Aβ leading to synaptic dysfunction is alarming, the physiological function of either APP or Aβ is still under investigation. It is highly plausible that Aβ peptides compete with the formation of APP dimer and interfere with normal APP function. Several signal transduction mechanisms appears to be regulated by a range of enzymatic reactions, which involve a sequence of proteolytic cleavages within the lipid bilayer.[56] Apparently, GxxxG motif plays a significant part in the cascade of reactions, ranging from APP dimerization to stable association of γ-secretase complex and generation of Aβ peptides.[59] Based on the experimental and computational analysis, this motif is required for certain structural and functional attributes that eventually leads to progress in amyloidosis. If this theory is correct, designing agents that can inhibit specific interactions within the lipid bilayer becomes a priority. Although it looks very intimidating, a number of attempts have been made to inhibit the receptor functions by designing synthetic peptides that mimic portions of
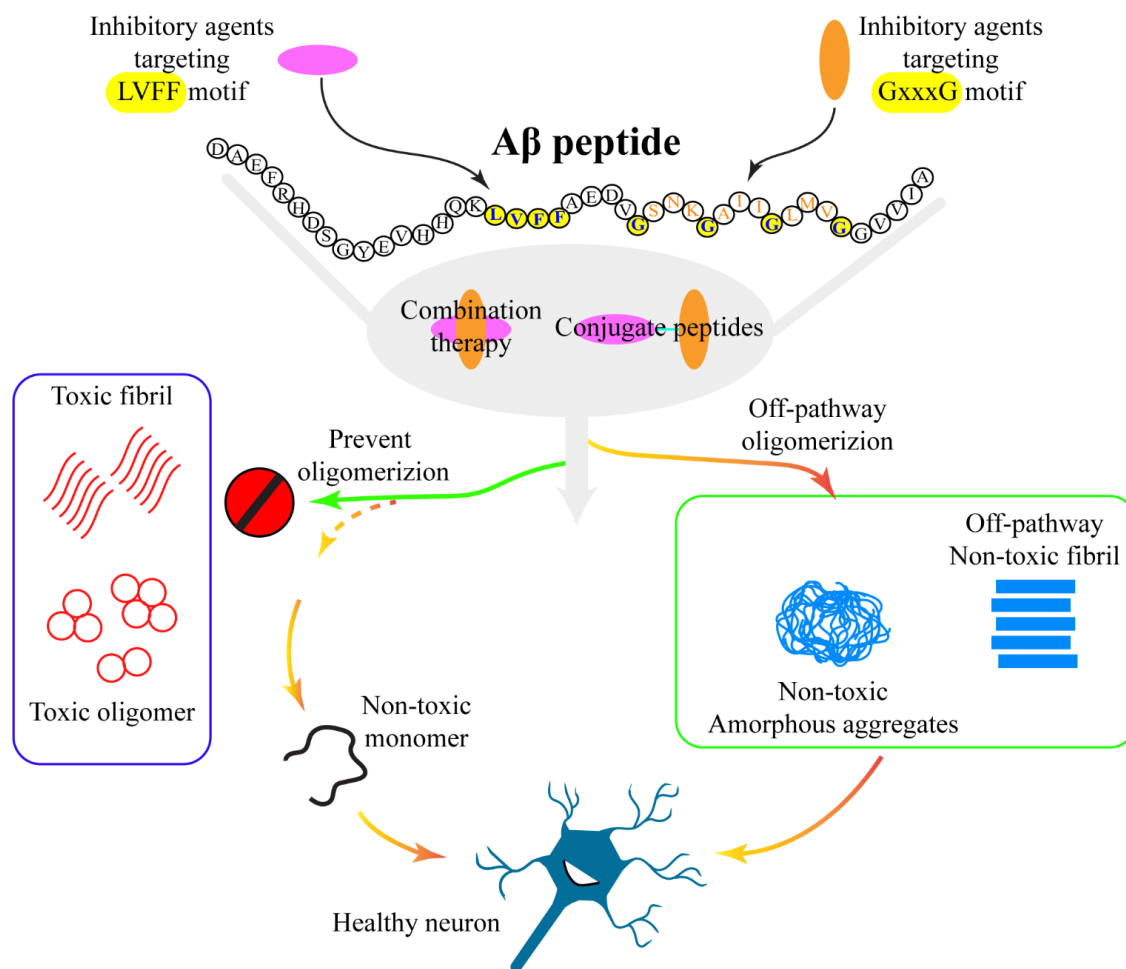
Figure 1.5. Schematic representation of amyloid inhibition targeting two most crucial sequence motif in Aβ. Design strategies include either combination of short peptide targeting individual motifs or a conjugate peptide that can interact with both motifs. This interaction may lead to prevention of oligomerization via strong association with monomers. An alternative mechanism could involve facilitating the formation of off-pathway fibrils or amorphous aggregates that do not harm neuronal cells.

the target receptor.[128] Moreover, the investigation of high throughput screening for drugs targeting APP dimerization, with the aim of reducing Aβ production, has also been undertaken.[129] Apart from that, research targeting the Aβ amyloidogenic pathway has been consistent. Based on the experimental evidences, it can be conjectured that polymorphic fibrils or transient oligomers are the main toxic entities. Interestingly, both *in vitro* and *in vivo* data demonstrate that the GxxxG motif, particularly the $G^{33}xxxG^{37}$ is crucial for prolonging certain oligomeric conformers. Evidently, these conformers need to be thoroughly characterized in order to develop inhibitory agents. We expect that upcoming research efforts will strongly focus on the inhibition and

degradation of such deleterious oligomers. Current knowledge of short peptide design with increased specificity and effectiveness will surely come handy on this journey of unwinding Aβ entanglement. Furthermore, since G33 or G37 mutants of Aβ give rise to fibrils that are surprisingly non-toxic to the neuronal cells, we propose that developing short peptide derivatives (Figure 1.5) which may facilitate such fibril formation would presumably open up novel avenues for AD treatment.

1.4. Peptide self-assembly into hydrogel formation
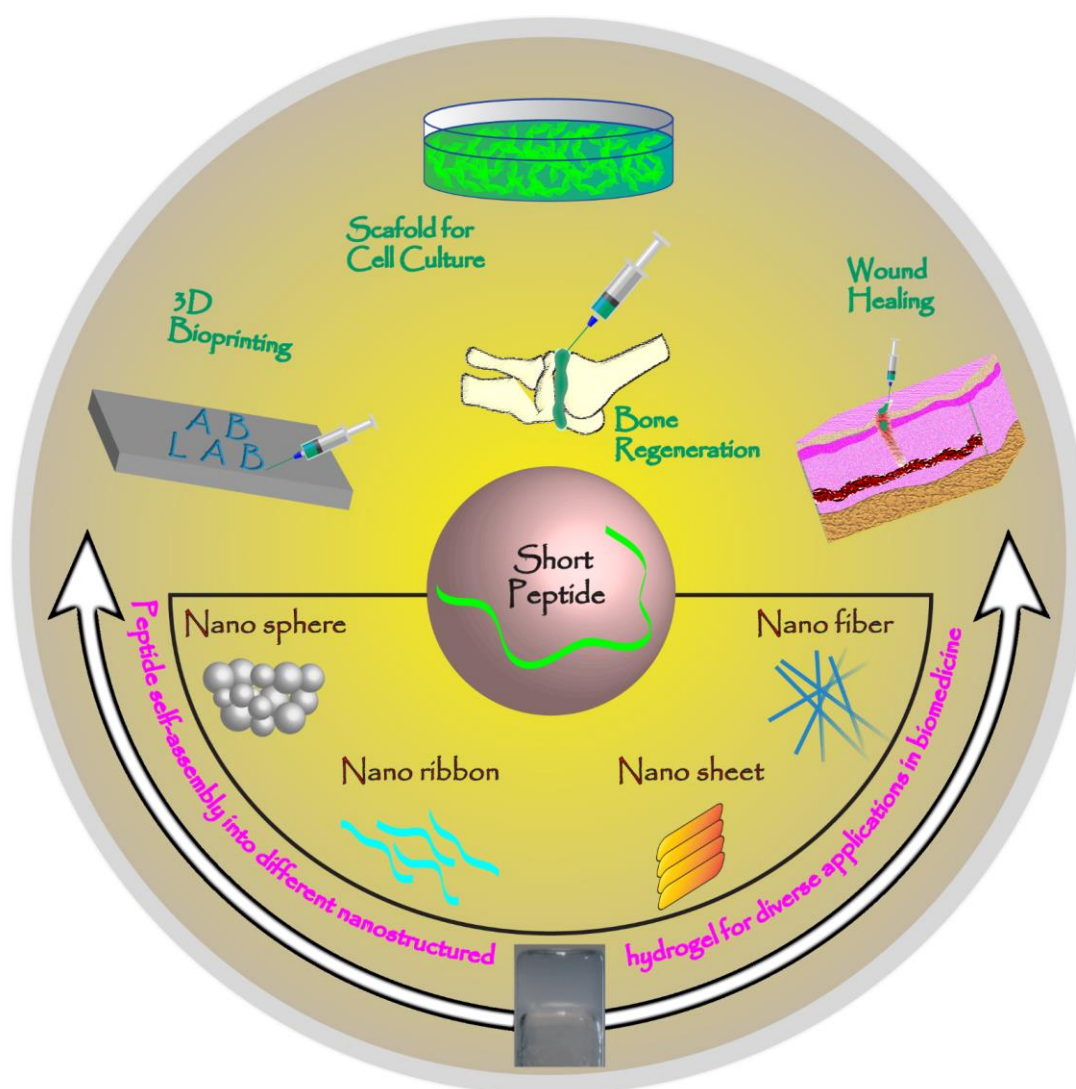
Figure 1.6. Schematic representation of peptide self-assembly intro various nano-architectures and their potential applications.

While understanding the link between peptide self-assembly and amyloid disorder provides significant insights into the disease pathogesis, the exploration of functional amyloids adds another intruiging dimention. This transtion from disease-associated aggregates to nanostructured functional materials emphasizes the dual nature of peptide self-assembly. As we navigate through this intersection, the implications of peptide self-assembly exceeds far beyond amyloid disorder, opening novel avenues for technological advancements in the field of biomedicine and bio-nanotechnology.

The recent roar of bio-nanotechnology provided a spark for the development of smart biomaterials, which is leading to a paradigm shift in the field of biomedicine.[130] For many decades delivery of drugs to a patient has been accomplished using pharmaceutical dosage forms, including tablets, pills, capsules, liquids, aerosols, and injections. Even now, the drug delivery systems we use are mostly the conventional one, which promptly releases the drug, causing a significant fluctuation in drug levels during the time course of drug action. On the other hand, an efficient drug delivery system not only introduce therapeutic substances in the body, but also improves the efficiency and safety by controlling the rate, time and place of drug release in the body, and helps to overcome certain barriers such as the low solubility due to drug's hydrophobicity, and its premature degradation before reaching the targeted tissues.[131] Hydrogels have emerged as a promising option in this regard and gone through an immense upgradation over the years. Hydrogels are semi-solid materials formed by small-molecule hydrogelators self-assembling into a three-dimensional (3D) network of nanostructures that can absorb and retain a large amount of water or biological fluids; thus, providing liquid-like properties of these solid-like rheological systems. Peptides are particularly interesting building block of hydrogel among all other self-assembling molecules due to their eminent role as a structural and functional element in biological systems. Numerous self-assembling peptide hydrogels have already been developed for advanced drug delivery, tissue engineering and to generate scaffolds for three-dimensional (3D) cell culture.[132] While most traditional smart gels were nonconductive in nature, conductive gels hold great promise for a wide range of applications in biosensors, fuel cells and super capacitors.[133]

1.4.1. Self-assembly is the key for developing peptide hydrogels

Peptide self-assembly is a multi-step process, which leads to the formation of diverse nanostructures (Figure 1.6). Peptide sequence certainly plays a decisive role in monitoring molecular folding. For example, substitution of alanine by more hydrophobic residues such as Val,

Leu, Ile, Phe or Trp results in greater tendency to self-assemble and form higher order nano-structures; while decreased hydrophobicity requires a higher temperature for molecular folding and intermolecular assembly. The designing of the primary structure is usually based on rational designing or segments of native proteins, that aggregate in suitable solvents into long, semi-flexible β-sheet. Side chain interactions happen to play a major role in β-sheet stability. Several reports have shown that peptides containing alternating hydrophilic and hydrophobic residue tend to favor β-sheet structures, whereas the addition of aromatic residue enhances aromatic pairing interaction. By altering the sequence of these peptides, it is possible to take control over the assembly kinetics, and biomolecular interactions.

In general, the key to peptide-based hydrogel formation is the self-assembly of the low molecular weight hydrogelators, driven by non-covalent interactions such as hydrogen bonding, π-π interactions, metal-ligand coordination, van der Waals forces, and hydrophobic effects. These interactions drive the formation of higher order structures, most frequently nano-fibers but also nano-ribbons, nano-sheets and nano-spheres. The hydrophilic moieties of these nanostructures are faced towards whereas the hydrophobic moieties are packed internally enabling encapsulation of large biomolecules. The balance between hydrophobic attraction with hydrophilic or ionic repulsion, the system entropy, as well as some directional interactions such as hydrogen bonding or π-π stacking, not only governs the final morphology, but also trigger responds to different environmental stimuli. Interestingly, the formation of these hydrogels does not involve any chemical cross-linking and can also be achieved at physiological pH and temperature. How fast a gel can form is also related to its physical property; faster gel formation (e.g. with a higher amount of salt/higher temperature) results in more hydrophobic packing defects/more resultant branch points providing a stiffer, final gel, which is generally more fitting as scaffold for cell encapsulation and delivery. Addition of co-geletors or non-gelating molecules have also been reported in gel systems to create an additional level of control and therefore allow tailoring of the physical properties of hydrogel through modification. Moreover, the self-assembly of peptides into nanostructures is much more energy efficient than directed assembly.

1.4.2. Fmoc-protected short peptide-based hydrogel

Over the years, the introduction of Fmoc group in the N-terminus of short peptides have gain considerable interest. Apart from the inherent π-π stacking interactions between the fluorenyl moieties, hydrophobic interactions, hydrogel bonding of the carbonyl group, as well as reduced

steric hindrance provide substantial driving forces in the peptide self-assembly.[134, 135] Moreover, the presence of aromatic residues (Phe, Tyr, and Trp) in the peptide sequence adds a synergistic effect to the assembly process by promoting π-π stacking interactions between the Fmoc group and the side-chain phenyl rings. Considering the inherent fluorescence and UV-active nature of the fluorenyl ring within the Fmoc group, there is unquestionable potential for Fmoc-modified self-assemblies to exhibit unique optical properties, offering potential bionanotechnological applications. While the primary application relies on the intense excitation of Fmoc at 270 nm with corresponding emission at 320 nm, the shift in the fluorescence peak position can be used to characterize the self-assembling mechanism of Fmoc-modified short peptide.

So far, Fmoc-FF, derived from the core amyloidogenic recognition motif of the Aβ peptide, has been the most extensively studied Fmoc-modified peptide for the development of hydrogels. The gelation of Fmoc-FF has been independently developed by both solvent switch and pH switch method.[136] It has been observed that the Fmoc-FF molecules self-assemble into cylindrical nanofibrils by interlocking four twisted antiparallel β-sheet through π-π interactions.[135] Additionally, changes in the pH, ratio of cosolvents, buffer, and agitation conditions have shown varying structural and mechanical properties of hydrogel formed.[137] Another extensively studied Fmoc-modified peptide for hydrogel formation is Fmoc-YL. It has been observed to form both dense fibrous network and spherical aggregates with varying mechanical strength.[138] In addition to modifications in Fmoc-FF or YL, various other dipeptides, including Fmoc-GG, GF, LL, LG, and GL, have also been investigated and found to form hydrogels with diverse self-assembled morphologies.[139]

Although relatively limited research has been done on the self-assembly of Fmoc-modified oligopeptides, there is growing interest in recent years. Pentapeptides, in particular, are gaining considerable attention for their ability to serve as functional epitopes in biological contexts. Furthermore, they offer greater flexibility and potential for modifications. For instance, Fmoc-modified TIGYG, a potassium ion-binding pentapeptide epitope derived from a natural ion-channel protein, demonstrated the ability to self-assemble into nanofibers of varying widths and crosslinking patterns at different potassium concentrations.[140] Additionally, hydrogelation was exclusively observed at a specific potassium-to-peptide ratio and was also sequence-specific. Similarly, VTEEI (the repeat sequence in the *Plasmodium falciparum* blood stage antigen),

GVGVP, and VPGVG (peptide-based epitopes in elastin), as well as VYGGG (an inhibitor in the binding monoclonal antibody 10D11), are pentapeptide-based epitopes that can also self-assemble to form nanofibrillar hydrogels when modified with Fmoc group in the N-terminus.[141] Hydrogelation was facilitated by a balance of intermolecular aromatic-aromatic interactions and hydrogen bonds. These findings clearly point towards the crucial role of Fmoc moieties in driving self-assembly; nevertheless, the comprehensive mechanisms underlying the formation of hydrogels are significantly complex, necessitating extensive investigation.

Overall, hydrogels developed from the self-assembly and physical cross-linking of short peptides are particularly intriguing for various biomedical and technological advancements. Modification in the N-terminus with aromatic moieties such as Fmoc group facilitates self-assembly and stable gel formation. Over the years, a large number of such building blocks have been identified and extensively studied; yet, the rational design of building blocks for precise control over gelation remains a challenge. Nevertheless, it is evident that the introduction of aromatic groups, whether within the sequence or at the terminus, provide greater gelation propensity and offers relevant applications in drug delivery, cell culture, tissue engineering, bio-sensing, opto-electronics and other biomedical and bionanotechnological fields.

1.5. Aim of the thesis

Comprehensive understanding of the structural and morphological characteristics of amyloid species is crucial for defining their pathogenicity and applicability. In the current context, while amyloid formation plays a significant role in various protein folding disorders, there is also a growing interest in the nanostructured functional materials resulting from peptide self-assembly. Keeping these considerations in mind, the aims of the thesis:

a) To investigate the role of sequence specificity within the amyloidogenic peptide and their fragments, in regulating aggregation kinetics and associated pathogenicity of amyloid disorders.

b) Investigation of self-assembly and membrane-mediated oligomerization of Aβ peptide in a near-native environment as well as the mechanistic insights into the role of GxxxG motif.

c) Finally, the design, development and characterization, as well as the underlying mechanism of hydrogel formation by Fmoc-pentapeptides derived from the C-terminal SARS CoV E protein.

1.6. References

[1] J. D. Sipe, A. S. Cohen, *J Struct Biol* **2000**, 130, 88.

[2] R. S. Harrison, P. C. Sharpe, Y. Singh, D. P. Fairlie, *Rev Physiol Biochem Pharmacol* **2007**, 159, 1.

[3] C. M. Dobson, *Trends Biochem Sci* **1999**, 24, 329; F. Chiti, C. M. Dobson, *Annu Rev Biochem* **2017**, 86, 27.

[4] O. V. Galzitskaya, E. I. Galushko, O. M. Selivanova, *Biochemistry (Mosc)* **2018**, 83, S62.

[5] E. D. Eanes, G. G. Glenner, *J Histochem Cytochem* **1968**, 16, 673; W. T. Astbury, S. Dickinson, K. Bailey, *Biochem J* **1935**, 29, 2351; H. Inouye, P. E. Fraser, D. A. Kirschner, *Biophys J* **1993**, 64, 502; L. C. Serpell, P. E. Fraser, M. Sunde, *Methods Enzymol* **1999**, 309, 526; M. Sunde, L. C. Serpell, M. Bartlam, P. E. Fraser, M. B. Pepys, C. C. Blake, *J Mol Biol* **1997**, 273, 729.

[6] S. B. Malinchik, H. Inouye, K. E. Szumowski, D. A. Kirschner, *Biophys J* **1998**, 74, 537.

[7] E. N. Cline, M. A. Bicca, K. L. Viola, W. L. Klein, *J Alzheimers Dis* **2018**, 64, S567; G. Forloni, C. Balducci, *J Alzheimers Dis* **2018**, 62, 1261; M. Verma, A. Vats, V. Taneja, *Ann Indian Acad Neurol* **2015**, 18, 138.

[8] I. Benilova, E. Karran, B. De Strooper, *Nat Neurosci* **2012**, 15, 349.

[9] P. Arosio, T. P. Knowles, S. Linse, *Phys Chem Chem Phys* **2015**, 17, 7606.

[10] L. E. Buchanan, E. B. Dunkelberger, H. Q. Tran, P. N. Cheng, C. C. Chiu, P. Cao, D. P. Raleigh, J. J. de Pablo, J. S. Nowick, M. T. Zanni, *Proc Natl Acad Sci U S A* **2013**, 110, 19285.

[11] U. Sengupta, A. N. Nilson, R. Kayed, *EBioMedicine* **2016**, 6, 42; S. Campioni, B. Mannini, M. Zampagni, A. Pensalfini, C. Parrini, E. Evangelisti, A. Relini, M. Stefani, C. M. Dobson, C. Cecchi, F. Chiti, *Nat Chem Biol* **2010**, 6, 140; B. Mannini, E. Mulvihill, C. Sgromo, R. Cascella, R. Khodarahmi, M. Ramazzotti, C. M. Dobson, C. Cecchi, F. Chiti, *ACS Chem Biol* **2014**, 9, 2309; R. Kayed, C. A. Lasagna-Reeves, *J Alzheimers Dis* **2013**, 33 Suppl 1, S67; R. Kayed, E. Head, J. L. Thompson, T. M. McIntire, S. C. Milton, C. W. Cotman, C. G. Glabe, *Science* **2003**, 300, 486.

[12] P. Alam, L. Bousset, R. Melki, D. E. Otzen, *J Neurochem* **2019**, 150, 522; B. Sarkar, V. S. Mithu, B. Chandra, A. Mandal, M. Chandrakesan, D. Bhowmik, P. K. Madhu, S. Maiti, *Angew Chem Int Ed Engl* **2014**, 53, 6888.

[13] G. Meisl, X. Yang, B. Frohm, T. P. Knowles, S. Linse, *Sci Rep* **2016**, 6, 18728; F. Bemporad, G. Calloni, S. Campioni, G. Plakoutsi, N. Taddei, F. Chiti, *Acc Chem Res* **2006**, 39, 620.

[14] M. S. Lin, L. Y. Chen, H. T. Tsai, S. S. Wang, Y. Chang, A. Higuchi, W. Y. Chen, *Langmuir* **2008**, 24, 5802.

[15] B. Morel, L. Varela, A. I. Azuaga, F. Conejero-Lara, *Biophys J* **2010**, 99, 3801.

[16] D. Bhattacharyya, R. Kumar, S. Mehra, A. Ghosh, S. K. Maji, A. Bhunia, *Chem Commun (Camb)* **2018**, 54, 3605.

[17] Y. Yoshimura, Y. Lin, H. Yagi, Y. H. Lee, H. Kitayama, K. Sakurai, M. So, H. Ogi, H. Naiki, Y. Goto, *Proc Natl Acad Sci U S A* **2012**, 109, 14446; E. Y. Chi, S. Krishnan, T. W. Randolph, J. F. Carpenter, *Pharm Res* **2003**, 20, 1325; S. Narayanan, B. Reif, *Biochemistry* **2005**, 44, 1444.

[18] A. T. Petkova, R. D. Leapman, Z. Guo, W. M. Yau, M. P. Mattson, R. Tycko, *Science* **2005**, 307, 262.

[19] W. Qiang, W. M. Yau, J. X. Lu, J. Collinge, R. Tycko, *Nature* **2017**, 541, 217.

[20] M. Törnquist, T. C. T. Michaels, K. Sanagavarapu, X. Yang, G. Meisl, S. I. A. Cohen, T. P. J. Knowles, S. Linse, *Chem Commun (Camb)* **2018**, 54, 8667.

[21] J. X. Lu, W. Qiang, W. M. Yau, C. D. Schwieters, S. C. Meredith, R. Tycko, *Cell* **2013**, 154, 1257.

[22] R. Liu, M. He, R. Su, Y. Yu, W. Qi, Z. He, *Biochem Biophys Res Commun* **2010**, 391, 862; A. Ahmad, I. S. Millett, S. Doniach, V. N. Uversky, A. L. Fink, *Biochemistry* **2003**, 42, 11404; T. Eichner, A. P. Kalverda, G. S. Thompson, S. W. Homans, S. E. Radford, *Mol Cell* **2011**, 41, 161.

[23] L. Breydo, V. N. Uversky, *FEBS Lett* **2015**, 589, 2640.

[24] H. LeVine, *Protein Sci* **1993**, 2, 404.

[25] T. P. Knowles, C. A. Waudby, G. L. Devlin, S. I. Cohen, A. Aguzzi, M. Vendruscolo, E. M. Terentjev, M. E. Welland, C. M. Dobson, *Science* **2009**, 326, 1533.

[26] S. I. Cohen, S. Linse, L. M. Luheshi, E. Hellstrand, D. A. White, L. Rajah, D. E. Otzen, M. Vendruscolo, C. M. Dobson, T. P. Knowles, *Proc Natl Acad Sci U S A* **2013**, 110, 9758.

[27] G. Meisl, J. B. Kirkegaard, P. Arosio, T. C. Michaels, M. Vendruscolo, C. M. Dobson, S. Linse, T. P. Knowles, *Nat Protoc* **2016**, 11, 252.

[28] E. E. Congdon, S. Kim, J. Bonchak, T. Songrug, A. Matzavinos, J. Kuret, *J Biol Chem* **2008**, 283, 13806; D. M. Walsh, A. Lomakin, G. B. Benedek, M. M. Condron, D. B. Teplow, *J Biol Chem* **1997**, 272, 22364.

[29] C. A. Lane, J. Hardy, J. M. Schott, *Eur J Neurol* **2018**, 25, 59.

[30] J. H. Grand, S. Caspar, S. W. Macdonald, *J Multidiscip Healthc* **2011**, 4, 125.

[31] M. P. Murphy, H. LeVine, *J Alzheimers Dis* **2010**, 19, 311; A. Serrano-Pozo, M. P. Frosch, E. Masliah, B. T. Hyman, *Cold Spring Harb Perspect Med* **2011**, 1, a006189; G. F. Chen, T. H. Xu, Y. Yan, Y. R. Zhou, Y. Jiang, K. Melcher, H. E. Xu, *Acta Pharmacol Sin* **2017**, 38, 1205; K. Rajasekhar, M. Chakrabarti, T. Govindaraju, *Chem Commun (Camb)* **2015**, 51, 13434; D. J. Selkoe, *Annu Rev Cell Biol* **1994**, 10, 373.

[32] G. G. Glenner, C. W. Wong, *Biochem Biophys Res Commun* **2012**, 425, 534.

[33] D. J. Selkoe, J. Hardy, *EMBO Mol Med* **2016**, 8, 595.

[34] G. Meisl, X. Yang, E. Hellstrand, B. Frohm, J. B. Kirkegaard, S. I. Cohen, C. M. Dobson, S. Linse, T. P. Knowles, *Proc Natl Acad Sci U S A* **2014**, 111, 9384.

[35] N. G. Sgourakis, Y. Yan, S. A. McCallum, C. Wang, A. E. Garcia, *J Mol Biol* **2007**, 368, 1448; N. L. Fawzi, J. Ying, R. Ghirlando, D. A. Torchia, G. M. Clore, *Nature* **2011**, 480, 268; S. Vivekanandan, J. R. Brender, S. Y. Lee, A. Ramamoorthy, *Biochem Biophys Res Commun* **2011**, 411, 312; T. D. Do, S. Sangwan, N. E. C. de Almeida, A. I. Ilitchev, M. Giammona, M. R. Sawaya, S. K. Buratto, D. S. Eisenberg, M. T. Bowers, *Protein Sci* **2018**, 27, 1181; M. R. Sawaya, S. Sambashivan, R. Nelson, M. I. Ivanova, S. A. Sievers, M. I. Apostol, M. J. Thompson, M. Balbirnie, J. J. Wiltzius, H. T. McFarlane, A. Madsen, C. Riekel, D. Eisenberg, *Nature* **2007**, 447, 453; O. Mancini, T. Wellbrock, O. J. Rolinski, K. Kubiak-Ossowska, P. A. Mulheran, *Phys Chem Chem Phys* **2018**, 20, 4216; V. H. Man, X. He, B. Ji, S. Liu, X. Q. Xie, J. Wang, *ACS Chem Neurosci* **2019**, 10, 4643; P. Flagmeier, S. De, T. C. T. Michaels, X. Yang, A. J. Dear, C. Emanuelsson, M. Vendruscolo, S. Linse, D. Klenerman, T. P. J. Knowles, C. M. Dobson, *Nat Struct Mol Biol* **2020**, 27, 886.

[36] H. Zhang, Q. Ma, Y. W. Zhang, H. Xu, *J Neurochem* **2012**, 120 Suppl 1, 9; S. Eggert, K. Paliga, P. Soba, G. Evin, C. L. Masters, A. Weidemann, K. Beyreuther, *J Biol Chem* **2004**, 279, 18146; B. De Strooper, W. Annaert, *J Cell Sci* **2000**, 113 (Pt 11), 1857; M. Yuksel, O. Tacal, *Eur J Pharmacol* **2019**, 856, 172415.

[37] D. M. Walsh, D. J. Selkoe, *J Neurochem* **2007**, 101, 1172; B. R. Sahoo, S. J. Cox, A. Ramamoorthy, *Chem Commun (Camb)* **2020**, 56, 4627; C. G. Glabe, *J Biol Chem* **2008**, 283, 29639; E. Hubin, N. A. van Nuland, K. Broersen, K. Pauwels, *Cell Mol Life Sci* **2014**, 71, 3507; W. L. Klein, G. A. Krafft, C. E. Finch, *Trends Neurosci* **2001**, 24, 219; D. Shea, C. C. Hsu, T. M. Bi, N. Paranjapye, M. C. Childers, J. Cochran, C. P. Tomberlin, L. Wang, D. Paris, J. Zonderman, G. Varani, C. D. Link, M. Mullan, V. Daggett, *Proc Natl Acad Sci U S A* **2019**, 116, 8895.

[38] J. P. Colletier, A. Laganowsky, M. Landau, M. Zhao, A. B. Soriaga, L. Goldschmidt, D. Flot, D. Cascio, M. R. Sawaya, D. Eisenberg, *Proc Natl Acad Sci U S A* **2011**, 108, 16938; R. Tycko, *Neuron* **2015**, 86, 632.

[39] G. Kleiger, R. Grothe, P. Mallick, D. Eisenberg, *Biochemistry* **2002**, 41, 5990.

[40] W. P. Russ, D. M. Engelman, *J Mol Biol* **2000**, 296, 911.

[41] A. Senes, M. Gerstein, D. M. Engelman, *J Mol Biol* **2000**, 296, 921.

[42] G. Arselin, M. F. Giraud, A. Dautant, J. Vaillier, D. Brèthes, B. Coulary-Salin, J. Schaeffer, J. Velours, *Eur J Biochem* **2003**, 270, 1875.

[43] H. Furthmayr, V. T. Marchesi, *Biochemistry* **1976**, 15, 1137.

[44] K. R. MacKenzie, J. H. Prestegard, D. M. Engelman, *Science* **1997**, 276, 131.

[45] M. A. Lemmon, J. M. Flanagan, H. R. Treutlein, J. Zhang, D. M. Engelman, *Biochemistry* **1992**, 31, 12719.

[46] C. M. Lawrie, E. S. Sulistijo, K. R. MacKenzie, *J Mol Biol* **2010**, 396, 924.

[47] E. V. Bocharov, Y. E. Pustovalova, K. V. Pavlov, P. E. Volynsky, M. V. Goncharuk, Y. S. Ermolyuk, D. V. Karpunin, A. A. Schulga, M. P. Kirpichnikov, R. G. Efremov, I. V. Maslennikov, A. S. Arseniev, *J Biol Chem* **2007**, 282, 16256.

[48] B. K. Mueller, S. Subramaniam, A. Senes, *Proc Natl Acad Sci U S A* **2014**, 111, E888.

[49] M. Coles, W. Bicknell, A. A. Watson, D. P. Fairlie, D. J. Craik, *Biochemistry* **1998**, 37, 11064.

[50] H. Shao, S. Jao, K. Ma, M. G. Zagorski, *J Mol Biol* **1999**, 285, 755.

[51] S. Isbert, K. Wagner, S. Eggert, A. Schweitzer, G. Multhaup, S. Weggen, S. Kins, C. U. Pietrzik, *Cell Mol Life Sci* **2012**, 69, 1353; S. Eggert, A. C. Gonzalez, C. Thomas, S. Schilling, S. M. Schwarz, C. Tischer, V. Adam, P. Strecker, V. Schmidt, T. E. Willnow, G. Hermey, C. U. Pietrzik, E. H. Koo, S. Kins, *Cell Mol Life Sci* **2018**, 75, 301; P. M. Gorman, S. Kim, M. Guo, R. A. Melnyk, J. McLaurin, P. E. Fraser, J. U. Bowie, A. Chakrabartty, *BMC Neurosci* **2008**, 9, 17.

[52] N. Sureshbabu, R. Kirubagaran, R. Jayakumar, *Eur Biophys J* **2009**, 38, 355.

[53] R. J. O'Brien, P. C. Wong, *Annu Rev Neurosci* **2011**, 34, 185.

[54] L. García-González, D. Pilat, K. Baranger, S. Rivera, *Front Aging Neurosci* **2019**, 11, 244; R. J. Andrew, K. A. Kellett, G. Thinakaran, N. M. Hooper, *J Biol Chem* **2016**, 291, 19235.

[55] X. Zhang, Y. Li, H. Xu, Y. W. Zhang, *Front Cell Neurosci* **2014**, 8, 427; B. De Strooper, T. Iwatsubo, M. S. Wolfe, *Cold Spring Harb Perspect Med* **2012**, 2, a006304.

[56] V. T. Marchesi, *Proc Natl Acad Sci U S A* **2005**, 102, 9093.

[57] L. M. Munter, P. Voigt, A. Harmeier, D. Kaden, K. E. Gottschalk, C. Weise, R. Pipkorn, M. Schaefer, D. Langosch, G. Multhaup, *EMBO J* **2007**, 26, 1702.

[58] S. Y. Chen, M. Zacharias, *Biophys J* **2022**, 121, 2330; G. Mao, J. Tan, M. Z. Cui, D. Chui, X. Xu, *J Alzheimers Dis* **2009**, 18, 167; W. Araki, S. Saito, N. Takahashi-Sasaki, H. Shiraishi, H. Komano, K. S. Murayama, *J Mol Neurosci* **2006**, 29, 35.

[59] S. F. Lee, S. Shah, C. Yu, W. C. Wigley, H. Li, M. Lim, K. Pedersen, W. Han, P. Thomas, J. Lundkvist, Y. H. Hao, G. Yu, *J Biol Chem* **2004**, 279, 4144.

[60] P. Kienlen-Campard, B. Tasiaux, J. Van Hees, M. Li, S. Huysseune, T. Sato, J. Z. Fei, S. Aimoto, P. J. Courtoy, S. O. Smith, S. N. Constantinescu, J. N. Octave, *J Biol Chem* **2008**, 283, 7733.

[61] E. Levy, M. D. Carman, I. J. Fernandez-Madrid, M. D. Power, I. Lieberburg, S. G. van Duinen, G. T. Bots, W. Luyendijk, B. Frangione, *Science* **1990**, 248, 1124; T. J. Grabowski, H. S. Cho, J. P. Vonsattel, G. W. Rebeck, S. M. Greenberg, *Ann Neurol* **2001**, 49, 697; L. Hendriks, C. M. van Duijn, P. Cras, M. Cruts, W. Van Hul, F. van Harskamp, A. Warren, M. G. McInnis, S. E. Antonarakis, J. J. Martin, *Nat Genet* **1992**, 1, 218; K. Kamino, H. T. Orr, H. Payami, E. M. Wijsman, M. E. Alonso, S. M. Pulst, L. Anderson, S. O'dahl, E. Nemens, J. A. White, *Am J Hum Genet* **1992**, 51, 998.

[62] C. De Jonghe, C. Zehr, D. Yager, C. M. Prada, S. Younkin, L. Hendriks, C. Van Broeckhoven, C. B. Eckman, *Neurobiol Dis* **1998**, 5, 281.

[63] T. C. Tang, Y. Hu, P. Kienlen-Campard, L. El Haylani, M. Decock, J. Van Hees, Z. Fu, J. N. Octave, S. N. Constantinescu, S. O. Smith, *Structure* **2014**, 22, 387.

[64] D. L. Minor, P. S. Kim, *Nature* **1994**, 367, 660.

[65] H. Higashide, S. Ishihara, M. Nobuhara, Y. Ihara, S. Funamoto, *J Neurochem* **2017**, 140, 955.

[66] T. L. Benzinger, D. M. Gregory, T. S. Burkoth, H. Miller-Auer, D. G. Lynn, R. E. Botto, S. C. Meredith, *Proc Natl Acad Sci U S A* **1998**, 95, 13407; B. R. Groveman, M. A. Dolan, L. M. Taubner, A. Kraus, R. B. Wickner, B. Caughey, *J Biol Chem* **2014**, 289, 24129; A. Gorkovskiy, K. R. Thurber, R. Tycko, R. B. Wickner, *Proc Natl Acad Sci U S A* **2014**, 111, E4615; O. N. Antzutkin, J. J. Balbach, R. D. Leapman, N. W. Rizzo, J. Reed, R. Tycko, *Proc Natl Acad Sci U S A* **2000**, 97, 13045.

[67] O. N. Antzutkin, J. J. Balbach, R. Tycko, *Biophys J* **2003**, 84, 3326.

[68] A. T. Petkova, Y. Ishii, J. J. Balbach, O. N. Antzutkin, R. D. Leapman, F. Delaglio, R. Tycko, *Proc Natl Acad Sci U S A* **2002**, 99, 16742.

[69] M. Ahmed, J. Davis, D. Aucoin, T. Sato, S. Ahuja, S. Aimoto, J. I. Elliott, W. E. Van Nostrand, S. O. Smith, *Nat Struct Mol Biol* **2010**, 17, 561.

[70] T. Sato, P. Kienlen-Campard, M. Ahmed, W. Liu, H. Li, J. I. Elliott, S. Aimoto, S. N. Constantinescu, J. N. Octave, S. O. Smith, *Biochemistry* **2006**, 45, 5503.

[71] G. Grasso, L. Leanza, U. Morbiducci, A. Danani, M. A. Deriu, *J Biomol Struct Dyn* **2020**, 38, 3908.

[72] F. E. Cohen, S. B. Prusiner, *Annu Rev Biochem* **1998**, 67, 793.

[73] A. Quist, I. Doudevski, H. Lin, R. Azimova, D. Ng, B. Frangione, B. Kagan, J. Ghiso, R. Lal, *Proc Natl Acad Sci U S A* **2005**, 102, 10427.

[74] H. Lin, R. Bhatia, R. Lal, *FASEB J* **2001**, 15, 2433; K. J. Barnham, R. Cappai, K. Beyreuther, C. L. Masters, A. F. Hill, *Trends Biochem Sci* **2006**, 31, 465; M. C. Lin, T. Mirzabekov, B. L. Kagan, *J Biol Chem* **1997**, 272, 44.

[75] M. S. McClain, H. Iwamoto, P. Cao, A. D. Vinion-Dubiel, Y. Li, G. Szabo, Z. Shao, T. L. Cover, *J Biol Chem* **2003**, 278, 12101.

[76] B. Martinac, Y. Saimi, C. Kung, *Physiol Rev* **2008**, 88, 1449.

[77] S. Kim, T. J. Jeon, A. Oberai, D. Yang, J. J. Schmidt, J. U. Bowie, *Proc Natl Acad Sci U S A* **2005**, 102, 14278.

[78] L. W. Hung, G. D. Ciccotosto, E. Giannakis, D. J. Tew, K. Perez, C. L. Masters, R. Cappai, J. D. Wade, K. J. Barnham, *J Neurosci* **2008**, 28, 11950.

[79] A. Harmeier, C. Wozny, B. R. Rost, L. M. Munter, H. Hua, O. Georgiev, M. Beyermann, P. W. Hildebrand, C. Weise, W. Schaffner, D. Schmitz, G. Multhaup, *J Neurosci* **2009**, 29, 7582.

[80] V. Fonte, V. Dostal, C. M. Roberts, P. Gonzales, P. N. Lacor, P. Lacor, P. T. Velasco, J. Magrane, N. Dingwell, E. Y. Fan, M. A. Silverman, G. H. Stein, C. D. Link, *Mol Neurodegener* **2011**, 6, 61.

[81] S. Sakagashira, T. Sanke, T. Hanabusa, H. Shimomura, S. Ohagi, K. Y. Kumagaye, K. Nakajima, K. Nanjo, *Diabetes* **1996**, 45, 1279.

[82] D. T. Meier, L. Entrup, A. T. Templin, M. F. Hogan, M. Mellati, S. Zraika, R. L. Hull, S. E. Kahn, *Diabetologia* **2016**, 59, 2166.

[83] L. Tosatto, A. O. Andrighetti, N. Plotegher, V. Antonini, I. Tessari, L. Ricci, L. Bubacco, M. Dalla Serra, *Biochim Biophys Acta* **2012**, 1818, 2876; T. K. Rostovtseva, P. A. Gurnev, O. Protchenko, D. P. Hoogerheide, T. L. Yap, C. C. Philpott, J. C. Lee, S. M. Bezrukov, *J Biol Chem* **2015**, 290, 18467; T. A. Mirzabekov, M. C. Lin, B. L. Kagan, *J Biol Chem* **1996**, 271, 1988; J. Zhao, Y. Luo, H. Jang, X. Yu, G. Wei, R. Nussinov, J. Zheng, *Biochim Biophys Acta* **2012**, 1818, 3121; J. Lee, Y. H. Kim, F. T Arce, A. L. Gillman, H. Jang, B. L. Kagan, R. Nussinov, J. Yang, R. Lal, *ACS Chem Neurosci* **2017**, 8, 1348; N. Arispe, J. C. Diaz, O. Simakova, *Biochim Biophys Acta* **2007**, 1768, 1952.

[84] H. Fatafta, B. Kav, B. F. Bundschuh, J. Loschwitz, B. Strodel, *Biophys Chem* **2022**, 280, 106700.

[85] P. Madhu, D. Das, S. Mukhopadhyay, *Phys Chem Chem Phys* **2021**, 23, 9686.

[86] M. F. Sciacca, S. A. Kotler, J. R. Brender, J. Chen, D. K. Lee, A. Ramamoorthy, *Biophys J* **2012**, 103, 702.

[87] K. J. Korshavn, C. Satriano, Y. Lin, R. Zhang, M. Dulchavsky, A. Bhunia, M. I. Ivanova, Y. H. Lee, C. La Rosa, M. H. Lim, A. Ramamoorthy, *J Biol Chem* **2017**, 292, 4638.

[88] Z. Niu, W. Zhao, Z. Zhang, F. Xiao, X. Tang, J. Yang, *Angew Chem Int Ed Engl* **2014**, 53, 9294.

[89] A. Kakio, S. I. Nishimoto, K. Yanagisawa, Y. Kozutsumi, K. Matsuzaki, *J Biol Chem* **2001**, 276, 24985.

[90] S. Bera, N. Gayen, S. A. Mohid, D. Bhattacharyya, J. Krishnamoorthy, D. Sarkar, J. Choi, N. Sahoo, A. K. Mandal, D. Lee, A. Bhunia, *ACS Chem Neurosci* **2020**, 11, 1965.

[91] M. F. Sciacca, F. Lolicato, C. Tempra, F. Scollo, B. R. Sahoo, M. D. Watson, S. García-Viñuales, D. Milardi, A. Raudino, J. C. Lee, A. Ramamoorthy, C. La Rosa, *ACS Chem Neurosci* **2020**, 11, 4336.

[92] C. Rando, G. Grasso, D. Sarkar, M. F. M. Sciacca, L. M. Cucci, A. Cosentino, G. Forte, M. Pannuzzo, C. Satriano, A. Bhunia, C. La Rosa, *Int J Mol Sci* **2023**, 24.

[93] M. Pannuzzo, D. Milardi, A. Raudino, M. Karttunen, C. La Rosa, *Phys Chem Chem Phys* **2013**, 15, 8940.

[94] A. Abelein, *Acc Chem Res* **2023**; P. Faller, C. Hureau, G. La Penna, *Acc Chem Res* **2014**, 47, 2252; T. L. Lau, J. D. Gehman, J. D. Wade, K. Perez, C. L. Masters, K. J. Barnham, F. Separovic, *Biochim Biophys Acta* **2007**, 1768, 2400.

[95] S. Jones, J. M. Thornton, *Proc Natl Acad Sci U S A* **1996**, 93, 13.

[96] A. C. Cheng, R. G. Coleman, K. T. Smyth, Q. Cao, P. Soulard, D. R. Caffrey, A. C. Salzberg, E. S. Huang, *Nat Biotechnol* **2007**, 25, 71.

[97] J. E. Gestwicki, G. R. Crabtree, I. A. Graef, *Science* **2004**, 306, 865.

[98] A. Ghosh, N. Pradhan, S. Bera, A. Datta, J. Krishnamoorthy, N. R. Jana, A. Bhunia, *ACS Chem Neurosci* **2017**, 8, 718.

[99] S. Jokar, M. Erfani, O. Bavi, S. Khazaei, M. Sharifzadeh, M. Hajiramezanali, D. Beiki, A. Shamloo, *Bioorg Chem* **2020**, 102, 104050; J. R. Horsley, B. Jovcevski, K. L. Wegener, J. Yu, T. L. Pukala, A. D. Abell, *Biochem J* **2020**, 477, 2039; A. Jha, M. G. Kumar, H. N. Gopi, K. M. Paknikar, *Langmuir* **2018**, 34, 1591; J. Milojevic, V. Esposito, R. Das, G. Melacini, *J Am Chem Soc* **2007**, 129, 4282; J. S. Choi, J. J. Braymer, R. P. Nanga, A. Ramamoorthy, M. H. Lim, *Proc Natl Acad Sci U S A* **2010**, 107, 21990; D. Goyal, S. Shuaib, S. Mann, B. Goyal, *ACS Comb Sci* **2017**, 19, 55.

[100] L. O. Tjernberg, J. Näslund, F. Lindqvist, J. Johansson, A. R. Karlström, J. Thyberg, L. Terenius, C. Nordstedt, *J Biol Chem* **1996**, 271, 8545.

[101] C. W. Wei, Y. Peng, L. Zhang, Q. Huang, M. Cheng, Y. N. Liu, J. Li, *Bioorg Med Chem Lett* **2011**, 21, 5818; L. Wang, L. Lei, Y. Li, F. Li, *FEBS Lett* **2014**, 588, 884.

[102] A. Paul, S. Kumar, S. Kalita, D. Sarkar, A. Bhunia, A. Bandyopadhyay, A. C. Mondal, B. Mandal, *Chem Sci* **2020**, 12, 2853.

[103] V. Castelletto, G. Cheng, I. W. Hamley, *Chem Commun (Camb)* **2011**, 47, 12470; T. Arai, D. Sasaki, T. Araya, T. Sato, Y. Sohma, M. Kanai, *Chembiochem* **2014**, 15, 2577.

[104] A. Francioso, P. Punzi, A. Boffi, C. Lori, S. Martire, C. Giordano, M. D'Erme, L. Mosca, *Bioorg Med Chem* **2015**, 23, 1671; L. Zhang, G. Yagnik, Y. Peng, J. Wang, H. H. Xu, Y. Hao, Y. N. Liu, F. Zhou, *Anal Biochem* **2013**, 434, 292.

[105] C. Soto, E. M. Sigurdsson, L. Morelli, R. A. Kumar, E. M. Castaño, B. Frangione, *Nat Med* **1998**, 4, 822.

[106] M. Tatarek-Nossol, L. M. Yan, A. Schmauder, K. Tenidis, G. Westermark, A. Kapurniotu, *Chem Biol* **2005**, 12, 797; R. Pariary, B. Ghosh, Z. Bednarikova, K. G. Varnava, B. N. Ratha, S. Raha, D. Bhattacharyya, Z. Gazova, V. Sarojini, A. K. Mandal, A. Bhunia, *Biochim Biophys Acta Proteins Proteom* **2020**, 1868, 140378.

[107] W. Liu, E. Crocker, W. Zhang, J. I. Elliott, B. Luy, H. Li, S. Aimoto, S. O. Smith, *Biochemistry* **2005**, 44, 3591.

[108] F. Yang, G. P. Lim, A. N. Begum, O. J. Ubeda, M. R. Simmons, S. S. Ambegaokar, P. P. Chen, R. Kayed, C. G. Glabe, S. A. Frautschy, G. M. Cole, *J Biol Chem* **2005**, 280, 5892.

[109] K. Rajasekhar, S. Samanta, V. Bagoband, N. A. Murugan, T. Govindaraju, *iScience* **2020**, 23, 101005.

[110] J. E. Kim, M. Lee, *Biochem Biophys Res Commun* **2003**, 303, 576.

[111] Y. Sun, Z. Qian, G. Wei, *Phys Chem Chem Phys* **2016**, 18, 12582.

[112] R. A. Rodriguez, L. Y. Chen, G. Plascencia-Villa, G. Perry, *ACS Chem Neurosci* **2018**, 9, 783; P. H. Nguyen, M. S. Li, G. Stock, J. E. Straub, D. Thirumalai, *Proc Natl Acad Sci U S A* **2007**, 104, 111; J. R. Brender, A. Ghosh, S. A. Kotler, J. Krishnamoorthy, S. Bera, V. Morris, T. B. Sil, K. Garai, B. Reif, A. Bhunia, A. Ramamoorthy, *Chem Commun (Camb)* **2019**, 55, 4483; R. K. Kar, J. R. Brender, A. Ghosh, A. Bhunia, *J Chem Inf Model* **2018**, 58, 1576.

[113] K. Tanaka, M. Nishimura, Y. Yamaguchi, S. Hashiguchi, S. Takiguchi, M. Yamaguchi, H. Tahara, T. Gotanda, R. Abe, Y. Ito, K. Sugimura, *J Neuroimmunol* **2011**, 236, 27.

[114] K. Rajasekhar, C. Madhu, T. Govindaraju, *ACS Chem Neurosci* **2016**, 7, 1300.

[115] T. L. Lowe, A. Strzelec, L. L. Kiessling, R. M. Murphy, *Biochemistry* **2001**, 40, 7882.

[116] J. Liu, W. Wang, Q. Zhang, S. Zhang, Z. Yuan, *Biomacromolecules* **2014**, 15, 931.

[117] C. Soto, M. S. Kindy, M. Baumann, B. Frangione, *Biochem Biophys Res Commun* **1996**, 226, 672.

[118] V. Minicozzi, R. Chiaraluce, V. Consalvi, C. Giordano, C. Narcisi, P. Punzi, G. C. Rossi, S. Morante, *J Biol Chem* **2014**, 289, 11242.

[119] O. Ashur-Fabian, Y. Segal-Ruder, E. Skutelsky, D. E. Brenneman, R. A. Steingart, E. Giladi, I. Gozes, *Peptides* **2003**, 24, 1413.

[120] B. M. Austen, K. E. Paleologou, S. A. Ali, M. M. Qureshi, D. Allsop, O. M. El-Agnaf, *Biochemistry* **2008**, 47, 1984; M. Taylor, S. Moore, J. Mayes, E. Parkin, M. Beeg, M. Canovi, M. Gobbi, D. M. Mann, D. Allsop, *Biochemistry* **2010**, 49, 3261.

[121] A. Henning-Knechtel, S. Kumar, C. Wallin, S. Król, S. K. Wärmländer, J. Jarvet, G. Esposito, S. Kirmizialtin, A. Gräslund, A. D. Hamilton, *Cell Reports Physical Science* **2020**, 1.

[122] A. Kapurniotu, A. Buck, M. Weber, A. Schmauder, T. Hirsch, J. Bernhagen, M. Tatarek-Nossol, *Chem Biol* **2003**, 10, 149.

[123] E. A. Fradinger, B. H. Monien, B. Urbanc, A. Lomakin, M. Tan, H. Li, S. M. Spring, M. M. Condron, L. Cruz, C. W. Xie, G. B. Benedek, G. Bitan, *Proc Natl Acad Sci U S A* **2008**, 105, 14175.

[124] C. Hetényi, Z. Szabó, E. Klement, Z. Datki, T. Körtvélyesi, M. Zarándi, B. Penke, *Biochem Biophys Res Commun* **2002**, 292, 931.

[125] S. Bansal, I. K. Maurya, N. Yadav, C. K. Thota, V. Kumar, K. Tikoo, V. S. Chauhan, R. Jain, *ACS Chem Neurosci* **2016**, 7, 615.

[126] T. Harkany, I. Abrahám, G. Laskay, W. Timmerman, K. Jost, M. Zarándi, B. Penke, C. Nyakas, P. G. Luiten, *Neuroreport* **1999**, 10, 1693; L. Fülöp, M. Zarándi, Z. Datki, K. Soós, B. Penke, *Biochem Biophys Res Commun* **2004**, 324, 64.

[127] M. H. Viet, K. Siposova, Z. Bednarikova, A. Antosova, T. T. Nguyen, Z. Gazova, M. S. Li, *J Phys Chem B* **2015**, 119, 5145.

[128] Y. Z. Lin, S. Y. Yao, R. A. Veach, T. R. Torgerson, J. Hawiger, *J Biol Chem* **1995**, 270, 14255; N. Manolios, S. Collier, J. Taylor, J. Pollard, L. C. Harrison, V. Bender, *Nat Med* **1997**, 3, 84.

[129] P. P. So, E. Zeldich, K. I. Seyb, M. M. Huang, J. B. Concannon, G. D. King, C. D. Chen, G. D. Cuny, M. A. Glicksman, C. R. Abraham, *Am J Neurodegener Dis* **2012**, 1, 75.

[130] H. M. El-Husseiny, E. A. Mady, L. Hamabe, A. Abugomaa, K. Shimada, T. Yoshida, T. Tanaka, A. Yokoi, M. Elbadawy, R. Tanaka, *Mater Today Bio* **2022**, 13, 100186.

[131] S. Adepu, S. Ramakrishna, *Molecules* **2021**, 26.

[132] W. A. Petka, J. L. Harden, K. P. McGrath, D. Wirtz, D. A. Tirrell, *Science* **1998**, 281, 389; M. C. Branco, J. P. Schneider, *Acta Biomater* **2009**, 5, 817.

[133] P. Beker, G. Rosenman, *Journal of Materials Research* **2010**, 25, 1661.

[134] S. Fleming, P. W. Frederix, I. Ramos Sasselli, N. T. Hunt, R. V. Ulijn, T. Tuttle, *Langmuir* **2013**, 29, 9510.

[135] A. M. Smith, R. J. Williams, C. Tang, P. Coppo, R. F. Collins, M. L. Turner, A. Saiani, R. V. Ulijn, *Advanced materials* **2008**, 20, 37.

[136] A. Mahler, M. Reches, M. Rechter, S. Cohen, E. Gazit, *Advanced Materials* **2006**, 18, 1365; V. Jayawarna, M. Ali, T. A. Jowitt, A. F. Miller, A. Saiani, J. E. Gough, R. V. Ulijn, *Advanced materials* **2006**, 18, 611.

[137] J. Raeburn, C. Mendoza-Cuenca, B. N. Cattoz, M. A. Little, A. E. Terry, A. Zamith Cardoso, P. C. Griffiths, D. J. Adams, *Soft Matter* **2015**, 11, 927; W. Helen, P. De Leonardis, R. V. Ulijn, J. Gough, N. Tirelli, *Soft Matter* **2011**, 7, 1732.

[138] S. Roy, N. Javid, P. W. Frederix, D. A. Lamprou, A. J. Urquhart, N. T. Hunt, P. J. Halling, R. V. Ulijn, *Chemistry* **2012**, 18, 11723.

[139] C. Tang, R. V. Ulijn, A. Saiani, *Langmuir* **2011**, 27, 14438; R. S. Jacob, D. Ghosh, P. K. Singh, S. K. Basu, N. N. Jha, S. Das, P. K. Sukul, S. Patil, S. Sathaye, A. Kumar, A. Chowdhury, S. Malik, S. Sen, S. K. Maji, *Biomaterials* **2015**, 54, 97.

[140] Y. Kuang, Y. Gao, J. Shi, H. C. Lin, B. Xu, *Chem Commun (Camb)* **2011**, 47, 8772.

[141] M. Ma, Y. Kuang, Y. Gao, Y. Zhang, P. Gao, B. Xu, *J Am Chem Soc* **2010**, 132, 2719.

Chapter II

Self-Assembly and Neurotoxicity of β-Amyloid (21–40) Peptide Fragment: The Regulatory Role of GxxxG Motifs

This chapter has been adapted from the following publication:

2.1. Introduction

The amyloidogenesis of Amyloid-beta (Aβ) peptides has been known to be the central event in Alzheimer's Disease (AD) pathogenesis.[1, 2] Despite several decades of research on the relationship between Aβ and AD, researchers are still skeptical about the structure-toxicity correlation. Although the recent evidences on Aβ neurotoxicity have shifted the focus towards the toxic oligomers,[3] fibrils which have long been considered as the cause of disease pathogenesis and cannot be ruled out as evidences pertaining to them are still coming along.[4, 5] A deeper understanding of the molecular mechanisms and pathways underlying Aβ self-aggregation remains a great challenge to current science. Over the years, several independent studies have identified the central (K16-G25) and the C-terminal region (K28-G37) play a vital role in Aβ self-assembly.[2, 6] Most of these studies have often highlighted a significance of the GxxxG repeating motif from the C-terminus.[7, 8] The GxxxG motif is a frequently occurring sequence in trans-membrane proteins and some soluble proteins that contain at least one α-helix.[9] The four residue separation aligns the Gly residues in a GxxxG motif to lie on one face of the helix, and has been reported to stabilize the helix-helix association and the folded state of proteins.[9, 10] The lack of side chain in Gly allows the two helices to come into close proximity, and the dimer is thought to be stabilized by van der Waals interactions.[11] The β-branched amino acids such as Ile, Val, and Thr that frequently occurs at the neighbouring positions, facilitates Gly to acts as a molecular notch that further strengthens the helix-helix interactions.[11] It has also been reported that AxxxG has a similar effect to the GxxxG motif.[9] Studies have shown that Gly→Leu mutation in these motifs affect amyloid precursor protein dimerization, processing, and subsequent Aβ production.[8] These motifs were suggested to have significant impact on β-sheet formation and the associated neurotoxicity.[7] Before converting into β-sheet, Aβ adopts an antiparallel β-hairpin structure at the G^{33}LMVG^{37} region.[12] Thus, mutation in this segment could favor oligomerization, and subsequent fibrillation. A comprehensive understanding of the system is necessary for a possible

structure-function correlation of Aβ pathogenesis. However, the mechanistic insight into this segment-specific aggregation resulting in the structured/unstructured aggregates remains elusive.

Surrounding water molecules have long been acknowledged to be a key player in determinig the aggregation propensity of a protein in solution.[13] The hydrogen bond networking with water has a significant influence on the structural stability and dynamics of a protein. Molecular dynamics (MD) simulation studies have indicated that water-mediated interactions can affect the energy landscape of monomers to drive oligomerization.[14] The major driving force behind protofibrilation is being the hydrophobic interaction that facilitates the dehydration of backbone hydrogen bonds i.e. removal of water molecules by the nearby non-polar group which is an entropically driven-process.[15, 16] It has also been reported that some of the conformational changes (such as β-sheet) require hydration of the particular segment of peptide chains rather than removal of water.[15] Therefore, in order to gain a deeper understanding of water-peptide interplay in the aggregation propensity of peptides, a detailed investigation of water dynamics is required.

In this chapter, we have focused mainly on the C-terminal segment of Aβ peptide to establish a dynamic relationship between toxicity and peptide aggregates. Here, we have designed a 20-residue peptide (namely, AV20), which harbours all the three GxxxG motiffs flanked by 3-4 residues on either side (Figure 2.1A). It should be noted that the flanking residues only provide conformational freedom and ease of study. Additonally, a peptide library was also designed by sequentially and sytematically mutating each of these Gly residues to Leu (Figure 2.1A) in order to understand the role of individual Gly residues in the C-terminal segment of Aβ. Our experiments show that the hydrophobic C-terminal Aβ containing the three repeat GxxxG motifs is evenly neurotoxic. In particular, the $G^{33}xxxG^{37}$ is the primary motif accountable for peptide's neurotoxicity. Moreover, using the solvent relaxation technique we have uncovered the guiding role of water molecules in determining the aggregation propensity of a peptide. It enabled us in discriminating the sequence-dependent mechanism of self-assembly between two peptides.

2.2. Materials and methods

2.2.1. Sample preparation

Chemicals and solvents were obtained from Sigma Aldrich, USA. Synthetic unlabelled peptides were purchased from GenScript (Piscataway, USA) and GL Biochem (Shanghai, China). The

purity of the peptides was checked by HPLC and mass spectra (data not shown). The peptides were dissolved in 5% NH₄OH, vortex well and kept at 4 °C for 1 h followed by a lyophilization. A stock solution of desired concentration was prepared by dissolving the lyophilized peptide in 20 mM phosphate buffer, 50 mM NaCl (pH 7.4, 0.01% sodium azide).

2.2.2. Aggregation kinetics experiment by Thioflavin T (ThT) fluorescence assay

We performed ThT fluorescence assay to study the kinetics of amyloid aggregation. Stock solutions of ~80 µM peptide concentration for wild type (WT) and mutant peptides were prepared in the buffer mentioned above, followed by a three minute of ultra-sonication and then incubated at 37 °C temperature under a shaking condition. All fluorescence measurements were carried out in Hitachi F-7000 FL spectrometer at various time points of aggregation with an excitation wavelength of 440 nm, emission range of 460-520 nm, using 5 nm slit width for both excitation and emission. Three independent experiments were performed throughout with maximum delay time of 5 min for sample preparation. Time-dependent ThT fluorescence data were normalized and fitted to a sigmoidal growth model[17] where the half-life $t_{1/2}$ is the time required to reach half of the fluorescence intensity, b is the apparent first-order constant and Y_{max}, and Y_0 are, respectively, the maximum and initial fluorescence values:

$$Y = Y_0 + (Y_{max} - Y_0)/(1 + \exp((t - t_{1/2}/b)) \qquad (2.1)$$

The lag time (t_{lag}) of amyloid kinetics was determined as $(t_{1/2} - b)$. To obtain the nucleation and elongation rates, we performed individual fits to the normalized ThT data for each peptide using the online fitting platform AmyloFit.[18]

2.2.3. Confocal microscopy

At different time intervals, aliquots of each peptide incubations were diluted to 10 µM final concentration. After the addition of 20 µM ThT in each aliquot, 10 µL sample mixer was placed on a glass slide. After air-drying, samples were mounted with Dibutyl phthalate Polystyrene Xylene (DPX), and the images were taken using a 63x objective in oil immersion in a confocal microscope (Leica TCSSP8 and the LAS AF Version 2.1.0 built-in 4316 software, Leica Microsystems GmbH, Germany).

2.2.4. Scanning Electron Microscopy (SEM)

Aliquots of each peptide solution were taken at the time of saturation phase and deposited on a glass slide followed by overnight air-drying. The slides were then coated with gold for 120 s at 10 kV voltage and 10 mA current. The sample images were recorded using a FEI Quanta 200 (Quanta^{TM}, USA) scanning electron microscope equipped with a tungsten filament gun operating at 10 kV.

2.2.5. Circular Dichroism (CD) Spectroscopy

CD measurements were taken on a JASCO J-1500 CD spectrometer using a 0.1 cm path length cell with a slit width of 2 nm. WT and mutant peptides of ~80 µM concentration were prepared in 20 mM phosphate buffer, 50 mM NaF (pH 7.4) and incubated at 37 °C under shaking condition. At different time intervals, Far-UV CD spectra were recorded at 25 °C, from 260 nm to 190 nm with a scan speed of 100 nm/min. Temperature-dependent CD spectra were recorded for AV20 (10-80 °C) and G37L (10-90 °C). For each spectrum, five readings were taken (i.e., five accumulations), and the average was considered. Smoothing and buffer subtraction was done for processing of raw data, as per the manufacturer's recommendation.

2.2.6. Surface Enhanced Raman Spectroscopy (SERS)

The (powder form) peptides were dissolved in 5% ammonium hydroxide, vortex well and kept at 4 °C for 1 h followed by lyophilisation. A stock solution of 80 µM peptide concentration was prepared by dissolving the lyophilized peptide in 20 mM phosphate buffer, 50 mM NaCl (pH 7.4, 0.01% sodium azide) and incubated at 37 °C under shaking condition (250 rpm). Fibrillation time for AV20 was 24 h, and for G25L, G29L, G33L, and G37L was 180 min. After the incubation, aliquots of stock solution were diluted in phosphate buffer to obtain 8 µM solutions. The solutions thus prepared were analysed by Raman spectroscopy using a 532 nm Laser with 10 accumulations and an exposition time of 10 seconds in back-scattering mode. A Witec Alpha 300 RS instrument was used for analyses.

2.2.7. Atomic Force Microscopy (AFM)

For AFM experiment, the sample aggregates were prepared as described above in SERS. AFM analysis was done by operating in contact mode with an etched-silicon probe with a pyramidal-shape tip having a nominal curvature of 10 nm and a nominal internal angle of 35°; the height

images were obtained by scanning 512×512 points. A Witec Alpha 300 RS instrument was used for analyses.

2.2.8. MTT assay

Human neuroblastoma SH-SY5Y cells were grown in DMEM culture media supplemented with 10% FBS. Cells were then harvested using trypsin and counted using a hemocytometer. 5×10^3 cells/well were seeded in 96 well cell culture plates. At 70% confluence, the cells were treated with Aβ40, AV20, G25L, G29L, G33L, and G37L at concentrations of 10 µM and 40 µM as a function of time for 24 hours. The media was then discarded, and cells were treated with 3-(4, 5-dimethylthiazol-2-yl)-2, 5-diphenyltetrazolium bromide (MTT reagent) and incubated at 37 °C for 4 h. After incubation, the MTT reagent was replaced by MTT solvent DMSO and kept at room temperature for 15 min. Absorbance was measured at OD-590 nm.

2.2.9. Dynamic Light Scattering (DLS)

DLS measurements were carried out to determine the hydrodynamic diameter of various species throughout the aggregation process, using Malvern Zetasizer Nano S (Malvern Instruments, UK) equipped with a 4 mW He−Ne gas laser (beam wavelength = 632.8 nm) and 173° back scattering measurement facility. All peptides were taken for fibrillation by the same process as mentioned in the ThT fluorescence assay. Measurements were taken for 10 µM peptide concentration at different time-point if aggregation using low volume disposable sizing cuvette. The Z-average diameter was calculated from the correlation function using Malvern technology software.

2.2.10. Nuclear Magnetic Resonance (NMR) Spectroscopy

All experiments were performed using Bruker Avance III 500 MHz NMR spectrometer equipped with a 5 mm SMART probe or on a Bruker Avance III 700 MHz NMR spectrometer, equipped with a RT probe. To the sample solution of 600 µL final volume, 10% D_2O was added along with TSP (Trimethylsilylpropionic acid) as a reference for all the NMR experiments performed. Two-dimensional ^1H-^1H total correlation spectroscopy (2D TOCSY) and two-dimensional ^1H-^1H Rotating frame Overhauser SpectroscopY (2D ROESY) were recorded for the free AV20 at 15 °C, with a mixing time of 80 ms and 250 ms, respectively. Total number of scans for TOCSY and ROESY were 48 and 64, respectively. Data processing and analysis were carried out using

Topspin^{TM} v3.2   software   (Bruker   Biospin,   Switzerland)   and   Sparky (https://www.cgl.ucsf.edu/home/sparky) software, respectively.

Temperature-dependent 1D ^{1}H NMR experiments were performed for AV20 and G37L at different temperatures (10 °C, 15 °C, 20 °C, 25 °C, 30 °C, and 37 °C). For the solvent relaxation experiments, AV20 and G37L sample solutions were prepared at a concentration of 160 µM where the solvent composition was 10% D_2O and 90% H_2O (v/v). To study the solvent isotope effect, we used the same sample concentration dissolved in the solvent with 40% D_2O and 60% H_2O (v/v).

Solid-state NMR ^{13}C cross-polarization spectra of AV20, AV20L, G33L, and G37L peptide aggregates were acquired at 500 MHz (^{1}H frequency), 10 kHz magic angle spinning, and natural isotope abundance. The contact time was 0.5 ms and the interscan delay 1.8 s. The amplitude of the 90° pulse on the proton channel was 80 kHz. For each sample, we manually packed 3 mg of lyophilized powder peptide directly packed in 3.2 mm rotors and the spectra were acquired with 35840 scans.

2.2.11. Solvent relaxation NMR

Transverse relaxation rates of solvent water were measured using CPMG with 8 π pulse block, where the block-time (T) for all the experiments was set at 10 ms. In the case of AV20 peptide, the temperature was fixed at 37 °C. This temperature was chosen in such a way that the timescale of the aggregation for this peptide would be quite compatible with the NMR timescale. In case of G37L, the entire set of solvent relaxation experiments were performed at three different temperatures. At 37 °C, it undergoes fibrillation very rapidly compared to NMR timescale. The other two temperatures were kept fixed at 18 °C and 10 °C, where it is expected to aggregate slowly within NMR time-regime. The recycle delay for every experiment was 35 s. As the signal to noise ratio is very high in case of water peak, only a single scan was used for every relaxation experiment to minimize the experimental time to record a single T_2. All raw data were processed by a script written using Julia version 0.6.2. The peak intensities were fit with Lorentzian and Gaussian functions where the fitting correlation in each case was nearly 0.999. T_2s were extracted from the monoexponential fit of deconvoluted echo-intensities of water peak versus time. The extracted T_2s were plotted against time.

2.2.12. Singular Value Decomposition (SVD) Analysis

Temperature-dependent CD data for AV20 and G37L were subjected to SVD analysis. The equation for singular value decomposition of A is as follows[19]:

$$A = USV^T \tag{2.2}$$

Where U is an M × N matrix whose columns are the left singular vectors, u_i (wavelength coefficient vectors); S is an N × N diagonal matrix, whose elements are called singular values, s_i; and V^T (transpose of V matrix) is also an N × N matrix, whose rows are the right singular vectors, v_i (temperature coefficient vectors).

Here, U represents the basis spectra (the spectral shapes) that make up the data set, and V contains the amplitudes of each component as a function of temperature. SVD analysis and subsequent plots have been done using the statistical R package (R Development Core Team, 2005, https://www.r-project.org/).

2.3. Results and discussion

2.3.1. GxxxG motifs modulate Aβ aggregation kinetics

The effect of mutation on the aggregation kinetics was evaluated using Thioflavin T (ThT), a β-sheet specific intrinsic dye.[20] The ThT kinetic curves (Figure 2.1B) were consistent with the secondary nucleation-dominated self-assembling model.[21] The normalized ThT data for each peptide were individually fitted with the secondary nucleation-dominated self-assembling model using the online fitting platform, AmyloFit[18] and the nucleation and elongation rates were obtained thereafter (Appendix II, Table S2.1). The primary nuleation rate of AV20 was much lower than that of the mutants, whereas we found a varied secondary nucleation and elongation rate profile for the peptide variants. Additionally, the time-dependent ThT kinetic curves were fitted to a sigmoidal growth model[17] to determine the corresponding half-time ($t_{1/2}$) and lag time (t_{lag}) of the aggregation kinetics (Figure 2.1C-D). AV20 exhibited slower kinetics with a t_{lag} of 622.8±21 min, reaching saturation at ~1200 min of incubation. In contrast, the Gly→Leu mutations dramatically increased the fibrillation rate, resulting in a saturation within 240 min of incubation (Figure 2.1B). While G25L displayed a t_{lag} of 36.36±3.80 min, G33L showed a higher t_{lag} of 69.65±6.63 min with a comparatively low fluorescence intensity at saturation, suggesting a low β-sheet content. G29L and G37L displayed almost comparable kinetics, reaching saturation
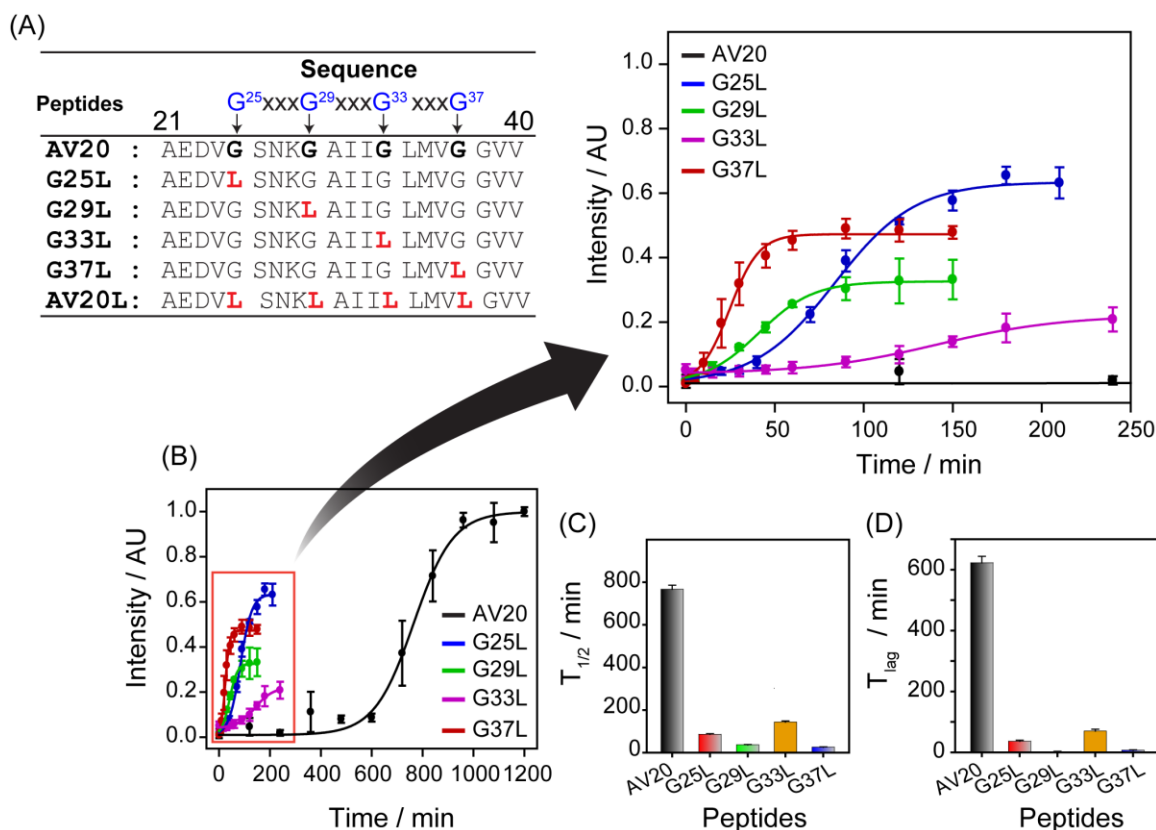
Figure 2.1. Effect of mutation on aggregation kinetics of AV20. (A) The amino acid sequence of the wild type and the designed mutant peptides. (B) Aggregation kinetics of ~80 μM peptide investigated by ThT based fluorescence assay at 37°C. All kinetic curves were normalized with respect to AV20. (C-D) The corresponding half-time ($t_{1/2}$) and lag time (t_{lag}) of the aggregation kinetics obtained from Boltzmann fit. All experiments were repeated three times, and the data were averaged (±SD).

as early as ~120 min. Thus the fine differences observed in the aggregation kinetics among the mutant variants indicated that the positions of these Gly residues also plays a significant role in the aggregation behavior. Due to the insolubility of AV20L (all Gly mutated), we could not perform any solution state experiments. Nevertheless, the ThT assay indicated a subtle difference in the aggregation behavior between the peptides, which might be a direct consequence of their structural transitions during fibrillation. Confocal microscopy confirmed the time-dependent fibrillation of the wild-type (WT) and mutant peptides (Appendix II, Figure S2.1). Further, scanning electron microscopy images of the peptide aggregates at their saturation phase confirmed the occurence of amyloid aggregation (Appendix II, Figure S2.2). The fibrils exhibited dendritic morphology, consisting of long branched rod-like fibers.[22] While the branching of Aβ40, AV20,

G25L, and G29L aggregates were random, G33L and G37L aggregates were more uniform and linear in nature.

2.3.2. Aggregation kinetics is dependant on the conformational transitions

Time-dependent Circular Dichroism (CD) spectroscopy was performed to compare the characteristic changes in the secondary conformation during fibrillation (Figure 2.2). Initially, all the peptide variants were in random coil conformation (negative band near 195-198 nm). AV20 underwent a structural transition from random coil to β-sheet conformation, via a comparatively stable α-helical intermediate. CD spectra of these intermediates (360 min and 720 min) showed negative bands at 208 nm and 222 nm, characteristic spectral signatures for α-helix and even at saturation (1440 min), the negative band at 208 nm was visible (Figure 2.2A). However, the predominant band was the negative band at 218 nm, characteristics of β-sheet conformation. Thus, it is most likely that the GxxxG motif maintains a helical conformation so that there exists a dynamic equilibrium between α-helix and β-sheet conformations. Interestingly, such helical intermediates were not clearly visible in case of mutant peptides (Figure 2.2B-E). Both G25L and
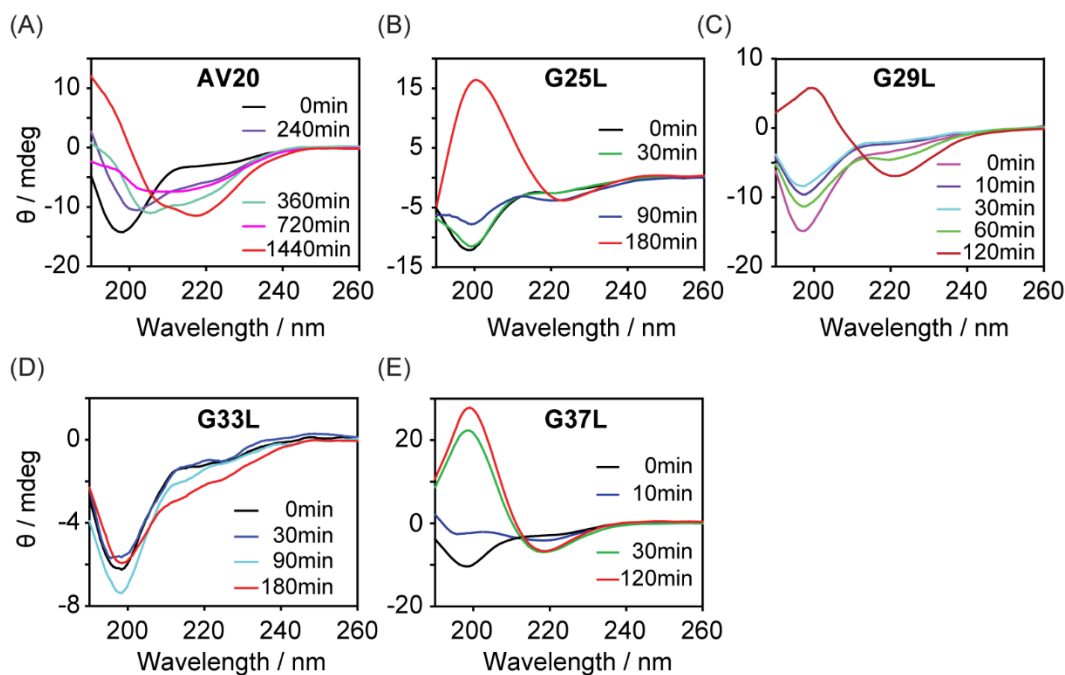
Figure 2.2. Effect of mutation on the secondary structure of the peptide variants investigated using CD spectroscopy. Far-UV spectra as a function of time for (A) AV20, (B) G25L, (C) G29L, (D) G33L, and (E) G37L showing the time-dependent structural transition from monomer to fibril. The sample contains 80 μM peptide in 20 mM sodium phosphate and 50 mM NaF, pH 7.4.

G29L underwent comparatively faster structural transition into complete β-sheet conformation (negative bands near 218 nm and positive bands near 198 nm). While, G33L displayed a small population of β-sheet, G37L underwent a swift transition from random coil to β-sheet, correlating well with the ThT data. Although fibrils formed by WT and mutant peptides were different at a macroscopic level, solid-state Nuclear Magnetic Resonance (NMR) spectroscopy revealed the presence of β-sheet conformation in the variants.[23, 24] The carbonyl peak ~175 ppm was clearly visible in the corresponding spectra for the tested variants including AV20L (Appendix II, Figure S2.3).

Signal Enhanced Raman Spectroscopy (SERS) enabled us to obtain detailed information on the aggregated conformations (Figure 2.3).[25] As already reported in other works, SERS spectroscopy can provide an accurate information on secondary structure within 1-2 nm from the nanoparticle (NP) surface.[25] The Raman signal is enhanced lead to the phenomenon of SERS, which decays depending on $1/r^{12}$, where r is the distance between NPs and the molecule.[25] The substrate was obtained by functionalization of Si wafer with silver NPs prepared with a chemical-free synthesis, thus shown the highest enhancement because of their shape and chemical-free surface. AV20 aggregate showed a band centred at 1287 cm^{-1} and 1304 cm^{-1} (amide III) characteristic of a polypeptide backbone in alpha-helix and β-turn conformation, respectively.
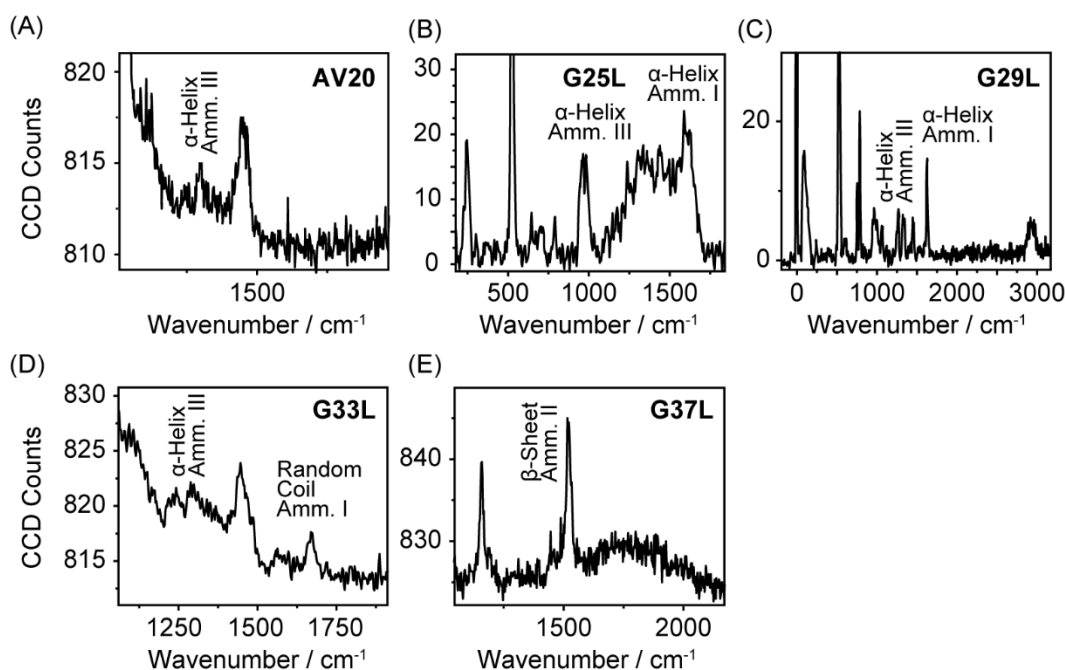
Figure 2.3. The SERS spectra of (A) AV20, (B) G25L, (C) G29L, (D) G33L, and (E) G37L peptides at saturation, showing the presence of different secondary structural conformation.

Both G25L and G29L aggregates showed the presence of α-helix (band at 1631 and 1266 cm^{-1}), β-sheet (1670 and 1248 cm^{-1}) and β-turn (1324 cm^{-1}) secondary structures. Interestingly, SERS spectrum of G33L showed the presence of random coil structures (amide I band centred at 1672 cm^{-1}), also found in CD spectrum. Both CD and SERS experiments showed strong β-sheet conformation for G37L aggregates (band centred at 1520 cm^{-1}). Thus, while G33 mutation exerts a negative effect, G37 has a stimulatory effect on β-sheet formation.

2.3.3. Atomic force microscopy characterizes the morphological differences of the peptide aggregates

High-resolution Atomic Force Microscopy (AFM) showed small cylindrical but well-dispersed aggregates for the AV20, where the average longitudinal and vertical lengths were 0.5±0.2 and 0.5±0.1 μm, respectively (Figure 2.4A). They were spread over a range goes from 0.1-1 μm with an average height of 15±3 nm (Appendix II, Figure S2.4). Shifting the mutation to G25 and G29 resulted in more compact and larger aggregates. G25L aggregates showed an average height increase up to 200±10 nm (transversal) and 110±20 nm (longitudinal). G29L mutant formed oblate aggregates of more ordered structures along a row having an average longitudinal height of 340±100 nm. Surprisingly, while G33L exhibited unorganized aggregates having an average height of 60 nm, G37L manifested in highly organized structures with an average height of 220 nm (Figure 2.4D-E). In fact, G37L showed single and continuous fibrillar structures.

2.3.4. G^{33}xxxG^{37} motif plays the pivotal role in Aβ neurotoxicity

To inspect whether the observed differences in aggregation behaviours are attributed to differences in toxicity, we performed MTT assay with human neuroblastoma SH-SY5Y cells at different timepoints of ThT aggregation kinetics (Appendix II, Figure S2.5). Interestingly, the cell viability assay depicted a specific structure-toxicity correlation for WT and mutant peptides. AV20 showed a similar toxicity profile when compared with Aβ40 (control), suggesting that the hydrophobic sequence present in the C-terminal fragment of Aβ40 is sufficient for oligomerization and Aβ neurotoxicity. The C-terminus strain of Aβ40 was previously shown to aggregate within lipid bilayers to assume a cone-shaped cross-section, inducing membrane curvature and non-specific ion channel.[26] At saturation, G25L and G29L aggregates also showed a high percentage of cytotoxicity (50-60%), indicating a negligible effect of these mutations on neurotoxicity. Surprisingly, both G33L and G37L showed negligible toxicity, signifying that G^{33}xxxG^{37} motif

plays a crucial role in Aβ neurotoxicity (Figure 2.4F). In contrast to the soluble monomeric state with a single conformation, aggregates have an intricate structural landscape allied with multiple aggregate-specific activities.[4]

2.3.5. Aggregate size and morphology is linked with neurotoxicity

Dynamic light scattering experiment showed a gradual increase in the hydrodynamic diameter of each peptide variants as a function of time (Appendix II, Figure S2.6). Interestingly, as the mutation shifted towards the C-terminal, the heterogeneity in the aggregate size decreases (Figure 2.4G), also found in AFM images. Particularly, the G33L and G37L aggregates were more
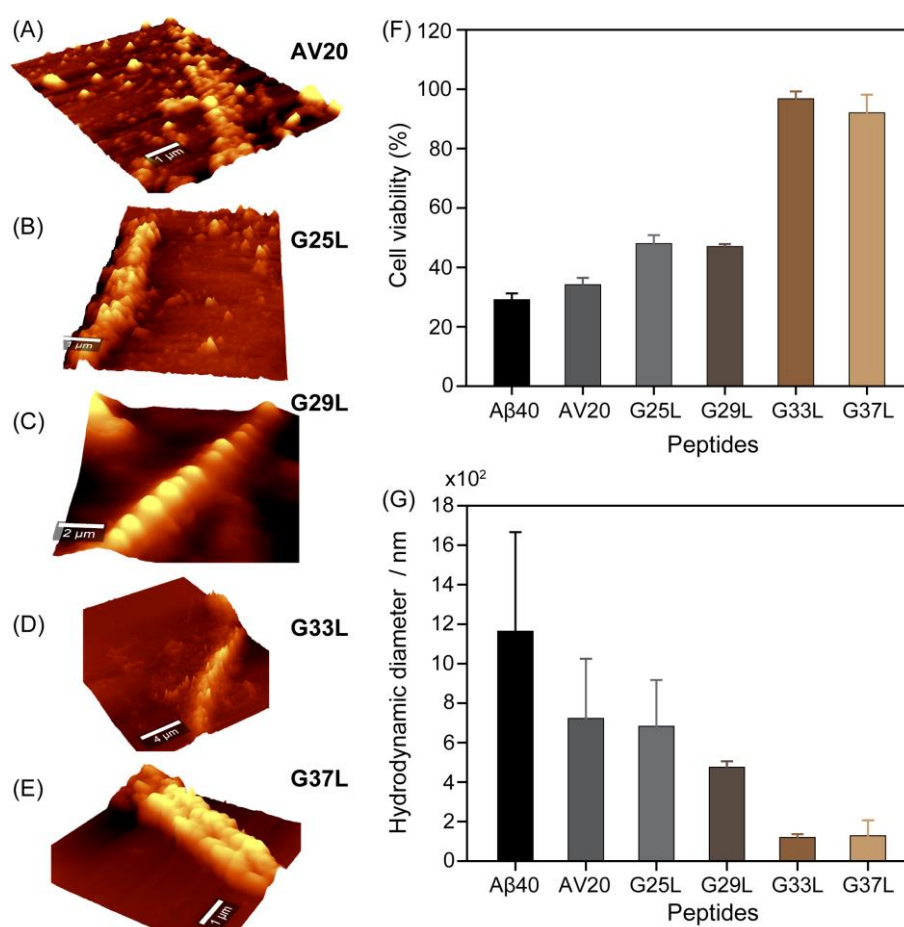
Figure 2.4. Correlation between aggregation size, morphology, and cytotoxicity. AFM images of (A) AV20, (B) G25L, (C) G29L, (D) G33L, and (E) G37L peptide aggregates. (F) Cytotoxicity of the tested peptide aggregates (10 µM) against SH-SY5Y cells as obtained from the MTT reduction assay. All experiments were repeated three times, and the data were averaged (±SEM). (G) The hydrodynamic diameters of the peptide variants studied using DLS. The values are average of ten accumulations (±SD).

uniform in size distribution when compared to the other variants. Thus, in correlation with the toxicity profile of respective peptides, structural dynamicity can be addressed as an important factor behind neutotoxicity.

Additionally, the unorganized and amorphous nature of G33L could explain its non-toxicity. In contrast, the equally non-toxic G37L has a definite β-sheet rich fibril. Moreover, this finding suggested that toxicity and β-sheet fibril are two independent phenomena as also recently suggested.[27] Thus to gain a clearer understanding of the structure-function correlation, we further investigated into the mechanistic pathway that differentiates AV20 and G37L aggregation.

2.3.6. Thermal stability plays a crucial role in determining the aggregation propensity

The thermal stability of peptide's secondary structures was investigated by a temperature-induced folding-unfolding study.[28] For this, CD experiments were performed for AV20 and G37L at different temperatures (Figure 2.5A,B). AV20 showed a minimal effect on the secondary conformation. The absorbance (θ) at 218 nm versus temperature plot showed an unstable partial β-sheet conformation (Figure 2.5A, inset). However, G37L developed a complete β-sheet structure which remained stable up to 90 °C (Figure 2.5B, inset), suggesting that Leu mutation stabilizes inter-chain hydrophobic contacts[29] and that the C-terminal region plays a pivotal role in fibril formation according to AFM data. Moreover, the temperature-dependent CD data indicates that G37L is more aggregation prone than AV20. These datasets were analyzed using singular value decomposition (SVD)[30] to determine the minimum number of spectrscopically distinct species during temperature-dependent structural transition. The number of principle components (PC), which represents the number of distinct structural species in the dataset, can be estimated by taking into account of (i) the significance of singular values (Figures 2.5C-D), and (ii) smooth shape of the v_i vectors (Figures 2.5E-F). Both AV20 and G37L showed that the primary two components have smooth shape that corresponds to the singular values with the highest magnitude. Thus the results of SVD analysis suggested that the temperature-dependent structural transition is a two-step process in either case. While, Figures 2.5G,H represents the left singular vectors corresponding to the 1st two components of AV20 and G37L, respectively (the spectral shapes), the right singular vectors contains the amplitudes of each component (1st five components) as a function of temperature (Figures 2.5E-F). Thus, in correlation with the left singular value plots, the right singular vector plots indicate a partial β-sheet conformation of AV20 with increasing the
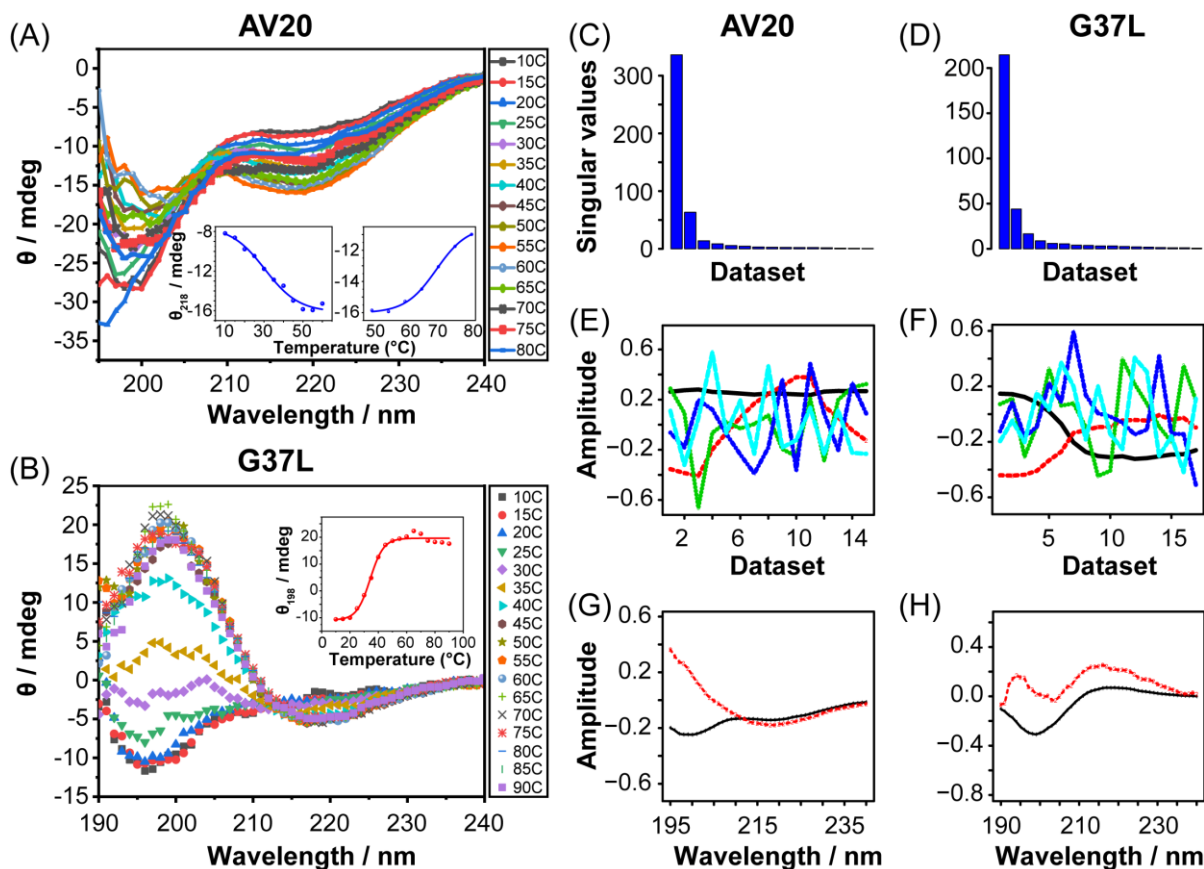
Figure 2.5. The temperature-dependent CD spectroscopy for (A) AV20, and (B) G37L. Inset images of (A) show the absorbance (θ) versus temperature plot at 218 nm. The plots were fitted using the Boltzmann equation. Inset image of (B) shows the same plot at 198 nm for G37L. In (C) and (D), blue-bars show the singular values in descending order, for AV20 and G37L, respectively. (E), and (F) represent the shape of the v_i vectors for the first five components plotted against the number of temperatures taken for AV20 and G37L respectively. The primary two components have a smooth shape that corresponds to the singular values with the highest magnitude. (G), and (H) are the first two u_i vectors corresponding to the principal components for AV20 and G37L, respectively.

temperature. It is worth mentioning that the amount of random coil remained almost same (Figure 2.5E).

To gain an atomic-resolution insight into this temperature-dependent structural change, 1D ¹H NMR spectra were recorded for AV20 and G37L (Appendix II, Figure S2.7). The chemical shift changes in the amide proton as a function of temperature have been used to examine the strength of hydrogen bond or the formation of intramolecular hydrogen bond.[31] The results of temperature-dependent 1D ¹H NMR spectra of the peptide tested here showed that all amide peaks exhibited a

temperature-dependent displacement of their chemical shifts in up-field direction. Distinct 1D peaks of AV20 were identified from 2D ^{1}H-^{1}H total correlation spectroscopy (TOCSY) and Rotating frame Overhauser SpectroscopY (ROESY) experiments (Appendix II, Figure S2.8). The temperature coefficient for these distinct peaks were calculated by plotting the amide proton chemical shift as a function of temperature, over the temperature range of 283 to 310 K. The co-efficients for AV20 suggested probable intramolecular hydrogen-bonding, resulting in a partial conformational uptake.[32] In contrast, G37L manifested in a very high negative temperature coefficient, corroborating well with its β-sheet pre-disposition. Apart from the observed amide proton chemical shift changes, a temperature-dependent line-broadening was also apparent. The line broadening rate was higher for G37L, suggesting a higher amide proton exchange with solvent molecule (Appendix II, Figure S2.7). The line broadening could also arise from the fact that the G37L peptide is more aggregation prone than AV20 at higher temperatures (Figure 2.5). Moreover, this further confirms the possible role of the adjacent solvent molecules in aggregation.

2.3.7. Differentiating the aggregation pathway using solvent dynamics NMR spectroscopy

The proteins or peptides that readily undergo amyloid fibrillation have a significant number of backbone H-bonds which are exposed to solvent water.[33] These exposed H-bonds are tightly bound to the water molecules via intermolecular interaction. The hydrophobic interaction facilitates the dehydration of backbone H-bonds by the nearby non-polar group. The stabilization of a secondary structure requires a higher-order organization of the chain, which facilitates further removal of water. In contrast, some the conformational changes (such as β-sheet) require more hydration of the peptide chains rather than removal of water. Therefore, those changes are facilitated by the inclusion of the water molecules on the peptide surface.

In a recently published paper by Chakraborty et al., it has been shown that during the coil-globule transition of PNIPAM polymer, the mixing of bound and free water molecules results in the lowering of the observed transverse relaxation time of a water molecule.[34] Depending on the rotational time scales of the water, molecules are classified into two categories. The slow, restricted molecules are termed as "*cold*" molecules, and the fast-rotating molecules belong to the bulk part are termed as "*hot*" molecules. Based on rotational kinetic energy exchange between "*cold*" and "*hot*" molecules, a phenomenological model has been constructed which nicely fit the solvent relaxation data as a function of temperature. The numerical values of the fitting parameters describe the phase transition of thermo-responsive polymers with more physical insight.

The underlying mathematical equation used to analyze all the relaxation data is given in the following:

The original equation, which gives the final form of observed T_2 of water molecules as a function of time, can be written in the following form from the basic idea reported by Chakraborty et al.[34]

$$(T_2)_{mean} = \frac{N_{bulk}(T_2(t))_{hot}}{N_H^0 - N_H(t) + N_{bulk}} \tag{2.3}$$

Where, N_{bulk} is the number of "hot" water molecules $N_H(t)$ is the number of bound water present at a particular time t in the sample solution, N_H^0 denotes the number of "cold" water molecules present at t=0, i.e. just after, the sample preparation. It has been assumed that the $(T_2)_{mean}$ is recorded after the system reaches the stead-state. So, every T_2 is recorded after some time gap so that the system can exhibit steady state condition. T_2 of free water molecules (or, experimentally measured T_2 of water molecule after the completion of aggregation) does not change with time (or fluctuate stochastically about a mean), so this is a constant denoted in equation (2.3) as K.

So, by rearranging the equation we can write,

$$(T_2)_{mean} = \frac{K}{\frac{N_H^0 - N_H(t)}{N_{H0}}\left(\frac{N_H^0}{N_{bulk}}\right) + 1} \tag{2.4}$$

or,

$$(T_2)_{mean} = \frac{K}{mn + 1} \tag{2.5}$$

So, the m represents the fraction of the "cold" water molecules excluded in the solution at a particular time, is the ratio of the number of initial bound water to free water molecules present in the sample solution. Here, we have assumed that the number of "bulk water" is so large compared to the "cold" water molecules that bulk waters is more or less constant as a function of time throughout the fibrillation. Thus, in the course of fibrillation, n can be considered as a constant.

Thus, from the equation (2.5) whenever the number of "cold" water molecules, $N_H(t)$ decreases i.e.,m increases during fibrillation, the $(T_2)_{mean}$ decreases. Conversely, whenever $N_H(t)$ starts to increase i.e. m decreases we see an increase in the $(T_2)_{mean}$. When $N_H{}^0 = N_H(t)$, T_2 should saturate to a constant value.
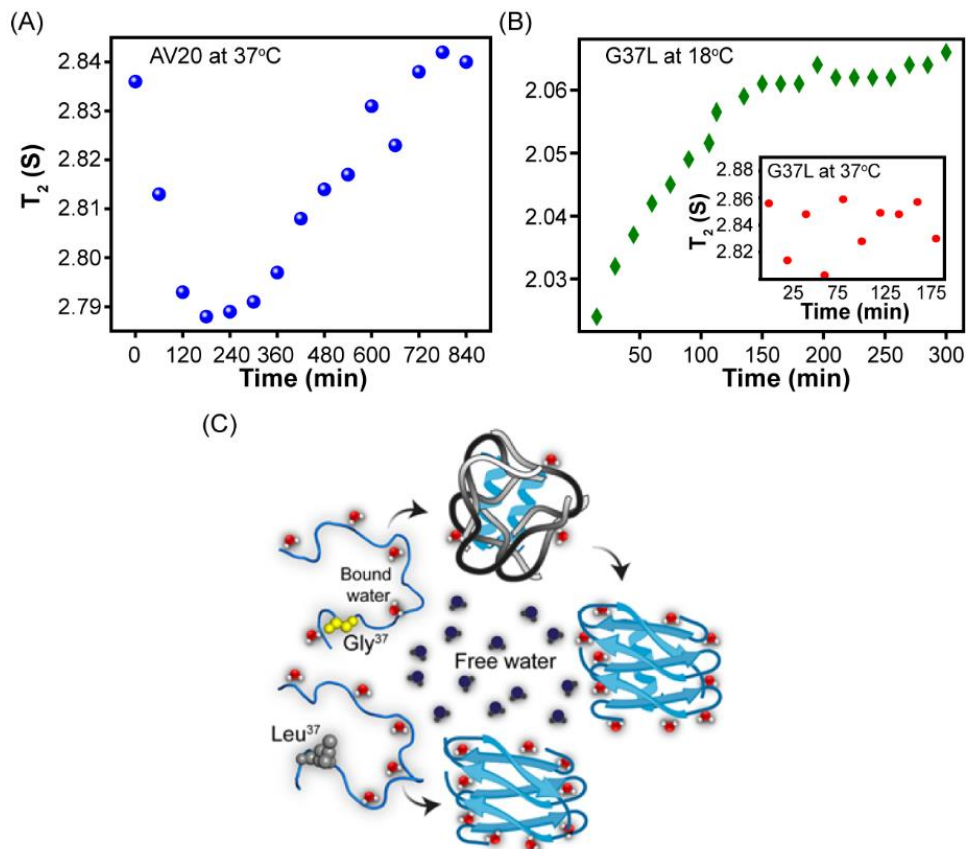
Figure 2.6. Solvent relaxation. (A) The transverse relaxation time of water measured at 37°C of AV20 solution plotted as a function of time. (B) The transverse relaxation time of water in G37L solution plotted as a function of time measured at 18°C, and 37°C (inset). The marker-size in each plot denotes the error in the measurement of T_2, which is in order of 10^{-3} (Appendix II, Figure S2.10C). (C) Schematic illustration of possible water mediated aggregation pathway followed by AV20 and G37L, respectively.

For the system where only increasing trend of T_2 is observed, the "hot" water population can be expressed as, $[N_{bulk} - N_H(t)]$.

Thus, the final form of T_2 will be,

$$(T_2)_{mean} = \frac{K}{1-pn} \tag{2.6}$$

where, $p = \frac{N_H(t)}{N_H{}^0}$. As with time "p" increases, T_2 increases.

Based on this hypothesis, the peptide-solvent interactions during aggregation were monitored using an efficient adaptation of solvent relaxation NMR technique.[35] This technique measured the T_2 of water using a Carr-Purcell-Meiboom-Gill (CPMG)[36] sequence (Appendix II, Figure S9) at different time points in the aggregation pathway. So we performed the solvent

relaxation experiments of both the peptides AV20, and G37L and the solvent relaxation behavior for the two peptides showed distinct water dynamics during fibrillation (Figure 2.6A,B). This dual nature of T_2s versus time plots can be satisfactorily explained by the previously proposed model.[34] At 37 °C the T_2s for solvent molecules associated with AV20 initially decreased as a result of an entropy-driven water exclusion that catalyzes hydrophobic interactions. This, probably drives the system to change its conformation from random coil to α-helix[15], as was previously seen using CD spectroscopy. During nucleus formation, α-helix compacts the chain via intra-segment hydrogen bonding and an intense van der Waals contact, in the expense of gaining translational entropy through expelling water.[37] This was followed by a gradual increase in T_2 after ~240 min of incubation (Figure 2.6A), as a significant population of the peptide begins to convert into β-sheet. This phenomenon is expected to be dominantly mediated by increased hydration of the polypeptide chains with subsequent ordering of water molecules on the surface.[16, 34, 38] The transition from α-helix to β-sheet is manifested by a sequential rearrangement of the hydrophilic side-chains to orient outwardly, facilitating intermolecular interactions with solvent molecules.[14, 39] The slower exchange rate with solvent water as a result of β-sheet formation may also contribute to the escalation of T_2.[40] Interestingly, G37L displayed no systematic change in T_2 values at 37°C, possibly due to the fast saturation upon rapid β-sheet formation (Figure 2.6B, inset). Even at a lower temperature (as low as 18 °C and 10 °C) where the kinetics is expected to be slower and comparable with the NMR time scale, G37L revealed a constant increase in the T_2 values reaching saturation as early as ~180 min (Figure 2.6B, Appendix II, Figure S2.10A). Thus, the Gly→Leu mutation either destabilizes the formation of helical intermediates resulting in a direct conversion into β-sheet structure or in a very fast transition into β-sheet that could not be detected in the NMR timescale. Additionally, from Appendix II, Figure S2.10B, it has been predicted that the addition of more D_2O (40%) enhances the water exclusion rate and also the water inclusion rate, so it reaches saturation earlier (within 480 min) compared to the former condition. This can be attributed due to the different energy profiles of the intermolecular interactions of peptides with D_2O and H_2O, which is conventionally referred to as solvent isotope effect.[34]

2.4. Conclusions

This study demonstrates the uniqueness of the GxxxG repeating motifs in the WT (AV20) peptide in maintaining structural dynamicity and subsequent neurotoxicity. Previous NMR studies on Aβ40 have shown that the solvent accessible turns at Gly[25]-Gly[29] and Gly[37]-Gly[38] facilitate the

compact foldings of the peptide.[41] In association with the adjacent β-branched residues (Ile and Val), Gly acts as a molecular notch facilitating the wild-type helix-helix interactions.[11] Mutation in these crucial structural motifs modulates the hydrogen bond networking that affects the helix-helix association, mediating in differential pathways of fibrillation. The solvent relaxation studies, further, proved as an effective strategy to differentiate between the aggregation pathways, giving an in-depth mechanistic insight. Our results indicate that the toxicity of the mutants decreases until it vanishes as the substitution with Leu moves closer to the C-terminal. The GxxxG motif contributes to the flexibility and subsequent conformational heterogeneity of the WT peptide, as suggested by the fast transition from random coil to β-sheet intermediates and the lack of intermediate α-helical conformations for Gly mutants. Thus, the enhanced structural heterogeneity observed for the GxxxG motif ranks in accordance with the observed cytotoxicity.

Theoretical models have suggested that the hydrogen bonding between the C=O and H-C$_\alpha$ of two contiguous chains facilitate the formation of a lock that stabilizes the membrane-compromising conformation of Aβ40.[26, 41] Moreover, the conformational selection is in part driven by hydrogen bonding networks. Gly→Leu mutation destabilizes this conformer by preventing the hydrogen bond formation, reducing the neurotoxicity. Conversely, Gly being non-chiral and with a very small side-chain has many degrees of freedom rendering an advantage to the WT peptide enabling successful insertion across the membrane through pore formation. Our data strongly agree with recent studies where just one stereoisomer of silybin inhibit Aβ40 toxicity by binding the C-terminal hydrophobic segment 35-40.[42] This would enable the designing of novel inhibitors against Aβ40/42 to aid in targetted therapy of neurotoxic Alzheimer's and other related diseases, such as type II diabetes and Parkinson since amylin and α-synuclein show the similar SxxxG or GxxxG/GxxxxG repeat motif, respectively.

2.5. Appendix II

Table S2.1. Primary nucleation rate, secondary nucleation rate, and elongation rate of AV20 AV20, G25L, G29L, G33L, and G37L obtained from ThT fluorescence kinetics.

Peptide Name	Primary Nucleation Rate ($mol^{-1} min^{-1}$)	Secondary Nucleation Rate ($mol^{-2} min^{-1}$)	Elongation Rate ($mol^{-1} min^{-1}$)
AV20	4.167E-5 (+5.833E-6,-1.05E-5)	5.72E+6 (+1.38E+6, -2.17E+6)	2.48E+7 (+1.17E+6, -6.17E+6)
G25L	1.5 (+0.40, -0.65)	3.68E+6 (+1.1E+6, -2.2E+6)	4.2E+5 (1.4E+5, -1.6E+5)

G29L	4.11 (+0.7, -0.94)	4.34E+5 (+5.3E+5, -1.7E+4)	1.71E+6 (+2.0E+5, -6.0E+5)
G33L	1.35 (+0.44, -0.15)	1.56E+7 (2.7E+6, -1.9E+6)	5.68E+4 (+2.8E+3, -1.3E+4)
G37L	1.64 (+0.54, -0.58)	2.43E+5 (+1.4E+4, -2.8E+5)	1.17E+7 (+1.9E+6, -2.2E+6)
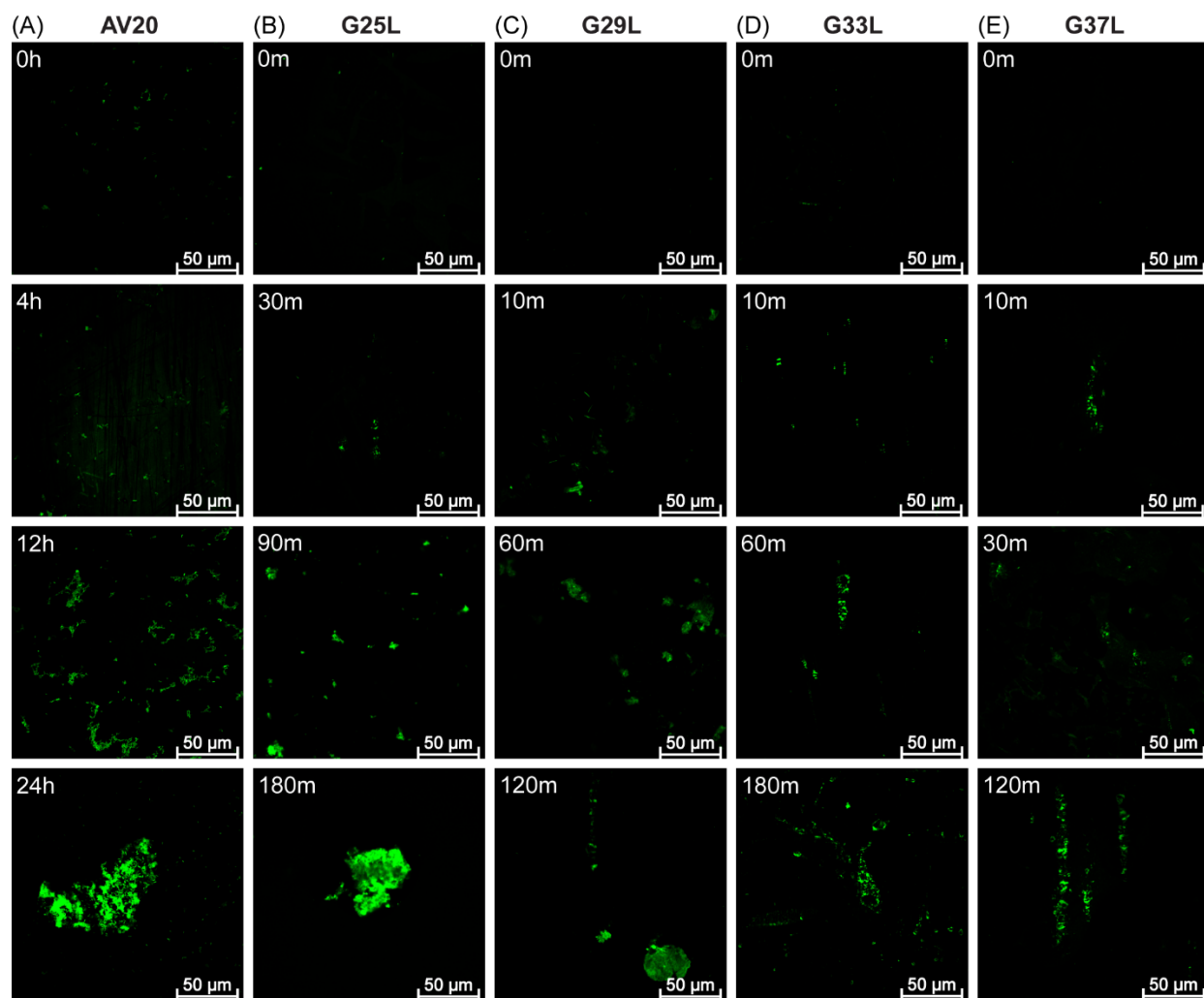
Figure S2.1. Confocal microscopy images of fibril formation in the presence of ThT. Fluorescence confocal images of (A) AV20, (B) G25L, (C) G29L, (D) G33L and (E) G37L peptides taken at different time points of aggregation. All samples contain 20 mM sodium phosphate buffer, 50 mM NaCl (pH 7.4, 0.01% sodium azide). The scale bar shows 50 μm.
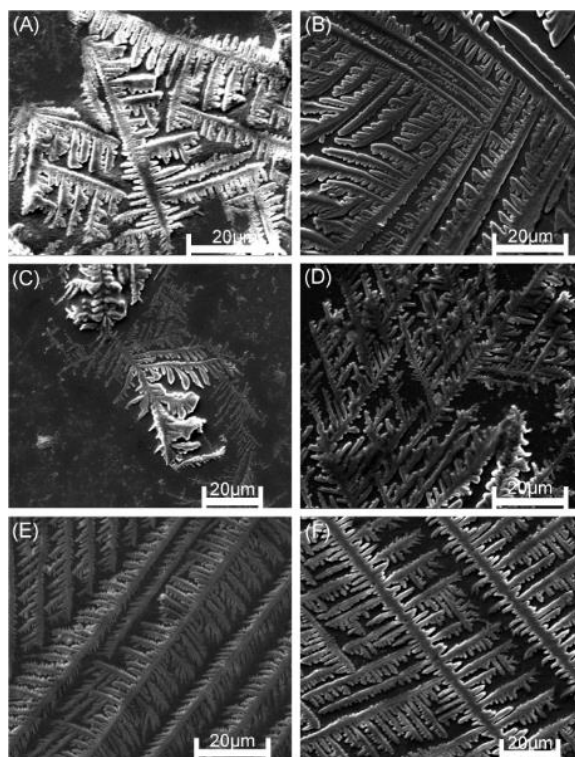
Figure S2.2. SEM images of the peptide aggregates from (A) Aβ40, (B) AV20, (C) G25L, (D) G29L, (E) G33L and (F) G37L taken from the saturation phase of ThT kinetics confirmed the formation of amyloid aggregates. The scale bar shows 20 μm.
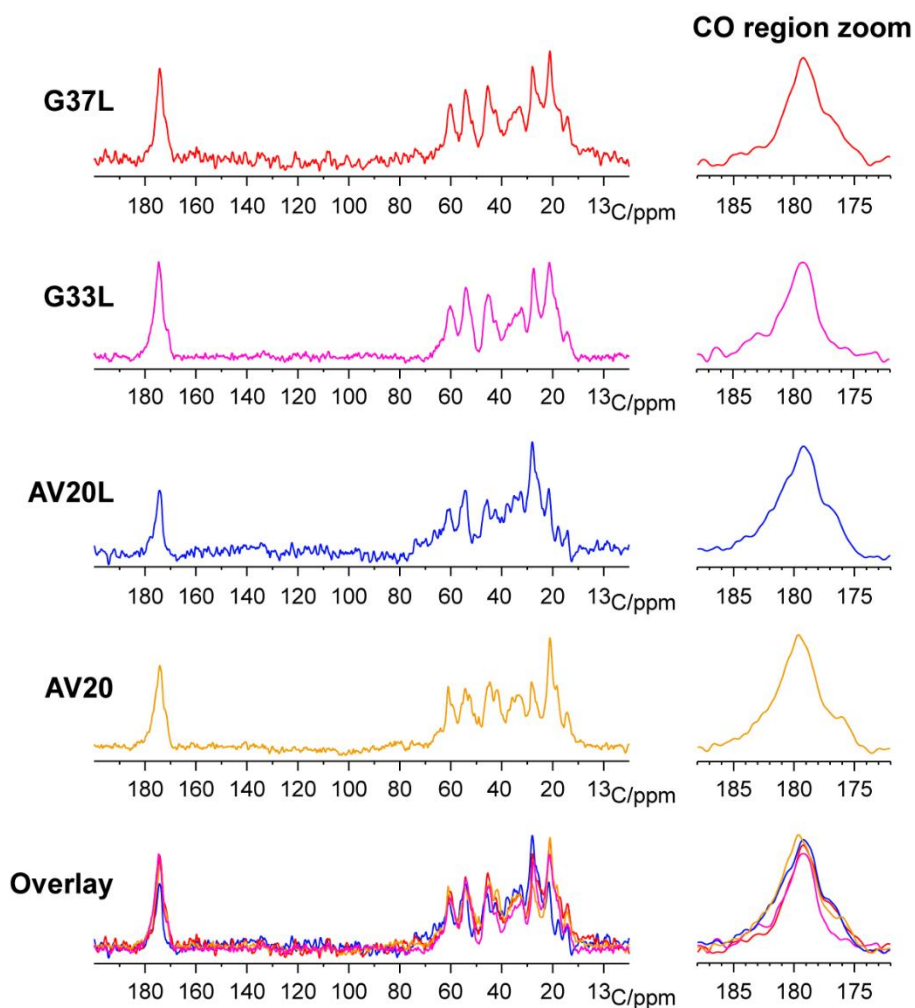
Figure S2.3. Solid-state NMR ^{13}C cross-polarisation spectra of AV20, AV20L, G33L, and G37L peptide aggregates acquired at 500 MHz (^1H frequency), 10 kHz magic angle spinning, and natural isotope abundance. All spectra show the presence of β-sheet conformation as visible by the highly characteristic chemical shift range of the centre of the (carbonyl peak at ~175 ppm). Spectra were referenced to Adamantane, as described previously.[24]
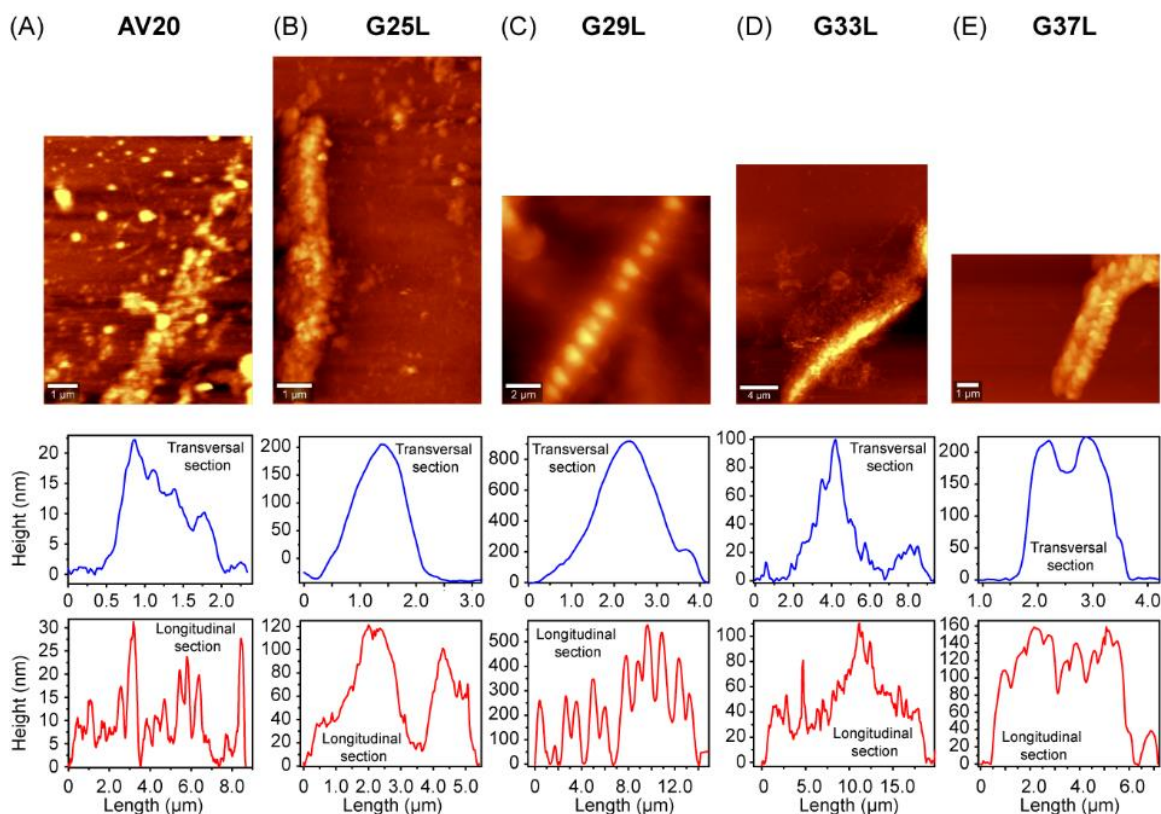
Figure S2.4. AFM images of (A) AV20, (B) G25L, (C) G29L, (D) G33L, and (E) G37L peptide aggregates along with their transverse and longitudinal-section length profiles. AV20 peptide aggregates showed a cylindrical morphology where the average longitudinal and vertical lengths were 0.5±0.2 and 0.5±0.1 μm, respectively. They were spread over a range goes from 0.1-1 μm with an average height of 15±3 nm. G25L showed a more ordered rows with an average height increase up to 200±10 nm (transversal) and 110±20 nm (longitudinal). G29L mutant displayed oblate aggregates of more ordered structures along a row having an average longitudinal height of 340±100 nm. G33L peptide formed unorganized structures having an average height of 60 nm, where G37L mutant has a highly organized structures with an average height of 220 nm.
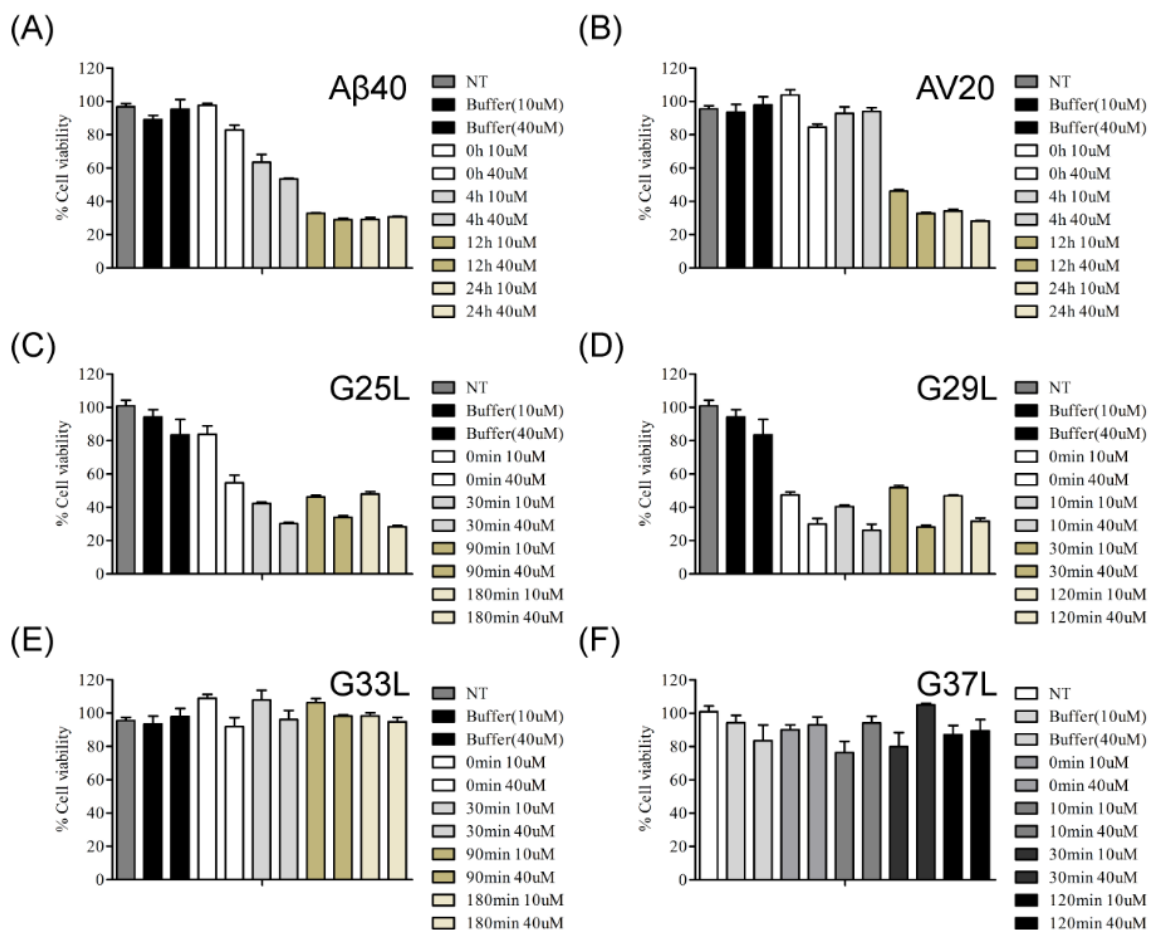
Figure S2.5. Cytotoxicity assay showing the percentage of viable cells upon peptide treatments. Effect of different concentrations (10 µM, 40 µM) of (A) Aβ40, (B) AV20, (C) G25L, (D) G29L, (E) G33L, and (F) G37L on SHSY5Y neuroblastoma cells at different time points of their aggregation process, studied by MTT reduction assay (NT stands for non-treated control cells, and buffer was used as negative control). Aβ40, AV20, G25L, and G29L showed high percentage of toxicity. On the other hand G33L and G37L showed a negligible amount of neurotoxicity.
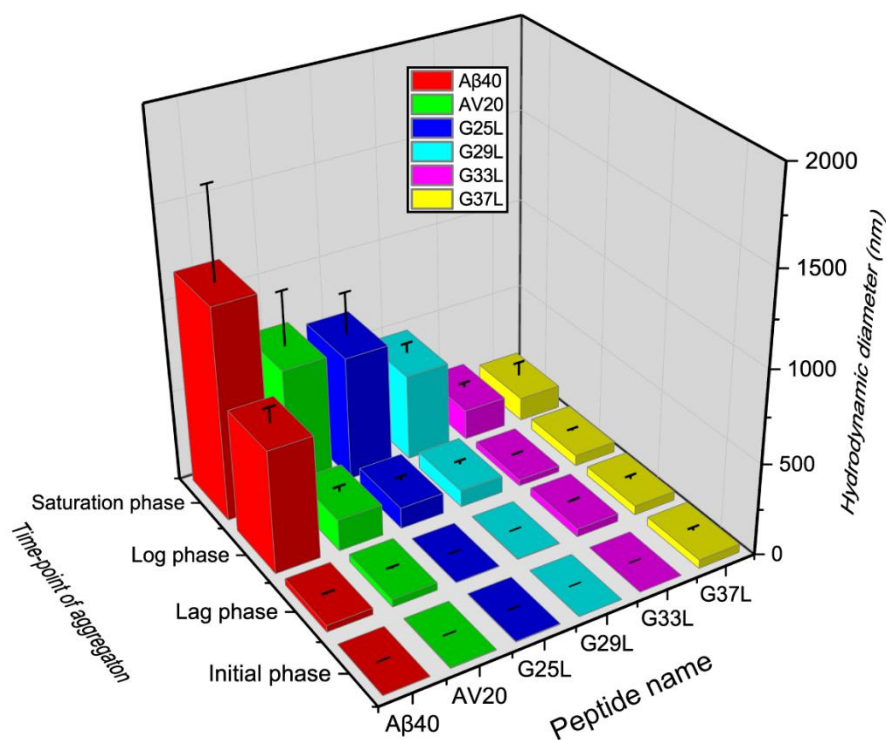
Figure S2.6. Hydrodynamic diameter measurements of Aβ 40, AV20, G25L, G29L, G33L and G37L by DLS taken as a function of time. Each of these peptides showed a gradual increase in the hydrodynamic diameter as a function of time. The order of size is as followed: Aβ40 ≥ AV20 ≥ G25L ≥ G29L ≥ G33L ≈ G37L. A more uniformly suspended fibrillar aggregates were found for G33L and G37L compared to other peptides.
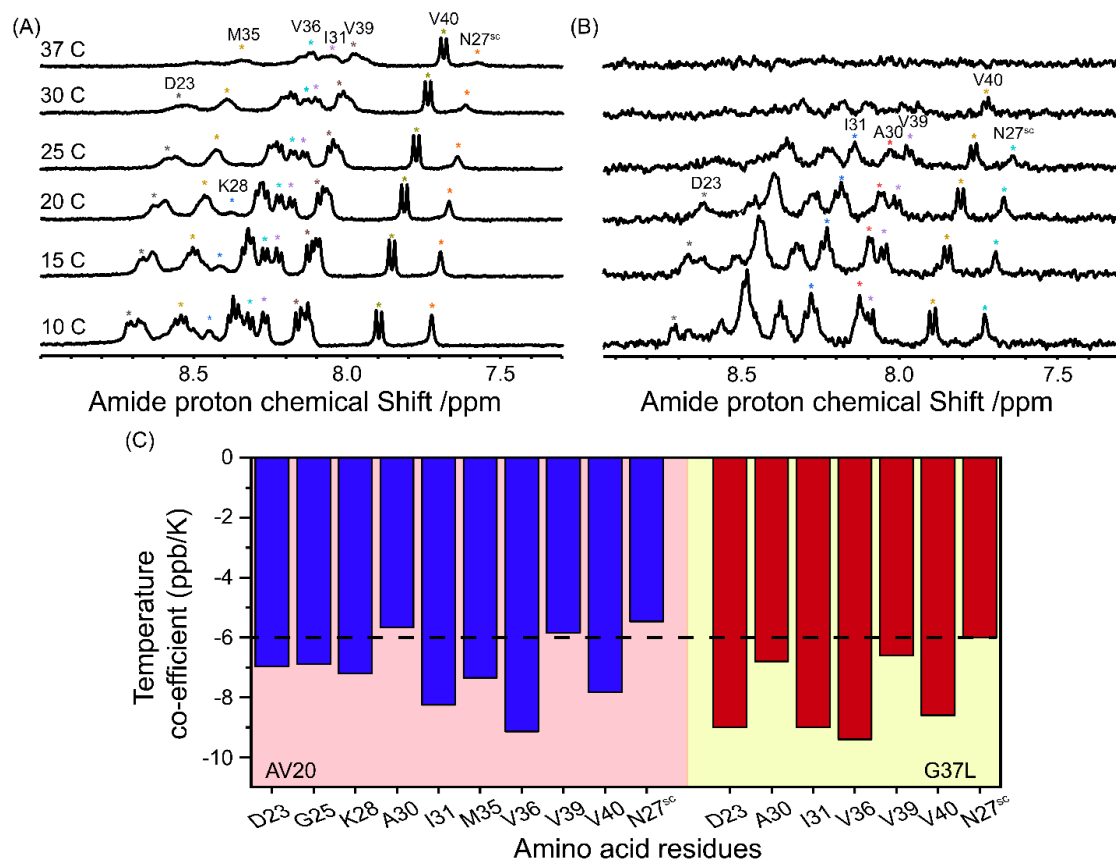
Figure S2.7. Temperature-dependent NMR spectroscopy. (A) 1D ^{1}H NMR of AV20, (B) 1D ^{1}H NMR of G37L a at different temperature showing amide proton chemical shift. (C) Temperature co-efficients for few distinct peaks from 1D ^{1}H NMR were calculated and plotted as bar diagram.
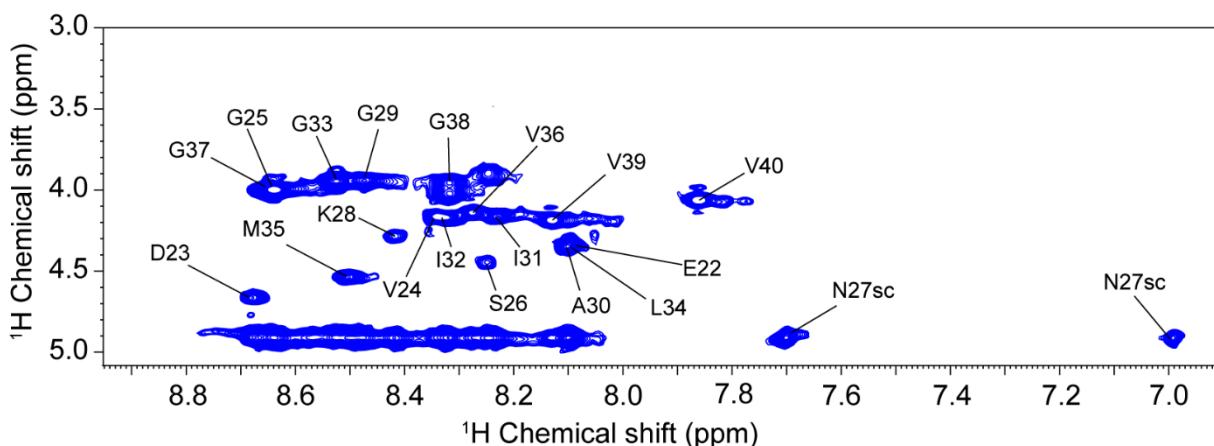
Figure S2.8. Assignment of AV20 TOCSY spectrum at 15 °C showing amide to Hᵅ peak of amino acid residues. The assignment was done using 2D TOCSY and 2D ROESY spectra of AV20 at 15 °C. 2D TOCSY are employed for the identification of amino acid spin systems and 2D ROESY experiment is used to sequentially connect the spin systems. The Hᵅ peak of N27 has merged with the peaks of water region. The side chain peaks of N27 are shown at ~7.7 ppm and ~7.0 ppm.
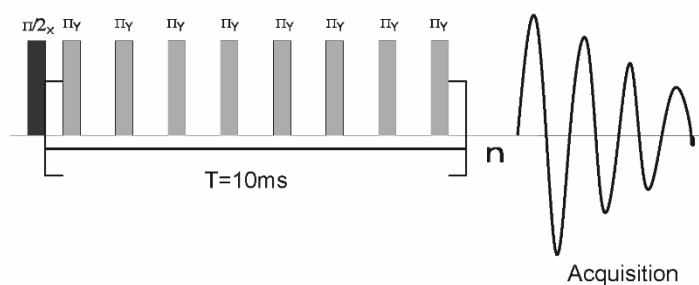
Figure S2.9. The schematic diagram of the CPMG 8π-block pulse sequence used for measuring the transverse relaxation times (T_2) of water molecules.
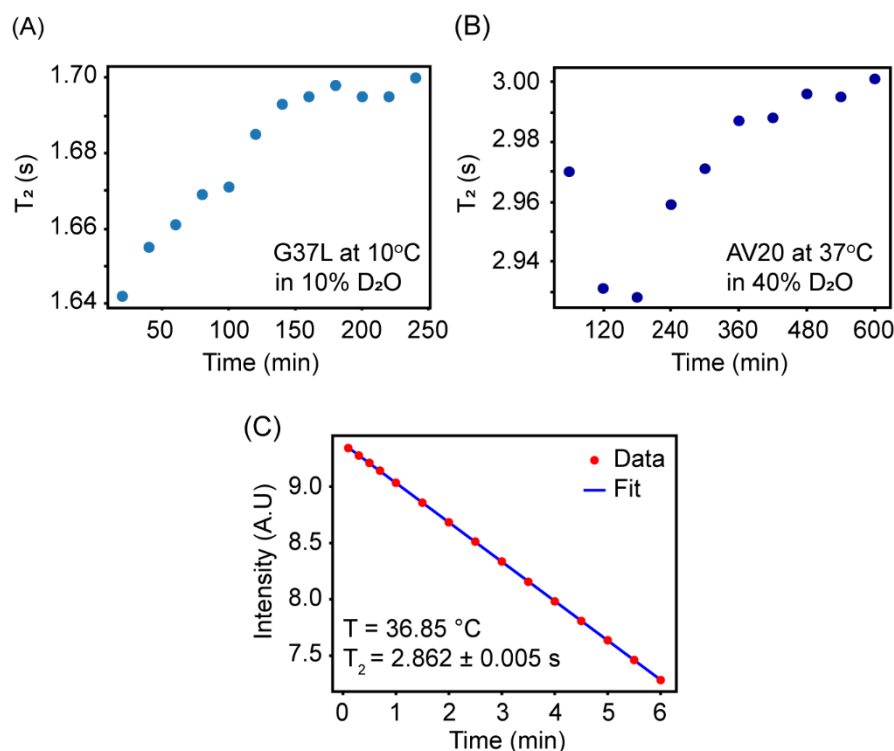
Figure S2.10. The NMR solvent relaxation data. (A) Transverse relaxation time versus time plot of G37L in 90% H_2O-10% D_2O (v/v) at 10 °C (B) Transverse relaxation time versus time plot of AV20 in 60% H_2O-40% D_2O (v/v) at 37 °C. The marker size denotes the error in the measurement of the T_2. (C) Plot of decaying deconvoluted echo intensities versus time in logarithm scale, showing the measurement of T_2 (magnitude and error) of water in G37L solution in 20 mM sodium phosphate buffer and 50 mM NaCl at at 37 °C.

2.6. References

[1] S. J. Lee, E. Nam, H. J. Lee, M. G. Savelieff, M. H. Lim, *Chem Soc Rev* **2017**, 46, 310; P. C. Ke, M. A. Sani, F. Ding, A. Kakinen, I. Javed, F. Separovic, T. P. Davis, R. Mezzenga, *Chem Soc Rev* **2017**, 46, 6492; N. L. Fawzi, D. S. Libich, J. Ying, V. Tugarinov, G. M. Clore, *Angew Chem Int Ed Engl* **2014**, 53, 10345; J. Hardy, D. J. Selkoe, *Science* **2002**, 297, 353; S. I. Cohen, S. Linse, L. M. Luheshi, E. Hellstrand, D. A. White, L. Rajah, D. E. Otzen, M. Vendruscolo, C. M. Dobson, T. P. Knowles, *Proc Natl Acad Sci U S A* **2013**, 110, 9758.
[2] R. Ahmed, G. Melacini, *Chem Commun (Camb)* **2018**, 54, 4644.
[3] T. L. Lau, J. D. Gehman, J. D. Wade, K. Perez, C. L. Masters, K. J. Barnham, F. Separovic, *Biochim Biophys Acta* **2007**, 1768, 2400; M. Sakono, T. Zako, *FEBS J* **2010**, 277, 1348.
[4] N. Itoh, E. Takada, K. Okubo, Y. Yano, M. Hoshino, A. Sasaki, M. Kinjo, K. Matsuzaki, *Chembiochem* **2018**, 19, 430.
[5] T. Okada, M. Wakabayashi, K. Ikeda, K. Matsuzaki, *J Mol Biol* **2007**, 371, 481; R. Ahmed, M. Akcan, A. Khondker, M. C. Rheinstädter, J. C. Bozelli, R. M. Epand, V. Huynh, R. G. Wylie, S. Boulton, J. Huang, C. P. Verschoor, G. Melacini, *Chem Sci* **2019**, 10, 6072; R. Cascella, M. Perni, S. W. Chen, G. Fusco, C. Cecchi, M. Vendruscolo, F. Chiti, C. M. Dobson, A. De Simone, *ACS Chem Biol* **2019**, 14, 1352.

[6] J. T. Jarrett, E. P. Berger, P. T. Lansbury, *Biochemistry* **1993**, 32, 4693; L. O. Tjernberg, D. J. Callaway, A. Tjernberg, S. Hahne, C. Lilliehöök, L. Terenius, J. Thyberg, C. Nordstedt, *J Biol Chem* **1999**, 274, 12619; J. R. Brender, A. Ghosh, S. A. Kotler, J. Krishnamoorthy, S. Bera, V. Morris, T. B. Sil, K. Garai, B. Reif, A. Bhunia, A. Ramamoorthy, *Chem Commun (Camb)* **2019**, 55, 4483; S. Bera, E. Arad, L. Schnaider, S. Shaham-Niv, V. Castelletto, Y. Peretz, D. Zaguri, R. Jelinek, E. Gazit, I. W. Hamley, *Chem Commun (Camb)* **2019**, 55, 8595.
[7] A. Harmeier, C. Wozny, B. R. Rost, L. M. Munter, H. Hua, O. Georgiev, M. Beyermann, P. W. Hildebrand, C. Weise, W. Schaffner, D. Schmitz, G. Multhaup, *J Neurosci* **2009**, 29, 7582; L. W. Hung, G. D. Ciccotosto, E. Giannakis, D. J. Tew, K. Perez, C. L. Masters, R. Cappai, J. D. Wade, K. J. Barnham, *J Neurosci* **2008**, 28, 11950.
[8] L. M. Munter, P. Voigt, A. Harmeier, D. Kaden, K. E. Gottschalk, C. Weise, R. Pipkorn, M. Schaefer, D. Langosch, G. Multhaup, *EMBO J* **2007**, 26, 1702.
[9] G. Kleiger, R. Grothe, P. Mallick, D. Eisenberg, *Biochemistry* **2002**, 41, 5990.
[10] W. P. Russ, D. M. Engelman, *J Mol Biol* **2000**, 296, 911.
[11] A. Senes, M. Gerstein, D. M. Engelman, *J Mol Biol* **2000**, 296, 921.
[12] M. Decock, S. Stanga, J. N. Octave, I. Dewachter, S. O. Smith, S. N. Constantinescu, P. Kienlen-Campard, *Front Aging Neurosci* **2016**, 8, 107.
[13] K. A. Dill, *Biochemistry* **1990**, 29, 7133.
[14] S. H. Chong, S. Ham, *Angew Chem Int Ed Engl* **2014**, 53, 3961.
[15] D. Thirumalai, G. Reddy, J. E. Straub, *Acc Chem Res* **2012**, 45, 83.
[16] U. Novak, J. Grdadolnik, *Journal of Molecular Structure* **2017**, 1135, 138.
[17] P. Arosio, T. P. Knowles, S. Linse, *Phys Chem Chem Phys* **2015**, 17, 7606.
[18] G. Meisl, J. B. Kirkegaard, P. Arosio, T. C. Michaels, M. Vendruscolo, C. M. Dobson, S. Linse, T. P. Knowles, *Nat Protoc* **2016**, 11, 252.
[19] V. Klema, A. Laub, *IEEE Transactions on automatic control* **1980**, 25, 164.
[20] D. Bhattacharyya, R. Kumar, S. Mehra, A. Ghosh, S. K. Maji, A. Bhunia, *Chem Commun (Camb)* **2018**, 54, 3605; M. Biancalana, S. Koide, *Biochim Biophys Acta* **2010**, 1804, 1405; R. Cukalevski, X. Yang, G. Meisl, U. Weininger, K. Bernfur, B. Frohm, T. P. J. Knowles, S. Linse, *Chem Sci* **2015**, 6, 4215; G. Meisl, X. Yang, C. M. Dobson, S. Linse, T. P. J. Knowles, *Chem Sci* **2017**, 8, 4352.
[21] M. Törnquist, T. C. T. Michaels, K. Sanagavarapu, X. Yang, G. Meisl, S. I. A. Cohen, T. P. J. Knowles, S. Linse, *Chem Commun (Camb)* **2018**, 54, 8667.
[22] A. Ghosh, A. S. Pithadia, J. Bhat, S. Bera, A. Midya, C. A. Fierke, A. Ramamoorthy, A. Bhunia, *Biochemistry* **2015**, 54, 2249.
[23] B. Chandra, D. Bhowmik, B. K. Maity, K. R. Mote, D. Dhara, R. Venkatramani, S. Maiti, P. K. Madhu, *Biophys J* **2017**, 113, 805.
[24] M. Rad-Malekshahi, K. M. Visscher, J. P. Rodrigues, R. de Vries, W. E. Hennink, M. Baldus, A. M. Bonvin, E. Mastrobattista, M. Weingarth, *J Am Chem Soc* **2015**, 137, 7775.
[25] L. D'Urso, M. Condorelli, O. Puglisi, C. Tempra, F. Lolicato, G. Compagnini, C. La Rosa, *Phys Chem Chem Phys* **2018**, 20, 20588.
[26] M. Pannuzzo, D. Milardi, A. Raudino, M. Karttunen, C. La Rosa, *Physical Chemistry Chemical Physics* **2013**, 15, 8940.
[27] F. Scollo, C. Tempra, F. Lolicato, M. F. Sciacca, A. Raudino, D. Milardi, C. La Rosa, *The journal of physical chemistry letters* **2018**, 9, 5125.
[28] G. Malgieri, G. D'Abrosca, L. Pirone, A. Toto, M. Palmieri, L. Russo, M. F. M. Sciacca, R. Tatè, V. Sivo, I. Baglivo, R. Majewska, M. Coletta, P. V. Pedone, C. Isernia, M. De Stefano, S. Gianni, E. M. Pedone, D. Milardi, R. Fattorusso, *Chem Sci* **2018**, 9, 3290.
[29] K. P. Murphy, E. Freire, in *Advances in protein chemistry*, Vol. 43, Elsevier, 1992.
[30] I. Wang, S. Y. Chen, S. T. Hsu, *Sci Rep* **2016**, 6, 31514.
[31] F. J. Blanco, G. Rivas, L. Serrano, *Nat Struct Biol* **1994**, 1, 584.
[32] K. Gademann, B. Jaun, D. Seebach, R. Perozzo, L. Scapozza, G. Folkers, *Helvetica chimica acta* **1999**, 82, 1.

[33] A. De Simone, G. G. Dodson, C. S. Verma, A. Zagari, F. Fraternali, *Proc Natl Acad Sci U S A* **2005**, 102, 7535.

[34] I. Chakraborty, K. Mukherjee, P. De, R. Bhattacharyya, *J Phys Chem B* **2018**, 122, 6094.

[35] C. L. Cooper, T. Cosgrove, J. S. van Duijneveldt, M. Murray, S. W. Prescott, *Soft Matter* **2013**, 9, 7211.

[36] H. Y. Carr, E. M. Purcell, *Physical review* **1954**, 94, 630.

[37] L. Cruz, B. Urbanc, J. M. Borreguero, N. D. Lazo, D. B. Teplow, H. E. Stanley, *Proc Natl Acad Sci U S A* **2005**, 102, 18258; L. PAULING, R. B. COREY, H. R. BRANSON, *Proc Natl Acad Sci U S A* **1951**, 37, 205.

[38] Y. Fichou, G. Schirò, F. X. Gallat, C. Laguri, M. Moulin, J. Combet, M. Zamponi, M. Härtlein, C. Picart, E. Mossou, H. Lortat-Jacob, J. P. Colletier, D. J. Tobias, M. Weik, *Proc Natl Acad Sci U S A* **2015**, 112, 6365.

[39] R. K. Kar, J. R. Brender, A. Ghosh, A. Bhunia, *Journal of chemical information and modeling* **2018**, 58, 1576.

[40] I. Kheterpal, S. Zhou, K. D. Cook, R. Wetzel, *Proc Natl Acad Sci U S A* **2000**, 97, 13597.

[41] M. Ahmed, J. Davis, D. Aucoin, T. Sato, S. Ahuja, S. Aimoto, J. I. Elliott, W. E. Van Nostrand, S. O. Smith, *Nat Struct Mol Biol* **2010**, 17, 561.

[42] M. F. Sciacca, V. Romanucci, A. Zarrelli, I. Monaco, F. Lolicato, N. Spinella, C. Galati, G. Grasso, L. D'Urso, M. Romeo, *ACS chemical neuroscience* **2017**, 8, 1767.

Chapter III

Nanodiscs-Mediated Oligomerization of Amyloid Beta in a Near-Native Membrane Environment: Mechanistic Insight into the Regulatory Role of GxxxG Motif

3.1. Introduction

Alzheimer's disease (AD), a severe neurodegenerative disorder and a leading cause of dementia worldwide, is primarily characterized by the accumulation of amyloid beta (Aβ) peptides in the brain.[1] Aβ peptides are produced through the sequential cleavage of the transmembrane amyloid precursor protein (APP),[2] which then undergoes self-association along a nucleated growth pathway, with oligomeric intermediates being the primary culprits behind AD-pathogenesis.[3] Despite several decades of research, the collective discoveries have not yet converged on a single universal mechanism of amyloidogenesis. One of the major challenges in understanding the comprehensive mechanisms of amyloidogenesis is due to the inherent conformational plasticity of these intrinsically disordered proteins, which leads to high degree of polymorphism in both fibrillar and pre-fibrillar structures.[4] Additionally, cell membrane plays a crucial role in modulating Aβ aggregation and directing aggregates to toxic intermediate states.[5]

Several studies have suggested that cell membrane disruption contributes to Aβ neurotoxicity, either through the formation of ion-selective pores by Aβ monomers or by fragmenting the lipid membrane during fibrillation.[6] The interaction between Aβ and cellular membranes has been reported to triggers conformational changes in the peptide's secondary structure, thereby influencing the fibrillation process.[7] Moreover, Aβ-membrane binding is greatly influenced by several factors like membrane composition, charge, fluidity, and curvature.[8] In fact, lipid bilayer can exert diverse effects on aggregation; depending on the lipid compositions, either it can accelerate or decelerate the fibrillation rate, leading to structural polymorphisms. In a recent study, our group has demonstrated the impact of different membrane compositions on Aβ40 aggregation dynamics at an atomic resolution.[9] By comparing a simplified blood-brain barrier mimic composed of POPC/POPG/cholesterol/GM1, and the native BBB composed of total brain lipid extract, we elucidated the crucial role of hydrophobic interactions between the lipid acyl chains and residues spanning K16-K28 and I31-V36 in forming transient conformations during peptide aggregation. We observed a temporal transition in the secondary structure of Aβ40 towards helical intermediates, highlighting membrane-induced transient folding.

Recent studies have shown emerging trends on the use of lipid nanodiscs (NDs) as membrane mimics to probe the influence of lipid membrane on amyloid aggregation.[10, 11] Although these phospholipid bilayer nanodiscs do not precisely replicate the physiological

scenario, they offer significant advantages over the use of traditional membrane mimics such as micelles or vesicles.[11, 12] Typically, NDs are very homogeneous and firmly soluble in a wide range of buffer systems.[13] They enable preparation of well-defined lipid mixtures, and allow precise control over bilayer size, and charge distribution.[14] On the other hand, small unilamellar vesicles (SUVs) are known to undergo rapid changes in the lipid environment (from homogeneous to heterogeneous) upon interaction with amyloid proteins.[15] Moreover, the increased stability of NDs offers the possibility of determining the interaction with a stable planar bilayer while reducing the effect of membrane curvature. Notably, NDs have been previously utilized for studying lipid specificity, as well as for the entrapment of Aβ oligomers.[16] Overall, the precise lipid composition embedded within nanodiscs of desired size, coupled with their high stability and homogeneity allows for comprehensive quantitative understanding of Aβ-membrane association.

Over the years, various studies have revealed the crucial role played by the central (K16-G25) and the C-terminal (K28-G37) region in Aβ self-assembly and membrane interaction.[17, 18] Interestingly, the conserved GxxxG motif present at the C-terminus (G25-G38) of Aβ harbors unique features throughout the Aβ pathway, making it a noteworthy target.[19] While this motif has been linked to APP processing and subsequent Aβ production,[20] its significant role in regulating Aβ oligomer formation and neurotoxicity is evident from previous studies.[21] In this context, the precise role of the GxxxG repeating motifs in the C-terminal of Aβ peptide fragment in maintaining structural dynamicity and neurotoxicity has been demonstrated in the previous chapter.[22] We showed that hydrogen bonding networks play a crucial role in conformation selection, and substitution with Leu residue at position 33 and 37 destabilizes intermediate conformers, leading to reduced neurotoxicity.[22, 23]

In this chapter, we investigate the significance of the GxxxG motif in Aβ self-assembly, especially its role in membrane-mediated oligomerization in a near-native membrane environment. In order to understand the role of the GxxxG motif, particularly the significance of G33 and G37 residues in membrane-mediated oligomerization of Aβ40, a peptide library was designed (Figure 3.1A). This library includes full-length Aβ40, peptides with Gly to Leu mutations at positions 33 (Aβ40G33L) and 37 (Aβ40G37L), as well as the C-terminal 20 residue fragment, AV20 (A21-V40). By elucidating the mechanistic insights into the involvement of the GxxxG motif in Aβ

aggregation, this research aims to advance our understanding of Alzheimer's disease pathogenesis and potentially contribute to targeted therapeutic strategies.

3.2. Materials and methods

3.2.1. Sample preparation

Lyophilized synthetic peptides Aβ40, Aβ40G33L, Aβ40G37L, and AV20 were purchased from Genscript Inc. USA. Peptides were weighed as 1 mg and dissolved in 500 μL 1,1,1,3,3,3-hexafluoro-2-propanol (HFIP; Sigma-Aldrich, USA) using gentle vertexing and 10 second sonication. It was then kept for 40 mins at 4 °C and separated into 10 aliquots. The aliquots were lyophilized for 48 h and stored at -20 °C for further use.

3.2.2. Nanodiscs preparation

A mixture of DMPC, DMPG lipid at certain ratios were mixed with MSP protein, followed by incubating for 1 h using magnetic stirrer at 25 °C. Then the mixture was incubated with bio-bead overnight to remove the detergent. The formation of nanodiscs were confirmed by using SEC and DLS experiments.

3.2.3. Thioflavin T (ThT) fluorescence assay

Stock solutions of ~80 μM Aβ40, Aβ40G33L, and Aβ40G37L peptides were prepared in a buffer containing 20 mM phosphate buffer (pH 7.4, 0.01% sodium azide) and 50 mM NaCl. Sample solutions were vortexed well, followed by a three-minute ultra-sonication and incubated at 37 °C temperature under shaking conditions (250 rpm). At several time intervals, aliquots from the peptide solutions were taken and diluted to 10 μM final concentration. 20 μM ThT was added in each sample before measurements. Fluorescence measurements were carried out using Hitachi F-7000 FL spectrometer (Japan) with excitation wavelength at 440 nm and an emission range of 460-520 nm. The scan speed was 240 nm/min with 5 nm slit width for both the excitation and emission.

Further, peptide aggregation was studied using BMG LABTECH POLARstar Omega spectrometer (Germany) in a 96 well plate under shaking conditions at 25 °C temperature. ThT was added into the sample solutions at equimolar ratio and fluorescence was monitored under controlled temperatures. All buffer solutions were filtered by using a 0.2 μm filter. Three independent experiments were performed throughout.

3.2.4. Size exclusion chromatography (SEC)

SEC experiments were performed for samples containing free NDs, free Aβ40 oligomers, and Aβ40 oligomers in presence of NDs (L/P=20) using a superdex 200 10/300 increase GL column (GE Healthcare,Freiburg, Germany) equilibrated with specific buffer solution and purified through Akta (GE Healthcare) FPLC. Flow rate was set at 0.4 ml/min for each run and absorbance was monitored at 280 and 215 nm wavelength. Data processing and peak detection was done using Origin software.

3.2.5. Dynamic light scattering (DLS)

DLS measurements were carried out using Malvern Zetasizer Nano S (Malvern Instruments, UK) equipped with a 4 mW He−Ne gas laser (beam wavelength = 632.8 nm) and 173° back scattering measurement facility. Measurements were taken using low volume disposable sizing cuvette. The Z-average diameter was calculated from the correlation function using Malvern technology software.

3.2.6. Transmission Electron Microscopy (TEM)

TEM samples were prepared by diluting the stock solution into 10 µM for each variant in milli-Q water. Then 10 µL of each sample was spotted on a carbon-coated copper grid (Electron Microscopy Sciences, USA), an incubation of 2 min followed by blotting to remove excess buffer. It was subsequently followed by washing with milli-Q water and staining with freshly prepared filtered 1% (w/v) uranyl acetate solution (Electron Microscopy Sciences, USA) for 5 min. Finally, samples were air-dried for overnight in a dust free space. Imaging was done using a transmission electron microscope FEI Tecnai TF20 at 200 kV with a point resolution of 0.24 nm and line resolution of 0.102 nm. Recording of images was done digitally, and analysis was done in EDS mode.

3.2.7. Scanning electron microscopy (SEM)

10 uL of aliquots were taken and deposited on a glass slide, followed by overnight air-drying. The slides were then coated with gold for 120 s at 10 kV voltage and 10 mA current. The sample images were recorded using a a FEI Quanta 200 (QuantaTM, USA) scanning electron microscope equipped with a tungsten filament gun operating at 10 kV.

3.2.8. Confocal microscopy

Confocal imaging was taken with a 63X objective in oil immersion using Leica TCSSP8 confocal microscope and the LAS AF Version 2.1.0 built-in 4316 software, Leica Microsystems GmbH, Germany.

3.2.9. FTIR spectroscopy

FTIR spectra were collected using a PerkinElmer 100 spectrometer at room temperature. The FTIR spectra of lyophilized Aβ40 oligomer in presence of NDs were measured using the conventional KBr method. A total 32 number of scans were taken in the spectral range of 1800-1400 cm^{-1} with a spectral resolution of 4 cm^{-1}. Processing and deconvolution of the spectra were acquired using Origin software.

3.2.10. Circular dichroism (CD) spectroscopy

CD measurements were taken on a JASCO J-1500 CD spectrometer (Japan) using a 0.1 cm path length cell with a slit width of 2 nm. Peptides of ~80 µM concentration were prepared in 20 mM phosphate buffer, 50 mM NaF (pH 7.3), and titrated with increasing concentration of SDS micelles. Far-UV CD spectra were recorded at 25 °C, from 260 nm to 190 nm, with a scan speed of 100 nm/min. For each spectrum, three readings were taken (i.e., three accumulations), and the average was considered. Smoothing and buffer subtraction were done to process raw data, as per the manufacturer's recommendation.

3.2.11. NMR experiments

NMR experiments were performed on a Bruker Avance 700 MHz spectrometer equipped with a 5 mm cryogenic probe or on a Bruker Avance III 500 MHz NMR spectrometer equipped with a 5 mm SMART probe. NMR experiments were performed at 10 °C or 25 °C. Prior to adding a fibril seed to the NMR tube containing monomeric Aβ40, a 2D spectrum was acquired to compare differences immediately before and after titration with NDs. Resonance assignments of the monomer 2D ^{1}H-^{15}N heteronuclear quantum coherence (HSQC) spectra were taken from the literature. To monitor Aβ40 aggregation in presence of NDs (L/P=20) with atomic resolution, real-time 2D NMR experiments were performed by consecutively acquiring ^{1}H-^{15}N HSQC spectra. Each spectrum was obtained from 64 t_1 experiments, 16 scans, 8 dummy scans, and a 0.1 s recycle delay. The spectral widths were 16 and 40 ppm, and the offsets were 4.7 and 117 ppm for the proton and nitrogen dimensions, respectively.

For AV20, 2D total correlation spectroscopy (TOCSY) NMR experiments were performed at 25 °C on the Bruker Avance 700 MHz spectrometer. Real-time 2D HSQC NMR experiments were performed for ^{15}N-labeled Gly residues of AV20 on the Bruker Avance III 500 MHz NMR spectrometer at 10 °C. For AV20 structure calculation in presence of SDS, AV20 were prepared with a peptide concentration of 1 mM. The peptide was dissolved in 100 mM sodium dodecyl-d$_{25}$ sulfate (SDS) with 20 mM sodium phosphate buffer and pH 5.2. NMR experiments were performed in the presence of 10% D$_2$O and at 298 K using Bruker Avance 500 MHz spectrometer. Topspin 3.5 (Bruker Biospin Germany) and SPARKY 3.113 (https://www.cgl.ucsf.edu/home/sparky) software were used for processing and analyzing the NMR data, respectively. 2D TOCSY and nuclear overhauser effect spectroscopy (NOESY) spectra were acquired using states-TPPI mode with 1024 and 512 complex data points along t$_2$ and t$_1$ dimensions, respectively. The sweep width and offset due to water were fixed at 14 and at 4.703 ppm with a 2 s relaxation delay. TOCSY spectra were performed using the standard Bruker pulse program (with the MLEV-17 spin lock block) and excitation sculpting being the mode of water suppression. A spin-lock mixing time of 80 ms was used for the TOCSY experiment, whereas 150 ms mixing times were set for NOESY experiments.

The three-dimensional NMR structures for AV20 in SDS micelles were calculated by CYANA 2.1 software suite. Upper bound distance constraints were calculated from NOE build-up curves and qualitatively categorized as strong (2.5 Å), medium (2.6–3.5 Å) and weak (3.6–5.0 Å). A lower bound cutoff of 2.0 Å was used for all distance restraints mentioned above. Finally, an ensemble of 100 structures, which satisfied all of the experimental distance and dihedral angle constraints, were selected. Among these 100 structures, the top 20 structures with the lowest target function values and RMSD were chosen for further structural analysis. The structures were further checked from Ramachandran plot analysis.

3.3. Results

3.3.1. GxxxG motif regulates Aβ40 self-assembly kinetics

We first examined the effect of Gly→Leu mutations at positions 33 and 37 within the GxxxG motifs on the aggregation kinetics of Aβ40 by using Thioflavin T (ThT) fluorescence assay (Figure 3.1B). The results obtained from the ThT fibrillation assay for Aβ40 are in alignment with

(A)

Peptides		Sequence

$G_{25}xxxG_{29}xxxG_{33}xxxG_{37}$

AβΑ40   : DAEFRHDSGYEVHHQKLVFFAEDVGSNKGAIIGLMVGGVV

Aβ40G33L : DAEFRHDSGYEVHHQKLVFFAEDVGSNKGAIILLMVGGVV

Aβ40G37L : DAEFRHDSGYEVHHQKLVFFAEDVGSNKGAIIGLMVLGVV

AV20   : AEDVGSNKGAIIGLMVGGVV
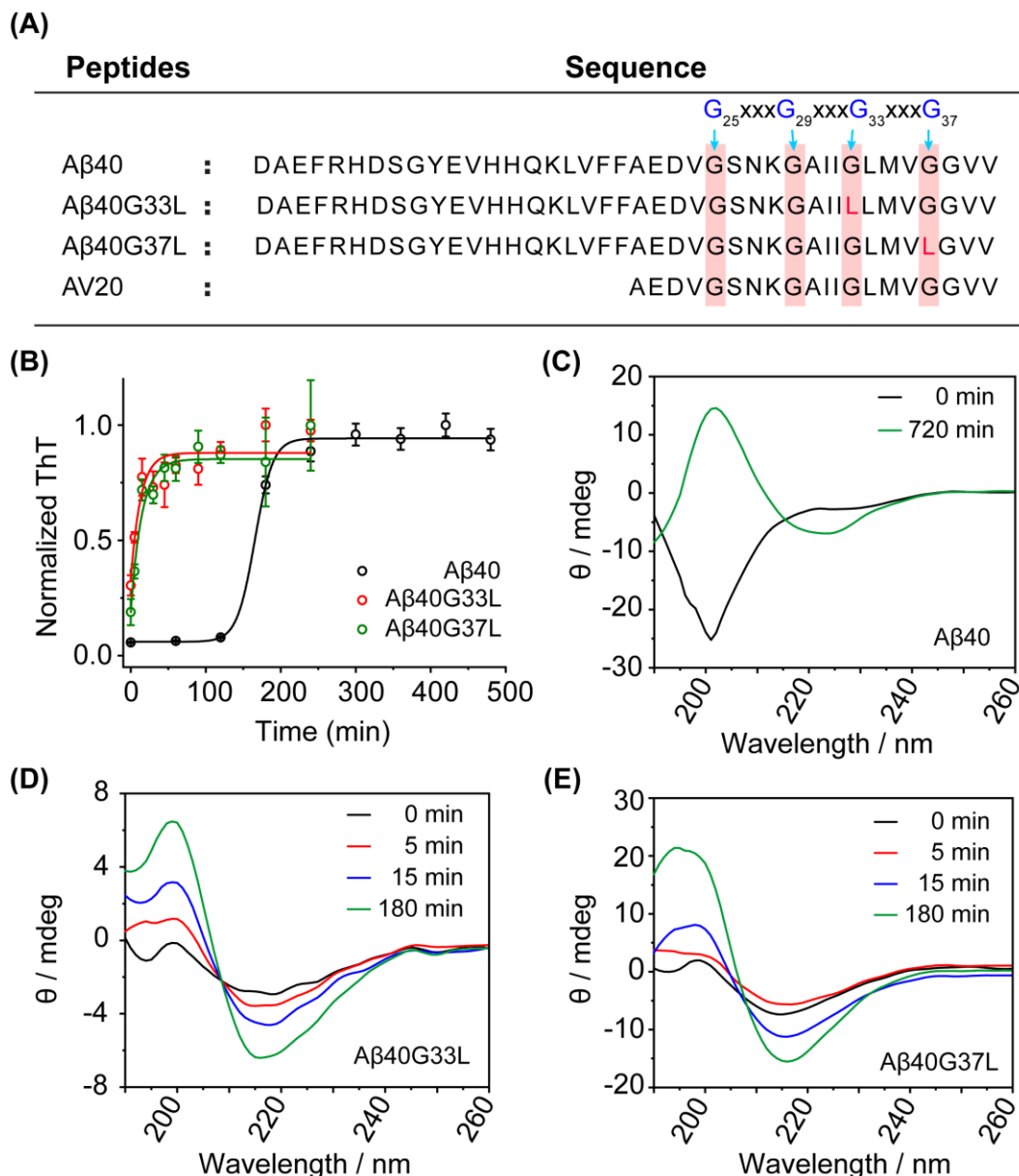
Figure 3.1. Effect of mutation on aggregation kinetics of Aβ40. (A) Amino acid sequences of peptides under investigation. (B) Aggregation kinetics of Aβ40, Aβ40G33L, and Aβ40G37L investigated by ThT-based fluorescence assay at 37°C. All experiments were repeated three times, and the data were averaged (±SD). Far-UV CD spectra of (C) Aβ40, (D) Aβ40G33L, and (E) Aβ40G37L at different time-point showing the time-dependent structural transition from monomer to fibril. The samples contain ~80 μM peptide in 20 mM sodium phosphate and 50 mM NaF, pH 7.4.

the sigmoidal growth model, consistent with previous findings reported by various research groups including our own.[9, 24] Aβ40 displayed a relatively slower aggregation kinetics, reaching saturation at approximately 360 min of incubation, with an observable lag time (t_{lag}) of 141 ± 3

min and half-life (t_{half}) of 165 ± 2.5 min. In contrast, the introduction of Gly→Leu substitutions at positions 33 (Aβ40G33L) and 37 (Aβ40G37L) resulted in a remarkable increase in the fibrillation rate. The mutants exhibited rapid aggregation, achieving saturation within only 120 min of incubation without any observable aggregation t_{lag}, indicating their propensity for rapid nucleation and aggregation. The observed differences in aggregation behavior between the wild-type (WT) Aβ40 and the mutants suggest that these Gly residues play a crucial role in influencing the structural transitions, leading to faster fibrillation.

To gain deeper insights into these structural transitions, we performed time-dependent Circular Dichroism (CD) spectroscopy and monitored the characteristic changes in secondary conformation during the fibrillation (Figure 3.1C-E). Initially, Aβ40 displayed a random coil conformation (negative minima around 200 nm), which gradually transitioned into a β-sheet conformation as the aggregation reached saturation (at 720 min of incubation). In contrast, the mutant peptides displayed a remarkably swift structural transition, with an apparent absence of a well-defined random coil structure in their early-stage CD spectra, indicative of their accelerated transition to the β-sheet conformation. In fact, within just 180 min of incubation, the mutants
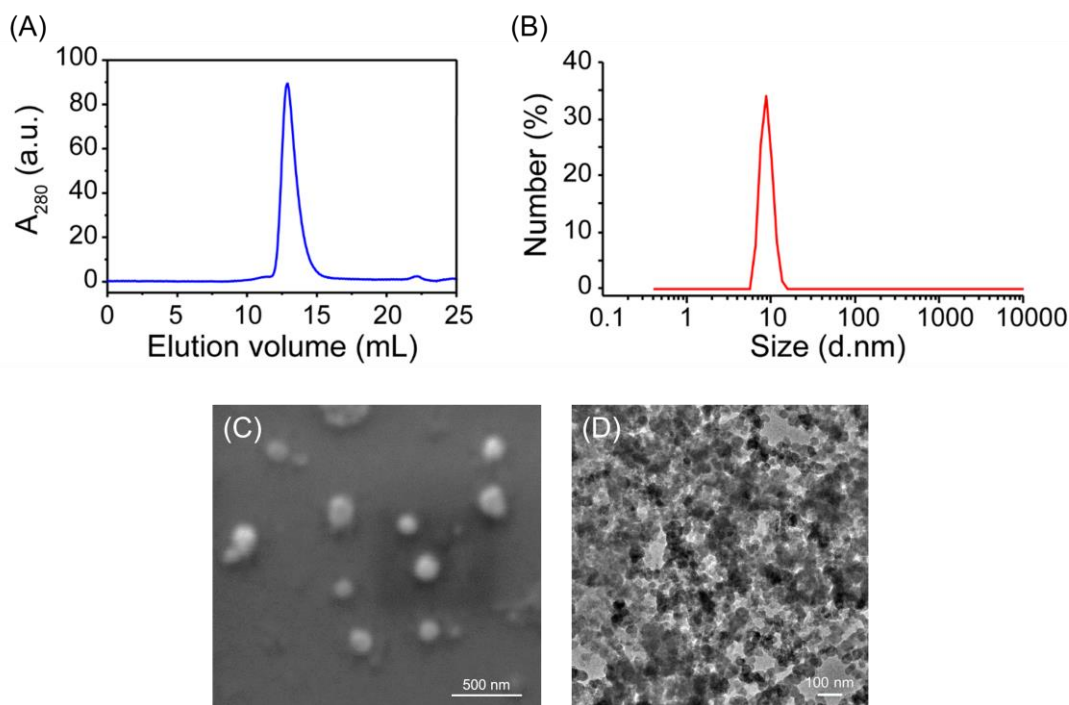

Figure 3.2. Characterization of NDs. (A) SEC profile of free NDs showing a peak at elution volume of 13.6 mL. (B) DLS data of free NDs showing a hydrodynamic diameter of ~8 nm. (C) SEM image of free NDs. (D) HR-TEM image of free NDs.

exhibited complete β-sheet conformation (negative minima around 218 nm), strongly corroborating the ThT data. Hence, both ThT kinetic assay and CD spectroscopy consistently demonstrate that the presence of Gly residues at positions 33 and 37 significantly impacts Aβ40 aggregation kinetics and its structural interconversion.

3.3.2. GxxxG-mediated membrane interaction modulates Aβ aggregation kinetics

The formation of NDs were achieved using a lipid composition of 3:1 DMPC/DMPG and MSP protein and characterized by using various biophysical and microscopy techniques and found a hydrodynamic diameter of ~8 nm (Figure 3.2). To gain insights into the effects of lipid-nanodiscs on Aβ40 aggregation kinetics and to elucidate the distinct roles played by G33/G37 residues, we employed the ThT fluorescence assay at different lipid-peptide ratios (L/P). This enabled us to investigate both the influence of the NDs and the significance of $G^{33}xxxG^{37}$ motif in modulating Aβ40 fibrillation in lipid bilayer. Our findings revealed that both the lipid concentration and the Gly residues play crucial roles in regulating Aβ40 fibrillation. As depicted in Figure 3.3A, the effects of NDs on Aβ aggregation kinetics were found to be complex, yet several discernible trends emerged. At L/P=1, nanodiscs promoted aggregation with a significant decrease in the t_{lag} (Figure 3.3B). As the concentration of lipids increased (L/P=10), nanodiscs further enhanced the Aβ40 aggregation. Intriguingly, with a further increase in lipid concentration (L/P=20), a substantial delay in Aβ40 aggregation was observed (Figure 3.3A). Subsequent increments in lipid concentration (L/P=50 and 100) resulted in a drastic increase in the lag time (Figure 3.3A, Appendix III, Figure S3.1). No increase in the ThT intensity was observed for NDs alone. We further executed the global fitting of the kinetic curves using the online platform Amylofit[25] and obtained the rate constants associated with individual microscopic steps (Figure 3.3C). We observed that the multi-step secondary nucleation dominated model best fitted the kinetic curves, whereas models excluding secondary nucleation did not properly fit the experimental data. From the model fitting we obtained the rate constants k_+ (elongation rate constant), k_n (primary rate constant), k_2 (secondary nucleation rate constant) as well as the Michaelis constant K_M (Figure 3.3C). Interestingly, at lower lipid concentration, both the combined rate constant for primary nucleation (k_+k_n) and secondary nucleation (k_+k_2) significantly increased whereas at higher lipid concentration both significantly decreased, which reflected in the aggregation t_{lag} and t_{half} (Figure 3.3B-C). We also found that k_+k_2 was much larger than k_+k_n, such that $k_2/k_n > 10^{12}$ and consistently
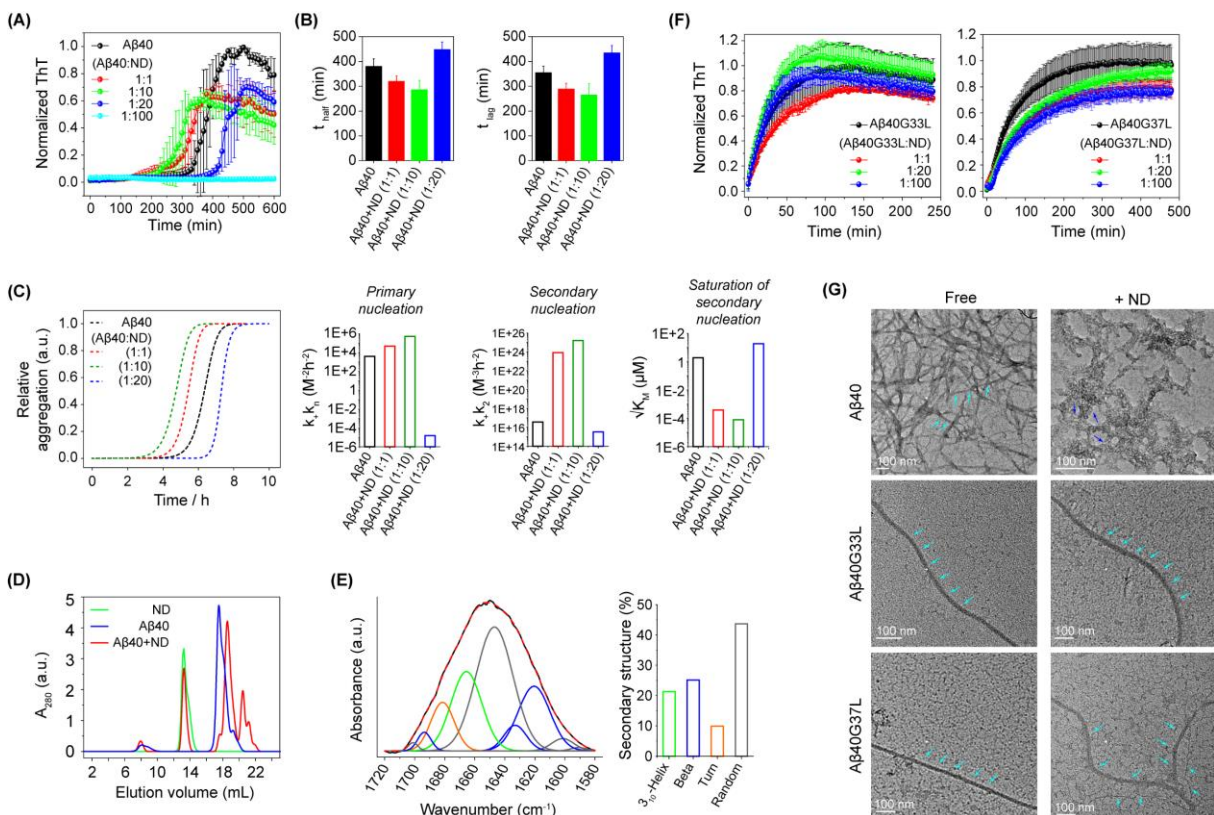
Figure 3.3. GxxxG motif modulates membrane-associated amyloid aggregation. Aggregation kinetics of (A) Aβ40 (20 μM) in absence and presence of different lipid ratios investigated by ThT based fluorescence assay at 37 °C under shaking (300 rpm) conditions. (B) Aggregation half-life (t_{half}) and lag time (t_{lag}) calculated from the curve fit. (C) Global fitting of the aggregation kinetics data of Aβ40 in absence and presence of different lipid ratios using multi-step secondary nucleation model. From the global fitting of the data, parameters like the combined rate constants (k_+k_n and k_+k_2) and monomer concentration of half-saturation of secondary nucleation ($\sqrt{K_M}$) were obtained and plotted in a bar diagram. All experiments were repeated three times, and the data were averaged (±SD). (D) SEC profile of Aβ40 oligomers in absence and presence of ND (L/P=20), indicating difference in the oligomer size. (E) Deconvolution of FTIR amide I band of Aβ40 oligomers obtained by co-incubating Aβ40 with ND (L/P=20) for 48 hours at 25 °C under non-shaking condition showing predominantly random coil conformation. (F) Aggregation kinetics of Aβ40G33L (20 μM), and Aβ40G37L (20 μM) in absence and presence of different lipid ratios investigated by ThT assay at 37 °C under shaking (300 rpm) conditions, showing no specific effect of ND on the aggregation kinetics. All experiments were repeated three times, and the data were averaged (±SD). (G) TEM images of Aβ40, Aβ40G33L, and Aβ40G37L in absence and in presence of ND (L/P=20), displaying the significance of G33 and G37 residues in membrane interaction and subsequent amyloid aggregation.

increased with increase in the lipid concentration, suggesting that most of the new aggregates are

formed through surface-catalyzed secondary nucleation rather than through primary nucleation.[26]

Size exclusion chromatography (SEC) revealed a distinct difference in the oligomer size between free Aβ40 and Aβ40 in presence of NDs (Figure 3.3D). These nanodiscs-mediated Aβ40 oligomers were further characterized by dynamic light scattering (DLS), which indicated a hydrodynamic diameter of 30 ± 7 nm (Appendix III, Figure S3.2A). This suggests presence of low molecular weight oligomeric species, which was then visualized using confocal microscopy (Figure S3.2B). As depicted in Figure 3.3E, when these oligomers were subjected to FTIR analysis, we observed predominantly random coil conformation. However, certain degree of 3_{10}-helix, β-sheet, and turn conformations were also observed from the deconvolution of the amide I band.

The mutant peptides, on the other hand, did not exhibit the same responses; no distinct impact of nanodiscs on the aggregation kinetics of mutant peptides was observed (Figure 3.3F). Even at higher lipid concentrations (L/P=100), no increase in lag time was noted. These findings highlight the crucial role of specific Gly residues (G33 and G37) within the GxxxG motifs in modulating Aβ40 fibrillation in the presence of lipid-nanodiscs, and reveal an intricate interplay between GxxxG-mediated membrane interactions and Aβ40 aggregation kinetics.

In order to visualize the differences in the aggregate morphology, we performed TEM imaging on Aβ40 and mutants in absence and presence of NDs (Figure 3.3G, Appendix III, Figure S3.3-8). In absence of NDs, Aβ40 exhibited a dense network of amyloid fibrils, whereas both Aβ40G33L and Aβ40G37L showed long isolated fibrils. Interestingly, in presence of NDs, Aβ40 did not undergo complete fibril formation, instead it remained as mostly in disordered oligomer and prefibrillar state. However, both the mutants (Aβ40G33L and Aβ40G37L) did not show any significant changes in the fibril morphology in the presence of NDs. Taken together, TEM imaging further confirms the significant role played by G33 and G37 residues in membrane interaction and regulating subsequent fibril formation.

3.3.3. Residue specific interaction between Aβ40 and nanodiscs by solution NMR

To obtain an atomic-level insights into the binding mechanism of Aβ40 with NDs as well as on the formation of these disordered oligomers, we used a combination of 1D, 2D, and 3D NMR experiments in solution-state. 1D ^{1}H NMR experiments revealed that upon titration with the NDs, the amide proton intensity decreased around 10% at L/P=20 concentration (Appendix III, Figure S3.9). This was followed by a 35% decrease in the signal intensity in a time dependent manner (44
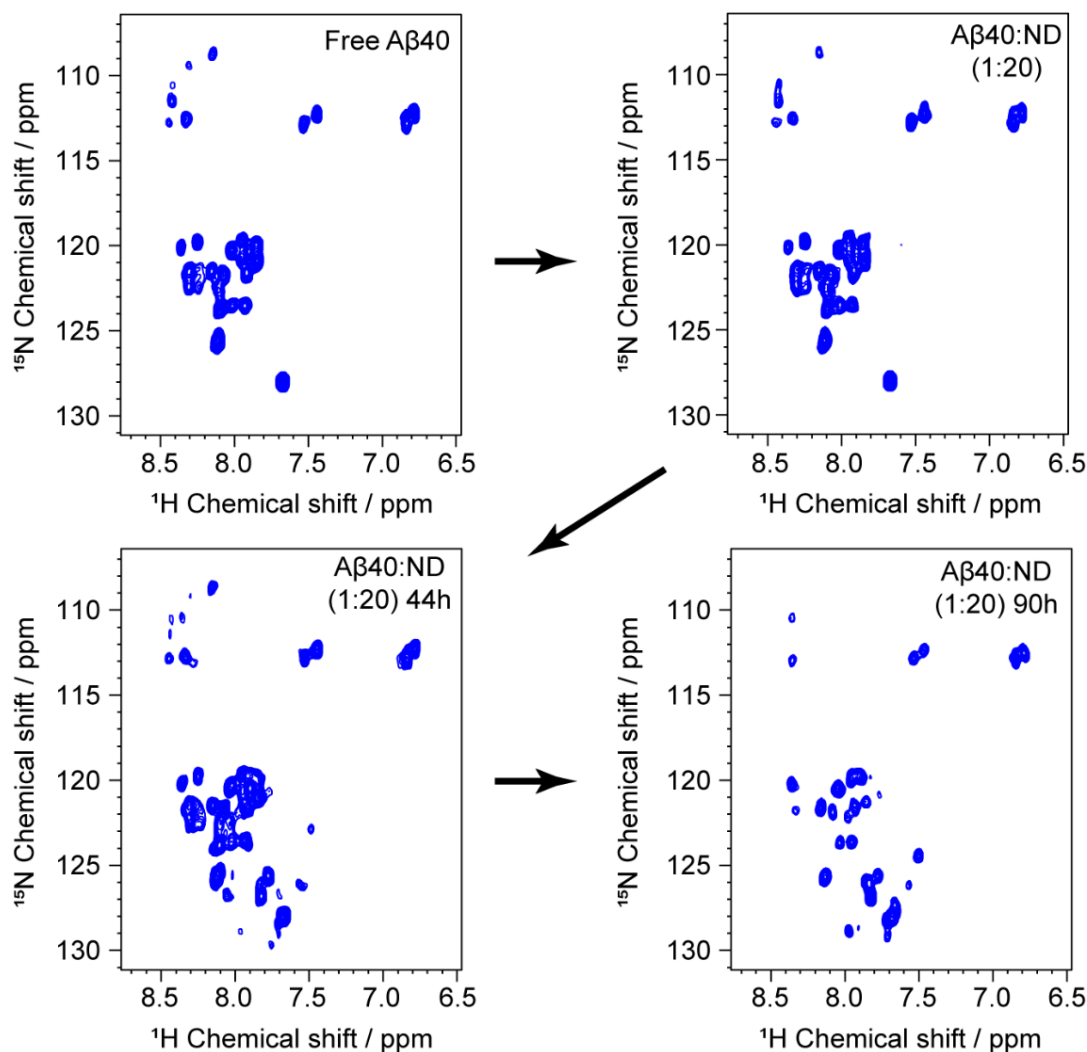
Figure 3.4. Representative real-time ^{1}H-^{15}N HSQC spectra of Aβ40 (80 μM) aggregation in presence of nanodiscs (L/P=20) at room temperature. HSQC spectra were acquired sequentially at 700 MHz over a period of 100 h at 25 ºC in 50 mM NaCl, 20 mM phosphate buffer, pH 7.4.

h). Remarkably, significant chemical shift perturbation (CSP) was observed after this time point, while the overall signal intensity remained almost unchanged.

2D ^{1}H-^{15}N Heteronuclear Single Quantum Coherence (HSQC) NMR further provided crucial information on the binding mechanism of Aβ40 with NDs and its temporal conformational states. HSQC spectra of Aβ40 at 25 °C were assigned based on a previous study.[27] HSQC spectra reveled that upon interaction with NDs (L/P=20), Aβ40 initially showed a slight decrease in the peak intensity without any notable CSPs (Figure 3.4, Appendix III, Figure S3.10). With time, however, significant decay (25%-35%) in the NMR peak intensity was observed for mainly
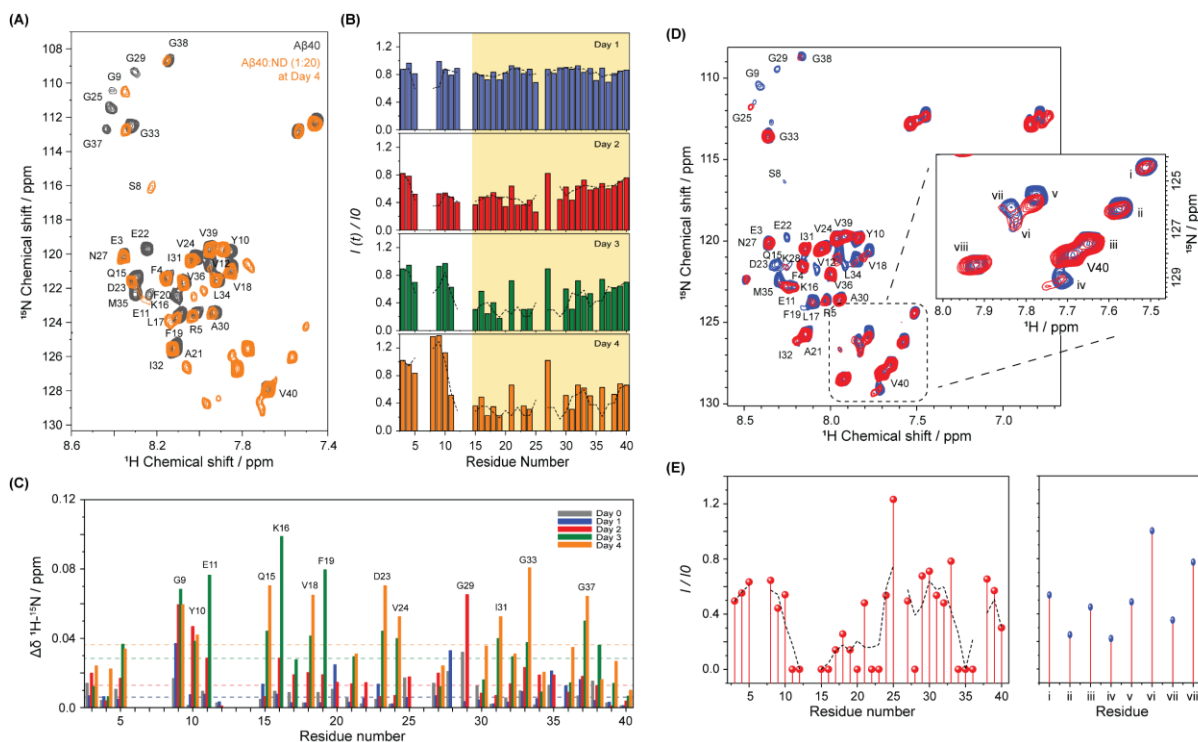
Figure 3.5. Interaction between Aβ40 and nanodiscs by solution NMR. (A) Overlay of 2D ^{1}H-^{15}N HSQC spectra of a freshly prepared Aβ40 (80 µM) sample and with nanodiscs (L/P=20) after formation of oligomers at 25 °C. (B) Time-dependent changes in the peak intensities along the peptide backbone measured from 2D ^{1}H-^{15}N HSQC spectra of a freshly prepared Aβ40 (80 µM) sample with nanodiscs (L/P=20) at 25 °C. Points represent the signal intensity of the peak maxima (*I(t)*) relative to the signal intensity in the absence of nanodiscs (*I$_0$*). Black dashed line represents the running average. (C) Chemical shift perturbations of Aβ40 over time following the addition of nanodiscs (L/P=20). The chemical shift perturbation was taken as the difference between the time point before and after nanodiscs addition. Dashed horizontal lines are the average chemical shift perturbations. The symbols (*) denote residues whose resonances did not display discernible resonances. (D) Quantification of solvent accessibility of nanodiscs-bound Aβ40. 2D ^{1}H-^{15}N HSQC spectra of Aβ40 in the presence of nanodiscs (blue), and upon titration with the paramagnetic quencher, MnCl$_2$ (red). (E) Relative signal intensities of Aβ40 residues were measured for titration with MnCl$_2$ (0.5 mM). The dashed line in the plots represents the running-average.

residues encompassing the central hydrophobic (Q15-F20) and C-terminal regions (Figure 3.5A-B). Following 44 h of incubation, the overall signal intensity remained constant; however, significant CSPs were observed from this point suggesting occurrence of oligomers with alternative conformations (Figure 3.4, Figure 3.5A, C). These oligomeric conformers surprisingly remained stable for a long period of time (120 h) before complete broadening of the peak intensity.

In contrast to Aβ40 alone, new peaks were detected in the vicinity of V40 chemical shift in 2D ^{1}H-^{15}N HSQC spectrum, suggesting generation of new oligomeric species at the surface of NDs. This experiment was repeated for more than three times and with different batch of peptides. Although not identical, significantly close resemblance was observed, suggesting that these oligomers are structurally similar in nature (Appendix III, Figure S3.11). However, no such new peaks were observed in absence of NDs.

Next, paramagnetic relaxation enhancement (PRE) NMR was conducted on these oligomers to identify the residues involved in membrane interaction. Mn^{2+} ions can selectively quench the NMR signals of solvent-exposed residues by enhancing their respective T_2 relaxation rates, while residues embedded within the membrane bilayers are shielded from Mn^{2+} quenching. PRE experiment in presence of 0.5 mM $MnCl_2$ revealed that the N-terminal as well as the C-terminal residues are partially embedded in the lipid bilayer (Figure 3.5D). The quenched central hydrophobic residues, however, indicate their involvement in dynamic interactions with the free peptides. Additionally, the newly appeared peaks were found to partially protected from solvent accessibility, suggesting that theses alternative conformers are in well associated with lipid bilayer.

We also performed NMR spectroscopy at high lipid concentration (L/P=50). The appearance of new peaks in the NMR spectra were well corroborated with ThT kinetics, revealing further delay in the aggregation process due to the presence of NDs at higher ratio (Appendix III, Figure S3.12-13). Moreover, similar new peaks were detected in the HSQC spectra at the vicinity of V40, at a later time point. Collectively, this further suggests that the new peaks could be ND catalysed oligomer formation.

3.3.4. AV20-membrane interaction resembles that of Aβ40

In order to gain a closer look into the role of the GxxxG repeated motif present at the C-terminus of Aβ40, we further investigated the interaction between AV20 (the C-terminal 20 residue peptide fragment of Aβ40) and NDs. AV20 was previously found to be significantly toxic, in which the role of the GxxxG motifs were extensively studied. Here, we observed the role of membrane interaction with AV20 in order to further explore the significance of the GxxxG motif in oligomer formation. Interestingly, the peptide was also found to be interacting with NDs in a similar way. ThT fibrillation assay indicated that the peptide in presence of NDs, rapidly underwent oligomer formation, which were comparatively stable as well (Figure 3.6A).
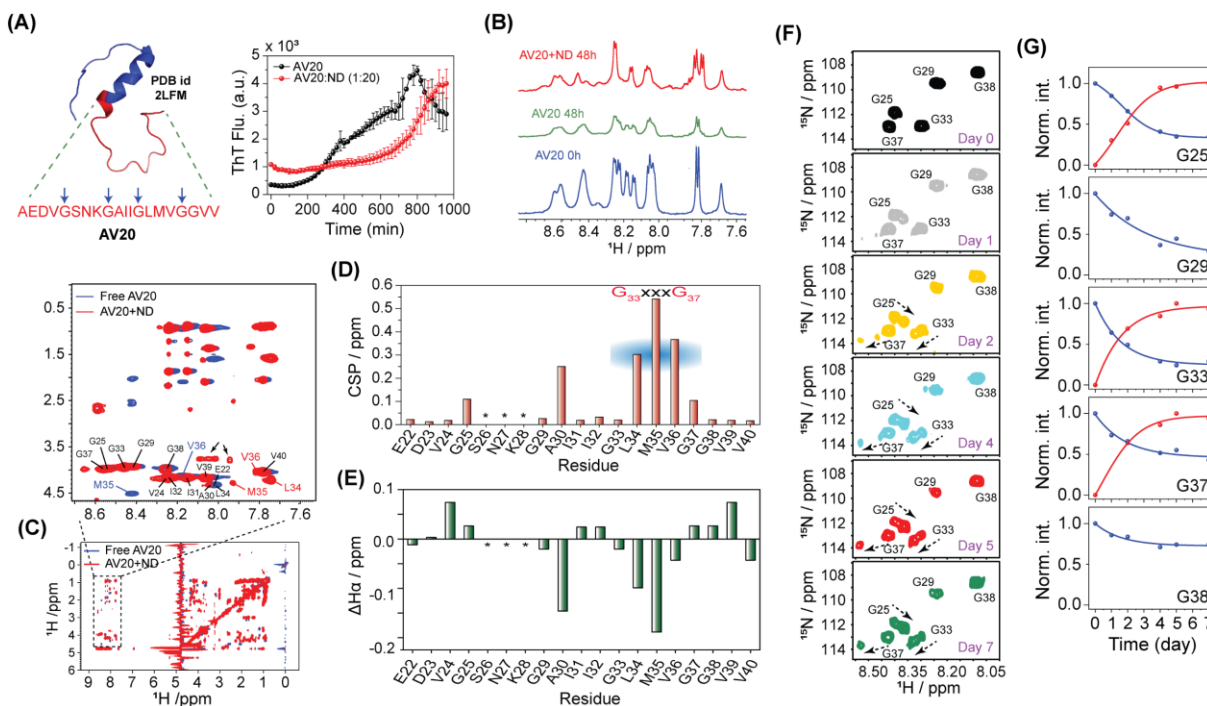
Figure 3.6. (A) Aggregation kinetics of the C-terminal 20 residue Aβ40 fragment, AV20 (50 µM) in absence and presence of nanodiscs (L/P=20) by ThT fluorescence assay. All experiments were repeated three times at 37 °C under shaking (300 rpm) conditions, and the data were averaged (±SD). (B) 1D ^{1}H NMR spectra of free AV20 at 0 hour, at 48 hours and AV20 in presence of NDs at 48 hours of incubation at 25 °C. While AV20 alone underwent line broadening, AV20 in presence of NDs showed both line broadening and significant CSPs (C) 2D TOCSY NMR of AV20 in absence (blue) and in presence of NDs (red), highlighting residue specific interactions. (D) Chemical shift perturbations for Hα resonances of each residue of AV20 in presence and absence of NDs. (E) The chemical shift deviation for Hα resonances of each residue of AV20 in presence of NDs from the standard random coil values. (F) Time-dependent ^{1}H-^{15}N HSQC spectra of a freshly prepared AV20 (Gly labelled with ^{15}N) sample with nanodiscs (L/P=20) at 10 °C, highlighting changes in the chemical shift and appearance of new peaks. (G) Temporal evolution of the monomers (red) and apparent exchange peaks (blue) of G25, G29, G33, G37, and G37.

Solution NMR studies were performed in order to understand the interaction between AV20 and NDs at an atomic resolution. While titrating with NDs, the peptide underwent line broadening upon interaction (Appendix III, Figure S3.14). However, no immediate chemical shift perturbation (CSP) was visible. Interestingly, unlike free AV20, which only underwent line broadening with time, upon binding with NDs, AV20 showed significant CSPs over time and remained stable for a comparatively longer duration (Figure 3.6B). This can be attributed to the conformation transition

and formation of stable oligomers. To get a closer look into the residue specific interaction between AV20 and nanodiscs, 2D TOCSY NMR experiments were performed on AV20 either in the presence and/or in the absence of NDs (Figure 3.6C). The spectra were then assigned and analysed, from which we calculated the CSPs of individual amino acid residues (Figure 3.6D). Interestingly, the residues spanning $G^{33}LMVG^{37}$ was found to be highly perturbed, suggesting significant involvement of this segment in membrane interactions. The chemical shift index was further calculated by correcting the Hα from random coil, to get an idea about the conformation (Figure 3.6E). Apparently, the CSI plot indicated mostly random coil conformation, except for residues L34 and M35, which showed inclination towards helical conformation. Next, to get an exclusive insight into the Gly residues, we performed 2D HSQC for the ^{15}N labeled Gly residues of AV20 in the presence of NDs, at low temperature (10 °C) as a function of time. Figure 3.6F displays the time dependent movement of individual Gly residues. While G25 showed up-field shift, G33 and G37 move towards down-field shift, suggesting exchanged conformer. Interestingly, the intensity buildups curves for three new peaks associated with residues G25, G33, and G37 closely match the intensity decrease observed for the peaks corresponding to their unbound form, suggesting that these peaks are in slow exchange (Figure 3.6G). G29 and G38, on the other hand, exhibited only intensity drop.

3.3.5. GxxxG motif facilitates AV20 to adopt helical conformation

Previous studies have well established that Aβ40 adopts helical structure in presence of membrane mimicking SDS micelles.[28] Our experimental observation involving CD spectroscopy revealed that AV20 also underwent a transition from random coil to helical conformation upon titration with SDS micelles (Figure 3.7A). However, the mutants Aβ40G3L and Aβ40G37L did not adopt complete α-helical conformation upon interaction with SDS (Figure 3.7A), suggesting that these Gly residues are essential for the peptide to interact and to adopt helical conformation.

Solution-state NMR further provided an atomic resolution insight into the conformational alteration of AV20 in the presence of SDS. Significant CSPs were apparent in the presence of SDS as observed in the 1D NMR spectra (Appendix III, Figure S3.15). AV20 in aqueous solution was less dispersed and showed sharp signals in the amide proton region, whereas, in the presence of SDS micelles, the spectra were more scattered and, broadened, owing to the well-defined conformational change induced by the micellar environment. Thus, to gain atomic resolution
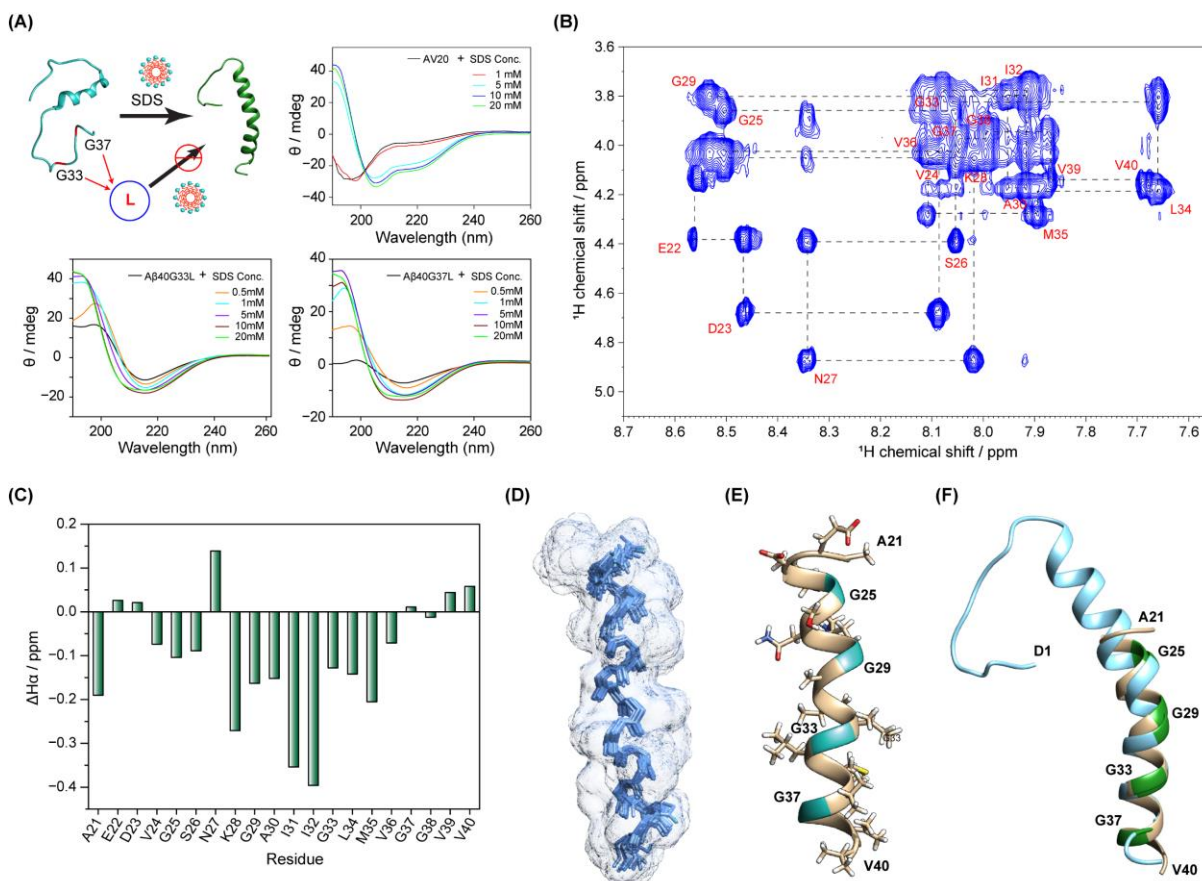
Figure 3.7. GxxxG motif facilitates to adopt helical conformation in AV20. (A) CD spectra of AV20, Aβ40G33L, and Aβ40G37L in presence of SDS micelles, highlighting the significance of G33 and G37 in adopting helical conformation. (B) Hα-HN region of the 150ms NOESY spectrum of AV20 in presence of SDS (pH 5.2, 298 K) measured in a 700 MHz NMR. The sequential assignments of all the residues are indicated in the NOESY walk. (C) The chemical shift deviation for Hα resonances of each residue of AV20 in SDS micelles from the standard random coil values. (D) The best 20 structures of AV20 in presence of SDS micelles, calculated from the NOE-derived distance constraints. (E) Three-dimensional solution structure of AV20 in SDS micelles. The side chain orientation of a representative NMR structure of AV20 bound to SDS is shown. The overall RMSD value is ~0.5 Å. The Gly residues are highlighted in sea green color, where G33 and G37 is present in the same face of the helix. The image was prepared using the Chimera software. (F) Structural comparison between AV20 (light brown) and Aβ40 (cyan) in presence of SDS micelles. The helical segment in the C-terminal shows structural similarity. Gly residues in both peptides are highlighted in green, indicating close resemblance, particularly the G33 residue. Residue numbering in AV20 is based on the sequence of Aβ40. The structure of Aβ40 is taken from "PDB id- 1BA4" for comparison.

understanding of the peptide's conformation, 2D ^{1}H-^{1}H NOESY spectra were acquired in the presence of SDS micellar environments, which were further assigned and used for the structural

elucidation of AV20. In contrast to aqueous solution, the NOESY spectra in SDS micelle contained a sufficient number of sequential and medium-range NOE cross peaks indicating the existence of a distinct structural fold. The fingerprint region in SDS micellar environments contained several characteristic, sequential and medium-range CαH/NH NOE contacts as illustrated in Figure 3.7B. In addition to the intense sequential CαH/ NH (i to i + 1) NOEs, medium range CαH/NH (i to i + 2) NOEs were observed throughout the sequence of AV20 namely between S26/K28, I32/L34, L34/V36, M35/G37, V36/G38 in SDS. Moreover, CαH/NH (i to i + 3) medium range NOEs for N27/A30, A30/G33, I31/L34, L34/G37, M35/G38, V36/V39 and G37/V40 were observed in SDS micelles (Appendix III, Figure S3.16). Also, M35/V39 and V36/V40 showed CαH/NH (i to i + 4) in SDS micelle.

The chemical shift deviation of the CαH resonances from the standard random coil value also provides the signature of the secondary structure of the peptide. A helical segment is characterized by negative chemical shift deviation of Hα for four consecutive residues while the reverse trend is a signature of the beta sheet structure. Deviations of more than -0.1 ppm from random coil are usually associated with helical structures. Figure 3.7C shows negative ΔHα values for a group of residues, K28 to V36, indicating that they may be in a helical conformation. Overall, this pattern of chemical shift deviation serves as a signature of the predominance of alpha helical conformation in SDS micelle.

Next, the three-dimensional solution conformations of AV20 in presence of SDS micelles was calculated based on the NOE-derived distance constraints using CYANA software package (Figure 3.7D-E). In SDS micelles, the ensemble of AV20 conformations were well-organized and converged with an average backbone atom and heavy atom root mean square deviation (RMSD) values of 0.52 ± 0.16 Å and 0.92 ± 0.16 Å, respectively. Next, we compared this structure with the previously[28] determined structure of Aβ40 in SDS and found a striking resemblance (Figure 3.7F). The same structural motif was observed in the residues encompassing G25-M35, with a kink involving residues G25-K28.

3.4. Discussion

Overall, our study provides unique insights into the role of the GxxxG motif in membrane-mediated oligomerization of Aβ40. While previous research has explored the interaction between nanodiscs and Aβ, the temporal evolution of distinct oligomeric species and the significance of
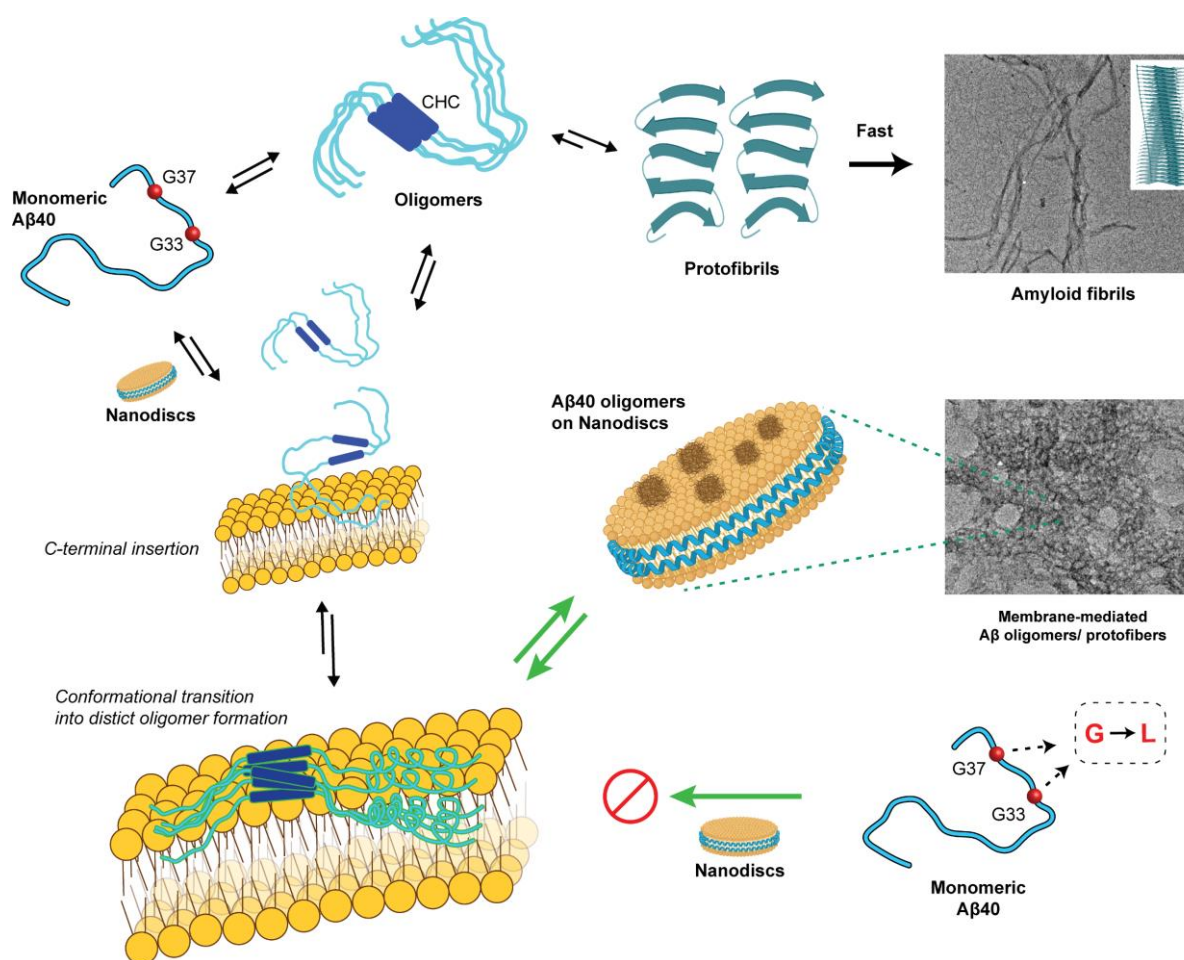
Figure 3.8. Schematic representation of membrane-mediated oligomerization of Aβ40. In aqueous solution monomeric Aβ40 self-assemble into oligomeric intermediates primarily via the central hydrophobic core (CHC in blue color). These oligomers are transient in nature and quickly convert into protofibrils and mature fibrils. In presence of NDs however, they form comparatively stable oligomers with distinct conformation. While a portion of Aβ40 self-assemble via the CHC, the presence of NDs leads the C-terminal consisting of the GxxxG motif to interact with the lipid bilayer. This facilitates a conformational transition, where the N-terminal then insert into the membrane, resulting in a membrane-bound distinct oligomer. Mutation in the G33 and G37, on the other hand, hampers this interaction and leads to a faster aggregation into long isolated fibrils.

G33/G37 have remained largely elusive. Our experimental findings offer a more detailed understanding of the molecular events surrounding this oligomerization process (Figure 3.8). In summary, our findings indicate that while at lower lipid concentrations, NDs accelerates the aggregation, with sufficient excess of lipids, NDs can significantly inhibit primary nucleation.

Collectively, however, NDs significantly promote secondary nucleation in a surface catalyzed manner. Interestingly, recent studies have suggested a dock-lock mechanism of fibril formation.[18, 29] The unstructured Aβ monomers transiently interact with the fibril surface primarily through the central hydrophobic core, followed by a slower conformational rearrangement. However, in case of ND-mediated oligomerization, the C-terminal region consisting of the GxxxG motif plays dominant role and are in slow exchange with the ND-bound conformers. Even the fragment peptide, AV20, displayed similar interaction dynamics with NDs.

Solution NMR revealed a complex interplay between Aβ40 and NDs. The C-terminal residues, particularly K28, G29, I31, G33, M35, and G37, displayed significant alterations in their temporal HSQC profile. Additionally, the C-terminus remained mostly solvent inaccessible, suggesting their profound involvement in membrane interaction and partial incorporation. The central hydrophobic region exhibited the highest intensity drop as well as chemical shift perturbations (CSPs) during oligomerization; however, PRE experiments showed that they are comparatively more solvent exposed. On the other hand, while the N-terminal residues spanning E3-S8 initially did not show significant intensity drop or CSPs, during oligomer formation, they were found to be surprisingly protected from solvent exposure, as found in the PRE experiments. Moreover, in presence of higher lipid concentration, similar interactive motif for Aβ40 (CHC) was found to show initial intensity drop, followed by appearance of similar new peaks at the vicinity of V40. This confirms the formation of distinct oligomer conformation that are specific to nanodiscs interaction.

Previously, it was observed that Aβ40 adopts a partially folded structure in aqueous solution,[27] while in the presence of SDS micelles,[28] it takes on a helical conformation. Our observation involving AV20 in the presence of SDS micelles also revealed striking similarities, suggesting the inherent ability of the C-terminal domain to adopt a helical conformation. Structural comparison of Aβ40 and AV20 in SDS micelles reveals two interesting features. Firstly, the formation of a helix between residues G25-V40 with a kink at G25-K28. Secondly, a similar pattern of Gly residues spaced four residues apart, occupying one face of the helix. This pattern has been previously predicted in ion-channel models.[30] It has also been reported that the GxxxG motif stabilizes ion-channel-like pores through Cα—H⋯O interaction.[6, 31] Mutations in G33/G37, which prevent the peptides from adopting a helical conformation in SDS micelles,

further confirm their direct involvement in this process. Meanwhile, the interaction between AV20 and NDs also revealed significant involvement of the $G^{33}LMVG^{37}$ motif in oligomerization. A detailed examination of the Gly residues during the temporal evolution AV20 into distinct oligomers revealed that G25, G33, and G37 are in slow exchange with their alternative conformers. Thus, the ability of the GxxxG motif to adopt diverse secondary conformations appears to be truly fascinating.

Since the oligomers formed directly in solution or *in vivo* may differ structurally and functionally from those mediated by NDs, this may not inherently translate to pathological relevance. Nonetheless, strategies like development of sequence or conformation specific antibodies or small molecules, which can stabilize distinct oligomeric intermediates, has been extremely valuable for therapeutic interventions. Moreover, this study will provide further insights into the underlying mechanism of membrane-mediated Aβ-oligomerization and pave the way for targeted therapy for AD and related disorders.

3.5. Conclusions

In conclusion, we have successfully demonstrated for the first time the role of G33/G37 in surface catalyzed oligomerization of Aβ40 in a near native membrane environment using MSP-based nanodiscs. The interactions between nanodiscs with both full-length Aβ40 and its C-terminal fragment peptide (AV20) highlights the crucial role played by the C-terminal residues particularly the GxxxG motifs. We illustrate how nanodiscs facilitates formation of comparatively stable oligomers which are conformationally distinct from native Aβ40 and other minor states of free Aβ40 oligomers.

3.6. Appendix III
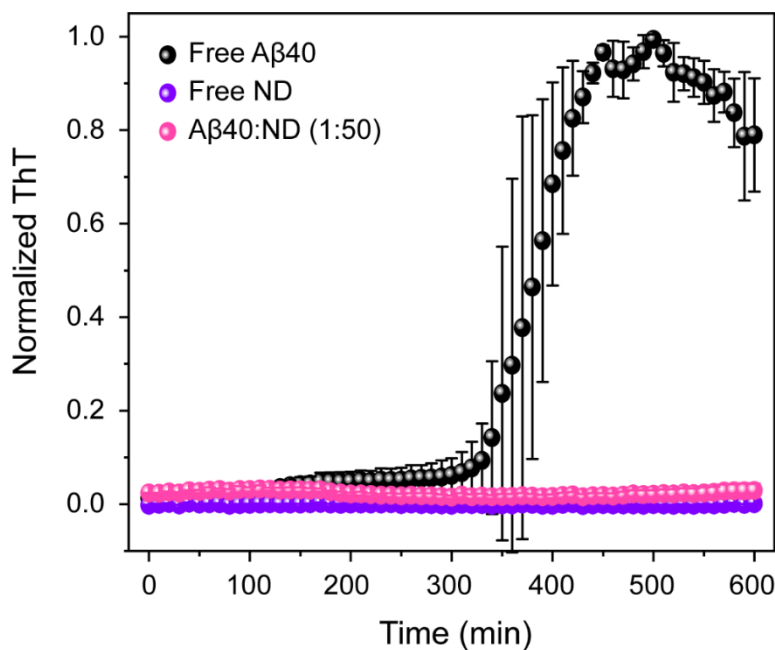
Figure S3.1. Aggregation kinetics of Aβ40 (20 μM) in the presence of NDs at 1:50 peptide-lipid ratios (L/P=50). A drastic increase in the lag time compared to free Aβ40 was observed at this lipid concentration. No increase in the ThT intensity was observed for nanodiscs (200 μM) alone. 20 μM ThT concentration was used for all experiments. Fluorescence measurements were taken in a 96 well plate under shaking (300 rpm) before each cycle (30s) at 37 °C. All experiments were repeated three times, and the data were averaged (±SD).
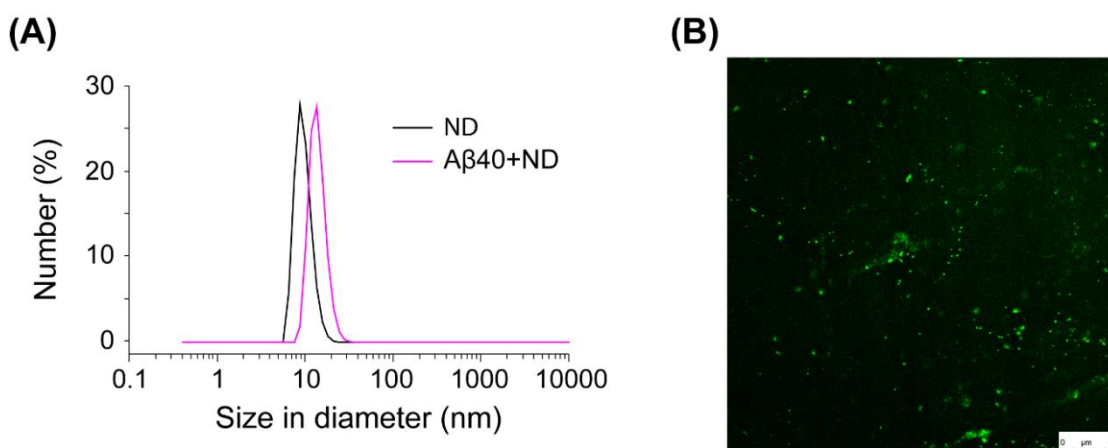
Figure S3.2. (A) Size distribution of nanodiscs-mediated Aβ40 oligomers from DLS measurements in 20 mM phosphate buffer, 50 mM NaCl, pH 7.4. (B) Confocal microscopy image of ThT-bound Aβ40 oligomer in presence of nanodiscs.
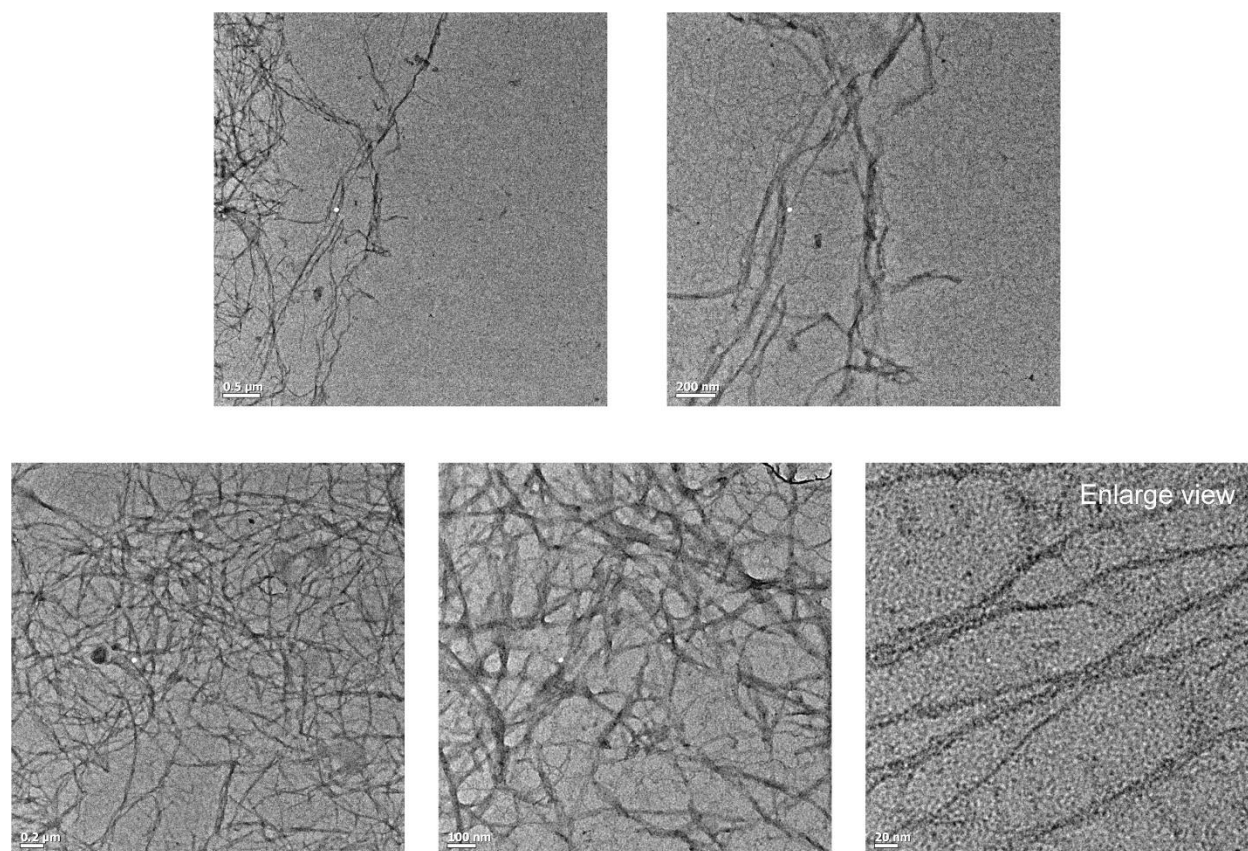
Figure S3.3. HR-TEM images of Aβ40 fibers at different magnifications showing dense network of amyloid fibers of different width.
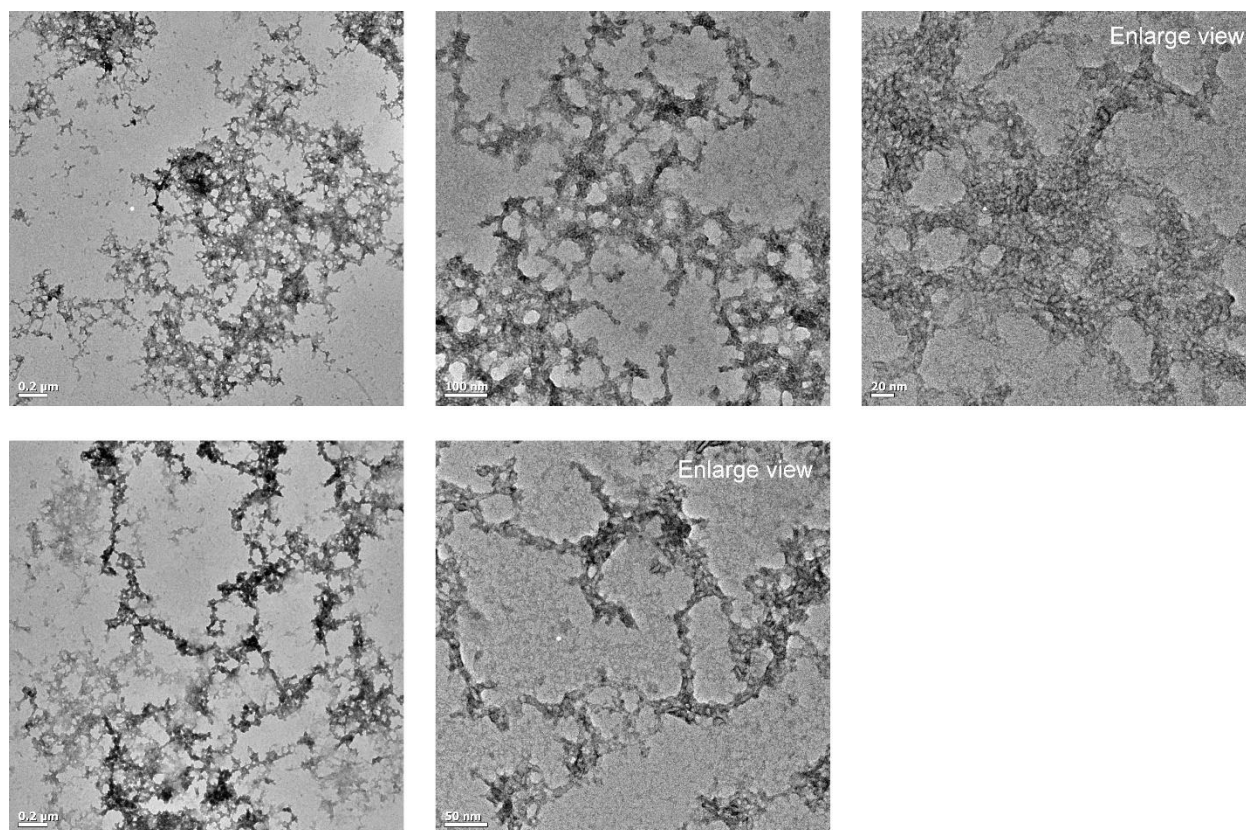
Figure S3.4. HR-TEM images of Aβ40 in presence of nanodiscs (L/P=20) different magnifications showing disordered aggregates. No dense network of amyloid fibers was detected.
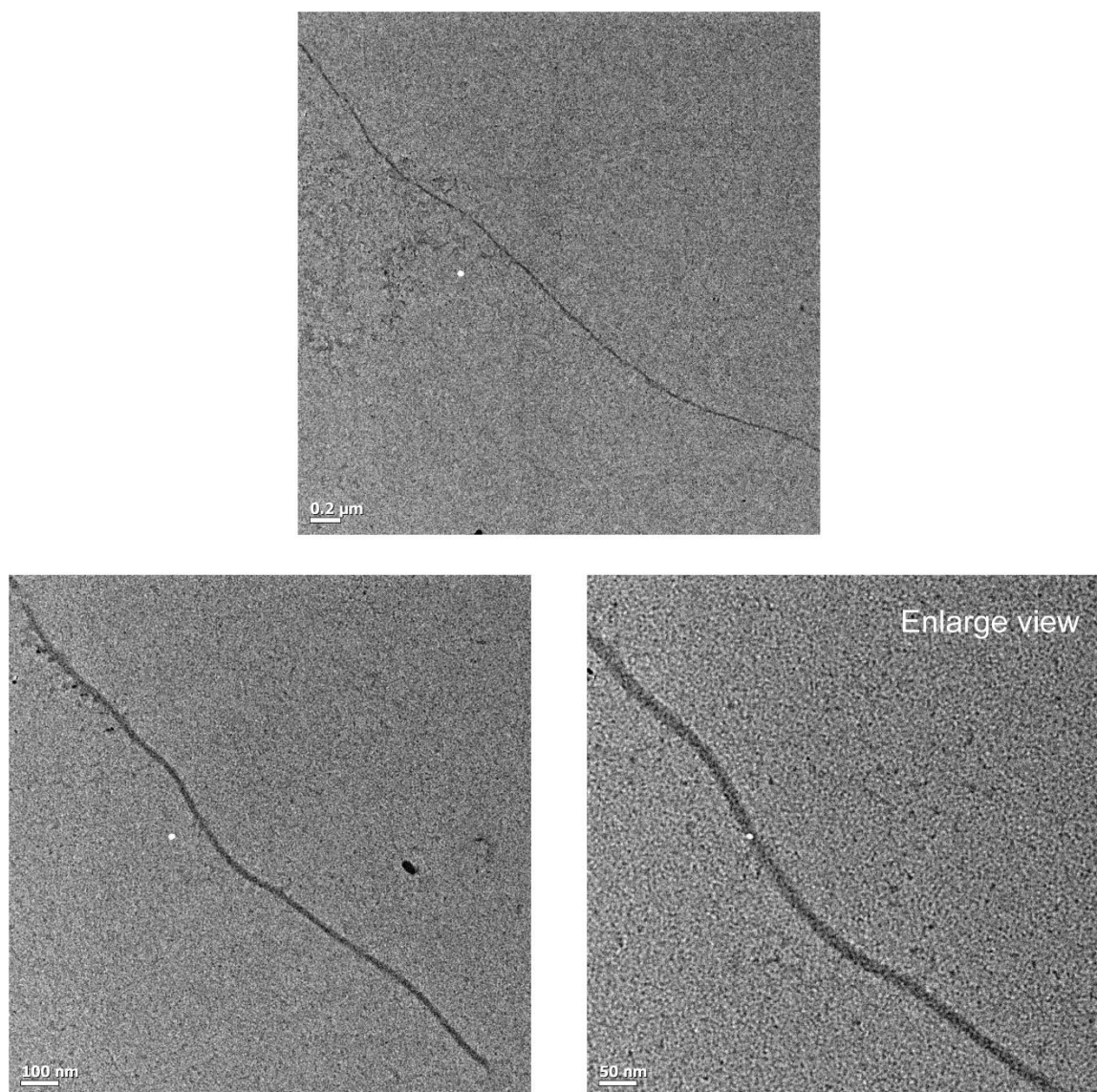
Figure S3.5. HR-TEM images of Aβ40G33L fibers at different magnifications showing long isolated fibers.
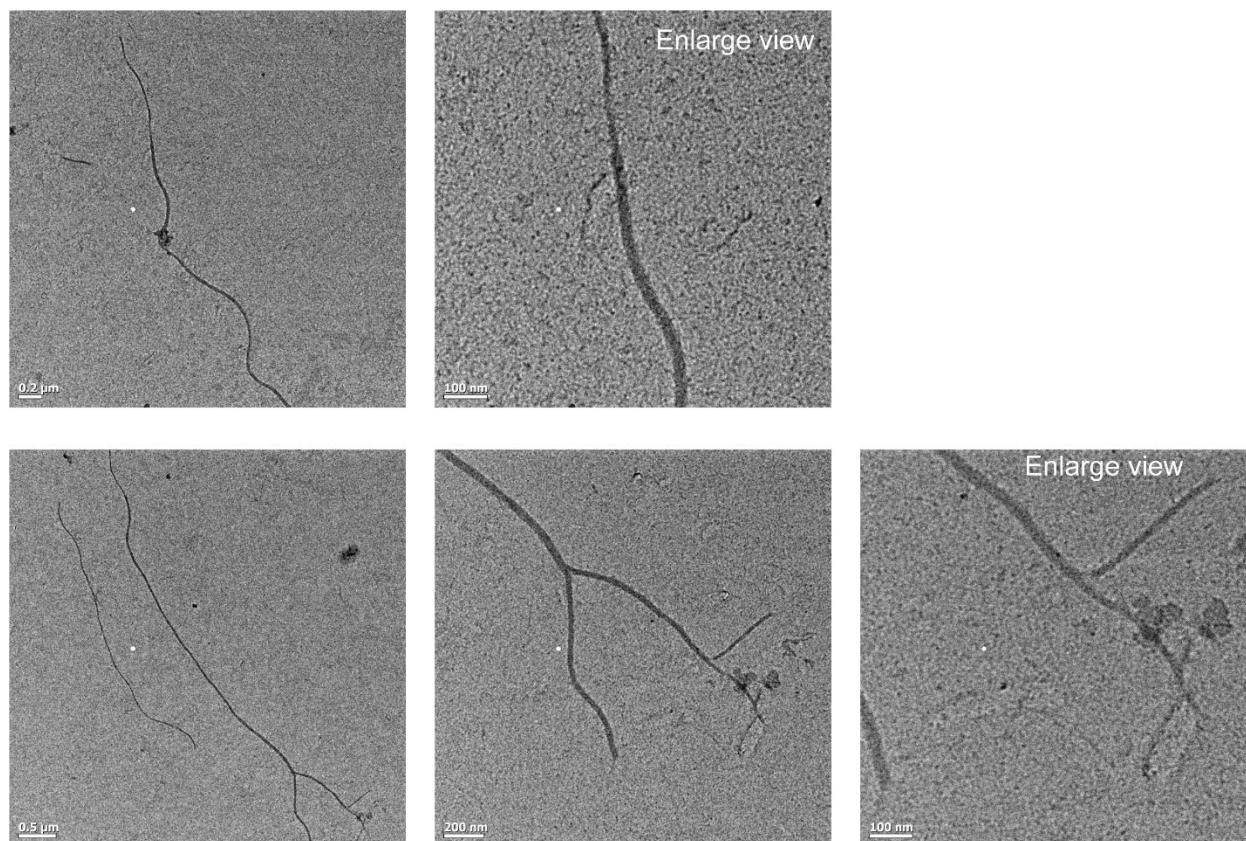
Figure S3.6. HR-TEM images of Aβ40G33L in presence of nanodiscs (L/P=20) at different magnifications showing long isolated fibers.
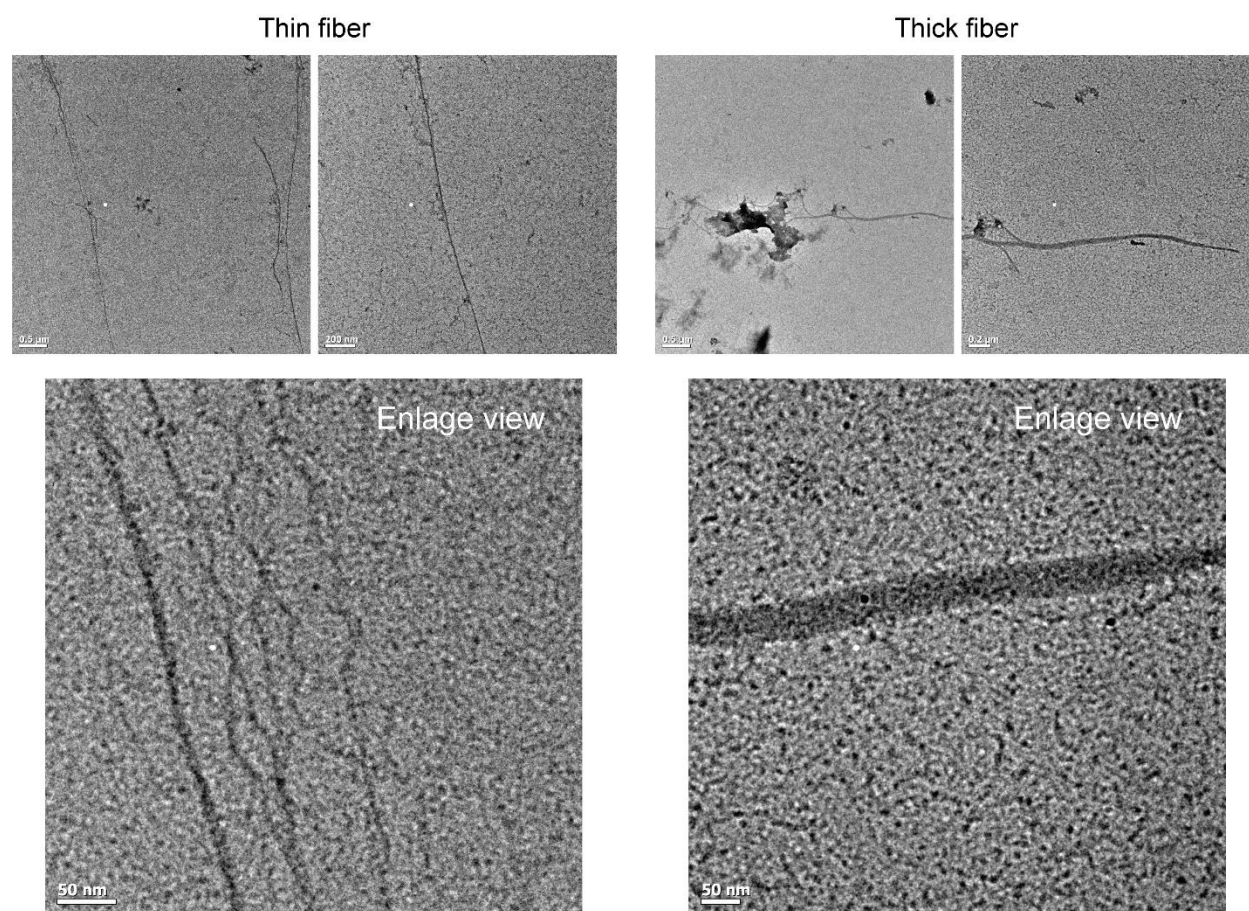
Figure S3.7. HR-TEM images of Aβ40G37L fibers at different magnifications showing long isolated fibers of different width. Both thin fibers with an average width of 12 ± 4 nm, and thick fibers with an average width of 43 ± 11 nm were detected.
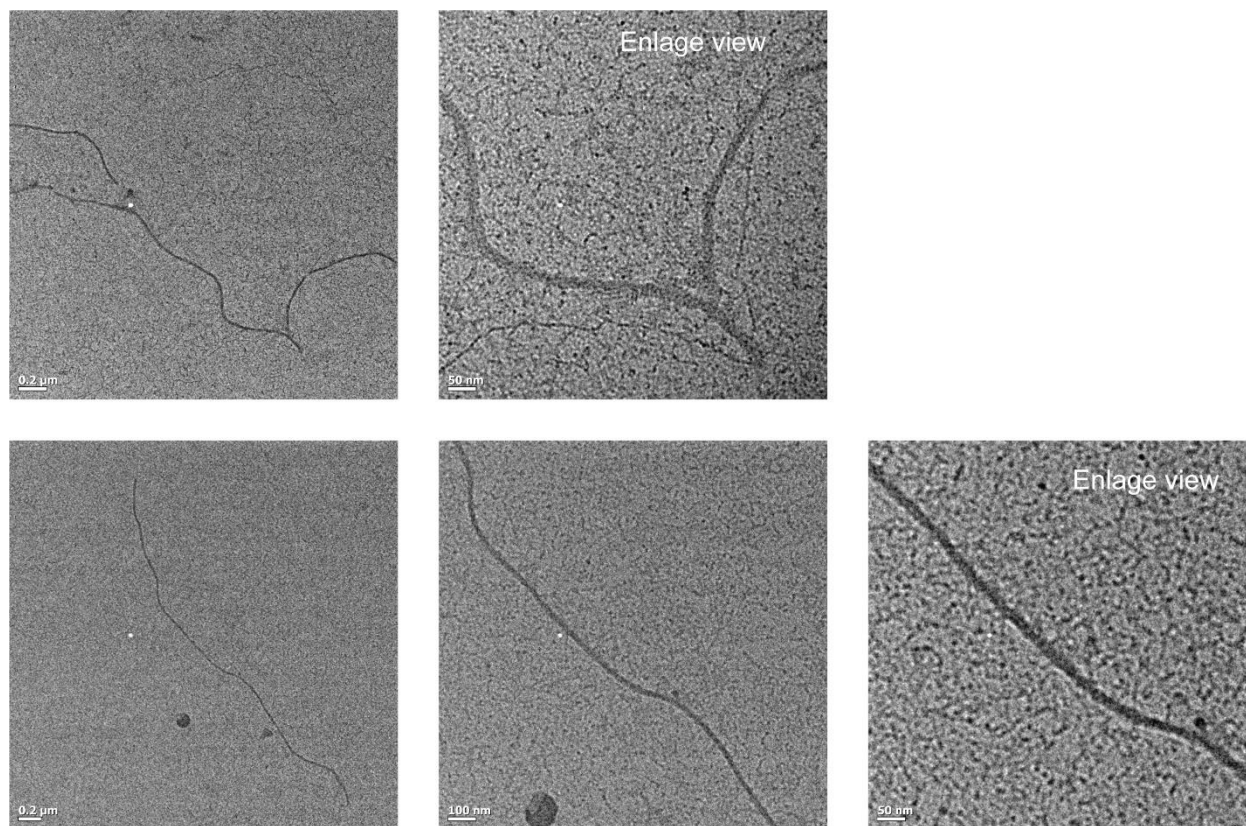
Figure S3.8. HR-TEM images of Aβ40G37L in presence of nanodiscs (L/P=20) at different magnifications showing long isolated fibers.

(A)

(B)
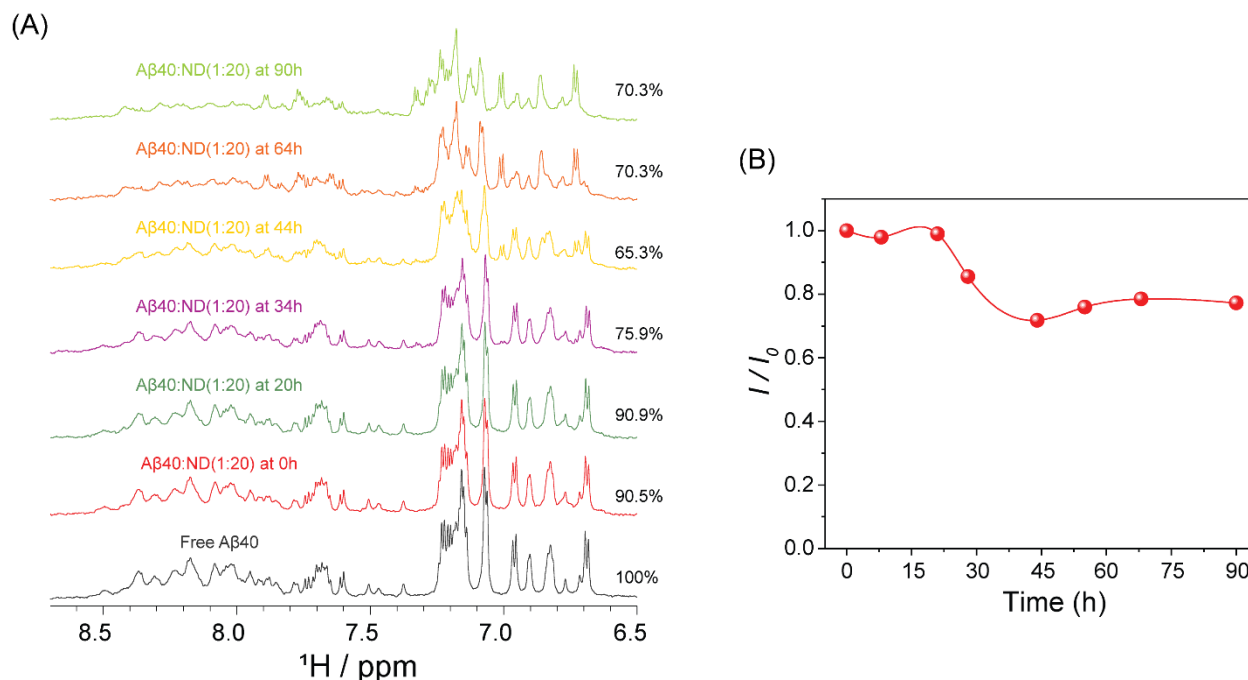
Figure S3.9. (a) 1D ^{1}H NMR spectra of Aβ40 in absence and presence of nanodiscs (L/P=20) at room temperature showing ~10% decrease in signal intensity in the amide proton. Following which, a time-dependent 1D NMR spectra showing an initial signal decay of 35% at 44 h, then significant chemical shift perturbations. (b) Decay of amide proton signal intensity of Aβ40 in presence of nanodiscs (L/P=20) as a function of time.
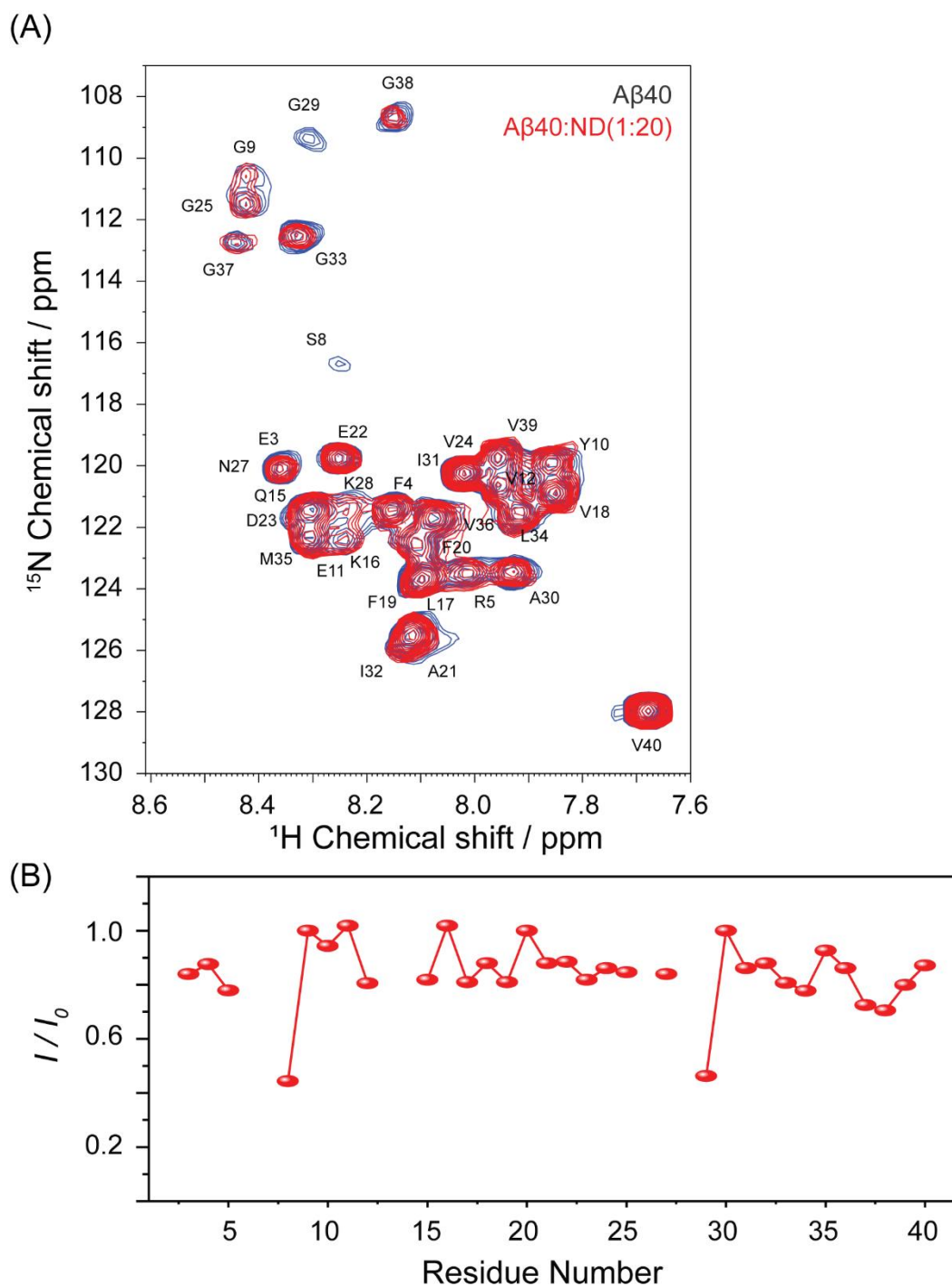
Figure S3.10. (a) 2D ^{1}H-^{15}N HSQC overlay spectra of Aβ40 in absence and presence of nanodiscs (L/P=20) at room temperature, suggesting slight intensity drop without any notable chemical shift perturbations. (b) Changes in the peak intensities along the peptide backbone measured from 2D ^{1}H-^{15}N HSQC spectra upon titration of a freshly prepared Aβ40 (80 µM) sample with nanodiscs (L/P=20) at 25 °C. Points represent the signal intensity of the peak maxima (*I*) relative to the signal intensity in the absence of nanodiscs (*I$_0$*).
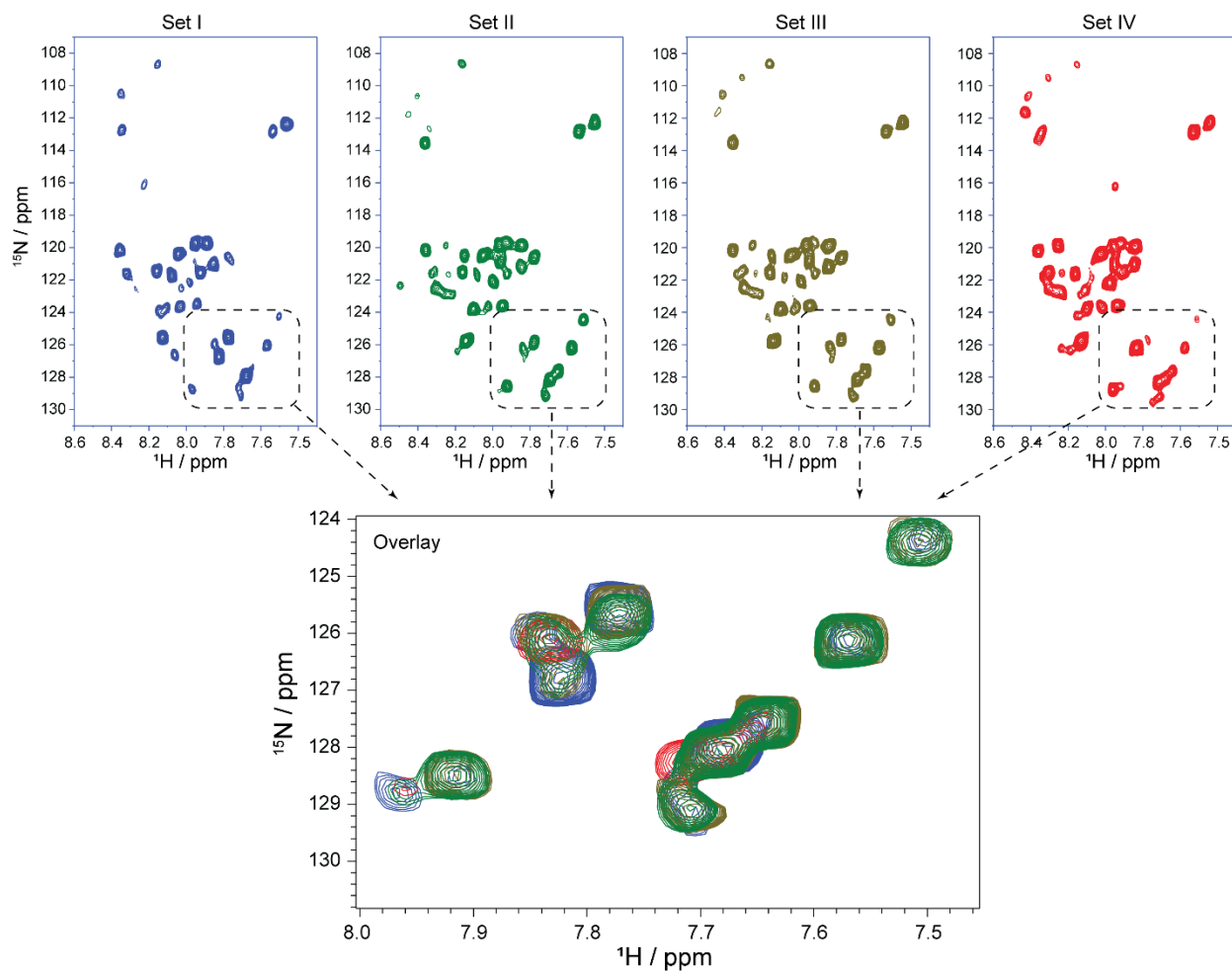
Figure S3.11. 2D ^{1}H-^{15}N HSQC spectra of Aβ40 (80 µM) aggregates in presence of nanodiscs (L/P=20) at room temperature, performed for multiple batches, showing generation of similar new peaks in the vicinity of V40.
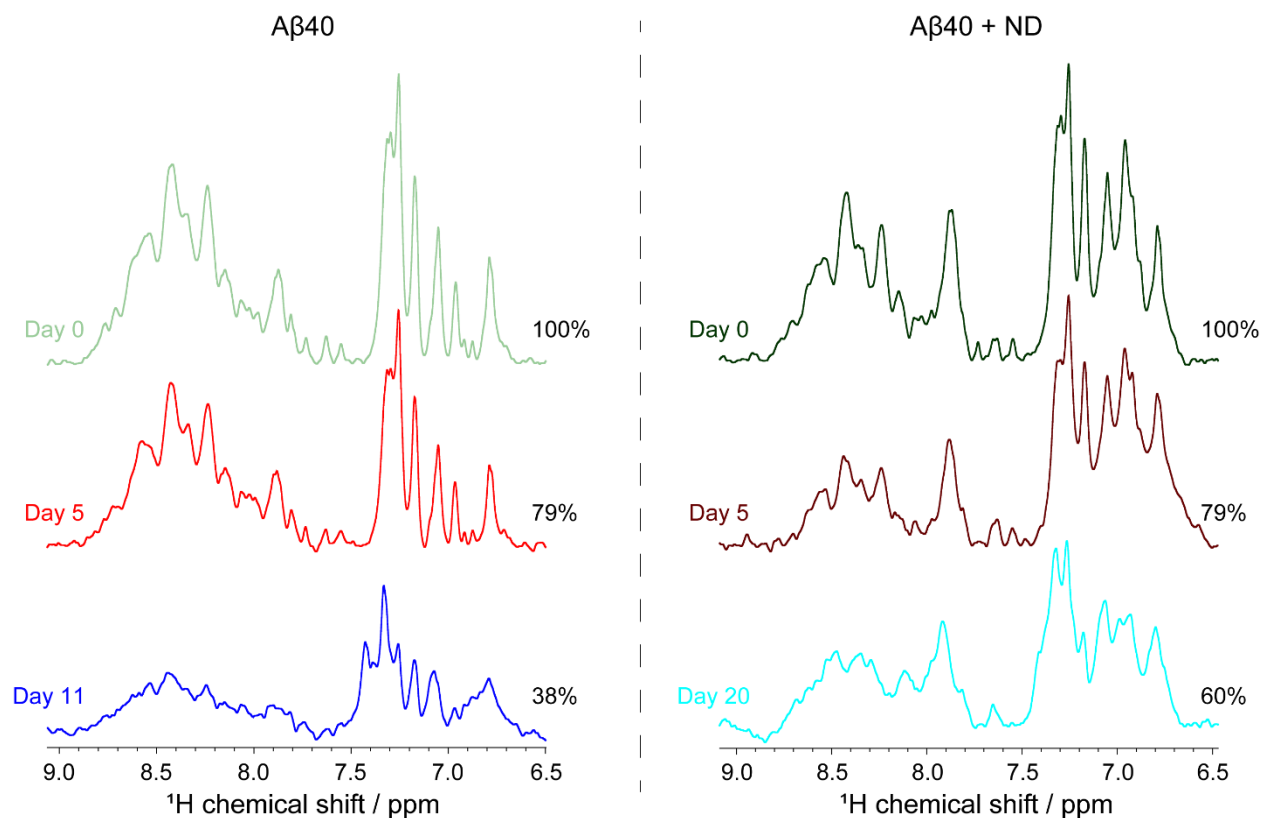
Figure S3.12. 1D ¹H NMR spectra of Aβ40 in absence and presence of nanodiscs at different time intervals. Samples were incubated at 25 °C under non-shaking conditions and spectra were taken at 10 °C. Initially both Aβ40 and Aβ40 in presence of high lipid concentration showed almost 20 % signal decay at day 5. After this time point, Aβ40 underwent drastic decrease in the signal intensity indicating fibrillation, whereas Aβ40 in presence of nanodiscs showed a slow decrease in the signal intensity. Even at 20 days of incubation, sufficient NMR signal was observed suggesting prolongation of oligomeric states.
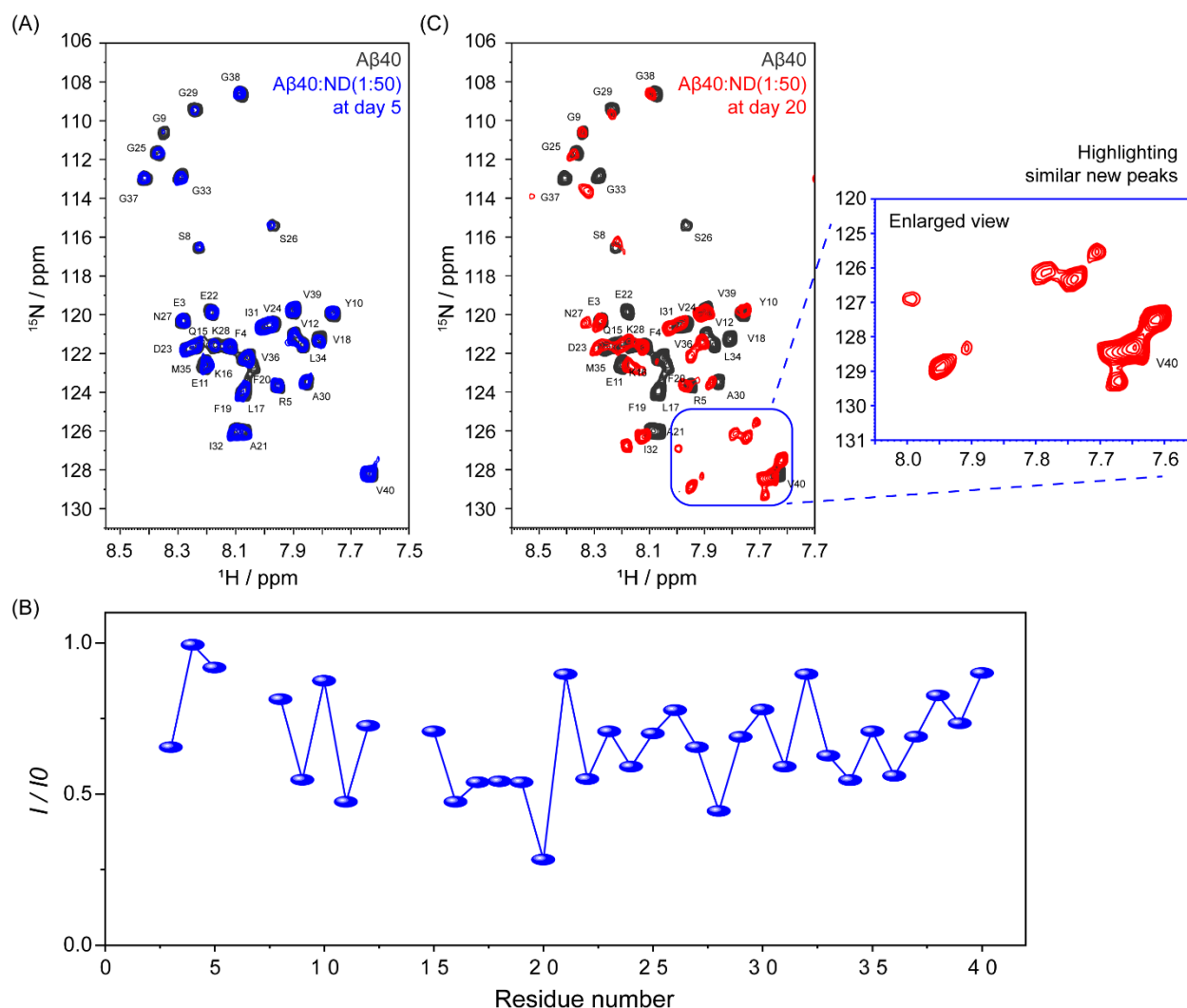
Figure S3.13. (a) Overlay of 2D ^1H-^{15}N HSQC spectra of a freshly prepared Aβ40 (80 µM) sample and with nanodiscs (L/P=50) at day 5 indicates only intensity drop and no significance CSPs. (b) Changes in the peak intensities along the peptide backbone measured from 2D ^1H-^{15}N HSQC spectra of a freshly prepared Aβ40 (80 µM) sample with nanodiscs (L/P=50) at day 5 indicates involvement of the central hydrophobic region in the interaction. Points represent the signal intensity of the peak maxima (*I(t)*) relative to the signal intensity in the absence of nanodiscs (*I₀*). (c) Overlay of 2D ^1H-^{15}N HSQC spectra of a freshly prepared Aβ40 (80 µM) sample and with nanodiscs (L/P=50) at day 20 indicates significant intensity drop and CSPs as well as similar new peaks at the vicinity of V40, thereby suggesting formation of similar oligomeric conformers.

(A)

(B)
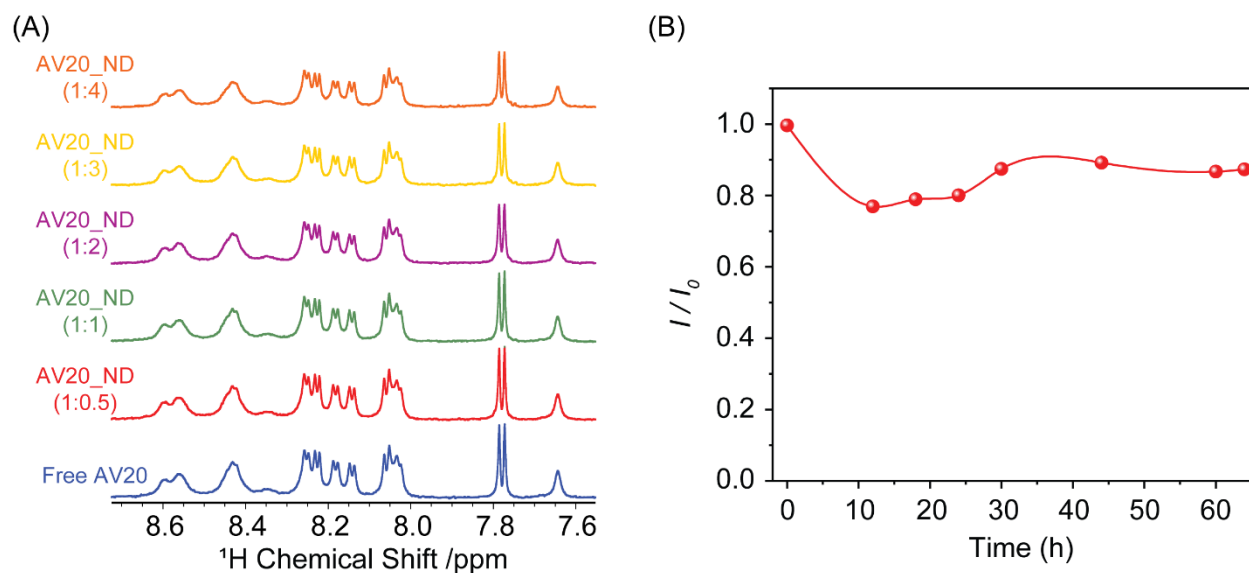
Figure S3.14. (a) 1D NMR spectra of AV20, titrating with NDs, showing line broadening of the amide protons. (b) Time-dependent overall relative intensity plot of AV20 in presence of NDs.
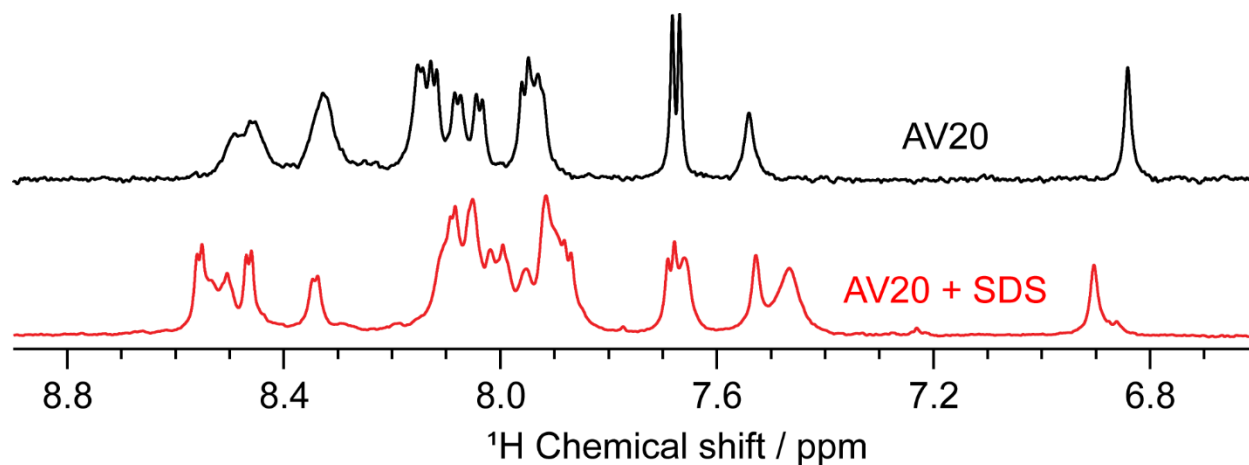
Figure S3.15. 1D NMR spectra of AV20 in the absence and in the presence of 100 mM SDS-d_{25} micelles.
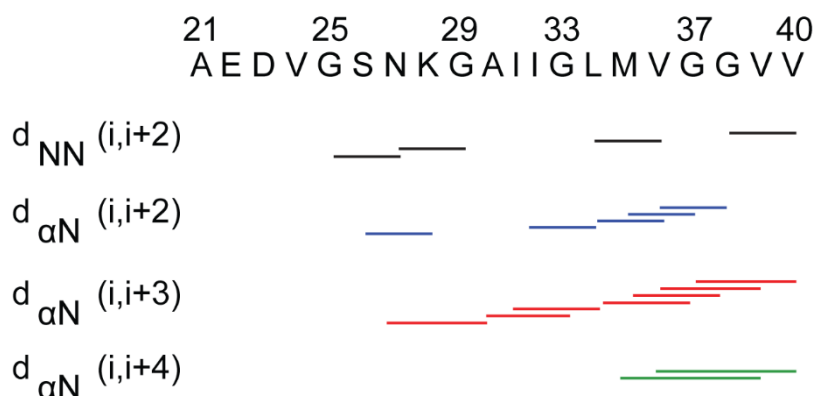
Figure S3.16. Short, Mid, and Long-range NOE connectivities obtained from the NOESY spectral assignment of AV20 in presence of SDS micelles.

3.7. References

[1] J. Hardy, D. J. Selkoe, *Science* **2002**, 297, 353.

[2] R. J. O'Brien, P. C. Wong, *Annu Rev Neurosci* **2011**, 34, 185.

[3] S. I. Cohen, S. Linse, L. M. Luheshi, E. Hellstrand, D. A. White, L. Rajah, D. E. Otzen, M. Vendruscolo, C. M. Dobson, T. P. Knowles, *Proc Natl Acad Sci U S A* **2013**, 110, 9758; S. J. Lee, E. Nam, H. J. Lee, M. G. Savelieff, M. H. Lim, *Chem Soc Rev* **2017**, 46, 310; I. Benilova, E. Karran, B. De Strooper, *Nat Neurosci* **2012**, 15, 349.

[4] J. P. Colletier, A. Laganowsky, M. Landau, M. Zhao, A. B. Soriaga, L. Goldschmidt, D. Flot, D. Cascio, M. R. Sawaya, D. Eisenberg, *Proc Natl Acad Sci U S A* **2011**, 108, 16938; K. Annamalai, K. H. Gührs, R. Koehler, M. Schmidt, H. Michel, C. Loos, P. M. Gaffney, C. J. Sigurdson, U. Hegenbart, S. Schönland, M. Fändrich, *Angew Chem Int Ed Engl* **2016**, 55, 4822.

[5] T. L. Williams, L. C. Serpell, *FEBS J* **2011**, 278, 3905.

[6] M. F. Sciacca, F. Lolicato, C. Tempra, F. Scollo, B. R. Sahoo, M. D. Watson, S. García-Viñuales, D. Milardi, A. Raudino, J. C. Lee, A. Ramamoorthy, C. La Rosa, *ACS Chem Neurosci* **2020**, 11, 4336.

[7] H. Fatafta, B. Kav, B. F. Bundschuh, J. Loschwitz, B. Strodel, *Biophys Chem* **2022**, 280, 106700.

[8] K. J. Korshavn, C. Satriano, Y. Lin, R. Zhang, M. Dulchavsky, A. Bhunia, M. I. Ivanova, Y. H. Lee, C. La Rosa, M. H. Lim, A. Ramamoorthy, *J Biol Chem* **2017**, 292, 4638; Z. Niu, W. Zhao, Z. Zhang, F. Xiao, X. Tang, J. Yang, *Angew Chem Int Ed Engl* **2014**, 53, 9294.

[9] S. Bera, N. Gayen, S. A. Mohid, D. Bhattacharyya, J. Krishnamoorthy, D. Sarkar, J. Choi, N. Sahoo, A. K. Mandal, D. Lee, A. Bhunia, *ACS Chem Neurosci* **2020**, 11, 1965.

[10] T. Viennet, M. M. Wördehoff, B. Uluca, C. Poojari, H. Shaykhalishahi, D. Willbold, B. Strodel, H. Heise, A. K. Buell, W. Hoyer, M. Etzkorn, *Commun Biol* **2018**, 1, 44.

[11] J. Borch, T. Hamann, *Biol Chem* **2009**, 390, 805.

[12] A. Viegas, T. Viennet, M. Etzkorn, *Biol Chem* **2016**, 397, 1335.

[13] T. H. Bayburt, Y. V. Grinkova, S. G. Sligar, *Nano letters* **2002**, 2, 853.

[14] I. G. Denisov, Y. V. Grinkova, A. A. Lazarides, S. G. Sligar, *J Am Chem Soc* **2004**, 126, 3477; C. Her, D. I. Filoti, M. A. McLean, S. G. Sligar, J. B. Alexander Ross, H. Steele, T. M. Laue, *Biophys J* **2016**, 111, 989.

[15] G. Fusco, T. Pape, A. D. Stephens, P. Mahou, A. R. Costa, C. F. Kaminski, G. S. Kaminski Schierle, M. Vendruscolo, G. Veglia, C. M. Dobson, A. De Simone, *Nat Commun* **2016**, 7, 12563.

[16] B. R. Sahoo, T. Genjo, M. Bekier, S. J. Cox, A. K. Stoddard, M. Ivanova, K. Yasuhara, C. A. Fierke, Y. Wang, A. Ramamoorthy, *Chem Commun (Camb)* **2018**, 54, 12883; B. R. Sahoo, T. Genjo, S. J. Cox, A. K. Stoddard, G. M. Anantharamaiah, C. Fierke, A. Ramamoorthy, *J Mol Biol* **2018**, 430, 4230; M. Thomaier, L. Gremer, C. Dammers, J. Fabig, P. Neudecker, D. Willbold, *Biochemistry* **2016**, 55, 6662.

[17] R. Ahmed, M. Akcan, A. Khondker, M. C. Rheinstädter, J. C. Bozelli, R. M. Epand, V. Huynh, R. G. Wylie, S. Boulton, J. Huang, C. P. Verschoor, G. Melacini, *Chem Sci* **2019**, 10, 6072; J. T. Jarrett, E. P. Berger, P. T. Lansbury, *Biochemistry* **1993**, 32, 4693.

[18] J. R. Brender, A. Ghosh, S. A. Kotler, J. Krishnamoorthy, S. Bera, V. Morris, T. B. Sil, K. Garai, B. Reif, A. Bhunia, A. Ramamoorthy, *Chem Commun (Camb)* **2019**, 55, 4483.

[19] D. Sarkar, A. Bhunia, *ACS Bio & Med Chem Au* **2023**.

[20] P. Kienlen-Campard, B. Tasiaux, J. Van Hees, M. Li, S. Huysseune, T. Sato, J. Z. Fei, S. Aimoto, P. J. Courtoy, S. O. Smith, S. N. Constantinescu, J. N. Octave, *J Biol Chem* **2008**, 283, 7733.

[21] S. Kim, T. J. Jeon, A. Oberai, D. Yang, J. J. Schmidt, J. U. Bowie, *Proc Natl Acad Sci U S A* **2005**, 102, 14278; L. W. Hung, G. D. Ciccotosto, E. Giannakis, D. J. Tew, K. Perez, C. L. Masters, R. Cappai, J. D. Wade, K. J. Barnham, *J Neurosci* **2008**, 28, 11950; A. Harmeier, C. Wozny, B. R. Rost, L. M. Munter, H. Hua, O. Georgiev, M. Beyermann, P. W. Hildebrand, C. Weise, W. Schaffner, D. Schmitz, G. Multhaup, *J Neurosci* **2009**, 29, 7582; V. Fonte, V. Dostal, C. M. Roberts, P. Gonzales, P. N. Lacor, P. Lacor, P. T. Velasco, J. Magrane, N. Dingwell, E. Y. Fan, M. A. Silverman, G. H. Stein, C. D. Link, *Mol Neurodegener* **2011**, 6, 61.

[22] D. Sarkar, I. Chakraborty, M. Condorelli, B. Ghosh, T. Mass, M. Weingarth, A. K. Mandal, C. La Rosa, V. Subramanian, A. Bhunia, *ChemMedChem* **2020**, 15, 293.

[23] I. Chakraborty, R. K. Kar, D. Sarkar, S. Kumar, N. C. Maiti, A. K. Mandal, A. Bhunia, *ACS Chem Neurosci* **2021**, 12, 2903.

[24] S. J. Bunce, Y. Wang, K. L. Stewart, A. E. Ashcroft, S. E. Radford, C. K. Hall, A. J. Wilson, *Sci Adv* **2019**, 5, eaav8216; G. Meisl, X. Yang, E. Hellstrand, B. Frohm, J. B. Kirkegaard, S. I. Cohen, C. M. Dobson, S. Linse, T. P. Knowles, *Proc Natl Acad Sci U S A* **2014**, 111, 9384.

[25] G. Meisl, J. B. Kirkegaard, P. Arosio, T. C. Michaels, M. Vendruscolo, C. M. Dobson, S. Linse, T. P. Knowles, *Nat Protoc* **2016**, 11, 252.

[26] Y. Xu, R. Maya-Martinez, N. Guthertz, G. R. Heath, I. W. Manfield, A. L. Breeze, F. Sobott, R. Foster, S. E. Radford, *Nat Commun* **2022**, 13, 1040.

[27] S. Vivekanandan, J. R. Brender, S. Y. Lee, A. Ramamoorthy, *Biochem Biophys Res Commun* **2011**, 411, 312.

[28] M. Coles, W. Bicknell, A. A. Watson, D. P. Fairlie, D. J. Craik, *Biochemistry* **1998**, 37, 11064.

[29] R. A. Rodriguez, L. Y. Chen, G. Plascencia-Villa, G. Perry, *ACS Chem Neurosci* **2018**, 9, 783; P. H. Nguyen, M. S. Li, G. Stock, J. E. Straub, D. Thirumalai, *Proc Natl Acad Sci U S A* **2007**, 104, 111; R. K. Kar, J. R. Brender, A. Ghosh, A. Bhunia, *J Chem Inf Model* **2018**, 58, 1576.

[30] S. R. Durell, H. R. Guy, N. Arispe, E. Rojas, H. B. Pollard, *Biophys J* **1994**, 67, 2137.

[31] C. Rando, G. Grasso, D. Sarkar, M. F. M. Sciacca, L. M. Cucci, A. Cosentino, G. Forte, M. Pannuzzo, C. Satriano, A. Bhunia, C. La Rosa, *Int J Mol Sci* **2023**, 24.

Chapter IV

Mechanistic Insight into Functionally Different Human Islet Polypeptide (hIAPP) amyloid: The Intrinsic Role of the C-terminal Structural Motifs

This chapter has been adapted from the following publication:

Sarkar, D., Maity, N.C., Shome, G., Varnava, K.G., Sarojini, V., Vivekanandan, S., Sahoo, N., Kumar, S., Mandal, A.K., Biswas, R. and Bhunia, A., 2022. Mechanistic insight into functionally different human islet polypeptide (hIAPP) amyloid: the intrinsic role of the C-terminal structural motifs. *Physical Chemistry Chemical Physics*, *24*(36), pp.22250-22262.

4.1. Introduction

Protein misfolding and subsequent amyloid formation is allied with the pathology of a wide range of human diseases, including Alzheimer's, Parkinson's, type-2 diabetes, Huntington diseases, etc.[1] Human islet amyloid polypeptide (hIAPP) is a 37-residue peptide implicated in type-2 diabetes resulting from aggregation under certain conditions.[2] With regards to the growing prevalence of diabetes worldwide, it is increasingly important to gain mechanistic insight into hIAPP amyloidosis.[3] For a comprehensive understanding of the mechanism of hIAPP aggregation, it is imperative to consider the aggregation-prone domains within the hIAPP sequence. Over the years, emphasis has been given on discovering the residues crucial for hIAPP fibrillation. For example, the N-terminal hIAPP$_{8-16}$ fragment has been found to form fibrils with similar properties to hIAPP where F15 is required for stabilizing an on-pathway α-helical dimer.[4, 5] Recent studies have revealed a crucial region-spanning the residue stretch, L^{12}ANFLVH^{18} associated with hIAPP aggregation.[4, 6] Despite the fact that this segment does not directly partake in amyloidogenesis, it was found to interact with hIAPP and strongly enhance the β-sheet transition and fibril formation.[7] Several other small fragments of hIAPP have also been reported to form amyloid.[8] The hIAPP$_{20-29}$ fragment has been exclusively reported to form amyloid fibril *in vitro* as well as play a significant role in the amyloid formation.[9, 10] However, the toxicity of this fragment was found to be considerably lower than that of the full-length peptide regardless of the strong tendency to form amyloid fibrils. The C-terminal segment harboring the N^{22}FGAIL^{27} sequence has been extensively reported and studied for understanding the mechanisms of amyloidogenesis.[10, 11] GxxxS/SxxxG motif present in this terminus is similar to the GxxxG repeating sequence in Amyloid β, which has been suggested to act as a modulator of fibrillation.[12] This segment has been shown to have a greater fibrillation propensity by several groups over the years. Recently, the C-termini of hIAPP oligomers were found to penetrate deeper into the lipid bilayer of the

disordered domain.[13] The fact that the hIAPP$_{17\text{-}37}$ peptide was previously identified as one of the minor component in the human pancreas, has made it further intriguing in delineating the direct role of this peptide fragment in modulating the overall aggregation propensity of hIAPP.[14] Undoubtedly, peptide fragments have been useful in streamlining the analysis of the complex aggregation process. Knowledge of the primary sequence of the peptide is essential in determining its intrinsic propensity to undergo subsequent structurally and functionally distinct conformers in the amyloidogenesis cascade.

Apart from the intrinsic susceptibility of specific peptide segments, several external factors have been found to highly influence the aggregation process.[15] A change in such conditions may alter the aggregation mechanism and result in either amyloid or disordered amorphous aggregates.[16] Over the years, the effect of peptide concentration, solvent pH, temperature, agitation, and ionic strength has been extensively studied.[17] Among them, temperature-dependent aggregation kinetics and agitation in the form of a magnetic stirrer or shaker table have been routinely used in studies of peptide and protein aggregation.[12, 18] Temperature variation may alter the frequency of molecular collisions and affect intermolecular hydrophobic interactions, a major force in controlling aggregation.[19] Thus, the investigation of the temperature dependence of the aggregation process of a protein/peptide can be a suitable method to clarify the mechanisms leading to different kinds of aggregates.[20] Agitation on the other hand, has been employed so as to accelerate otherwise slow aggregation kinetics. While some found deviations in aggregation rate and structure, others showed that not agitation but the liquid-air or liquid-solid interface serve as the main culprit.[21] Despite the frequent use, little is understood about the impact of agitation on the aggregation nucleation process.

In this chapter, we undertook a systematic approach to gain high-resolution insight into the intrinsic and extrinsic factors involved in hIAPP amyloidosis. For this purpose, we compared the aggregation kinetics of hIAPP along with its N-terminal 18 residue peptide fragment KH18 (K1-H18) comprising the L^{12}ANFLVH^{18} sequence and the C-terminal 21 residue peptide VY21 (V17-Y37) harbouring the core N^{22}FGAIL^{27} fibrillating sequence as well as GxxxS/SxxxG motif (Figure 4.1A) in different temperature and agitation conditions. This enabled us to gain a comprehensive understanding of hIAPP amyloidogenesis and subsequent toxicity in progressive pathogenesis.

Further, our biophysical studies suggested a possible cooperative interaction of the specific fragments in seeding the overall pathogenesis.

4.2. Materials and methods

4.2.1. Sample preparation

Lyophilized synthetic peptides hIAPP and KH18 were purchased from Genscript Inc. USA and VY21 was synthesized using Fmoc protocols as previously published.[22] Briefly, the peptide was assembled on 2-chlorotrityl chloride resin (0.2 mmol scale) as C-terminal acid. Excess of each amino acid (4×), 3.9 equivalents of coupling reagent (HCTU) and OxymaPure® (3.9 equiv.) as suppressor of racemization were used. N,N-Diisopropylethylamine (DIPEA) was used as the base for couplings. Fmoc deprotection was performed using 20% piperidine in DMF. Cleavage from the resin was done using 10 mL of the trifluoroacetic acid (TFA) cocktail mixture (TFA−TIS−H_2O- 95:2.5:2.5 v/v) per gram of the resin. TFA was evaporated and the crude peptide was precipitated using diethyl ether. The crude peptide was subsequently lyophilized and purified using reversed-phase high performance liquid chromatography (RP-HPLC) on a GE Pharmacia ÄKTA purifier 10 system or Thermo Scientific Dionex VWD 3×00 system using a Phenomenex Luna 5 μm C_{18} 100 Å (250 mm×10 mm) column. Solvent A was 0.1% TFA in water and solvent B was 0.1% TFA and 0.09% water in 99% acetonitrile and the flow rate was 10 mL per min. The peptide was purified to >95% purity as shown by the analytical RP-HPLC trace on a Phenomenex Luna 5 μm C_{18} 100 Å (250 mm×4.6 mm) column using the same solvent system as above at a flow rate of 1 mL per min. Matrix assisted laser desorption/ionisation – time of flight mass spectrometry (MALDI-TOF MS) recorded on a Bruker Ultraflextreme MALDI/TOF was used to characterize the peptide. 1 mg peptides were weighed and dissolved in 500 μL1,1,1,3,3,3-hexafluoro-2-propanol (HFIP; Sigma-Aldrich, USA) and kept for 40 mins at 4 °C and then separated into 10 aliquots. The aliquots were lyophilized for 48 h and stored at −20 °C for further use.

4.2.2. Thioflavin T (ThT) fluorescence assay

Stock solutions of ~80 μM hIAPP, KH18, and VY21 peptides were prepared in a buffer containing 20 mM phosphate buffer (pH 7.3, 0.01% sodium azide) and 50 mM NaCl. Then the sample solutions were vortexed well, followed by a three-minute ultra-sonication and

incubated at 25 °C or 37 °C temperature under shaking conditions. At various time-points, aliquots of peptides from incubations were taken and diluted to 10 µM final concentration, followed by the addition of 20 µM ThT for fluorescence intensity measurement. Fluorescence measurements were carried out using Hitachi F-7000 FL spectrometer with 240 nm/min scan speed. The excitation wavelength was kept at 440 nm and the emission range used was 460-520 nm, with 5 nm slit width for both the excitation and emission.

Further, peptide aggregation was studied under non-shaking conditions at different temperatures. 20 µM ThT was added into the sample solutions and ThT fluorescence was monitored under controlled temperatures using BMG LABTECH POLARstar Omega spectrometer in a 96 well plate.

Time-dependent ThT fluorescence data were fitted to a sigmoidal growth model:

$$Y = Y_0 + (Y_{max} - Y_0)/(1 + exp\,((t - t_{1/2}/b))$$

Where the half-life $t_{1/2}$ is the time required to reach half of the fluorescence intensity, b is the apparent first-order constant and Y_{max}, and Y_0 are, respectively, the maximum and initial fluorescence values.

The lag-time (t_{lag}) of amyloid kinetics was determined as $(t_{1/2} - 2b)$.

Three independent experiments were performed throughout. All buffer solutions were filtered by using a 0.2 µm filter.

4.2.3. MTT assay

Cell culture and cell viability assay:

RIN-5f cells derived from rat pancreatic β-cells were obtained from National Centre for Cell Science (NCCS, India) and maintained in complete RPMI-1640 media (Gibco) supplemented with 10% FBS, 1 unit/ml penicillin-streptomycin, 50 µg/mL gentamycin, and 2.5 µg/ml amphotericin B at 37 °C in a humidified 5% CO_2 incubator. Experiments were carried out at 70-80% confluency.

Cell viability was measured using 3-(4,5-dimethylthiazol-2-yl)-2,5-diphenyltetrazolium bromide (MTT), which reflects the mitochondrial activity of living cells. Viable cells were able to reduce MTT into purple formazan by mitochondrial enzyme; and the amount of formazan formation indicates cell viability. Briefly, 1×10^4 cells/well were seeded in 96-well plate for 24 h. Cells were then treated with 10µM of each hIAPP, KH18 and VY21

peptides taken out at various time-points (0, 10, 60 and 240 min) in shaking conditions. In addition, RIN-5f cells were also treated with 10 µM of hIAPP, KH18, VY21 and hIAPP+VY21 (1:1 molar ratio) peptides which were taken at various time-points (0, 2, 5, and 24 h) in non-shaking conditions. After 24 h of treatment, MTT was added to the wells at a final concentration of 0.5 mg/ml and incubated at 37 °C and 5% CO_2 humidified incubator for another 3.5 h. 100 µL of dimethyl-sulfoxide (DMSO) was added to each well to dissolve the formazan precipitate. The absorbance was taken at 570 nm using a microplate reader. Results were expressed as a percentage of control.

4.2.4. Circular dichroism (CD) spectroscopy

CD measurements were taken on a JASCO J-1500 CD spectrometer using a 0.1 cm path length cell with a slit width of 2 nm. Peptides of ~80 µM concentration were prepared in 20 mM phosphate buffer, 50 mM NaF (pH 7.3), and incubated at 37 °C under shaking conditions as well as at 25 °C under non-shaking conditions. At different time intervals, Far-UV CD spectra were recorded at 20 °C, from 260 nm to 190 nm, with a scan speed of 100 nm/min. For each spectrum, three readings were taken (i.e., three accumulations), and the average was considered. Smoothing and buffer subtraction were done to process raw data, as per the manufacturer's recommendation.

4.2.5. Time-resolved fluorescence assay

Time-resolved fluorescence (TRF) experiments were performed via time-correlated single-photon counting (TCSPC, LifeSpec-ps, Edinburgh Instrument, U.K.) technique.[23] All TRF samples were excited with 409 nm wavelength LED laser. The scattering solution was excited at 409 nm, and the emission was also collected at 409 nm with the magic angle orientation of the emission polarizer with respect to excitation, and the instrument response function (IRF) was collected. The full-width half maxima (FWHM) of IRF was 85 ps. The TRF emission of ThT in these experiments was collected at 485 nm. The average excited-state lifetime $\langle \tau_{life} \rangle$ of ThT was calculated from the magic angle TRF decay collected at the emission peak wavelength of ThT in these samples considering the formula $\langle \tau_{life} \rangle = \sum_i a_i \tau_i$, where $\sum_i a_i = 1$. The TRF samples were prepared by mixing the required amount of

hIAPP, VY21, and their 1:1 mixture (80 µM) in the buffer mentioned above containing 20 µM ThT. All TRF measurements were performed for up to 6 h at 25 °C. The isothermal condition was made by using the Julabo temperature controller (accuracy ±1 K).

4.2.6. Nuclear magnetic resonance spectroscopy

The lyophilized samples were re-suspended in 20 mM sodium phosphate, 50 mM NaCl (pH 7.3). All NMR samples were prepared in sodium phosphate buffer containing 10% deuterated water (v/v). ^{1}H NMR spectra were obtained using 128 scans with a recycle delay of 1.5 s. All NMR experiments were carried out on a 500 MHz Bruker spectrometer equipped with RT probe at 25 °C. All NMR spectra were processed using Topspin^{TM} 4.0.6 (Bruker software suite).

4.2.7. Transmission electron microscopy (TEM)

TEM sample preparation was done by diluting the stock solution into 10 µM for each variant in milli-Q water. Then 10 µL of each sample was spotted on a carbon-coated copper grid (Electron Microscopy Sciences, USA), followed by an incubation of 30 minutes. It was subsequently followed by washing with Milli Q water and staining with freshly prepared filtered 1% (w/v) uranyl acetate solution (Electron Microscopy Sciences, USA) for 5 minutes. Finally, samples were air-dried for 30 minutes. Imaging was done using a transmission electron microscope FEI Tecnai TF20 at 200 kV with a point resolution of 0.24 nm and line resolution of 0.102 nm. Recording of images was done digitally, and analysis was done in EDS mode.

4.2.8. Scanning electron microscopy (SEM)

Aliquots of each peptide solution were taken at the saturation phase and deposited on a glass slide, followed by overnight air-drying. The slides were then coated with gold for 120 s at 10 kV voltage and 10 mA current. The sample images were recorded using a ZEISS EVO-MA 10 scanning electron microscope equipped with a tungsten filament gun operating at 10 kV.

4.3. Results

4.3.1. Fibrillation kinetics of hIAPP, KH18, and VY21

We first compared the aggregation kinetics of hIAPP, KH18 (K^1-H^{18}), and VY21 (V^{17}-Y^{37}) (Figure 4.1A) using Thioflavin T (ThT) dye[24] at physiological pH, but, at
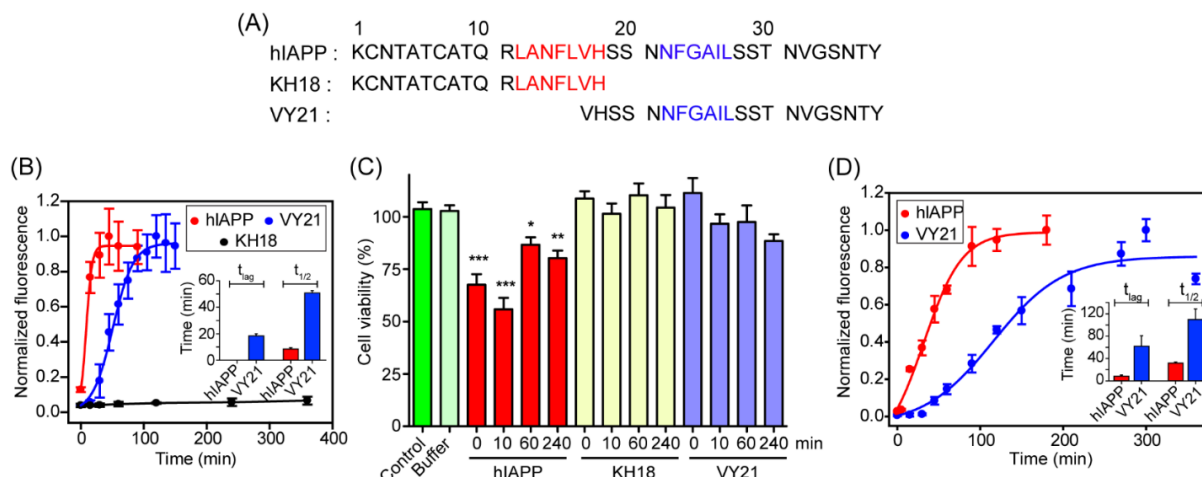
Figure 4.1. (A) Amino acid sequence of peptides under investigation with highlighted crucial motifs. (B) Aggregation kinetics of peptides investigated by ThT based fluorescence assay at 37 °C under shaking conditions (250 rpm). (C) RIN-5F cells were treated with hIAPP (10μM), KH18 (10μM) and VY21 (10μM) for 24h and cell viability was measured by MTT assay under shaking condition. Values are represented as mean ± SEM, n=9. Significance was analysed using one-way ANOVA, * p < 0.05, ** p<0.01, *** p<0.001. (D) ThT fluorescence kinetics of hIAPP (red) and VY21 (blue), at 25 °C under shaking conditions (250 rpm). All kinetic curves were normalized with respect to hIAPP. Insets show the corresponding half-time ($t_{1/2}$) and lag-time (t_{lag}) of the aggregation kinetics obtained from Boltzmann fit. All experiments were repeated three times, and the data were averaged (±SD).

different temperatures. Under shaking conditions (250 rpm) at 37 °C, hIAPP displayed a rapid aggregation profile. VY21, the C-terminal fragment, on the other hand, showed slower aggregation kinetics, while the N-terminal, KH18, did not induce any increase in the ThT fluorescence intensity over the experimental time-frame. The respective time-dependent kinetic curves were fitted with a sigmoidal growth model to determine the corresponding half-time ($t_{1/2}$) and lag-time (t_{lag}) of the aggregation kinetics (Figure 4.1B).[25] At the given temperature and shaking conditions, hIAPP exhibited no t_{lag}, reaching $t_{1/2}$ within just 8.45 ± 1.07 min of incubation. While KH18 did not show any aggregation, VY21 displayed a sigmoidal growth kinetics with a t_{lag} of 18.40 ± 1.60 min and a $t_{1/2}$ of 50.85 ± 1.77 min (Appendix IV, Table S4.1). Having this distinct difference in the overall aggregation propensities between the peptides, we measured their corresponding fibrillar cytotoxicity to correlate their pathogenic propensity (Figure 4.1C).

4.3.2. Cytotoxicity of amyloid fibrils formed at 37 °C, under shaking conditions

To compare the cytotoxic effects of fibrillar/oligomeric hIAPP with the fragment peptides generated at 37 °C,   under shaking conditions (250 rpm), we performed MTT reduction assay with RIN-5F cells using 3-(4,5-dimethylthiazol-2-yl)2,5-diphenyltetrazolium bromide (MTT) dye reduction as an indicator of good metabolic health.[26] RIN-5F insulinoma cells, which closely resemble pancreatic β-cells, were chosen as an *ex vivo* model system to measure the cytotoxicity of the respective peptides whose effects are more pronounced in the pancreas and closely represent type II diabetes pathology. Figure 4.1C shows that hIAPP preparations containing amyloid fibrils/oligomers are significantly more toxic than either KH18 or VY21 as compared to untreated control. Incubating the cells with hIAPP at different time-points of 0 min, 10 min, 60 min, and 240 min reduces the viability to 32%, 44%, 13%, and 20%, respectively as compared to the controls. Correlating with the ThT fluorescence, we observed a correlation between the aggregated states and cytotoxicity. Samples at 0 min and 10 min, which largely contain oligomers, are highly toxic. On the other hand, the cell viability increased with the predominance of growing protofibrils and mature fibrillar species (samples at 60 min and 240 min, respectively). The non-aggregating KH18 peptide fragment was found to be non-toxic at the aforesaid time points. Similarly, VY21 did not show any toxicity at 0-, 10- or 60-min time points. However, only slight reduction in cell viability was observed at 240 mins. Thus, despite the ThT-positive aggregates, VY21 amyloid aggregates were less toxic to the RIN-5F cells. This suggested that the intrinsic amyloidogenic propensity of the full-length or C-terminal fragment cannot directly correlate to the functional attributes of the eventual conformers. Probably, some other factors might be dictating much of the functional pathogenesis. This prompted us to extend our studies into understanding the direct role played by the extrinsic factors.

4.3.3. Effect of temperature on aggregation kinetics

The very fast aggregation kinetics of hIAPP and VY21 at 37 °C, under shaking conditions, made it difficult to distinctively correlate the cytotoxicity with the aggregated species. Small temperature variations can significantly impact the protein folding and may cause non-native aggregation.[15] Thus, modulating the experimental temperature might help regulate the overall aggregation rate for a better structural insight into the functional toxicity. Here, we investigated the aggregation kinetics of the peptide variants at a lower

temperature (25 °C) while keeping the shaking conditions (250 rpm) the same (Figure 4.1D). Consequently, an increased t_{lag} of 8.41 ± 2.10 min and 61.78 ± 18.54 min was detected at 25 ° temperature for hIAPP and VY21, respectively. Similarly, the $t_{1/2}$ value for hIAPP and VY21 was found to be 31.73 ± 2.14 min and 109.72 ± 18.94 min, respectively (Appendix IV, Table S4.2). Thus, lowering the temperature reduced the aggregation rates for both hIAPP and VY21.

4.3.4. Aggregation kinetics under quiescent conditions

Studies have shown that agitation may induce protein/peptide aggregation.[27] Therefore, in order to examine the influence of agitation on the aggregation kinetics, we performed a ThT fluorescence assay under quiescent conditions at different temperatures. At 25 °C, hIAPP displayed a typical sigmoidal growth curve of amyloid formation. The fluorescence intensity started to increase gradually after a lag-time of 160.70 ± 2.00 min, reached $t_{1/2}$ at 210.00 ± 1.00 min, and saturated at ~360 min of incubation (Figure 4.2A). To gain mechanistic insights into the formation hIAPP fibrillation, we performed the global fitting of the ThT curves using the online platform AmyloFit[28] and obtained the rate constants for the individual microscopic steps. Different kinetic models were checked for fitting of the experimental data. Interestingly, we found that the models that do not include secondary nucleation failed to properly fit the experimental kinetic curve. The multi-step secondary nucleation model best fitted the experimental data (Appendix IV, Figure S4.1). In this model, peptide monomers first bind to the surface of the fibrils, which is monomer concentration-dependent. This is followed by monomer concentration-independent steps that could involve conformational rearrangement, the formation of a nucleus, and detachment from the surface of the fibrils. From the model fitting we obtained the rate constants k_+ (elongation rate constant), k_n (primary rate constant), k_2 (secondary nucleation rate constant) as well as the Michaelis constant K_M all of which were comparable to the previously reported data on hIAPP aggregation[29]. We also found that the combined rate constant for secondary nucleation, k_+k_2, is larger than the combined rate constant k_+k_n containing primary nucleation, such that $k_2/k_n > 10^8$, suggesting that most of the new aggregates are formed through surface-catalyzed secondary nucleation rather than through primary nucleation. Interestingly, VY21 displayed completely different aggregation
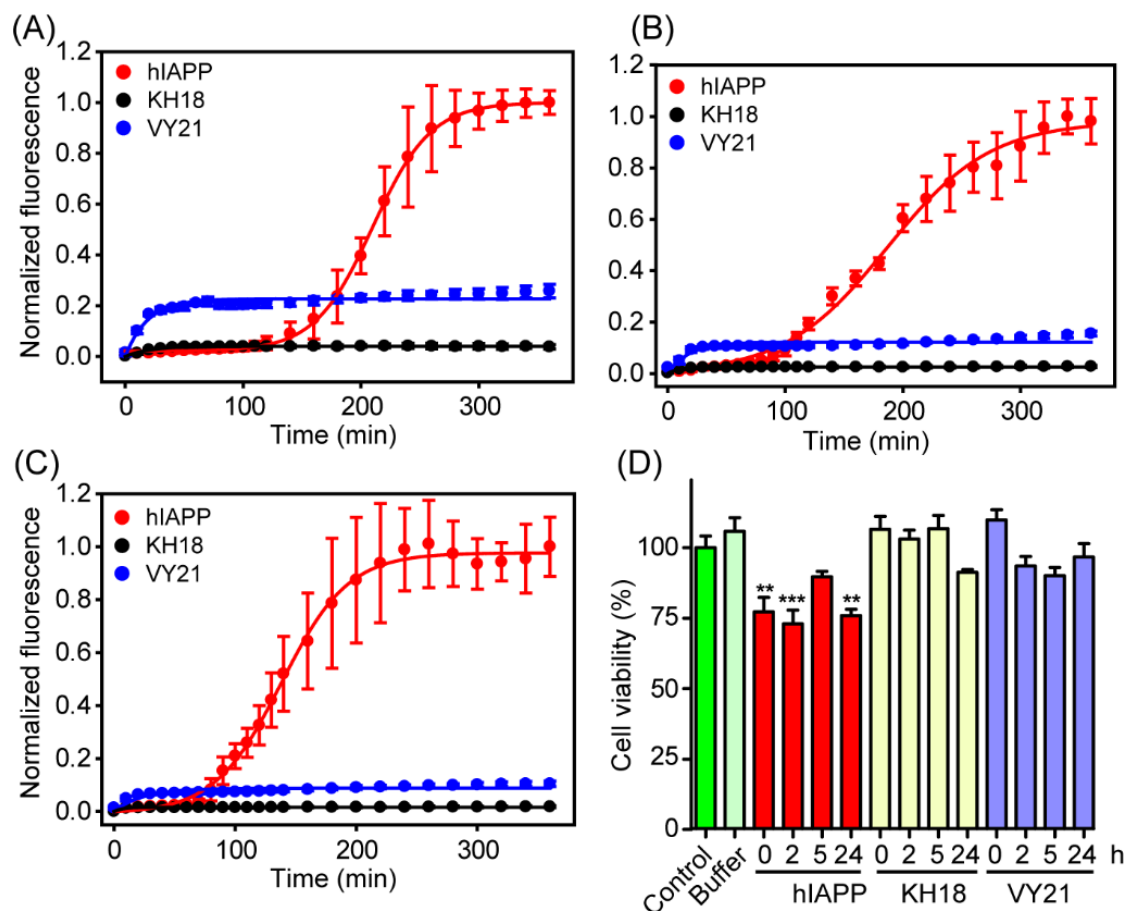
Figure 4.2. Aggregation kinetics of hIAPP (red), KH18 (black), and VY21 (blue) at under non-shaking condition (A) 25 °C, (B) 32 °C, and (C) 37 °C, monitored by ThT fluorescence. All experiments were repeated three times, and the data were averaged (±SD). (D) Cell viability was measured by incubating equimolar (10 µM) concentrations of indicated peptides generated at 25°, under non-shaking condition. Values are represented as mean ± SEM, n=6. Significance was calculated using one-way ANOVA, ** $p < 0.01$, *** $p < 0.001$.

kinetics. Despite the composite core fibrillating sequence, VY21 displayed considerable differences under quiescent conditions with very little increase in the ThT intensity compared to hIAPP. Due to the complex nature of oligomerization, we could not fit the data using the online platform Amylofit. KH18, on the other hand, did not show any aggregation whatsoever (Figure 4.2A).

Interestingly, at a higher temperature (32 °C) under non-shaking conditions, hIAPP displayed a considerably faster aggregation with $t_{1/2}$ of 188.00 ± 3.40 min and t_{lag} of 100.00 ± 5.70 min (Figure 4.2B). VY21 exhibited similar kinetics to that of 25 °C, which suggests that in order to undergo fibrillation, VY21 requires shaking. KH18, on the other hand, did

not show any aggregation. Similarly, a further increase in the incubation temperature resulted in lowering of lag-time for hIAPP but did not affect the aggregation kinetics KH18 or VY21 substantially (Figure 4.2C). At 37 °C, hIAPP displayed a t_{lag} of 82.00 ± 2.80 min, reaching $t_{1/2}$ at 138.00 ± 1.50 min of incubation. The fibrillation t_{lag} of hIAPP was plotted as a function of temperature, which suggested a drastic difference in the initial elongation rates (Appendix IV, Figure S4.2A). The Arrhenius plot of initial elongation rates on a logarithmic scale vs. inverse temperature indicated data points well fitted (R=0.99) with a straight line (Appendix IV, Figure S4.2B). From the slope of the straight line, we calculated the activation energy, E_A to be 43.8 ± 5.6 kJ/mol, suggesting a significant conformation change associated with the addition of hIAPP monomer to the fibrils.[30]

Since the hIAPP sample in non-shaking conditions and at 25 °C resulted a distinct observation of lag phase, we performed MTT assay to assess the cytotoxicity of the aggregated species. Figure 4.2D clearly depicts the distinct effect of the different aggregated states of hIAPP on the survival rates of RIN-5F cells. Interestingly, when compared to the aggregation kinetics, we observed a strong connection between the time frame of lag phase $(0 - 3\ h)$ and the pronounced cytotoxicity detected for the hIAPP species. hIAPP sample at 2 h of incubation showed the most cytotoxic effect because of the predominant existence of the oligomers. As the nucleation and growth phase proceeds, a significant decrease in the toxicity was apparent. While the cells treated with the oligomers (sample obtained at 2 h) showed ~70% of survival, the growing protofibrils (collected at 5 h) resulted in ~90% cell viability. Interestingly, KH18 retained its non-toxic nature up to 5 h of incubation (no significant reduction of cell viability), with only 8% decrease in the cell viability observed for the sample collected at 24 h. Nonetheless, a possible explanation would be the generation of few low molecular weight oligomers, which may attribute to the observed toxicity. When cells were incubated with an equimolar concentration of VY21 at different time-points of incubation, we found a slight reduction in the cell viability compared to the control. This is intriguing, as under the given conditions, the ThT assay indicated that VY21 remains mostly as oligomers. Thus, it is possible that the structural difference and the non-transient nature of these oligomeric species decide the difference in toxicity profile with hIAPP oligomers. Therefore, our experimental observations indicated only a direct correlation between cytotoxicity and aggregated state for hIAPP alone,
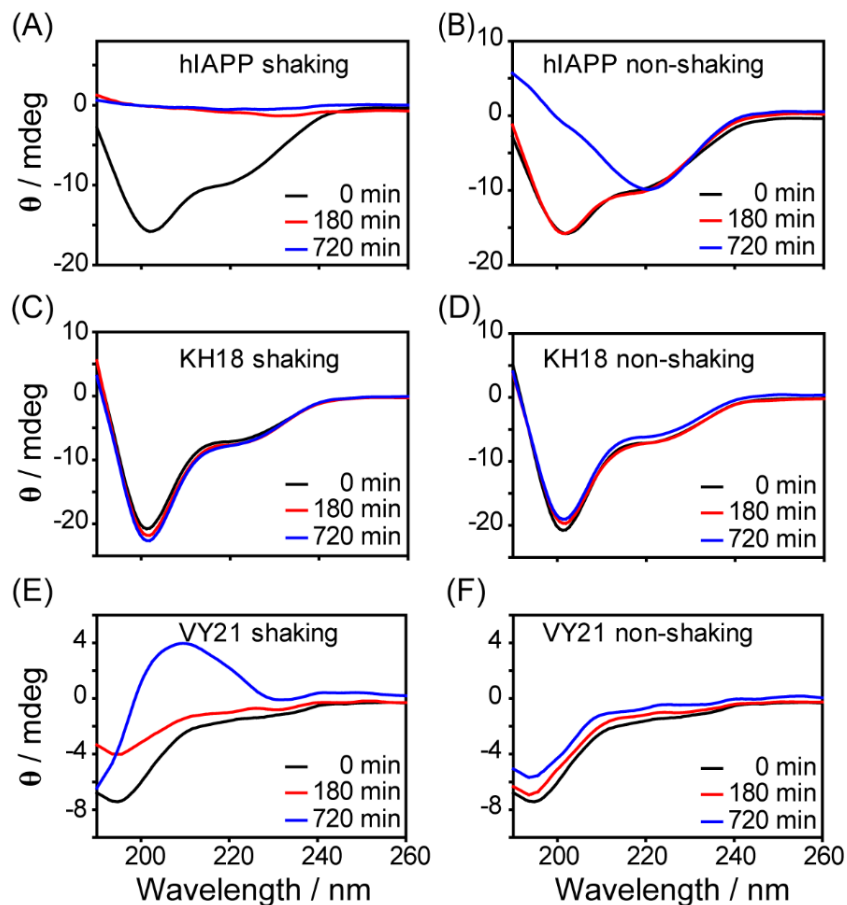
Figure 4.3. Monitoring secondary structural changes during aggregation by CD spectroscopy. Time-dependent CD spectra of (A) hIAPP, (C) KH18, and (E) VY21 at 37 °C under shaking conditions. Time-dependent CD spectra of (B) hIAPP, (D) KH18, and (F) VY21 at 25 °C under non-shaking conditions. All kinetic profiles are color coded.

supporting the "oligomer hypothesis" of amyloidosis. Neither VY21 nor KH18 displayed a profile that clearly correlates the toxicity and the aggregation state. Overall, these findings suggest that under non-shaking conditions, VY21 forms stable oligomers; however, it could not trigger substantial cellular death.

4.3.5. Secondary structure determination by CD spectroscopy

To compare the characteristic changes in the secondary conformation during aggregation, we performed Circular Dichroism (CD) spectroscopy at different time-points of incubation (Figure 4.3). Initially, hIAPP displayed α-helical conformation, with representative double minima near 206 nm and 222 nm (Figures 4.3A-B). At 37 °C, under shaking conditions (250 rpm), the conformational transition to β-sheet occurred very

rapidly (within 180 min). Within the same time interval, hIAPP showed negligible changes in the secondary structure when incubated at 25 °C under non-shaking conditions, suggesting a slower aggregation rate. Thus, the aggregation rates are highly dependent on the external factors, correlating well with the ThT assay. However, the overall population of the intermediate toxic oligomers retained their helical conformation-preventing further characterization from the CD spectra. Similarly, the toxic hIAPP fibrils generated under different aggregation conditions manifested in β-sheet secondary conformations. Figure 4.3C, D indicates that KH18 did not show noticeable changes in the CD spectra within the experimental time under both experimental conditions. Overall, the non-toxic KH18 exhibited double minima near 206 nm and 222 nm, representing α-helical conformation, and remained unchanged throughout the experiment. Surprisingly, the VY21 fibrils formed under shaking conditions (250 rpm) at 37 °C, which are non-toxic in nature, have β-sheet secondary conformation (Figure 4.3E). Under the given conditions, we observed a swift change from the random coil (minima at 196 nm) to β-sheet fibrils. Under non-shaking conditions, the percentage of random coil decreased with time; however, no visible β-sheet conformation was observed in the CD spectra, corroborating well with the ThT data (Figure 4.3F). Thus, the less-toxic VY21 aggregates have predominantly disordered secondary conformation.

4.3.6. Time-resolved fluorescence (TRF) of ThT provides a better understanding of fibril formation

In order to have a better understanding of the origin of the above-described fluorescence intensity variances between hIAPP and VY21, the fluorescence lifetime of ThT molecules during the aggregation process was measured by Time-resolved fluorescence (TRF) emission decay, collected at the emission polarizer's magic angle orientation at 25 °C temperature under non-shaking conditions (Figure 4.4). The lifetime emission decay was fitted to a sum of three exponential functions of time, and the average lifetime $\langle \tau_{life} \rangle$ was obtained via time integration of the fit parameters. Earlier femtosecond up-conversion experiments reported tri-exponential ThT fluorescence intensity decay in bulk water.[31] On the other hand, bi-exponential or multi-exponential fluorescence lifetime decays of ThT in normal high viscous solvents, binary mixtures and in amyloid fibril
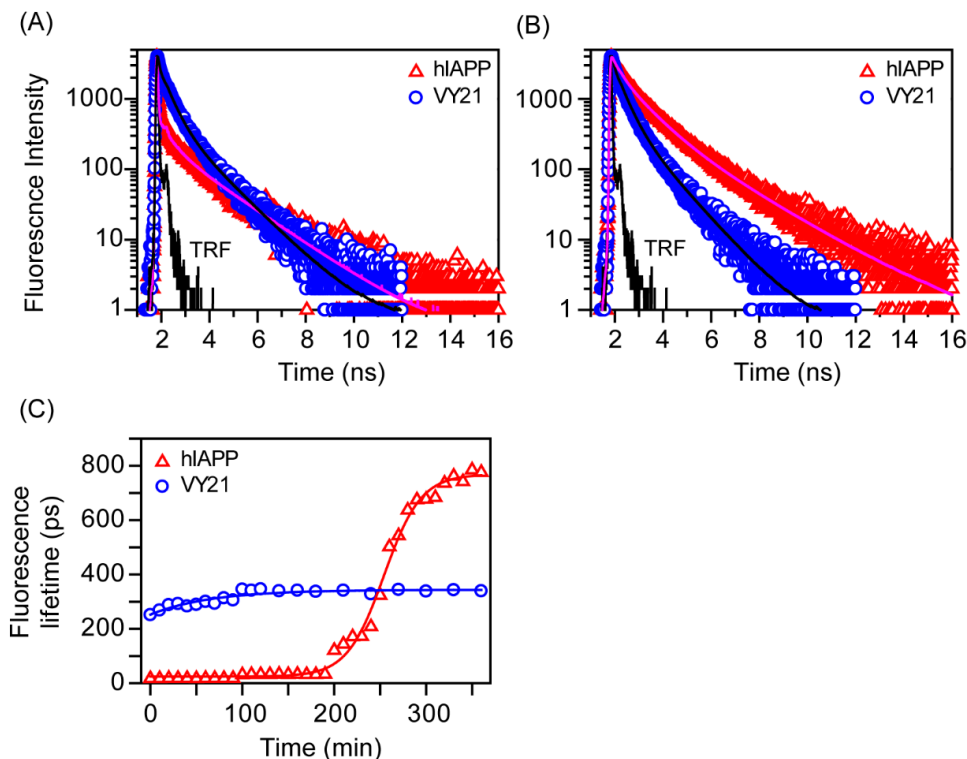
Figure 4.4. (A) Time-resolved fluorescence decay of ThT in presence of hIAPP (red) and VY21 (blue) at 0 min and (B) after 360 min of incubation at 25 °C under non-shaking conditions. (C) Time-resolved fluorescence lifetime kinetics of ThT in presence of hIAPP (red), and VY21 (blue).

systems have been reported by detection systems with temporal resolutions of a few tens of picosecond.[31-33] The multi-exponential ThT intensity decay kinetics, measured by us in this work, is, therefore, a reflection of the inherent multi-exponential character of ThT fluorescence lifetime decay. We have found that the fluorescence lifetime of ThT corroborated well with the ThT fluorescence kinetic assay (Figure 4.2A). Note that the average lifetime of ThT did not increase considerably during the lag time of hIAPP aggregation. After ~180 min of incubation, the lifetime of ThT gradually increased due to oligomerization and subsequent amyloid formation. In contrast, the ThT lifetime kinetics in the presence of VY21 showed no lag-time; however, it did not increase much compared to hIAPP. The lifetime of ThT largely depends on the torsional restriction between benzothiazole moiety and the amino benzene ring. Thus, ThT lifetime can increase if the torsional restriction imposed by molecular friction is enhanced through either solvent viscosity[32, 34], medium confinement[35] or incorporation of ThT inside β-sheets.[31] CD

spectra of VY21 under non-shaking condition (Figure 4.3F) indicates that aggregation of VY21 in aqueous solution dose not lead to formation of β-sheet during incubation period. It is noteworthy to mention that the steady state fluorescence intensity (I_{ss}^f) depends non-linearly on radiative (K_r) and non-radiative (K_{nr}) rates via the relation,[36]$I_{ss}^f = \varphi_f I_0 (1 - 10^{-A})$, where $\varphi_f = K_r/(K_r + K_{nr})$. φ_f denotes quantum yield, I_0 and A are intensity of incident light and absorbance respectively. Average fluorescence lifetime, on the other hand depends on K_r and K_{nr} as follows: $\langle \tau_{life} \rangle = 1/(K_r + K_{nr})$. As the aggregation proceeds, ThT experiences increasing restriction on its torsional mode during twisted intramolecular charge transfer (TICT) under photo-excitation. This in turn decreases K_{nr} and lengthens average lifetime$\langle \tau_{life} \rangle$. Although I_{ss}^f and $\langle \tau_{life} \rangle$ depends on K_r and K_{nr} of ThT, the connecting relations are not the same. The small increase of I_{ss}^f in the beginning of the incubation period and the relatively weaker increase of the $\langle \tau_{life} \rangle$ during the same time therefor suggest that ThT experienced somewhat restricted environment due to VY21 aggregation. The absence of β-sheets in VY21, on the other hand, resulted in a reduced lifetime $\langle \tau_{life} \rangle$ of ThT because of the relatively less frictional resistance on ThT torsional mode. The time-dependent changes in the intensity decay amplitudes (a_1, a_2, and a_3) of the respective samples suggest that progressive formation of β-sheets followed by amyloid formation increases the local friction, which, in turn, increases the population with longer lifetimes (Appendix IV, Figure S4.3). With time, the decrease of 'free' ThT molecules and the simultaneous increase of the 'bound' ThT molecules leads to lengthening of the average fluorescence lifetime. ThT molecules located in disorder oligomeric environments or inside β-sheet channels in fibril, naturally experiences enhanced frictional resistance and contributes to the lengthening of the average fluorescence lifetime of ThT in peptide aggregations shown in the present measurements.

4.3.7. Insights from NMR spectroscopy

We next performed solution state ^{1}H NMR spectroscopy to monitor the kinetics of monomer loss, and detect soluble intermediate species. Time-dependent one-dimensional (1D) NMR spectroscopy has often been used to detect the intensity drop of the peptides during aggregation for its advantage of not requiring any external fluorophore like ThT (Figure 4.5A-C).[37] The signal intensity of the amide peaks for each peptide was measured
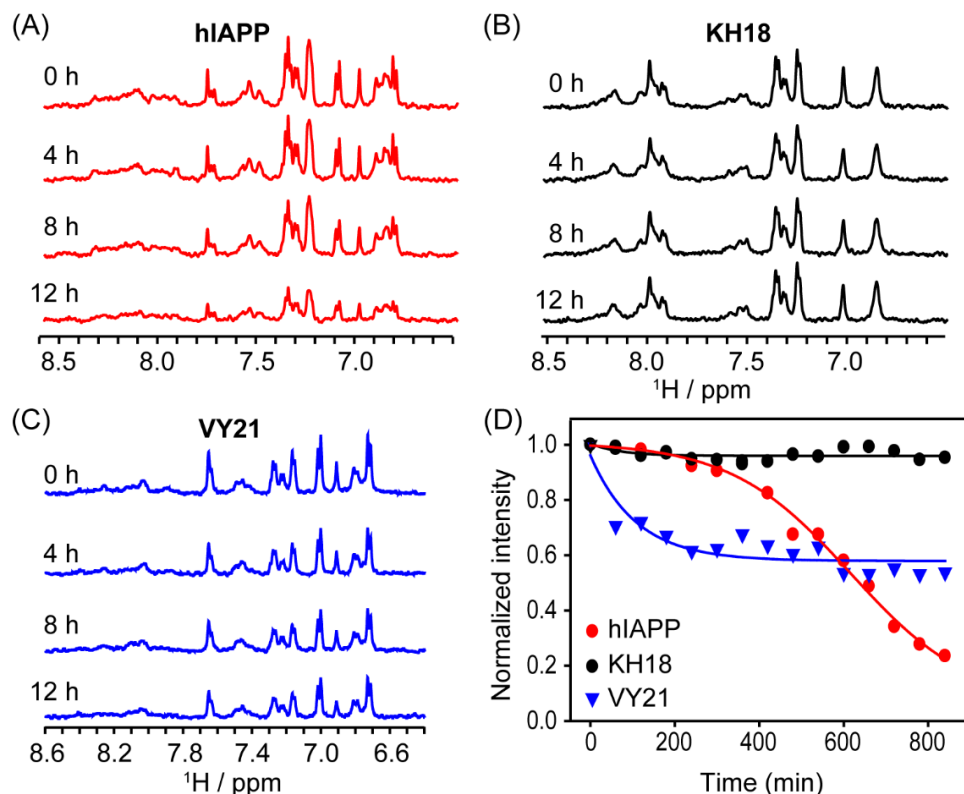
Figure 4.5. Time-dependent 1D NMR spectra of (A) hIAPP, (B) KH18, (C) VY21 at 25 °C under non-shaking conditions. (D) ^{1}H NMR intensity decay kinetics of hIAPP (red), KH18 (black), and VY21 (blue). All kinetic profiles are color coded.

at 25 °C under non-shaking conditions and plotted as a function of time intensity (Figure 4.5D). hIAPP exhibited a gradual decrease in the monomer concentration and showed ~80% decay in the signal intensity at the time of saturation. Apart from the line broadening no new peaks appeared in the 1D spectra during the experimental time-frame. The kinetics of hIAPP measured by NMR tend to be slower than that observed by ThT fluorescence. It can be attributed to interface effects with the container well and air-water interface that are different between NMR tubes and 96-well plates.[38] Also, the absence of ThT molecules can slightly affect the kinetics of aggregation.[39] KH18 displayed negligible decrease in the NMR signal intensity throughout the experimental time. In case of VY21, the most striking changes occurred within just 60 min of incubation. There is a 30% drop in the overall amide peak intensity within that time and then the system gradually stabilized with a final decay of ~40% signal intensity. Thus, while a significant decrease in the VY21 amide peak intensity occurs immediately after dissolution that plateaus at around 60 min, a slower
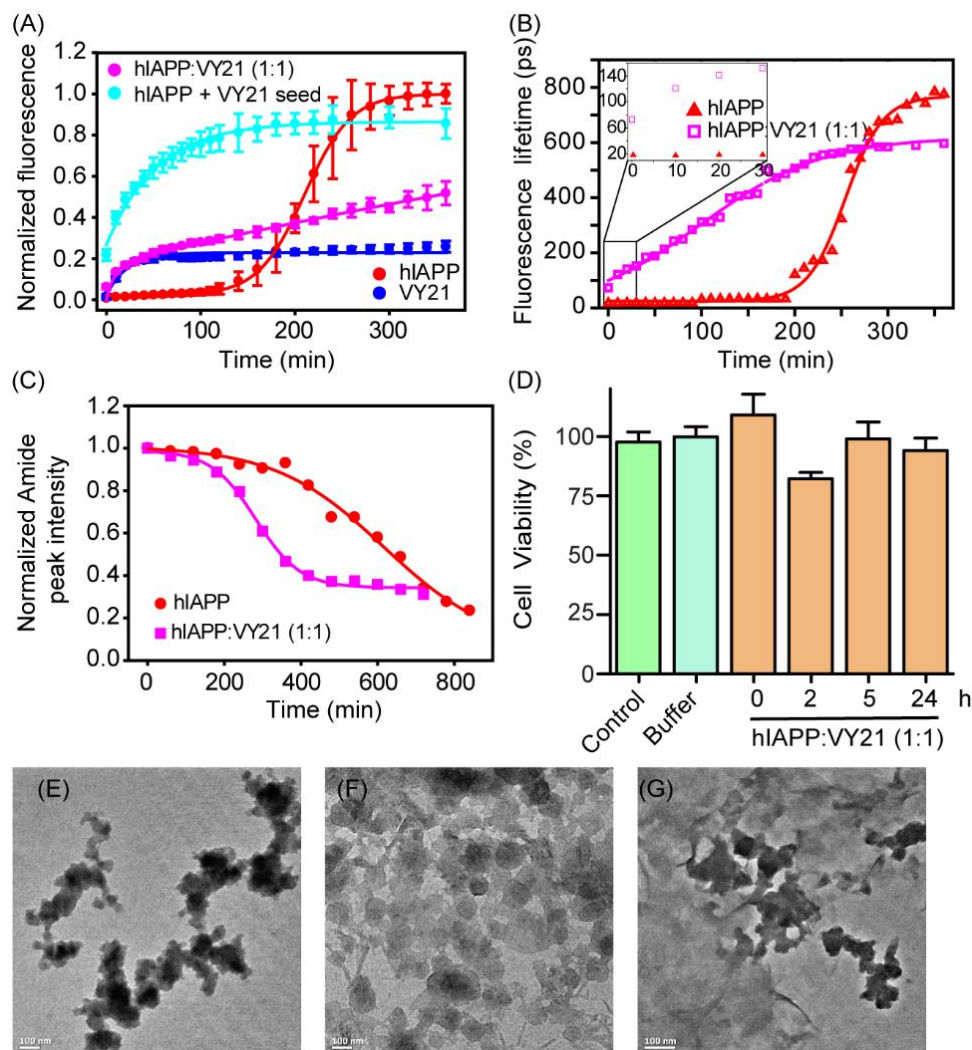
Figure 4.6. (A) ThT fluorescence kinetics of hIAPP (red), VY21 (blue), hIAPP co-incubated with VY21 at a 1:1 molar ratio aggregate (pink), and hIAPP after addition of VY21 oligomers (cyan). (B) Time-resolved fluorescence lifetime kinetics of ThT in presence of hIAPP (red), and hIAPP co-incubated with VY21 at a 1:1 molar ratio aggregate (pink). Inset highlights the initial time points. (C) ^{1}H NMR intensity decay kinetics of hIAPP with VY21 at a 1:1 molar ratio. (D) Cell viability was measured by incubating (10μM) aggregated peptide generated from hIAPP co-incubated with VY21 at a 1:1 molar ratio. Values are represented as mean ± SEM, n=6. TEM images of (E) hIAPP, (F) VY21, and (G) hIAPP co-incubated with VY21 at a 1:1 molar ratio aggregate. All experiments were done at 25 °C, under non-shaking conditions.

sigmoidal type transition for hIAPP was apparent. The time-dependent NMR kinetics suggests that the rate of oligomerization in VY21 is much higher than that of hIAPP. However, the VY21 oligomeric intermediates remains stable unlike hIAPP, which gradually converts into amyloid fibrils within the same experimental time frame.

4.3.8. The C-terminus of hIAPP acts as an enhancer of aggregation

We further examined the effect of VY21 on hIAPP under the same non-shaking conditions. Studying such interaction has also been proven to be effective in developing inhibitory agents for both Aβ and hIAPP.[40] We co-incubated hIAPP and VY21 at a 1:1 molar ratio and measured the time-dependent ThT fluorescence intensity. Interestingly, we observed an initial increase in the ThT intensity with no lag time, suggesting a rapid oligomerization (Figure 4.6A). Possibly, VY21 interacted with the full-length hIAPP and interfered with the hIAPP amyloid formation. Even when added in sub-stoichiometric concentration, VY21 accelerates the hIAPP assembly significantly. Upon increasing the concentration of VY21, a clear decrease in the lag-phase of hIAPP was observed, which signifies the dose-dependency on hIAPP aggregation (Appendix IV, Figure S4.4). Further, VY21 was incubated for 3 h in the presence of ThT, and the hIAPP monomer was then added to check the effect of oligomeric VY21 on the aggregation of hIAPP. As soon as the monomeric hIAPP was added, we observed an exponential increase in the ThT intensity, suggesting that VY21 aggregates act as a seed and drastically accelerate the aggregation process of hIAPP (Figure 4.6A).

Co-incubation of hIAPP with VY21 at a 1:1 molar ratio is also reflected in the disappearance of lag-time of ThT lifetime kinetics as observed in TRF kinetics (Figure 4.6B). We have already discussed the different dependencies of $\langle \tau_{life} \rangle$ and I_{ss}^{f} on K_r and K_{nr}. Because the dependencies of I_{ss}^{f} and $\langle \tau_{life} \rangle$) on K_r and K_{nr} are not the same, slightly different time profiles for $\langle \tau_{life} \rangle$ and I_{ss}^{f} are seen in Figures 4.6A, B. The rate of increase in the ThT lifetime was higher than hIAPP alone, suggesting a higher oligomerization rate of hIAPP in the presence of VY21. The saturation time of ThT lifetime in the co-incubated sample also reached earlier than hIAPP alone. However, the saturating lifetime value was slightly less than that of hIAPP, suggesting a difference in the aggregate structure or size. VY21 thus primarily promotes oligomerization but leads to alteration of mature fibril formation. The average lifetime $\langle \tau_{life} \rangle$ of ThT in hIAPP or the equimolar mixture (hIAPP: VY21=1:1) indicates that the formation of β-sheet during aggregation of hIAPP alone ($\langle \tau_{life} \rangle_{ThT} \sim 776$ ps) is more pronounced than that in the equimolar mixture ($\langle \tau_{life} \rangle_{ThT} \sim 597$ ps).

The effect of VY21 on the aggregation of hIAPP was also monitored by NMR spectroscopy. The monomer depletion plot showed that VY21 induced a sigmoidal decay curve with a higher rate and ~70% decay of signal intensity at the time of saturation (Figure 4.6C). Unlike ThT assay, NMR data showed that monomer intensity decrease is comparatively slow in the initial phase for both hIAPP and co-incubated sample. This may appear to be a lag. However, this 'lag' period is not real because the NMR intensity does decrease with time but at a rate slower than that found in fluorescence measurements. This can be ascribed to interface effects with the container well and air, as well as the influence of ThT as described previously. Qualitatively, however, the NMR data showed similar kinetic profiles to that of ThT fluorescence kinetics. Both data suggested that co-incubation with VY21 greatly influenced the aggregation kinetics of hIAPP.

MTT assay was also performed for the assessment of cytotoxicity of the co-incubated sample at different time points of aggregation. Interestingly, the toxicity profile of the mixed sample at different time points showed significantly reduced cell death as compared to hIAPP alone (Figure 4.6D). The effect of VY21 on the hIAPP pathogenesis was profound only in the 2 h sample, where the cell viability reduced to 18%. This may be attributed to free hIAPP oligomers- still present in the sample solution. Interestingly, at later stages, collected at 5 h and 24 h (similar to hIAPP alone for comparison, Figure 4.2D) of aggregation, where growing protofibrils and fibrils are predominant, we observed almost no cytotoxicity (94-99% cell viability). Thus, VY21 alters the overall fibrillation pathway reducing the concentration of toxic soluble prefibrillar species. Taken together, these findings suggest that under non-shaking conditions at 25 °C, VY21 amplified the rate of fibrillation drastically, playing a rather protective role.

4.3.9. Morphology of aggregated species

Next, we attempted to visualize the morphology of the aggregates generated at 25 °C under non-shaking conditions by employing high-resolution electron microscopy. An array of microscopic imaging was executed to determine the morphological characteristics of the aggregates under examination. Scanning electron microscope (SEM) image confirmed that hIAPP forms amyloid both in the absence and presence of VY21, while VY21 alone did not (Appendix IV, Figure S4.5). High-resolution transmission electron microscope (TEM) images revealed the presence of hIAPP aggregates with an average

width of ~110 ± 43 nm (Figure 4.6E). In contrast, VY21 aggregates were amorphous with few spherical structures with a 203 ± 20 nm diameter (Figure 4.6F). Interestingly, when co-incubated with VY21, the overall fibril density of hIAPP aggregates was less than the hIAPP alone, with an average width of 84 ± 14 nm (Figure 4.6G).

4.4. Discussion

Studying peptide fragments have been promising in understanding the differential behaviour of the full-length peptide, as different regions of an aggregating peptide may be involved in different structural and functional attributes.[41] Previously, Brender et al. showed that the N-terminal hIAPP$_{1-19}$ fragment could disrupt synthetic lipid vesicles to a similar extent as the full-length IAPP peptide without forming amyloid fibers.[42]Our results also indicate that the N-terminal KH18 fragment could not undergo fibrillation; this could possibly be due to the disulphide bond between the two cysteine residues at positions 2 and 7. This conformationally restricts the peptide to adopt β-sheet and may influence the overall propensity to form amyloid fibrils.[43] In contrast, both hIAPP and VY21 showed a time-dependent increase in ThT intensity. Differences in ThT intensity could possibly be either due to the number of ThT accommodations or the different affinity of the ThT binding sites or the difference in quantum yields.[44] The observed difference in ThT fluorescence lifetime between hIAPP and VY21 aggregates suggests that the ThT molecules bound to different aggregates do have different quantum yields.

Misfolding of proteins/peptides may lead to two primary forms of aberrant aggregates: ordered amyloid fibrils and disordered amorphous aggregates.[16, 45] While studying the aggregation kinetics of individual peptides, we observed that for the same peptide, the fibrils formed under agitation differ greatly from those formed under quiescent conditions. Our observation showed that at physiological pH, VY21 could evolve through two distinct pathways, leading to the formation of either disordered or ordered amyloid aggregates. It preferentially forms disordered oligomers at low temperatures under non-shaking conditions, whereas agitation results in the ThT-positive amyloid fibrils. With
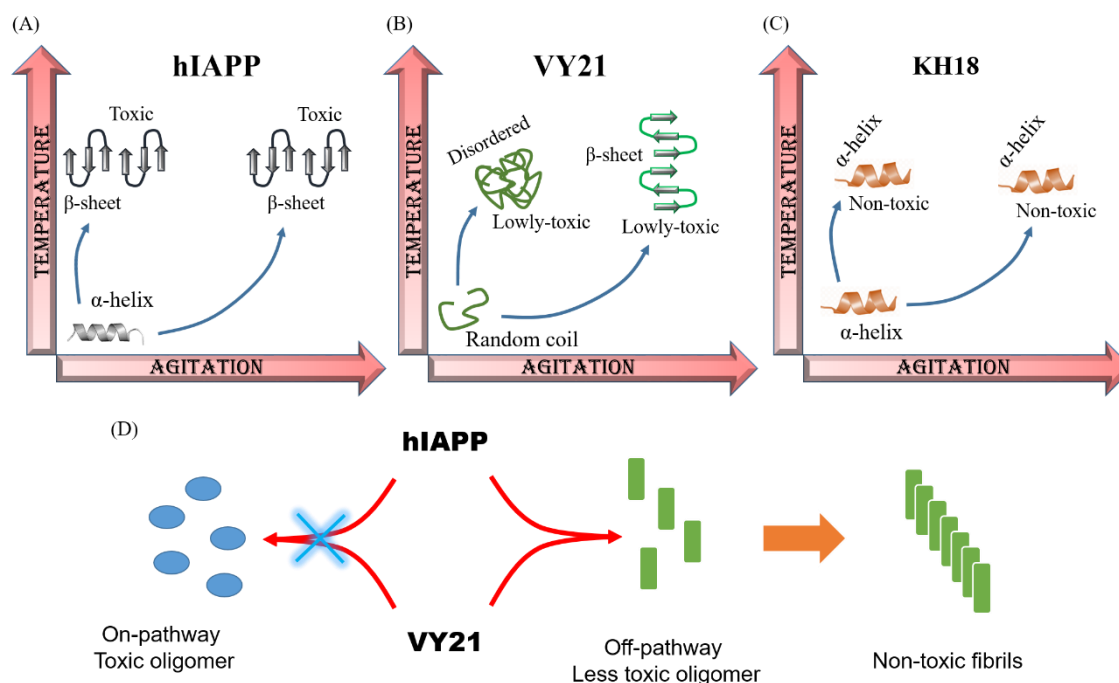
Figure 4.7. Schematic representation illustrating effect of temperature and agitation on the self-assembly of hIAPP, VY21, and KH18. (A) hIAPP undergoes fibrillation under different temperature and agitation conditions, generating toxic fibrils. (B) VY21 can evolve into either disordered oligomer under non-shaking conditions or ordered fibrils under shaking conditions at different temperatures, both cases generating less-toxic species. (C) KH18 remains in helical conformation even at elevated temperature and shaking conditions and are non-toxic in nature. (D) VY21 reduces the presence of toxic hIAPP oligomers by altering the hIAPP fibrillation kinetics which drastically increases the formation of non-toxic fibrils.

respect to the disordered aggregates, the fibril formation requires higher conformational changes, and agitation serves that purpose. Although, amyloid oligomers have been extensively reported in the literature to impart much of the cytotoxicity when compared to the corresponding fibrillar species,[46] to our surprise, VY21 oligomers were not significantly toxic when compared to hIAPP. The disordered conformation of these oligomers (confirmed by CD spectroscopy) may result in reduced toxicity. Moreover, these can form potential seeds that can prompt a cascade of aggregation kinetics, where upon the peptide can either undergo conformational changes or induce changes in dynamic exchange with the monomeric species resulting in differential amyloidosis. Nevertheless, VY21 acts as a scavenger by drastically reducing the availability of toxic soluble hIAPP oligomers. Further, the less toxic oligomers of VY21 proved to be an antagonist of hIAPP oligomers

since no lag phase was observed in the presence of such oligomers. This, in turn, suggests the shortening of lifetime for the toxic hIAPP oligomers. A recent study by Sheena E. Radford and co-workers also reported small molecule accelerator of hIAPP aggregation.[29] However, there are very few studies of such kind. A comprehensive understanding of such accelerated aggregation by small molecules/peptides would pave the way for designing therapeutic interventions in the field of amyloidosis.

Overall, our results indicate that the aggregation of VY21 is more complicated than simply a transition from random coil to β-sheet. It clearly has a diverse and intriguing free-energy landscape with multiple barriers, resulting in different kinds of aggregate and cytotoxicity. However, for full-length hIAPP peptides, the amyloid formation occurred irrespective of temperature or agitation (Figure 4.7). The results suggest that a high free energy barrier of nucleation is decided by the ordered structures of amyloid fibrils and that disordered aggregation occurs promiscuously without a high free energy barrier. The introduction of agitation may influence the conformational transitions of VY21, leading to the exposure of usually buried regions, such as hydrophobic groups. Thus, new intermolecular interaction may come forward, regulating the aggregation process.

The formation of amyloid fibril and disordered aggregates from full-length hIAPP and its C-terminal segment encoded by the VY21 peptide fragment suggests a possible exciting collaboration between the two in the subsequent pathological aggregation propensity of hIAPP. Thus, the $N^{22}FGAIL^{27}$ sequence motif present in the C-terminal segment of hIAPP (VY21) may not be sufficient to undertake amyloid formation under quiescent conditions. The interaction between the C-terminal and the N-terminal segment may influence the aggregation pathway of full-length hIAPP under quiescent conditions.[47] This is interesting, given this alternatively suggests that prevention of this interaction might directly enable efficient therapeutic solution development. Moreover, the ability of VY21 oligomers to act as an enhancer of hIAPP aggregation while reducing overall cytotoxicity makes it a potential target for inhibitor designing.

4.5. Conclusion

We accentuated the significance of the VY21 peptide in generating structurally different oligomers. The introduction of agitation modifies the phase diagram dramatically,

releasing the kinetic trap and establishing the equilibrium determined by the intrinsic solubility of VY21. Even though the disordered oligomers were structurally different, they act as templates for hIAPP, drastically accelerating the aggregation process while reducing the overall fibrillar toxicity. Our findings thus may assist in finding the therapeutics based on the kinetic differences in the aggregation behaviour.

4.6. Appendix IV

Table S4.1. Fitting parameters of ThT fluorescence kinetics at 37 °C, under shaking conditions (250 rpm).

Peptide	hIAPP	VY21
T_{half}	8.45 ± 1.07 min	50.85 ± 1.77 min
t_{lag}	Not determined	18.4 ± 1.6 min

Table S4.2. Fitting parameters of ThT fluorescence kinetics at 25 °C, under shaking conditions (250rpm).

Peptide	hIAPP	VY21
T_{half}	31.73 ± 2.14 min	109.72 ± 18.94 min
t_{lag}	8.41 ± 2.10 min	61.78 ± 18.54 min

Table S4.3. Fitting parameters of time-resolve fluorescence lifetime magic angle (54.7º) decay of 20 µM ThT with 80 µM hIAPP at 25 °C, under non-shaking condition.

Time/min	a_1	τ_1/ps	a_2	τ_2/ps	a_3	τ_3/ps	$<\tau_{life}>$/ps
0	0.99	5	0.005	498	0.005	1851	17
10	0.99	5	0.005	512	0.005	1907	17
20	0.99	5	0.005	551	0.005	1973	18
30	0.99	5	0.005	540	0.005	1970	18
40	0.99	5	0.005	537	0.005	1968	18
50	0.99	5	0.005	510	0.005	1973	17
60	0.99	5	0.005	592	0.005	2058	18
70	0.99	5	0.005	559	0.005	2044	18
80	0.99	5	0.005	585	0.005	2055	18
90	0.99	5	0.005	529	0.005	2034	18
100	0.98	5	0.01	572	0.01	2050	31

110	0.98	6	0.01	577	0.01	2072	32
120	0.98	6	0.01	557	0.01	2042	32
130	0.98	6	0.01	579	0.01	2068	32
140	0.98	6	0.01	595	0.01	2080	33
150	0.98	6	0.01	566	0.01	2077	32
160	0.98	6	0.01	594	0.01	2077	33
170	0.98	6	0.01	574	0.01	2063	32
180	0.98	6	0.01	571	0.01	2042	32
190	0.98	7	0.01	557	0.01	2017	33
200	0.90	14	0.06	511	0.04	1951	121
210	0.88	14	0.07	503	0.05	1921	144
220	0.86	15	0.08	528	0.06	1929	171
230	0.85	14	0.09	515	0.06	1896	172
240	0.81	16	0.12	522	0.07	1889	208
250	0.70	24	0.19	527	0.11	1872	323
260	0.55	53	0.30	614	0.15	1925	502
270	0.50	60	0.34	612	0.16	1908	543
280	0.45	97	0.38	685	0.17	1961	637
290	0.42	108	0.40	697	0.18	1951	675
300	0.40	100	0.40	648	0.20	1887	677
310	0.40	109	0.41	673	0.19	1912	683
320	0.40	148	0.41	737	0.19	1972	736
330	0.41	188	0.42	810	0.17	2028	762
340	0.41	183	0.42	790	0.17	2007	742
350	0.44	224	0.42	907	0.14	2185	785
360	0.46	241	0.42	951	0.12	2217	776

Table S4.4. Fitting parameters of time-resolve fluorescence lifetime magic angle (54.7º) decay of 20 μM ThT with 80 μM VY21 at 25 °C, under non-shaking condition.

Time/min	a_1	τ_1/ps	a_2	τ_2/ps	a_3	τ_3/ps	$<\tau_{life}>$/ps
0	0.61	42	0.31	398	0.08	1278	251
10	0.57	49	0.35	408	0.08	1210	268
20	0.54	57	0.37	410	0.09	1175	288

30	0.52	59	0.39	402	0.09	1163	292
40	0.52	53	0.39	389	0.09	1156	283
50	0.51	53	0.39	381	0.10	1131	289
60	0.49	55	0.41	387	0.10	1147	300
70	0.49	58	0.41	376	0.10	1105	293
80	0.51	75	0.39	420	0.10	1118	313
90	0.54	78	0.36	417	0.10	1127	305
100	0.47	79	0.43	432	0.10	1221	345
110	0.46	75	0.43	410	0.11	1182	341
120	0.46	82	0.43	414	0.11	1187	346
140	0.46	81	0.43	404	0.11	1160	339
160	0.46	77	0.43	412	0.11	1164	341
180	0.45	77	0.44	397	0.11	1155	337
210	0.46	78	0.43	411	0.11	1167	341
240	0.45	72	0.44	389	0.11	1132	328
270	0.45	86	0.44	407	0.11	1147	344
300	0.45	84	0.44	397	0.11	1140	338
330	0.45	85	0.44	405	0.11	1153	343
360	0.45	83	0.44	402	0.11	1138	339

Table S4.5. Fitting parameters of time-resolve fluorescence lifetime magic angle (54.7º) decay of 20 µM ThT with 80 µM of both hIAPP and VY21 (1:1 molar ratio) at 25 °C, under non-shaking condition.

| Time/min	a_1	τ_1/ps	a_2	τ_2/ps	a_3	τ_3/ps	$<\tau_{life}>$/ps
0	0.94	10	0.04	565	0.02	2038	73
10	0.91	13	0.05	581	0.04	1995	121
20	0.90	15	0.05	582	0.05	1975	141
30	0.89	16	0.06	625	0.05	2005	152
40	0.85	17	0.09	574	0.06	1958	184
50	0.85	18	0.09	608	0.06	1989	189
60	0.83	20	0.10	591	0.07	1956	213
70	0.81	21	0.11	612	0.08	1982	243
80	0.80	23	0.12	615	0.08	1968	250

90	0.77	26	0.14	616	0.09	1974	284
100	0.75	27	0.15	624	0.10	1979	312
110	0.74	28	0.16	606	0.10	1954	313
120	0.72	30	0.18	620	0.10	1963	329
130	0.68	35	0.20	694	0.12	1969	399
140	0.66	36	0.21	634	0.13	1917	406
150	0.64	37	0.23	613	0.13	1894	411
160	0.63	38	0.24	607	0.13	1890	415
170	0.60	46	0.26	643	0.14	1905	461
180	0.59	45	0.26	628	0.15	1890	473
190	0.58	48	0.27	639	0.15	1909	487
200	0.55	50	0.30	644	0.15	1911	507
210	0.54	58	0.31	659	0.15	1909	522
220	0.53	60	0.31	670	0.16	1924	547
230	0.52	63	0.32	673	0.16	1925	556
240	0.51	60	0.32	649	0.17	1895	560
250	0.52	65	0.32	691	0.16	1935	564
260	0.50	68	0.33	669	0.17	1900	577
270	0.50	68	0.33	669	0.17	1898	577
280	0.49	70	0.34	695	0.17	1926	598
290	0.49	68	0.34	674	0.17	1898	585
300	0.49	67	0.34	673	0.17	1903	585
330	0.48	70	0.35	672	0.17	1887	590
360	0.48	72	0.36	706	0.16	1924	597

| K_+K_n (M^{-2}min^{-2})	K_+K_2 (M^{-3}min^{-2})	K_M (M^2)
2.2 x 10^2	3.45 x 10^{13}	1.7 x 10^{-13}
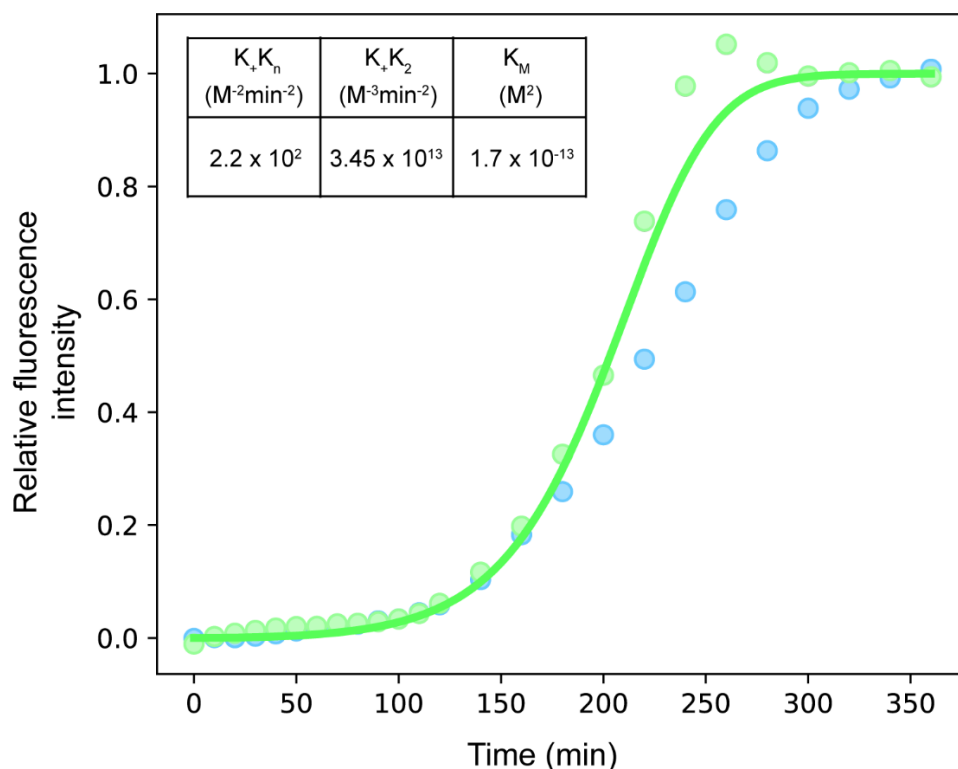
Figure S4.1. Fitting of ThT fluorescence curve of hIAPP at 25 °C under non-shaking conditions using the online platform Amylofit. Inset table shows the combined rate constant for secondary nucleation, k_+k_2, the combined rate constant for primary nucleation, k_+k_n, and the Michaelis constant, K_M, calculated from the fitting.
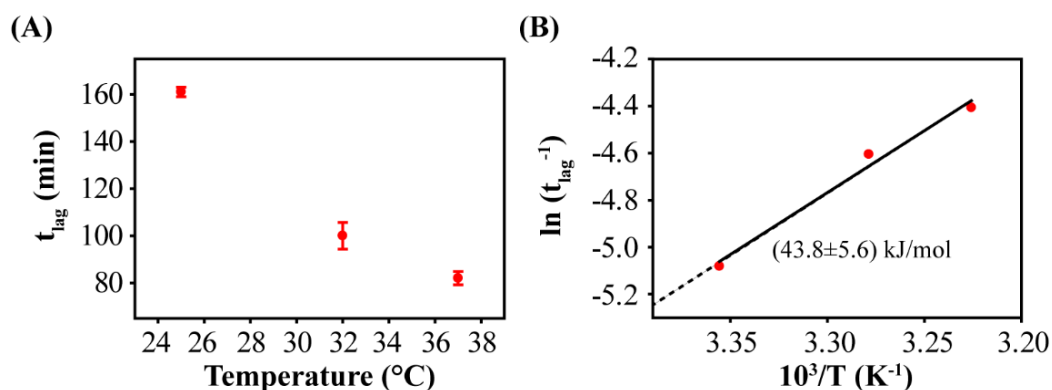

Figure S4.2. (A) Aggregation lag time (t_{lag}) of hIAPP under non-shaking conditions plotted as a function of aggregation reaction temperature. (B) Arrhenius plot of initial elongation rate vs. inverse temperature for 80 µM hIAPP samples. The activation energy calculated from the well fitted (R = 0.99) data was 43.8 ± 5.6 kJ/mol.
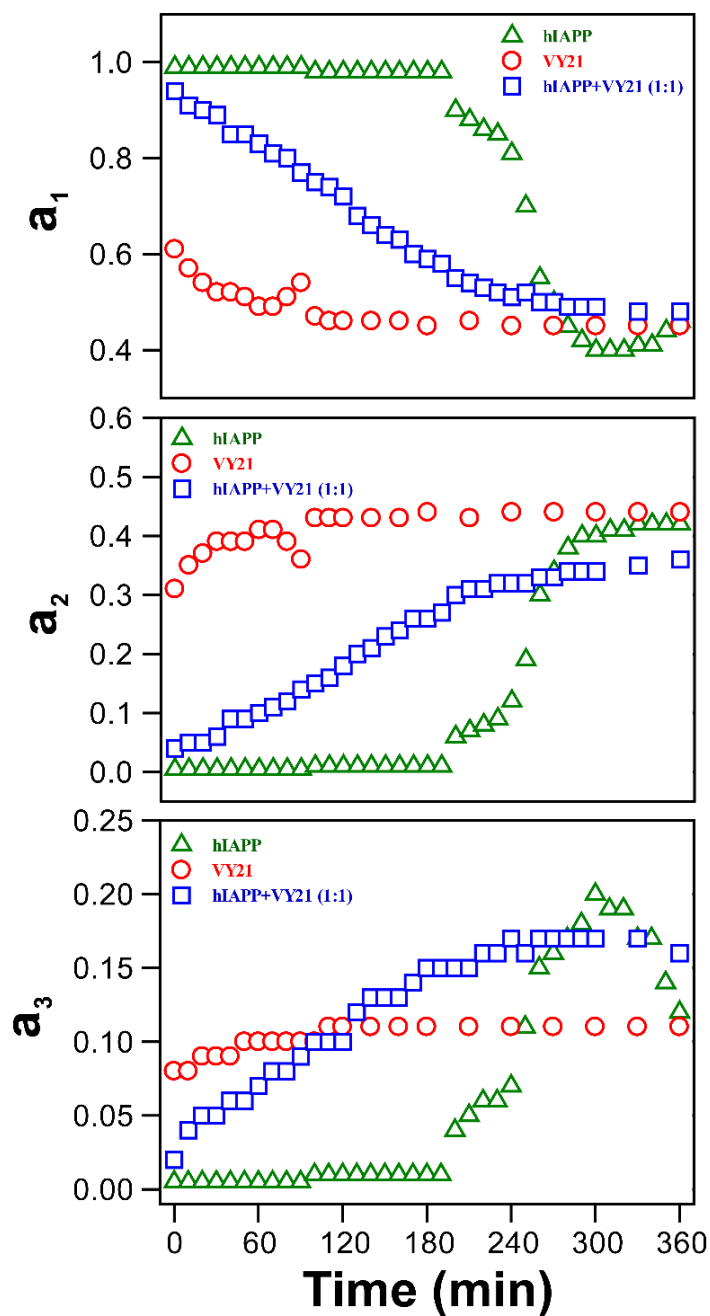
Figure S4.3. Stoichiometry of respective time scale in time-resolved fluorescence average lifetime of ThT with hIAPP, VY21, 1:1 mixture of hIAPP and VY21 (80 µM) in phosphate buffer (20 µM) solution up to 360 min at 25 °C, under non-shaking conditions. All representations are color-coded.
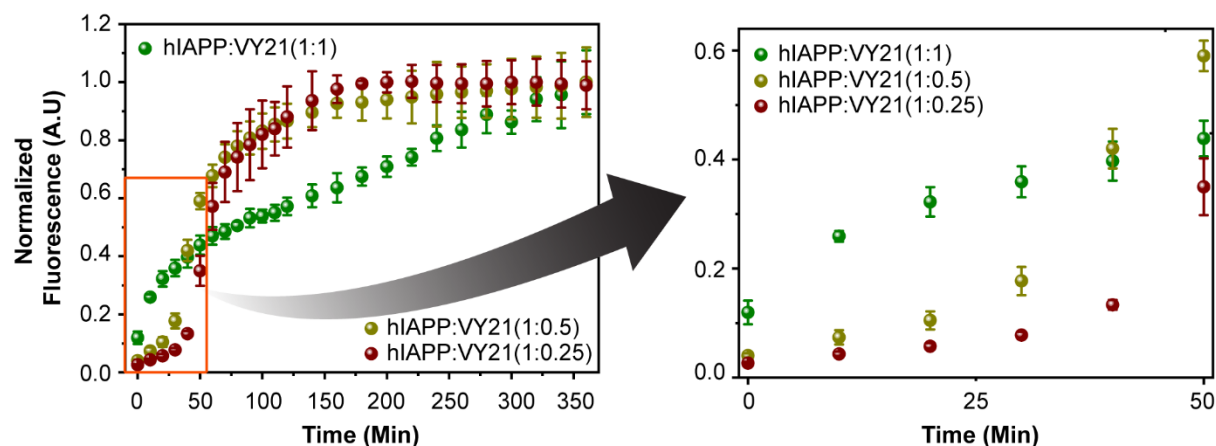
Figure S4.4. ThT fluorescence assay of hIAPP co-incubated with different ratios of VY21. Inset shows the aggregation kinetics of individual samples at the initial phase. With decreasing concentration of VY21, an increase in the lag-time was apparent.
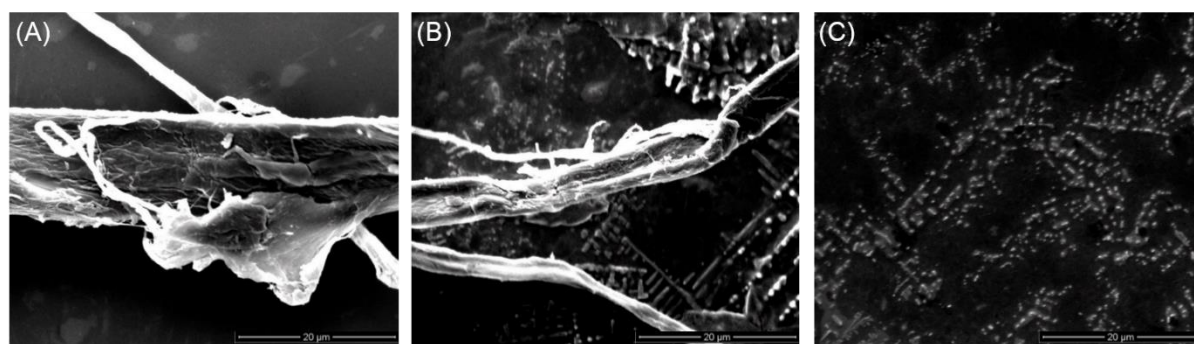
Figure S4.5. SEM images of (A) hIAPP, (B) hIAPP co-incubated with VY21 at a 1:1 molar ratio, and (C) VY21 aggregates at 25 °C, under non-shaking conditions.

4.7. References

[1] F. Chiti, C. M. Dobson, *Annu Rev Biochem* **2017**, 86, 27; A. S. DeToma, S. Salamekh, A. Ramamoorthy, M. H. Lim, *Chem Soc Rev* **2012**, 41, 608; A. Mukherjee, D. Morales-Scheihing, P. C. Butler, C. Soto, *Trends Mol Med* **2015**, 21, 439; M. Zaman, A. N. Khan, Wahiduzzaman, S. M. Zakariya, R. H. Khan, *Int J Biol Macromol* **2019**, 134, 1022; B. Bolognesi, J. R. Kumita, T. P. Barros, E. K. Esbjorner, L. M. Luheshi, D. C. Crowther, M. R. Wilson, C. M. Dobson, G. Favrin, J. J. Yerbury, *ACS Chem Biol* **2010**, 5, 735.
[2] G. J. Cooper, A. C. Willis, A. Clark, R. C. Turner, R. B. Sim, K. B. Reid, *Proc Natl Acad Sci U S A* **1987**, 84, 8628; P. Cao, P. Marek, H. Noor, V. Patsalo, L. H. Tu, H. Wang, A. Abedini, D. P. Raleigh, *FEBS Lett* **2013**, 587, 1106.
[3] D. Raleigh, X. Zhang, B. Hastoy, A. Clark, *J Mol Endocrinol* **2017**, 59, R121; M. S. Fernández, *Cell Calcium* **2014**, 56, 416; S. Bedrood, Y. Li, J. M. Isas, B. G. Hegde, U. Baxa, I. S. Haworth, R. Langen, *J Biol Chem* **2012**, 287, 5235; P. Krotee, J. A. Rodriguez, M. R. Sawaya, D. Cascio, F. E. Reyes, D. Shi, J. Hattne, B. L. Nannenga, M. E. Oskarsson, S. Philipp, S. Griner, L. Jiang, C. G. Glabe, G. T. Westermark, T. Gonen, D. S. Eisenberg, *Elife* **2017**, 6; S. Luca, W. M. Yau, R. Leapman, R. Tycko, *Biochemistry*

2007, 46, 13505; A. Mascioni, F. Porcelli, U. Ilangovan, A. Ramamoorthy, G. Veglia, *Biopolymers* **2003**, 69, 29.

[4] N. N. Louros, P. L. Tsiolaki, A. A. Zompra, E. V. Pappa, V. Magafa, G. Pairas, P. Cordopatis, C. Cheimonidou, I. P. Trougakos, V. A. Iconomidou, S. J. Hamodrakas, *Biopolymers* **2015**, 104, 196.

[5] J. J. Wiltzius, S. A. Sievers, M. R. Sawaya, D. Eisenberg, *Protein Sci* **2009**, 18, 1521.

[6] E. T. Jaikaran, C. E. Higham, L. C. Serpell, J. Zurdo, M. Gross, A. Clark, P. E. Fraser, *J Mol Biol* **2001**, 308, 515.

[7] L. A. Scrocchi, K. Ha, Y. Chen, L. Wu, F. Wang, P. E. Fraser, *J Struct Biol* **2003**, 141, 218.

[8] M. R. Nilsson, D. P. Raleigh, *J Mol Biol* **1999**, 294, 1375.

[9] P. Westermark, U. Engström, K. H. Johnson, G. T. Westermark, C. Betsholtz, *Proc Natl Acad Sci U S A* **1990**, 87, 5036; C. Goldsbury, K. Goldie, J. Pellaud, J. Seelig, P. Frey, S. A. Müller, J. Kistler, G. J. Cooper, U. Aebi, *J Struct Biol* **2000**, 130, 352.

[10] K. Tenidis, M. Waldner, J. Bernhagen, W. Fischle, M. Bergmann, M. Weber, M. L. Merkle, W. Voelter, H. Brunner, A. Kapurniotu, *J Mol Biol* **2000**, 295, 1055.

[11] W. Hoffmann, K. Folmert, J. Moschner, X. Huang, H. von Berlepsch, B. Koksch, M. T. Bowers, G. von Helden, K. Pagel, *J Am Chem Soc* **2018**, 140, 244; M. Tatarek-Nossol, L. M. Yan, A. Schmauder, K. Tenidis, G. Westermark, A. Kapurniotu, *Chem Biol* **2005**, 12, 797; C. Wu, H. Lei, Y. Duan, *Biophys J* **2004**, 87, 3000.

[12] D. Sarkar, I. Chakraborty, M. Condorelli, B. Ghosh, T. Mass, M. Weingarth, A. K. Mandal, C. La Rosa, V. Subramanian, A. Bhunia, *ChemMedChem* **2020**, 15, 293.

[13] A. Gupta, S. Dey, D. Bhowmik, S. Maiti, *J Phys Chem B* **2022**, 126, 1016.

[14] M. Miyazato, M. Nakazato, K. Shiomi, J. Aburaya, K. Kangawa, H. Matsuo, S. Matsukura, *Diabetes Res Clin Pract* **1992**, 15, 31.

[15] W. Wang, S. Nema, D. Teagarden, *Int J Pharm* **2010**, 390, 89.

[16] Y. Yoshimura, Y. Lin, H. Yagi, Y. H. Lee, H. Kitayama, K. Sakurai, M. So, H. Ogi, H. Naiki, Y. Goto, *Proc Natl Acad Sci U S A* **2012**, 109, 14446.

[17] I. Chakraborty, R. K. Kar, D. Sarkar, S. Kumar, N. C. Maiti, A. K. Mandal, A. Bhunia, *ACS Chem Neurosci* **2021**, 12, 2903; J. Zhang, J. Tan, R. Pei, S. Ye, *Langmuir* **2020**, 36, 1530; J. R. Brender, K. Hartman, R. P. Nanga, N. Popovych, R. de la Salud Bea, S. Vivekanandan, E. N. Marsh, A. Ramamoorthy, *J Am Chem Soc* **2010**, 132, 8973; K. Klement, K. Wieligmann, J. Meinhardt, P. Hortschansky, W. Richter, M. Fändrich, *J Mol Biol* **2007**, 373, 1321.

[18] S. Bera, N. Gayen, S. A. Mohid, D. Bhattacharyya, J. Krishnamoorthy, D. Sarkar, J. Choi, N. Sahoo, A. K. Mandal, D. Lee, A. Bhunia, *ACS Chem Neurosci* **2020**, 11, 1965.

[19] E. van Dijk, A. Hoogeveen, S. Abeln, *PLoS Comput Biol* **2015**, 11, e1004277; C. Camilloni, D. Bonetti, A. Morrone, R. Giri, C. M. Dobson, M. Brunori, S. Gianni, M. Vendruscolo, *Sci Rep* **2016**, 6, 28285.

[20] G. Wei, Z. Su, N. P. Reynolds, P. Arosio, I. W. Hamley, E. Gazit, R. Mezzenga, *Chem Soc Rev* **2017**, 46, 4661; M. Bhattacharya, N. Jain, S. Mukhopadhyay, *J Phys Chem B* **2011**, 115, 4195.

[21] A. T. Petkova, R. D. Leapman, Z. Guo, W. M. Yau, M. P. Mattson, R. Tycko, *Science* **2005**, 307, 262; A. K. Paravastu, A. T. Petkova, R. Tycko, *Biophys J* **2006**, 90, 4618; S. Campioni, G. Carret, S. Jordens, L. Nicoud, R. Mezzenga, R. Riek, *J Am Chem Soc* **2014**, 136, 2866.

[22] K. G. Varnava, S. A. Mohid, P. Calligari, L. Stella, J. Reynison, A. Bhunia, V. Sarojini, *Bioconjug Chem* **2019**, 30, 1998.

[23] R. Biswas, A. R. Das, T. Pradhan, D. Touraud, W. Kunz, S. Mahiuddin, *J Phys Chem B* **2008**, 112, 6620.

[24] D. Bhattacharyya, R. Kumar, S. Mehra, A. Ghosh, S. K. Maji, A. Bhunia, *Chem Commun (Camb)* **2018**, 54, 3605; H. LeVine, *Methods Enzymol* **1999**, 309, 274.

[25] B. N. Ratha, A. Ghosh, J. R. Brender, N. Gayen, H. Ilyas, C. Neeraja, K. P. Das, A. K. Mandal, A. Bhunia, *J Biol Chem* **2016**, 291, 23545.

[26] T. Mosmann, *J Immunol Methods* **1983**, 65, 55.

[27] A. Tiiman, A. Noormägi, M. Friedemann, J. Krishtal, P. Palumaa, V. Tõugu, *J Pept Sci* **2013**, 19, 386.

[28] G. Meisl, J. B. Kirkegaard, P. Arosio, T. C. Michaels, M. Vendruscolo, C. M. Dobson, S. Linse, T. P. Knowles, *Nat Protoc* **2016**, 11, 252.

[29] Y. Xu, R. Maya-Martinez, N. Guthertz, G. R. Heath, I. W. Manfield, A. L. Breeze, F. Sobott, R. Foster, S. E. Radford, *Nat Commun* **2022**, 13, 1040.

[30] Y. Kusumoto, A. Lomakin, D. B. Teplow, G. B. Benedek, *Proc Natl Acad Sci U S A* **1998**, 95, 12277.

[31] P. K. Singh, M. Kumbhakar, H. Pal, S. Nath, *J Phys Chem B* **2010**, 114, 2541.

[32] V. I. Stsiapura, A. A. Maskevich, V. A. Kuzmitsky, V. N. Uversky, I. M. Kuznetsova, K. K. Turoverov, *J Phys Chem B* **2008**, 112, 15893.

[33] S. K. Saha, P. Purkayastha, A. B. Das, S. Dhara, *Journal of Photochemistry and Photobiology A: Chemistry* **2008**, 199, 179.

[34] A. I. Sulatskaya, A. A. Maskevich, I. M. Kuznetsova, V. N. Uversky, K. K. Turoverov, *PLoS One* **2010**, 5, e15385.

[35] P. K. Singh, M. Kumbhakar, H. Pal, S. Nath, *Phys Chem Chem Phys* **2011**, 13, 8008.

[36] J. R. Lakowicz, *Principles of fluorescence spectroscopy*, Springer, **2006**.

[37] P. Bharadwaj, T. Solomon, B. R. Sahoo, K. Ignasiak, S. Gaskin, J. Rowles, G. Verdile, M. J. Howard, C. S. Bond, A. Ramamoorthy, R. N. Martins, P. Newsholme, *Sci Rep* **2020**, 10, 10356.

[38] L. Jean, C. F. Lee, D. J. Vaux, *Biophys J* **2012**, 102, 1154.

[39] M. D'Amico, M. G. Di Carlo, M. Groenning, V. Militello, V. Vetri, M. Leone, *J Phys Chem Lett* **2012**, 3, 1596.

[40] L. O. Tjernberg, C. Lilliehöök, D. J. Callaway, J. Näslund, S. Hahne, J. Thyberg, L. Terenius, C. Nordstedt, *J Biol Chem* **1997**, 272, 12601; D. J. Gordon, K. L. Sciarretta, S. C. Meredith, *Biochemistry* **2001**, 40, 8237; L. A. Scrocchi, Y. Chen, S. Waschuk, F. Wang, S. Cheung, A. A. Darabie, J. McLaurin, P. E. Fraser, *J Mol Biol* **2002**, 318, 697; A. Ghosh, A. S. Pithadia, J. Bhat, S. Bera, A. Midya, C. A. Fierke, A. Ramamoorthy, A. Bhunia, *Biochemistry* **2015**, 54, 2249.

[41] R. Akter, P. Cao, H. Noor, Z. Ridgway, L. H. Tu, H. Wang, A. G. Wong, X. Zhang, A. Abedini, A. M. Schmidt, D. P. Raleigh, *J Diabetes Res* **2016**, 2016, 2798269; S. M. Ulamec, D. J. Brockwell, S. E. Radford, *Front Neurosci* **2020**, 14, 611285.

[42] J. R. Brender, E. L. Lee, M. A. Cavitt, A. Gafni, D. G. Steel, A. Ramamoorthy, *J Am Chem Soc* **2008**, 130, 6424.

[43] B. W. Koo, A. D. Miranker, *Protein Sci* **2005**, 14, 231.

[44] M. Biancalana, S. Koide, *Biochim Biophys Acta* **2010**, 1804, 1405; M. Ziaunys, A. Sakalauskas, V. Smirnovas, *Biomacromolecules* **2020**, 21, 4989; A. I. Sulatskaya, N. P. Rodina, M. I. Sulatsky, O. I. Povarova, I. A. Antifeeva, I. M. Kuznetsova, K. K. Turoverov, *Int J Mol Sci* **2018**, 19.

[45] M. Stefani, S. Rigacci, *Int J Mol Sci* **2013**, 14, 12411.

[46] C. G. Glabe, *J Biol Chem* **2008**, 283, 29639; S. J. Lee, E. Nam, H. J. Lee, M. G. Savelieff, M. H. Lim, *Chem Soc Rev* **2017**, 46, 310; B. Mannini, E. Mulvihill, C. Sgromo, R. Cascella, R. Khodarahmi, M. Ramazzotti, C. M. Dobson, C. Cecchi, F. Chiti, *ACS Chem Biol* **2014**, 9, 2309.

[47] S. M. Vaiana, R. B. Best, W. M. Yau, W. A. Eaton, J. Hofrichter, *Biophys J* **2009**, 97, 2948.

Chapter V

Application of Singular Value Decomposition Analysis: Insights into the Complex Mechanisms of Amyloidogenesis

This chapter has been adapted from the following publications:

(A) **Sarkar, D.**, Saha, S., Krishnamoorthy, J. and Bhunia, A., 2023. Application of singular value decomposition analysis: Insights into the complex mechanisms of amyloidogenesis. *Biophysical Chemistry*, p.107157.

(B) Paul, A., Kumar, S., Kalita, S., Kalita, S., **Sarkar, D**., Bhunia, A., Bandyopadhyay, A., Mondal, A.C. and Mandal, B., 2021. An explicitly designed paratope of amyloid-β prevents neuronal apoptosis in vitro and hippocampal damage in rat brain. *Chemical Science*, *12*(8), pp.2853-2862.

5.1. Introduction

Protein misfolding and subsequent amyloid accumulation is associated with a variety of human disorders, including Alzheimer's, Parkinson's, and type 2 diabetes, among others.[1] Understanding the mechanisms that underlie amyloidogenesis is of utmost significance,[2] given the increasing prevalence of these disorders and their profound impact on human health.[3] Typically, the process of amyloidogenesis involves an array of steps that results in the self-association of unfolded or partially folded protein/peptides, which eventually leads to the development of β-sheet rich mature fibrils.[4] Initially, during lag phase, the monomers undergo conformational transitions that give rise to oligomeric intermediates. These short-lived structures rapidly evolve into proto-fibrillar species during an exponential growth phase, eventually giving rise to well-defined fibrillar structures. Another key aspect to this multifaceted disorders is the process of seeded growth, where pre-existing aggregates catalyze the assembly of new fibrils.[5] This process not only underscores how aggregates act as templates but also highlights their ability in propagating pathological protein assembly.[6] The interplay between different amyloid proteins or their fragments are equally significant, which shapes the diverse landscapes of amyloid disorders, from structural diversity to complex aggregation pathways.[7] Additionally, amyloidogenic peptide's ability to interact with cellular membranes has also created significant attention as a pivotal step in the progression of amyloidosis.[8] While recent experimental findings have shifted the focus towards the crucial role played the oligomeric intermediates in cellular toxicity, the effect of lipid bilayer in this regard is quite diverse. Depending on the lipid compositions, cell membrane can accelerate or modulates aggregation rate and results in structural polymorphism. However, the intrinsic ability of toxic oligomers in disrupting lipid bilayer or in forming ion-channel-like pores that eventually leads to cellular dysfunction appears to be most striking.[9] Nonetheless, the intricate interplay between processes like self-assembly, cross-

assembly, seeded growth, and membrane-mediated structural transition, collectively drives the progression of amyloid disorders.[10]

In recent years, the application of advanced analytical techniques has provided novel insights into the molecular events that drive amyloidogenesis. Singular Value Decomposition (SVD) analysis, a powerful mathematical tool for extracting patterns from complex datasets, has emerged as an invaluable approach to unravel intricate relationships within experimental data. By decomposing data matrices, SVD reveals primary modes of variation, and illuminate hidden mechanisms. In addition, SVD has proven its utility in a wide range of scientific domains. It has been employed to analyze spectral data of protein folding and ligand binding to macromolecules. Equilibrium unfolding data collected from far-UV CD, intrinsic fluorescence, and Small-Angle X-ray Scattering have been subjected to SVD analysis to determine the number of states associated with the equilibrium unfolding of many proteins.[11] SVD has also identified the mechanisms and refined the time-independent structural intermediates from time-resolved experimental crystallographic data.[12] In the field of large-scale gene expression data analysis, SVD has shown promising results as well.[13] Furthermore, SVD-based low-rank denoising has enhanced signal-to-noise ratios and quantified undetectable peaks in metabolomics studies.[14] In the context of biomolecular interactions, SVD has been instrumental in revealing insights. It has been applied to two-dimensional NMR datasets to map allosteric interaction networks within protein-ligand complexes.[15] The binding of intrinsically disordered p53 transactivation subdomains with the TAZ2 domain of CBP has been characterized through SVD analysis.[16] However, the application of SVD in amyloid disorder largely remains unexplored.

In this chapter, we focus on application of SVD in elucidating the interactions between amyloidogenic peptide and cellular membranes mimic, as well as the complex process of peptide self-assembly, co-assembly, and seeded amyloid growth. By combining circular dichroism (CD) spectroscopy to probe peptide-membrane interactions and nuclear magnetic resonance (NMR) spectroscopy to study the peptide aggregation kinetics, we aim to dissect the intricate dynamics involved in amyloid disorders. Moreover, by providing a comprehensive roadmap of SVD analysis, this study contributes to a deeper understanding of amyloidogenesis mechanisms.

5.2. Materials and methods

5.2.1. Preparation of TLBE LUVs

TLBE lipid films were first prepared by drying the stock solution in chloroform under continuous N_2 flow. The dried films were then rehydrated in 20 mM phosphate buffer (pH 7.4) containing 50 mM NaCl. This was followed by several cycles of freeze-thaw and vigorous vertexing (at least 5 times). The resulted suspension was then extruded through a 100 nm polycarbonate nucleopore membrane filter (Whatman) for a minimum of 23 times using a mini-extruder set up (Avanti polar lipids) to prepare a homogeneous lipid vesicle solution.

5.2.2. Circular Dichroism (CD) Spectroscopy

CD measurements were conducted using a Jasco J-815 spectrophotometer, employing a quartz cuvette with a path length of 0.1 cm. AV20 at a concentration of 80 μM were titrated with Total Lipid Brain Extract (TLBE) Large Unilamellar Vesicles (LUVs) in a 20 mM phosphate buffer (pH 7.4) containing 50 mM NaF. This titration process covered a lipid/peptide ratio ranged from 0 to 9. Readings were promptly taken following each titration step, employing a wavelength range of 195-260 nm and a scan rate of 100 nm/min. Each spectrum depicted in the plot is an average of three scans.

5.2.3. Nuclear Magnetic Resonance (NMR) Spectroscopy experiments

NMR experiments were performed on a Bruker Avance III 500 MHz NMR spectrometer equipped with a 5 mm SMART probe. Prior to adding a fibril seed to the NMR tube containing monomeric Aβ40, a 2D band-Selective Optimized-Flip-Angle Short Transient (SOFAST) heteronuclear multiple quantum coherence (HMQC) spectrum was acquired to compare differences immediately before and after titration with fibrillar Aβ. Resonance assignments of the monomer 2D ^{1}H/^{15}N HMQC spectra were taken from the literature. To monitor Aβ40 aggregation with atomic resolution, real-time 2D NMR experiments were performed by consecutively acquiring ^{1}H-^{15}N SOFAST-HMQC spectra. Each ^{1}H-^{15}N SOFASTHMQC spectrum was obtained from 64 t_1 experiments, 48 scans, 8 dummy scans, and a 0.1 s recycle delay. The spectral widths were 12 and 26 ppm, and the offsets were 4.7 and 118 ppm for the proton and nitrogen dimensions, respectively. Spectral intensities for selected amino acids were plotted against time for both before and after SVD operation and fitted using exponential decay equation:

$$y = A_1 * exp\ (-x/t_1) + y_0$$

To determine the half-life of aggregation from the V component of SVD analysis, Boltzmann equation was used which is as follows

$$Y = Y_0 + (Y_{max} - Y_0)/(1 + exp\,((t - t_{1/2}/b))$$

Where the half-life $t_{1/2}$ is the time required to reach half of the aggregation saturation, b is the apparent first-order constant.

The lag-time (t_{lag}) of amyloid kinetics was determined as $(t_{1/2} - 2b)$.

The aggregation rate can be obtained as $1/t_{lag}$.

Similarly, the structural insight into the atomic level interaction between Aβ40 and SP1 was obtained from 2D SOFAST-HMQC NMR experiment with 48 scans and eight dummy scans at 283 K for each titration of SP1 to uniformly 15N labeled Aβ40. The spectral width was fixed to 12 and 28 ppm, with the offset at 4.7 ppm and 118 ppm, respectively for proton and nitrogen dimensions. Topspin 3.1 (Bruker Biospin software suite) and SPARKY 3.113 software (UCSF) were used for processing and analysis, respectively, of 2D spectra using previously available assignments for Aβ40 as a guide.

5.2.4. R-code for generating simulated dataset

```
#Script for generating simulated data matrix with specified row, column, and using specified
equation – by Dibakar Sarkar
# Set the working directory
setwd("path")
# Set the matrix dimensions
num_rows <- 16
num_cols <- 39
# Set the time points (column headers)
time <- 0:(num_rows - 1)
# Set the residues (row headers)
residues <- 1:num_cols
# Function to generate well-fitted values
generate_values <- function(x, A1, x0, t1) {
  return(A1 * exp(-(x - x0) / t1))
}
# Function to generate noisy values
generate_noisy_values <- function(x, A1, x0, t1, noise_sd) {
```

```r
  true_value <- generate_values(x, A1, x0, t1)
  noisy_value <- true_value + rnorm(1, mean = 0, sd = noise_sd)
  return(noisy_value)
}
# Initialize lists to store parameters for each column
A1_list <- vector("numeric", length = num_cols)
x0_list <- vector("numeric", length = num_cols)
t1_list <- vector("numeric", length = num_cols)
# Generate parameters for each column
for (j in 1:num_cols) {
  if (j <= 10) {
    A1_list[j] <- runif(1, min = 50, max = 100)
    t1_list[j] <- runif(1, min = 1, max = 5)
  } else if (j <= 20) {
    A1_list[j] <- runif(1, min = 20, max = 50)
    t1_list[j] <- runif(1, min = 5, max = 10)
  } else {
    A1_list[j] <- runif(1, min = 5, max = 20)
    t1_list[j] <- runif(1, min = 10, max = 20)
  }
  x0_list[j] <- runif(1, min = 0, max = num_rows - 1)
}
# Set the standard deviation of the noise
noise_sd <- 0.1  # You can adjust this value to control the amount of noise
# Generate the matrix with noisy values
noisy_matrix_data <- matrix(NA, nrow = num_cols, ncol = num_rows)
for (i in 1:num_cols) {
  for (j in 1:num_rows) {
    A1 <- A1_list[i]
    x0 <- x0_list[i]
    t1 <- t1_list[i]
```

```
    noisy_value_at_time_0 <- generate_noisy_values(0, A1, x0, t1, noise_sd)

    noisy_value <- generate_noisy_values(time[j], A1, x0, t1, noise_sd)

    noisy_normalized_value <- noisy_value / noisy_value_at_time_0

    noisy_matrix_data[i, j] <- noisy_normalized_value

  }

}

# Add headers to the matrix

rownames(noisy_matrix_data) <- residues

colnames(noisy_matrix_data) <- time

# Save the noisy_matrix_data as a CSV file

noisy_csv_filename <- "noisy_simulated_matrix.csv"

write.csv(noisy_matrix_data, file = noisy_csv_filename)

cat("Noisy matrix data saved as 'noisy_simulated_matrix.csv' in the working directory.\n")
```

5.2.5. Data Collection and Preprocessing

Data collected either from CD spectroscopy or NMR spectroscopy were first arranged in a matrix format. The first column must be the x values (e.g., wavelength for CD spectra and chemical shift or residues for NMR spectra). Several columns can follow for individual experiments that correspond to the elements of first row, where the first row contains the concentration ratios for CD or time for NMR.

5.2.6. Singular Value Decomposition (SVD)

We have taken the above-mentioned datasets as A matrix, where A is an M × N matrix of real-valued data with rank r. As depicted in Figure 1, the equation for singular value decomposition of A is as follows:

Figure 5.1. Graphical representation of SVD of matrix A.

$A = USV^T$

Where U is an M × N matrix whose columns are the left singular vectors, Ui; S is an N × N diagonal matrix, whose elements are called singular values, Si; and V^T (transpose of V matrix) is also an N × N matrix, whose rows are the right singular vectors, Vi. By convention, the ordering of the singular vectors is determined by high-to-low sorting of singular values, with the highest singular value in the upper left index of the S matrix.

After performing the SVD analysis of matrix data, the singular value plot and right singular value plot are generated from where the 'K-value' can be acquired. The 'K-value' represents the number of non-noise components in the dataset and estimated by taking into account (1) the significance of singular values, (2) smooth shape of the Vi vectors and their high auto-correlation, and (3) a small root-mean-square-deviation (RMSD) between the reconstructed matrix and the raw dataset. After estimation of the number of noise-free components, data matrix was reconstructed using only the noise-free components and discarding the noise components. Ui represents the ith principal component of A, and Vi determines the contribution of an individual dataset (i = 1···N) to each principal component.

5.3. Results & Discussion

5.3.1. Model systems

To underscore the potential of the Singular Value Decomposition (SVD) analysis in elucidating the multifaceted mechanisms of amyloidogenesis, we adopted three intricate model system. These systems were chosen to demonstrate both the complexity of amyloid-related processes and the ability of SVD analysis to uncover crucial information.

Our first model system explores the membrane-mediated structural transitions within amyloidogenic peptides. In this context, we centered our investigation on AV20 (AV20:

Peptide	Sequence
Aβ40	DAEFRHDSGYEVHHQKLVFFAEDVGSNKGAIIGLMVGGVV
AV20	AEDVGSNKGAIIGLMVGGVV
hIAPP	KCNTATCATQRLANFLVHSSNNFGAILSSTNVGSNTY
VY21	VHSSNNFGAILSSTNVGSNTY

Table 5.1. Amino acid sequence of the peptides under investigation.

A^{21}EDVGSNKGAIIGLMVGGVV^{40}), a C-terminal 20 residues fragment from Amyloid-β 40 (Aβ40) peptide (Table 5.1). AV20 is an intrinsically disordered peptide that has recently been reported to exhibit a toxicity profile similar to that of Aβ40.[17] Notably, the presence of GxxxG motifs within this fragment has sparked interest due to their potential role in modulating amyloidogenic propensity and neurotoxicity.[17, 18] While it is well-established that Aβ-membrane interactions can profoundly impact the aggregation pathway, the underlying molecular mechanisms remain elusive. The interaction between Aβ and cellular membranes triggers conformational changes in the peptide's secondary structure, influencing the fibrillation process.[19] Moreover, cell membrane disruption plays a crucial role in Aβ neurotoxicity.[20] In this context, CD spectroscopy has proven valuable in monitoring membrane-assisted secondary structural changes in amyloidogenic peptides.[21] Yet, the intricate nature of these peptide-membrane interactions often obscures the identification of key intermediates or steps involved in the process. Thus, the application of SVD analysis to this system emerges as a valid choice, and offer a comprehensive understanding of the complex interplay between AV20 and a neuronal membrane mimic: total lipid brain extract (TBLE). The composition of TBLE includes Phosphatidylcholine (PC), Phosphatidylethanolamine (PE), phosphatidylinositol (PI), Phosphatidylserine (PS). However, more than 55% of the lipids in TBLE are unknown, which includes glycolipids, gangliosides, brain ceramides, cerebrosides, sterols, sphingolipids, lipoproteins, and isoprenoids. Each of these lipid components are crucial for Aβ-membrane interaction, making TBLE a physiologically relevant neuronal membrane interface.

To further validate the versatility of SVD analysis, we explored several other distinct systems: the self-assembly of hIAPP, the co-assembly of hIAPP in presence of hIAPP$_{17-37}$ (VY21: V^{21}HSSNNFGAILSSTNVGSNTY^{37}), and the seeded growth of Aβ40 fibrils. Self-assembly of amyloidogenic peptides have been a key contributor underlying amyloid formation. Here, we utilized the power of 1D-^{1}H NMR to monitor the monitor loss kinetics as a potential dataset for SVD analysis. Furthermore, the interactions between monomers and the surfaces of amyloid fibers can redirect the aggregation pathway, influencing kinetics and generating potentially toxic species. Despite their significance, many questions persist about the molecular determinants governing fiber-monomer interactions. In this context, we utilized the broadening of NMR peaks due to exchanges between unbound Aβ40 and fiber-associated monomers within a sample seeded with amyloid fibers. Leveraging the capabilities of the SOFAST-HMQC experiment, which enables
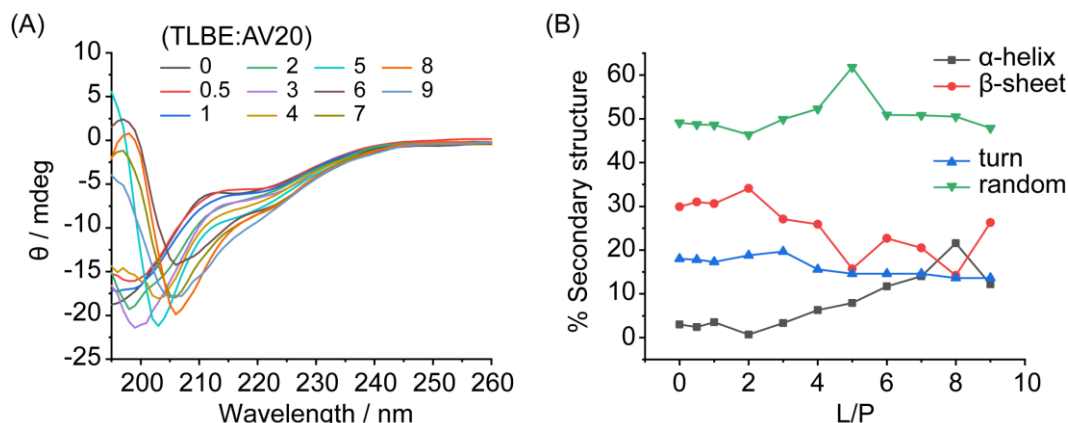
Figure 5.2. (A) CD spectra of AV20 in the absence and presence of neuronal membrane mimic TLBE LUVs at different molar ratios. The concentration of AV20 was ~80 µM. (B) Deconvolution of these CD spectra using the online server BeStSel, revealing the calculated percentage of secondary conformation during structural transition. All spectra are color-coded for clarity.

atomic-resolution monitoring of Aβ aggregation without the temporal constraints of traditional 2D NMR experiments, we obtained residue-specific insights into the kinetic processes of fibril assembly. We aim to employ SVD analysis to identify distinct spectral modes closely tied to the dynamics of seeded fibril growth.

Overall, the integration of SVD analysis with these diverse model systems allows us to unravel the hidden intricacies of amyloidosis mechanisms and offers a comprehensive view of the processes governing amyloid aggregation.

5.3.2. Membrane-mediated structural transition of the C-terminal Aβ40 fragment (AV20) into helical conformations

In a recent study, our investigation revealed that while the initial interaction between Aβ40 and total lipid brain extract (TLBE) did not induce immediate changes in peptide conformation, a subsequent time-dependent transition towards helical intermediates highlighted a membrane-induced transient folding of the peptide backbone.[22] Here, using CD spectroscopy, we observed the interaction between TLBE and the C-terminal Aβ40 fragment (AV20), which contains the well-known "GxxxG" motifs. Figure 5.2A shows the CD spectra of AV20 in the absence and presence of varying concentrations of TLBE large unilamellar vesicles (LUVs). Initially, CD spectra of free AV20 exhibited a negative minimum around 195 nm, representative of random coil conformation.
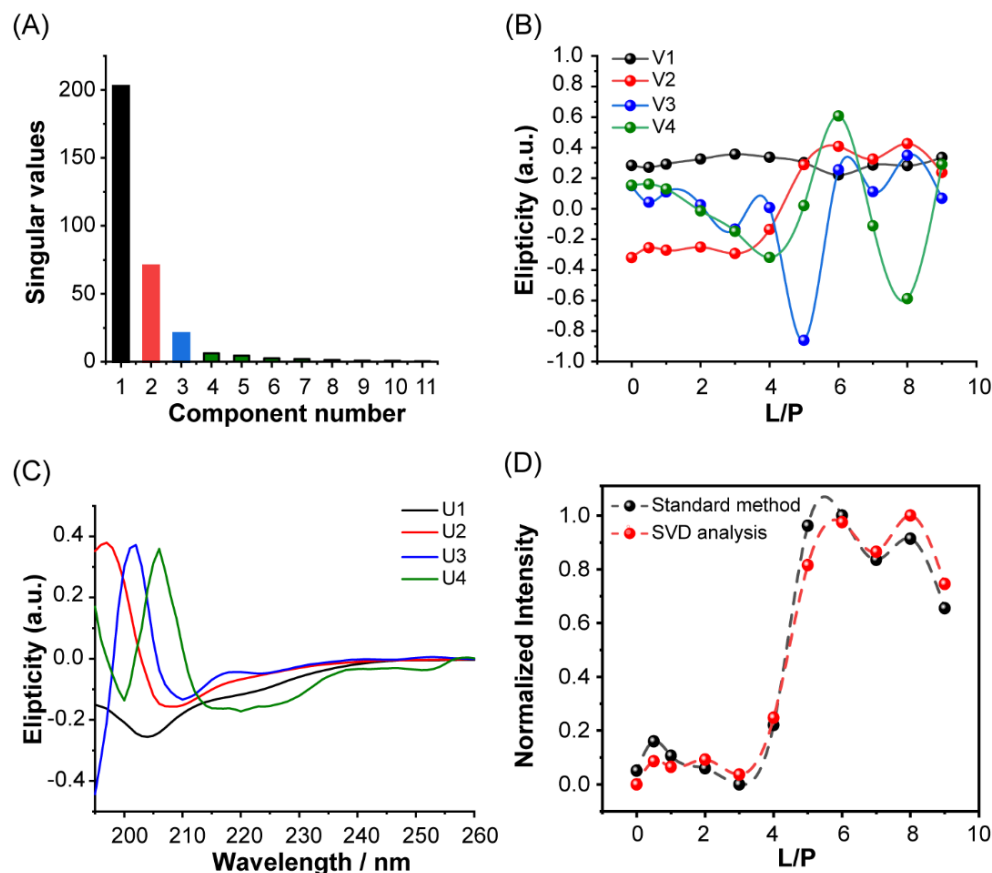
Figure 5.3. The SVD analysis for observed CD spectral transition of AV20 upon interaction with increasing TLBE:AV20 (L/P) molar ratios (A) Bars show the singular values sorted in descending order. (B) The coefficients corresponding to four basic functions, which were given as the principal component vectors (V_i) to the molar ratios of TLBE. (C) First four left singular vectors associated with wavelength profile. (D) Comparison between standard procedure and SVD binding. The normalized absorbance (θ) versus L/P ratio plotted in black for wavelength 197 nm, indicating a sigmoidal growth of helical conformation. Similar growth curve was observed from SVD analysis, when the 2nd Vi vector (also represent helical species) was normalized and plotted against L/P molar ratio.

Upon titrating with TLBE LUVs, we observed a transition from disordered to ordered conformation. With increasing lipid concentration, a gradual shift in the negative minima from 195 nm to 208 nm with a concomitant increase in the positive maxima at 197 nm was observed. At a higher lipid/peptide (L/P) ratio of 8, the peptide noticeably adopted alpha helical structure (negative minima at 208 nm and 222 nm, and a positive maximum at 197 nm). This transition to helical conformations is of utmost significance due to their crucial role in stabilizing the oligomeric amyloid intermediates.[23] Although the scattering of free LUVs resulted in the dampening of CD

absorbance, it did not significantly hamper the shape of the spectra (Figure S5.1). We further performed deconvolution of these CD spectra using online platform BeStSel, and calculated the percentage of secondary conformation upon titration (Figure 5.2B).[24] Interestingly, an increase in the alpha helical conformation with concomitant decrease in the β-sheet conformation was evident from the deconvolution. Therefore, rather than a transition from disordered to ordered structure, a restructuring of the conformation is apparent from the deconvolution. Nonetheless, the occurrence of several distinct spectrum during titration indicated the presence of multiple intermediate states.

5.3.3. AV20-membrane interaction dynamics revealed through SVD analysis

To gain deeper insights into the spectral transitions observed during the interaction between AV20 and TLBE LUVs, we employed the SVD approach. Of note, SVD analysis is a robust mathematical technique that allows for the extraction of hidden patterns and significant variations from complex datasets. In this context, it provides a means to uncover underlying structural changes and relationships within the CD spectral data. Through SVD analysis, we transformed the raw CD spectra into orthogonal components, revealing dominant modes of variation. We found three major structural species that describe the trend of CD spectra over the whole concentration range. These three species with largest singular values contributes to 94 % of the total singular values, while rest of the components consist of mainly noise (Figure 5.3A). Figure 5.3B shows the concentration dependent profiles associated with the first four principal components, whereas their corresponding spectral profiles are illustrated in Figure 5.3C. Component 1 represents the spectrum associated with a structural species that remains almost same throughout the concentration range. Interestingly, component 2 indicates a major structural species that follows a sigmoidal growth curve, saturating at higher lipid concentration. The third structural species, which is associated with Component 3, on the other hand, displays a dip in the curve at L/P of 5, thus suggesting a significant molecular event occurring at this concentration. Component 4 and the rest follows an oscillating profile that mainly contains noise. Another noteworthy outcome is the ability of this analysis to complement the results of conventional methods. As depicted in Figure 5.3D, the data generated by both classical and SVD methods exhibit notable similarity. Furthermore, SVD analysis yielded a dissociation constant of ~345 µM, a slight deviation from the standard method (~325 µM), but with significantly improved fitting (Appendix V, Figure S5.2). This discrepancy can be attributed to the fact that while the standard method relies on a
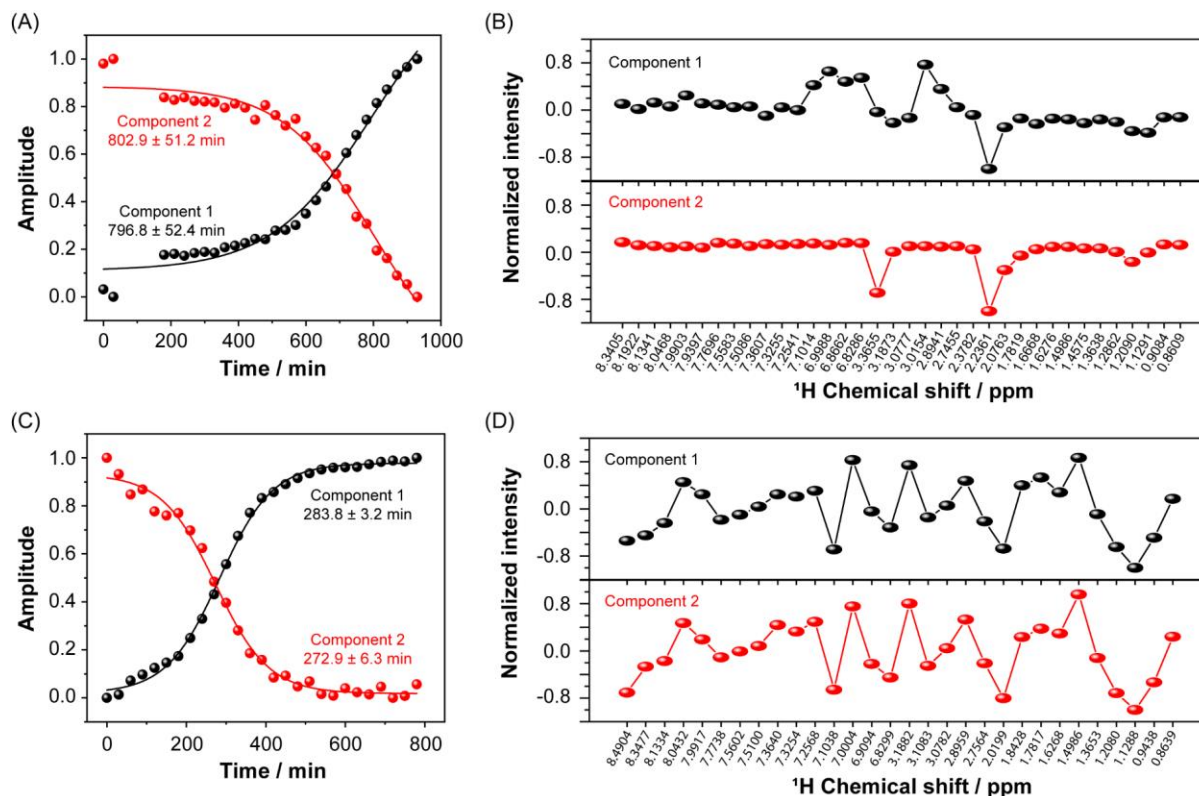
Figure 5.4. SVD analysis of time-dependent 1D NMR dataset of (A, B) hIAPP self-assembly and (C, D) hIAPP assembly in presence of VY21. (A, C) the temporal profile of two major components obtained from SVD analysis of 1D NMR datasets associated with hIAPP and hIAPP co-incubated with VY21, respectively. (B, D) corresponds to the normalized chemical shift profile of two major components obtained from SVD analysis of 1D NMR datasets associated with hIAPP and hIAPP co-incubated with VY21, respectively. Positive and negative intensity represent higher and lower global variations, respectively.

single spectral point, SVD binding analysis utilizes the complete spectral dataset, offering greater precision and reduced susceptibility to noise.

The application of SVD thus led to the identification of three distinct spectral modes associated with AV20's conformational changes. The SVD-derived spectral modes further complemented the traditional analysis methods, providing a multidimensional perspective that enhanced our understanding of the spectral evolution during peptide-membrane interaction.

5.3.4. Mechanism of peptide self-assembly and co-assembly by SVD analysis

Understanding the complex mechanisms behind peptide self-assembly holds significant importance in grasping amyloid disorders. To unravel these complexities, we employ the power of

SVD analysis, offering a simplified yet profound method to decipher the pathways guiding peptide aggregation. Utilizing one dimensional (1D) ^{1}H NMR spectroscopy, we investigate the kinetics of monomer loss during aggregation.[25] By organizing temporal ^{1}H peak intensities into a matrix and applying SVD, we reveal two principal components with significant singular values (Appendix V, Figure S5.3). Notably, the first component (V1) displays a sigmoidal growth curve, while the second exhibits sigmoidal decay kinetics. These observations yield dual insights: the kinetics of monomer loss, outlining the transition from monomeric units to aggregates, and sigmoidal growth kinetics, akin to the established nucleation-dependent ThT profile linked to amyloid aggregation. Fitting of these curves with Boltzmann equation resulted in almost identical half-life for these two components, signifying their inter connections. Moreover, the U1 and U2 components unveil a striking finding, where peaks associated with hIAPP demonstrate consistent kinetic behavior.

Our recent investigation on the effect of VY21 on the aggregation kinetics revealed a comparatively faster aggregation.[26] Here, we performed SVD analysis on the NMR derived dataset consisting of temporal changes in the hIAPP aggregation in presence of VY21. Interestingly, the analysis revealed a similar two-step mechanism of aggregation, as indicated by two major singular values (depicted in Appendix V, Figure S5.4). However, the rate of aggregation was found to be much faster. In contrast to hIAPP, the presence of VY21 resulted in a substantially reduced half-life of 272.9 ± 6.3 minutes, as determined through global fitting (Figure 5.4A, C). We further calculated the fibrillation rates for both cases from the kinetic fitting. While hIAPP alone exhibited a fibrillation rate of $1.895 \times 10^{-3} \pm 0.24 \times 10^{-3}$ min^{-1}, hIAPP co-incubated with VY21 showed much higher rate of $6.62 \times 10^{-3} \pm 0.2 \times 10^{-3}$ min^{-1}, which was almost three-fold. Additionally, greater variations in the spectral profile were also apparent (Figure 5.4B, D). Thus, by dissecting monomer loss kinetics, sigmoidal growth kinetics, and shared proton peak behavior, we have demonstrated the intricate self-assembly process.

5.3.5. The mechanism of Aβ40 seeded growth by SVD analysis

Next, to test the significance of SVD analysis on seeded growth of amyloid fibril, we have used a time-dependent NMR dataset of ^{15}N-labeled Aβ40 incubated with unlabeled Aβ40 fibril, where the spectral intensity of amino acid residues gets broaden with time as a result of aggregation.[27] The intensities of each residue were calculated as a function of time and arranged in a matrix as mentioned above. The analysis showed two smooth curves of Vi vectors that
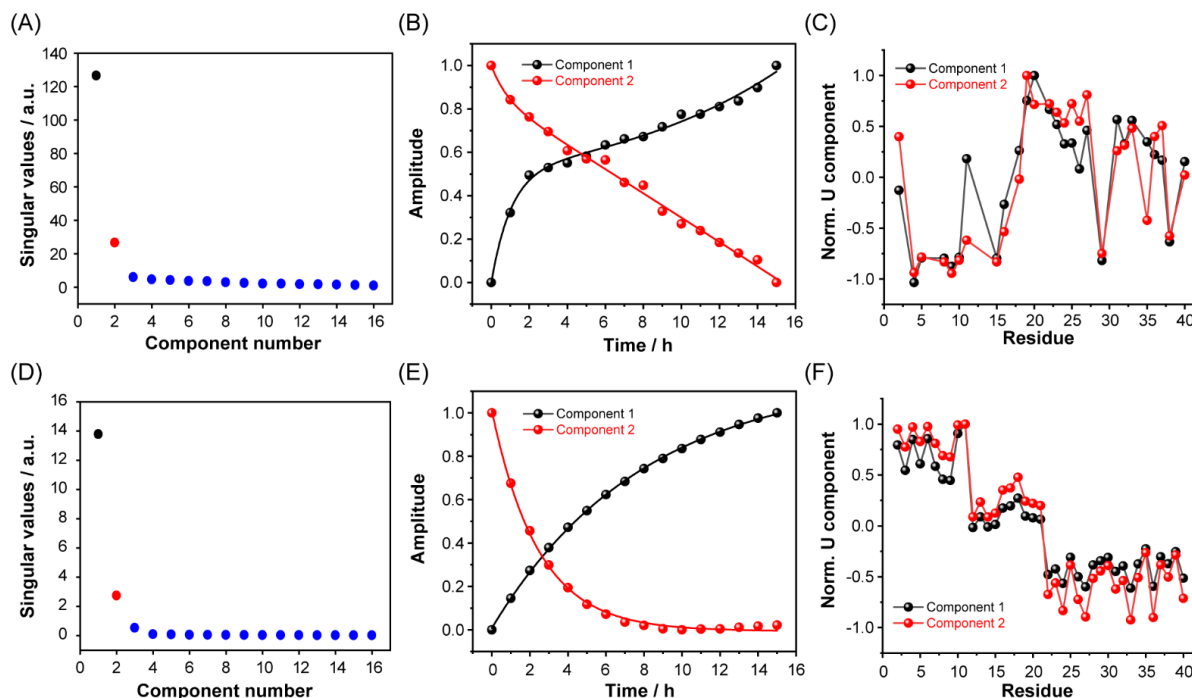
Figure 5.5. SVD analysis of seeded amyloid growth showing (A) Scatter plot of singular values. (B) Normalized V-components of temporal profile. (C) First two normalized spectral components from SVD analysis. SVD analysis of simulated dataset showing (D) Scatter plot of singular values. (E) Normalized V-components of temporal profile. (F) First two normalized spectral components from SVD analysis. Components 1 and 2 at each interface are shown in black and red, respectively, in all figures.

correspond to the two highest singular values, (Figure 5.5A, Appendix V, Figure S5.5) indicating Aβ40 aggregation to be a two-state process. While the temporal profile of component 1 fits well with a bi-exponential growth curve, component 2 follows a tri-exponential decay curve (Figure 5.5B). The residue profile associated with component 1 and 2 indicates that the C-terminal (G33, V36, G37, and V40) and the central hydrophobic region (V18, F19, F20, E22, D23, V24, and G25) of Aβ40 are mainly responsible for the aggregation process (Figure 5.5C). Note that, the residues with negative values associated with these components indicate negligible changes in the NMR intensity during time- dependent aggregation. Therefore, these residues do not significantly participate the assembly process. However, the residues with more positive values are associated with significant intensity drop during aggregation. Additionally, the noise-filtered dataset was reconstructed using the two principal components by providing the 'K-value' as 2. The time-dependent intensity curves were fitted exponentially, from which the decay rates were extracted.

The decay rates obtained for both before and after SVD operation confirms a more reliable fitting as a result of SVD analysis (Appendix V, Figure S5.6, Table S5.1).

Thus, SVD analysis provided a model-free global kinetic information. Based on the information obtained from the analysis, an optimum kinetic model among all possible candidate models was considered.

5.3.6. Validation of physical interpretation using simulated datasets

To validate the physical interpretation derived from our SVD analysis results, we employed a simulated dataset. This dataset was generated using the R-programming language, and the corresponding code is provided in the supplementary information. Briefly, this dataset comprises normalized intensity values that align well with an exponential decay curve (Appendix V, Figure S5.7). The choice of decay rates was deliberate, with high decay rates assigned to N-terminal residues, moderate decay rates to central residues, and low decay rates to C-terminal residues. Additionally, a minor amount of noise was introduced into the dataset to mimic experimental conditions. This dataset was then subjected to SVD analysis. The SVD analysis revealed two principal components with higher singular values similar to that obtained from seeded amyloid growth (Figure 5.5D, Appendix V, Figure S5.8). Figure 5E illustrates the normalized temporal profiles associated with these components. Component 1 exhibited exponential growth kinetics, while component 2 displayed an exponential decay curve. Both of these curves were well-fitted with mono-exponential functions, generating corresponding kinetic rates. Intriguingly, both components exhibited similar variations in their residue space, implying their association with the same underlying process (Figure 5.5F). Moreover, the variations in the residue profile revealed that the N-terminus exhibited a higher decay rate than the central residues, followed by the C-terminus, consistent with the characteristics embedded in the simulated dataset. Therefore, by comparing the results obtained from the peptide self-assembly and seeded growth, it can be conjectured that the component 1 is associated with the fibril growth, whereas the component 2 cab be linked with concomitant monomer loss as a result of fibrillation.

5.3.7. SVD analysis on the inhibition of amyloid aggregation

The application of SVD was further tested for the analysis of amyloid inhibition. As depicted in Figure 5.6A, the interaction between Aβ40 and **SP1** was studied. **SP1**, a synthetic paratope, can significantly inhibit aggregation of Aβ40. Therefore, high-resolution 2D

Heteronuclear Multiple Quantum Coherence (HMQC) NMR experiments were performed with 80
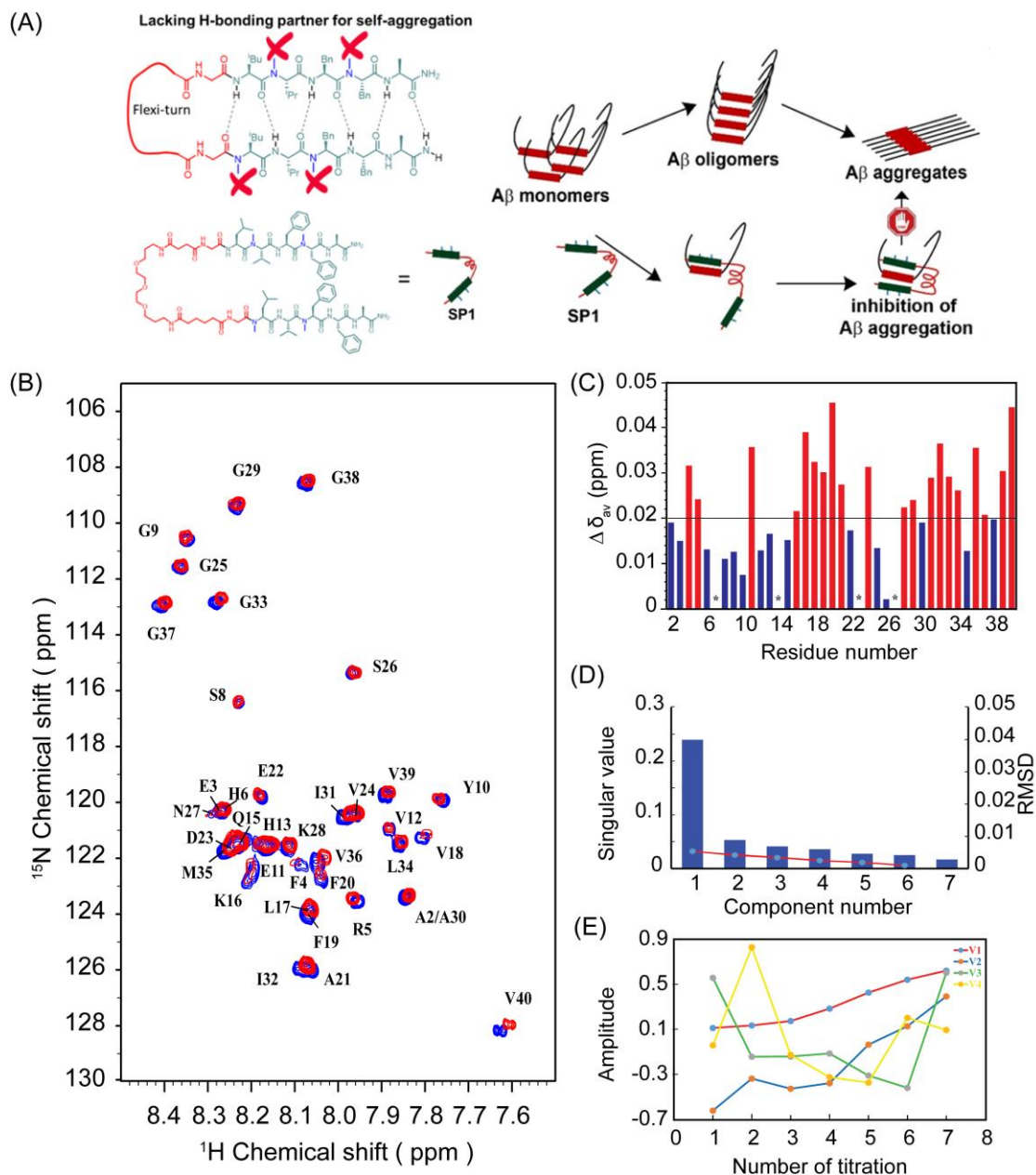
Figure 5.6. (A) Schematic representation of possible molecular interaction between Aβ40 and **SP1**. (B) 2D ^{1}H-^{15}N SOFAST HMQC spectra of ^{15}N labeled Aβ40 (80 μM), before (blue) and after (red) addition of **SP1** at 1:10 molar ratio. (C) Bar plot of CSP in Aβ40 due to binding of **SP1**. The black threshold line represents mean of all CSP values. Red bars indicate most interacting residues. Overlapping residues with similar chemical shift are marked with an asterisk (*). (D) Blue bars indicating singular values in descending order. The root mean square deviation (RMSD) between raw dataset and reconstructed dataset are indicated by solid red circles. (E) The first four components of Vi vectors are plotted against the number of titrations.

µM Aβ40 upon increasing concentrations of **SP1** (titrated up to a molar ratio of 1:10). The Aβ40 backbone amide resonances resulted in concentration-dependent residue-specific chemical shift perturbations (CSP) in the presence of **SP1** (Figure 5.6B). At a molar ratio of 1:10, the molecular interaction resulted in notable CSPs, specifically for the central hydrophobic- $K^{16}LVFFA^{21}$ region (Figure 5.6C). Similar observations were also made for the C-terminal region, particularly the $I^{31}IGL^{34}$ stretch and the hydrophobic V36, V39, and V40 residues (Figure 5.6C). These observations clearly indicated the specific involvement of these hydrophobic-rich segments in the molecular association with **SP1**. Thus, the **SP1** mediated perturbation of this crucial domain suggests upon molecular interference in the dock-lock interactions of monomeric Aβ, explaining the altered fibrillation. Our recent studies have, in fact, shown the crucial role played by the C-terminal residues in mediating cytotoxicity. Our mutation-based studies have suggested the role played by the GxxxG motifs from the C-terminal to partake in the helix-helix association consequent to the Aβ fibrillation pathway. Thus, a direct molecular association of **SP1** with these segments indicates the inaccessibility of these segments necessary for wild-type Aβ amyloidogenesis. Singular value decomposition (SVD) was used to obtain a residue-specific binding affinity of **SP1** to Aβ40 (Figure 5.6D-E, Appendix V, Figure S5.9). The CSPs for Aβ40 with **SP1** were adjusted for both ΔδN and ΔδH to extract the dissociation constant (K_D) for certain residues (Appendix V, Table 5.2). Comparatively lower K_D values of ~200 µM were obtained for the residues R5, L17, V24, K28 and G29 of Aβ40, indicated their functional unavailability in fibrillation. Once again, this data supports the inhibition of dock-lock mechanism of Aβ40 by **SP1**.

5.4. Conclusions

Here, we demonstrate the potential of SVD in analyzing a wide spectrum of amyloidogenic processes. This analytical tool proves highly efficient as it allows for the fitting of pertinent SVD parameters in a straightforward manner, resulting in notably precise outcomes compared to standard methods. It not only provides a noise free determination of the binding constant in a peptide-membrane interaction but also reveals the number of relevant intermediate conformers during subsequent membrane-mediated structural transitions. Moreover, it offers a global kinetic information of the assembly processes associated with amyloidogenesis. SVD act as an intermediate filter of the data matrix, which not only provides a rigorous and model-independent determination of principle modes but also enormously simplifies the fitting problem.

5.5. *Appendix V*
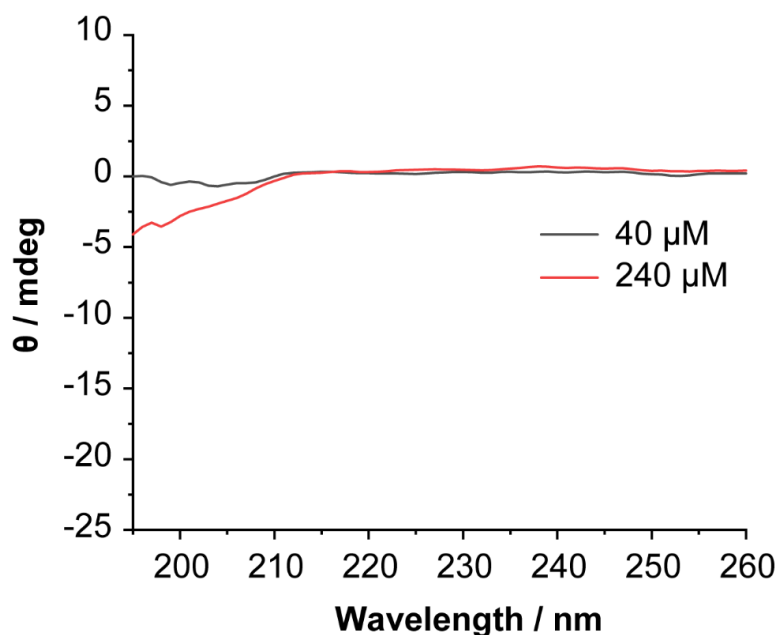
Figure S5.1. CD spectra of free TLBE LUVs, showing little effect of scattering on the CD absorption.
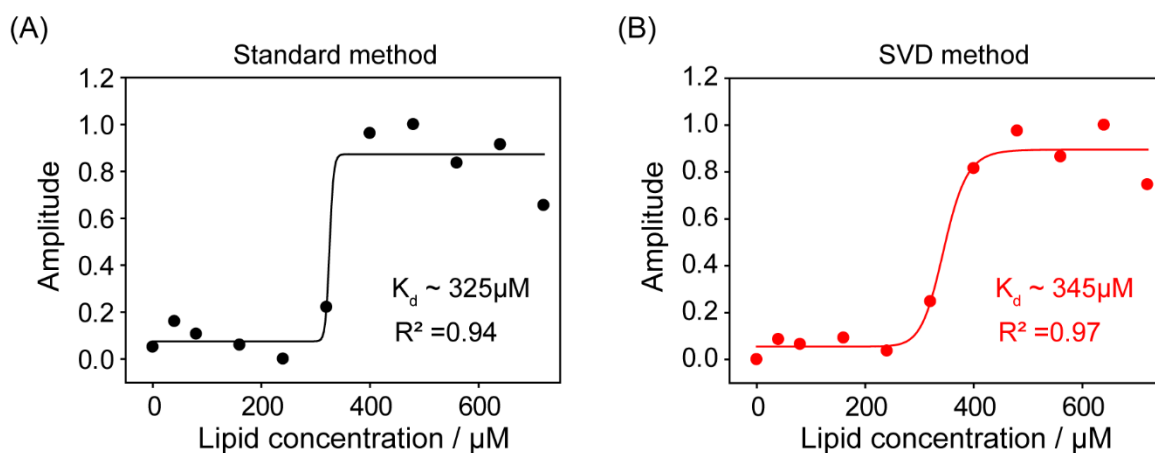

Figure S5.2. Comparison between standard method and SVD analysis. (A) Scatter plot displaying CD absorbance at 197 nm, taken as a function of lipid concentration followed by normalization. (B) Scatter plot displaying component 2 (V2) from SVD analysis, taken as a function of lipid concentration followed by normalization. Dissociation constant was calculated from the fitted curves using Hill equation.
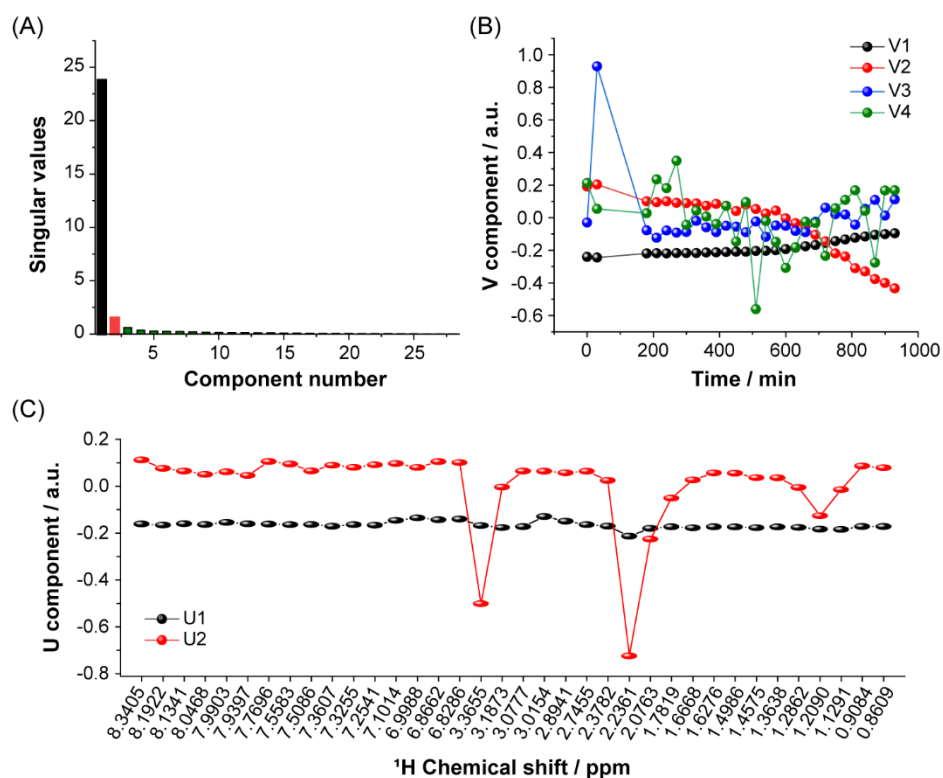
Figure S5.3. Direct results of SVD analysis for hIAPP self-assembly monitored by 1H-NMR spectroscopy (A) Bar plot showing singular values. (B) First four V-components showing temporal profile. (C) First two spectral components from SVD analysis. Components 1 and 2 at each interface are shown in black and red, respectively, in all figures.
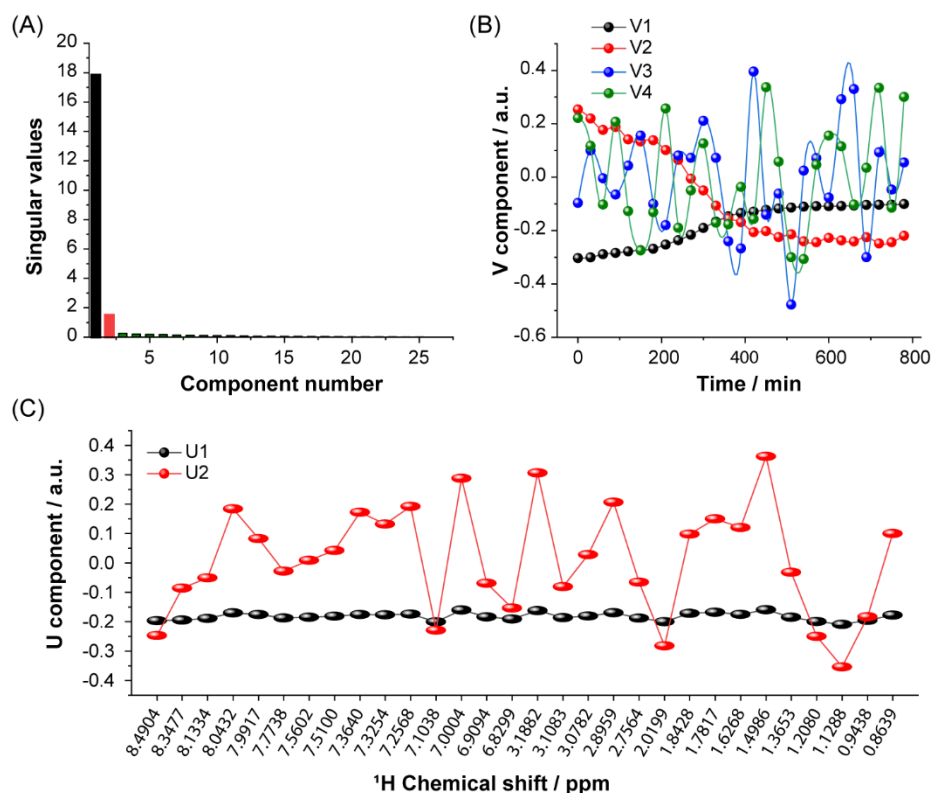
Figure S5.4. Direct results of SVD analysis for hIAPP self-assembly co-incubated with VY21 monitored by 1H-NMR spectroscopy (A) Bar plot showing singular values. (B) First four V-components showing temporal profile. (C) First two spectral components from SVD analysis. Components 1 and 2 at each interface are shown in black and red, respectively, in all figures.
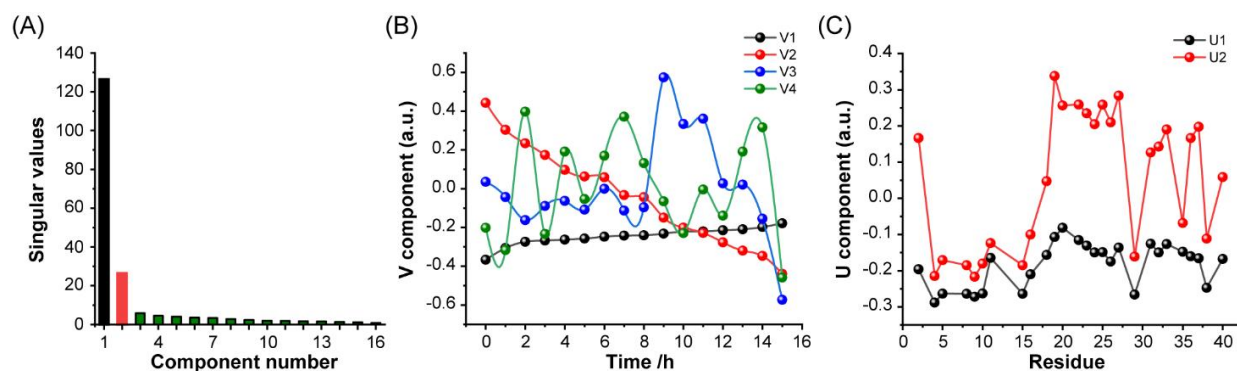
Figure S5.5. Direct results of SVD analysis for seeded growth of ^{15}N-labeled Aβ40 incubated with unlabeled Aβ40 fibril monitored by 1H-NMR spectroscopy (A) Bar plot showing singular values. (B) First four V-components showing temporal profile. (C) First two spectral components from SVD analysis. Components 1 and 2 at each interface are shown in black and red, respectively, in all figures.
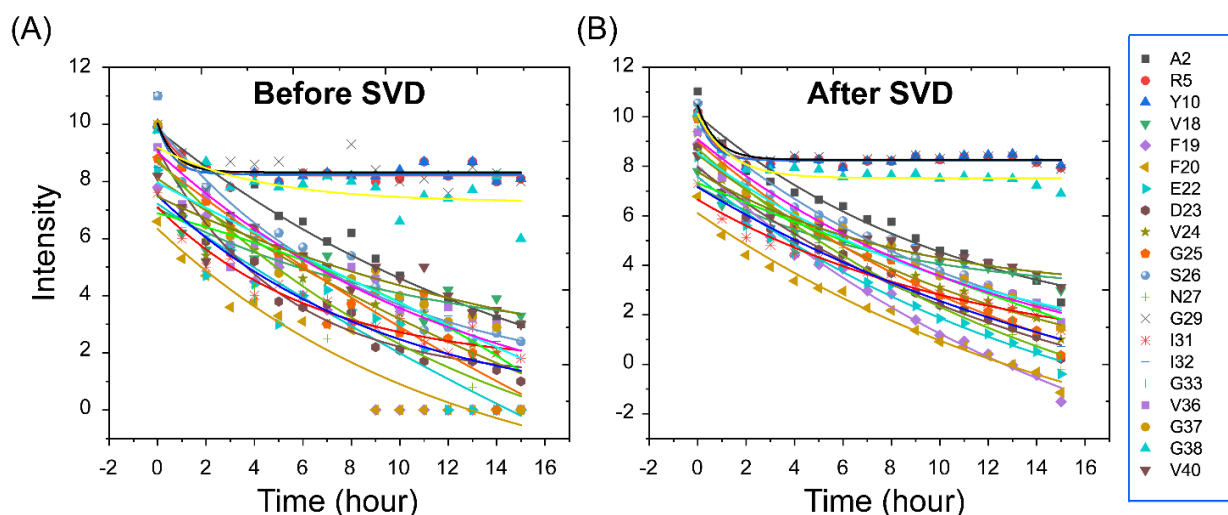
Figure S5.6. Time course intensity changes of selected residues fitted using single exponential decay equation. (A) Fitted raw data before SVD, (B) Fitted reconstructed data after SVD operation with two non-noise components. As a result, we get more reliable fitting.
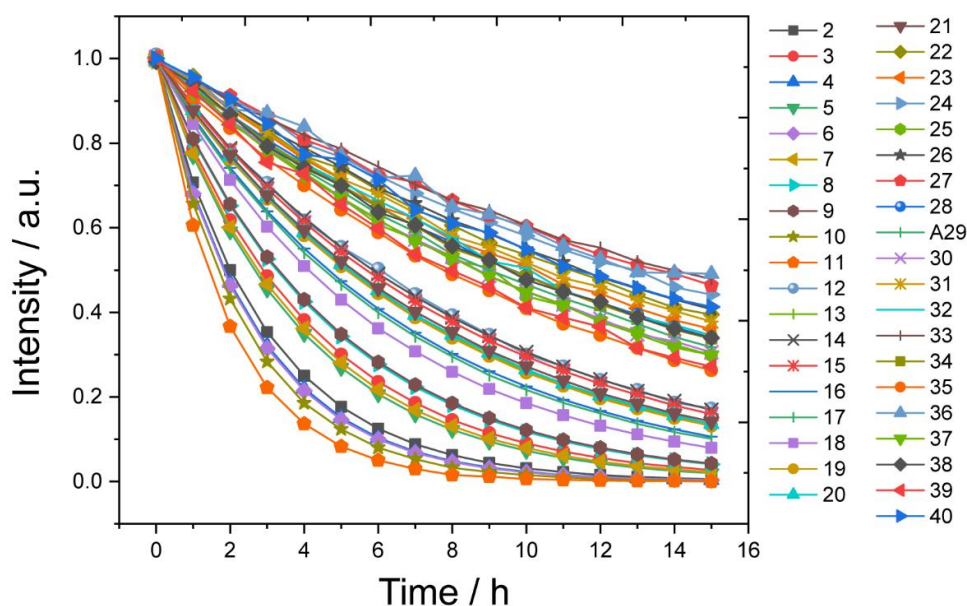
Figure S5.7. Simulated dataset generated using R-programming language. The dataset comprises normalized intensity values that align well with an exponential decay curve. High decay rates were assigned to N-terminal residues, moderate decay rates to central residues, and low decay rates to C-terminal residues.
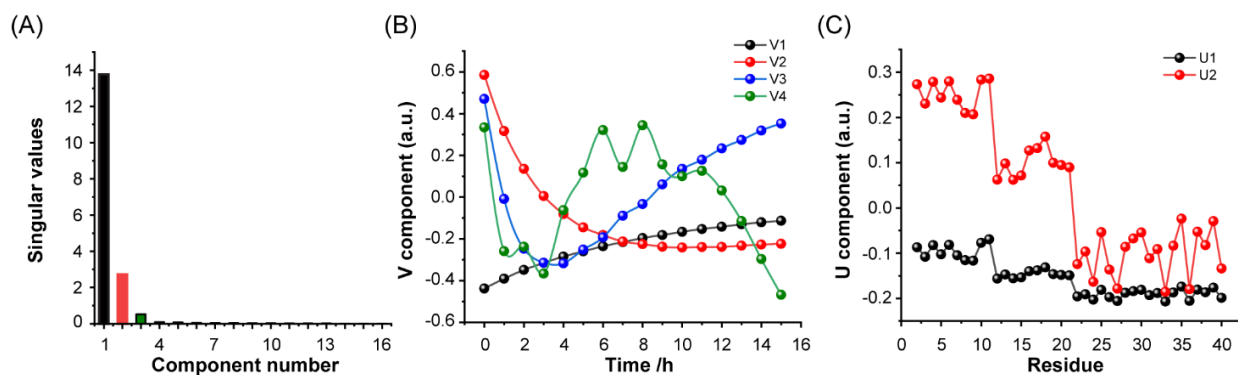
Figure S5.8. Direct results of simulated dataset (A) Bar plot showing singular values. (B) First four V-components showing temporal profile. (C) First two spectral components from SVD analysis. Components 1 and 2 at each interface are shown in black and red, respectively, in all figures.
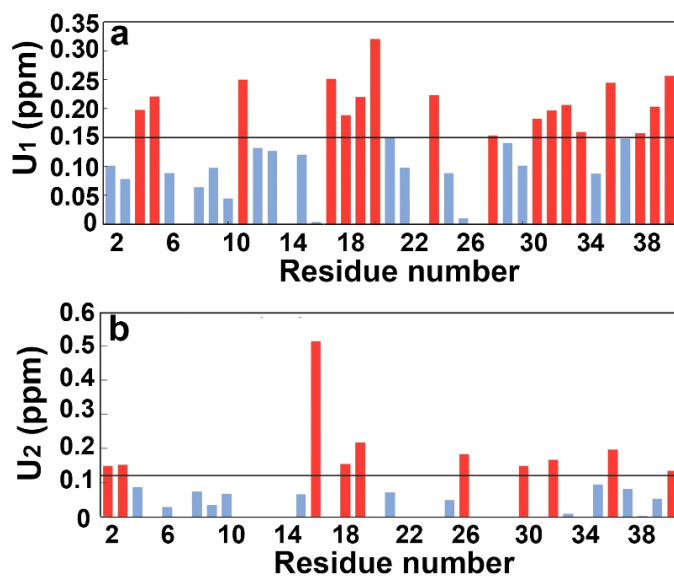
Figure S5.9. Bar plot of (a) first left singular vector, U_1 (b) second singular vector, U_2 plotted against residue number. Overlapping residues or residues with negative values are not shown in the figure.

Table S5.1. Decay rates and their corresponding R-square value of selected residues obtained from curve fitting for both before and after SVD. Comparisons between R-square values clearly shows better fitting after SVD operation.

Residue	Decay rate (t_1) [Before SVD]	R-Square [Before SVD]	Decay rate (t_1) [After SVD]	R-Square [After SVD]
A2	16.65548 ± 10.12171	0.93497	10.93798 ± 3.37512	0.96219
R5	0.96117 ± 0.33976	0.7812	0.67209 ± 0.17332	0.90327
Y10	0.60673 ± 0.27101	0.78225	0.59512 ± 0.19823	0.86942
V18	10.3688 ± 6.32022	0.85559	7.79604 ± 2.23847	0.94239
F19	13.8013 ± 7.00978	0.93513	17.56253 ± 5.96806	0.98073
F20	12.12734 ± 6.16478	0.91882	17.52219 ± 5.95111	0.98067
E22	42.19961 ± 84.90147	0.89028	15.68857 ± 5.19884	0.97735
D23	5.11382 ± 0.94359	0.95508	14.51022 ± 4.73188	0.97463
V24	29.49151 ± 43.40747	0.88177	13.10322 ± 4.18815	0.97062
G25	37.12553 ± 53.20261	0.92539	14.32424 ± 4.6592	0.97416
S26	8.58702 ± 2.46382	0.95061	12.46743 ± 3.94669	0.96847
N27	13.40087 ± 7.9072	0.90998	15.28594 ± 5.03798	0.97648
G29	0.70493 ± 0.53419	0.50498	0.77567 ± 0.16502	0.92116
I31	6.47956 ± 1.65496	0.9392	11.67739 ± 3.64991	0.96543
G33	9.483 ± 4.67242	0.88564	19.48319 ± 11.66423	0.95246
V36	88.29064 ± 451.08075	0.84564	11.8037 ± 3.69714	0.96595
G37	12.91841 ± 8.91517	0.87345	12.42568 ± 3.93092	0.96832
G38	4.23361 ± 3.40856	0.47223	1.30598 ± 0.26972	0.90126
V40	17.72836 ± 18.49232	0.84618	8.12872 ± 2.35622	0.94505

Table S5.2. Equilibrium dissociation constant calculated both before and after SVD.

Residue	K_d before SVD	K_d after SVD
R5	99.84	183.1
L17	336.5	132.4
F20	301.3	398
E22	961.2	419.9
V24	247.6	282.5
K28	196.6	180
G29	446.8	236.7
I31	396.2	398.2
G33	376.2	583
L34	435	385.6
G38	336	472.2

5.6. References

[1] H. Oakley, S. L. Cole, S. Logan, E. Maus, P. Shao, J. Craft, A. Guillozet-Bongaarts, M. Ohno, J. Disterhoft, L. Van Eldik, R. Berry, R. Vassar, *J Neurosci* **2006**, 26, 10129; K. Hensley, J. M. Carney, M. P. Mattson, M. Aksenova, M. Harris, J. F. Wu, R. A. Floyd, D. A. Butterfield, *Proc Natl Acad Sci U S A* **1994**, 91, 3270; S. Ray, N. Singh, R. Kumar, K. Patel, S. Pandey, D. Datta, J. Mahato, R. Panigrahi, A. Navalkar, S. Mehra, L. Gadhe, D. Chatterjee, A. S. Sawner, S. Maiti, S. Bhatia, J. A. Gerez, A. Chowdhury, A. Kumar, R. Padinhateeri, R. Riek, G. Krishnamoorthy, S. K. Maji, *Nat Chem* **2020**, 12, 705; D. Roy, N. C. Maity, S. Kumar, A. Maity, B. N. Ratha, R. Biswas, N. C. Maiti, A. K. Mandal, A. Bhunia, *Int J Biol Macromol* **2023**, 241, 124470; Y. Xu, R. Maya-Martinez, N. Guthertz, G. R. Heath, I. W. Manfield, A. L. Breeze, F. Sobott, R. Foster, S. E. Radford, *Nat Commun* **2022**, 13, 1040; M. C. Owen, D. Gnutt, M. Gao, S. K. T. S. Wärmländer, J. Jarvet, A. Gräslund, R. Winter, S. Ebbinghaus, B. Strodel, *Chem Soc Rev* **2019**, 48, 3946.

[2] P. H. Nguyen, A. Ramamoorthy, B. R. Sahoo, J. Zheng, P. Faller, J. E. Straub, L. Dominguez, J. E. Shea, N. V. Dokholyan, A. De Simone, B. Ma, R. Nussinov, S. Najafi, S. T. Ngo, A. Loquet, M. Chiricotto, P. Ganguly, J. McCarty, M. S. Li, C. Hall, Y. Wang, Y. Miller, S. Melchionna, B. Habenstein, S. Timr, J. Chen, B. Hnath, B. Strodel, R. Kayed, S. Lesné, G. Wei, F. Sterpone, A. J. Doig, P. Derreumaux, *Chem Rev* **2021**, 121, 2545.

[3] D. Eisenberg, M. Jucker, *Cell* **2012**, 148, 1188.

[4] E. Chatani, N. Yamamoto, *Biophys Rev* **2018**, 10, 527; A. K. Bishoyi, P. H. Roham, K. Rachineni, S. Save, M. A. Hazari, S. Sharma, A. Kumar, *Biol Chem* **2021**, 402, 133.

[5] J. D. Harper, C. M. Lieber, P. T. Lansbury, *Chem Biol* **1997**, 4, 951; T. Ban, K. Yamaguchi, Y. Goto, *Acc Chem Res* **2006**, 39, 663.

[6] A. K. Paravastu, I. Qahwash, R. D. Leapman, S. C. Meredith, R. Tycko, *Proc Natl Acad Sci U S A* **2009**, 106, 7443.

[7] M. I. Ivanova, Y. Lin, Y. H. Lee, J. Zheng, A. Ramamoorthy, *Biophys Chem* **2021**, 269, 106507; D. Ghosh, M. Mondal, G. M. Mohite, P. K. Singh, P. Ranjan, A. Anoop, S. Ghosh, N. N. Jha, A. Kumar, S. K. Maji, *Biochemistry* **2013**, 52, 6925; O. Gursky, X. Mei, D. Atkinson, *Biochemistry* **2012**, 51, 10.

[8] C. Cecchi, M. Stefani, *Biophys Chem* **2013**, 182, 30; J. R. Brender, S. Salamekh, A. Ramamoorthy, *Acc Chem Res* **2012**, 45, 454; C. Rando, G. Grasso, D. Sarkar, M. F. M. Sciacca, L. M. Cucci, A. Cosentino, G. Forte, M. Pannuzzo, C. Satriano, A. Bhunia, C. La Rosa, *Int J Mol Sci* **2023**, 24.

[9] M. F. Sciacca, F. Lolicato, C. Tempra, F. Scollo, B. R. Sahoo, M. D. Watson, S. García-Viñuales, D. Milardi, A. Raudino, J. C. Lee, A. Ramamoorthy, C. La Rosa, *ACS Chem Neurosci* **2020**, 11, 4336.

[10] G. Di Natale, G. Sabatino, M. F. M. Sciacca, R. Tosto, D. Milardi, G. Pappalardo, *Molecules* **2022**, 27.

[11] I. Wang, S. Y. Chen, S. T. Hsu, *Sci Rep* **2016**, 6, 31514; M. Kojima, M. Tanokura, M. Maeda, K. Kimura, Y. Amemiya, H. Kihara, K. Takahashi, *Biochemistry* **2000**, 39, 1364; T. Shiratori, S. Goto, T. Sakaguchi, T. Kasai, Y. Otsuka, K. Higashi, K. Makino, H. Takahashi, K. Komatsu, *Biochem Biophys Rep* **2021**, 28, 101153.

[12] M. Schmidt, S. Rajagopal, Z. Ren, K. Moffat, *Biophys J* **2003**, 84, 2112.

[13] O. Alter, P. O. Brown, D. Botstein, *Proc Natl Acad Sci U S A* **2000**, 97, 10101.

[14] J. R. Brender, S. Kishimoto, H. Merkle, G. Reed, R. E. Hurd, A. P. Chen, J. H. Ardenkjaer-Larsen, J. Munasinghe, K. Saito, T. Seki, N. Oshima, K. Yamamoto, P. L. Choyke, J. Mitchell, M. C. Krishna, *Sci Rep* **2019**, 9, 3410.

[15] R. Selvaratnam, S. Chowdhury, B. VanSchouwen, G. Melacini, *Proc Natl Acad Sci U S A* **2011**, 108, 6133; A. Paul, S. Kumar, S. Kalita, D. Sarkar, A. Bhunia, A. Bandyopadhyay, A. C. Mondal, B. Mandal, *Chem Sci* **2020**, 12, 2853.

[16] M. Arai, J. C. Ferreon, P. E. Wright, *J Am Chem Soc* **2012**, 134, 3792.

[17] D. Sarkar, I. Chakraborty, M. Condorelli, B. Ghosh, T. Mass, M. Weingarth, A. K. Mandal, C. La Rosa, V. Subramanian, A. Bhunia, *ChemMedChem* **2020**, 15, 293.

[18] I. Chakraborty, R. K. Kar, D. Sarkar, S. Kumar, N. C. Maiti, A. K. Mandal, A. Bhunia, *ACS Chem Neurosci* **2021**, 12, 2903.

[19] H. Fatafta, B. Kav, B. F. Bundschuh, J. Loschwitz, B. Strodel, *Biophys Chem* **2022**, 280, 106700.

[20] M. F. Sciacca, S. A. Kotler, J. R. Brender, J. Chen, D. K. Lee, A. Ramamoorthy, *Biophys J* **2012**, 103, 702.

[21] C. Dong, M. Hoffmann, X. Li, M. Wang, C. R. Garen, N. O. Petersen, M. T. Woodside, *Sci Rep* **2018**, 8, 6755; A. Olofsson, T. Borowik, G. Gröbner, A. E. Sauer-Eriksson, *J Mol Biol* **2007**, 374, 186.

[22] S. Bera, N. Gayen, S. A. Mohid, D. Bhattacharyya, J. Krishnamoorthy, D. Sarkar, J. Choi, N. Sahoo, A. K. Mandal, D. Lee, A. Bhunia, *ACS Chem Neurosci* **2020**, 11, 1965.

[23] C. A. De Carufel, N. Quittot, P. T. Nguyen, S. Bourgault, *Angew Chem Int Ed Engl* **2015**, 54, 14383.

[24] A. Micsonai, F. Wien, L. Kernya, Y. H. Lee, Y. Goto, M. Réfrégiers, J. Kardos, *Proc Natl Acad Sci U S A* **2015**, 112, E3095.

[25] S. M. Ramalhete, K. P. Nartowski, N. Sarathchandra, J. S. Foster, A. N. Round, J. Angulo, G. O. Lloyd, Y. Z. Khimyak, *Chemistry* **2017**, 23, 8014; G. Bellomo, S. Bologna, L. Gonnelli, E. Ravera, M. Fragai, M. Lelli, C. Luchinat, *Chem Commun (Camb)* **2018**, 54, 7601; M. T. Hutchison, G. Bellomo, A. Cherepanov, E. Stirnal, B. Fürtig, C. Richter, V. Linhard, E. Gurewitsch, M. Lelli, N. Morgner, T. Schrader, H. Schwalbe, *Chembiochem* **2023**, 24, e202200760.

[26] D. Sarkar, N. C. Maity, G. Shome, K. G. Varnava, V. Sarojini, S. Vivekanandan, N. Sahoo, S. Kumar, A. K. Mandal, R. Biswas, A. Bhunia, *Phys Chem Chem Phys* **2022**, 24, 22250.

[27] J. R. Brender, A. Ghosh, S. A. Kotler, J. Krishnamoorthy, S. Bera, V. Morris, T. B. Sil, K. Garai, B. Reif, A. Bhunia, A. Ramamoorthy, *Chem Commun (Camb)* **2019**, 55, 4483.

Chapter VI

Multiscale Materials Engineering via Self-Assembly of Pentapeptide Derivatives from SARS CoV E Protein

6.1. Introductions

Hydrogels are semi-solid materials formed by self-assembled hydrogelator molecules into a three-dimensional (3D) network of nanostructures. This network possesses a unique ability to absorb and retain significant amounts of water or biological fluids, rendering it a promising candidate for a wide range of applications. Peptide self-assembly that leads to hydrogel formation are being widely investigated for a variety of biomedical applications such as targeted drug delivery, scaffolds for cell culture and tissue regeneration, and biosensing applications etc.[1, 2] In this context, short peptides have emerged as a promising building block for gelation. They are highly biocompatible, easy to modify and offers controlled self-assembly and supramolecule formation.[3] Although a large number of research have been done on the fabrication and characterization of peptide hydrogels, a comprehensive structural understanding behind hydrogel formation is still inadequate. A number of ultrashort peptides (2-3 amino acids) have been identified to self-assemble into hydrogels and nanomaterials in an aqueous solution, resulting in micelle-like nanospheres, nanotubes, fibrils, ribbon-like assemblies and heterogenous nanostructures.[4, 5] While many peptide gelators contain hydrophobic alkyl chains in their sequence, only a few include aromatic moieties and rely on aromatic-aromatic interactions to induce hydrogelation.[6] Among them the Fmoc-FF has been the most extensively studied hydrogel system.[7, 8] However, oligopeptide sequences that are slightly extended in length (4-8 amino acids) are gaining considerable attention.[9, 10] In this context, the design of a pentapeptide may offer more flexibility and versatility in controlling self-assembly and nanostructure formation. Since, pentapeptide sequences are typically the most common motifs of a protein that dictates biological functions, it may also provide a broad spectrum of bio-applicability. Moreover, introduction of an aromatic group to the peptide sequence may facilitate self-assembly by allowing π-π stacking and reducing steric hindrance, which will eventually lead to a mechanically stable hydrogel formation.

In this chapter, we report the evaluation of three pentapeptide derivatives to elucidate the role of sequence distribution and the driving forces behind a molecule containing aromatic motif to act as a gelator. The peptide sequence originates from the SARS CoV E protein.[11, 12] E protein is well-known for its crucial role in the assembly of virions. It has been reported to possess ion channel activity, ability to interact with host proteins, and display potential variations in membrane curvature.[13] Therefore, pentapeptides derived from the SARS CoV E protein could be significant due to their ability to retain antiviral activity or immunogenicity, and may holds potential for

medicinal applications. In fact, previous studies have shown that the "T^{55}VYVY^{59}" sequence from the C-terminal SARS CoV E protein could form nano-rod like structures in water.[14] Mutation within the V^{56}YVY^{59} region has been reported to induce a shift in the secondary structure, resulting in a more distinct β-sheet conformations.[12] Here, we have introduced a Fmoc group in the N-terminus of the "T^{55}VYVY^{59}" sequence followed by rearrangement in the amino acid sequence, and aimed to uncover the propensity of hydrogel formation (Figure 6.1). Notably, very few research have shown the effect of sequence rearrangement as minimal structural modification compared to mutation or addition/ subtraction of amino acids to develop multiscale nanostructures such as nano tape, fiber or sphere. By combining various spectroscopic techniques including fluorescence, CD, FTIR, and NMR, we found that all three peptides form 3$_{10}$-helix in the monomeric state (in DMSO) and undergoes conformational transition into self-assembled antiparallel β-sheet in water. High-resolution microscopy further reveled a variety of nanoarchitectures, which attributes to the differential aggregate morphology and subsequent gelation propensity.

6.2. Materials and Methods

6.2.1. Material preparation

Fmoc-modified pentapeptides were purchased from Genscript Inc. USA (Appendix VI, Figure S6.1). Lyophilysed Fmoc-pentapeptides powders were first dissolved in DMSO at 100 mg/ml concentration, followed by dilution in either water or 20 mM phosphate buffer (pH 7.4). It was then subjected to repeated vertexing and sonication to trigger gelation or supramolecular assemblies.

6.2.2. Rheology

Rheological experiments were done using the cone and plate geometry (diameter 25 mm) with cone angle 1° on the rheometer plate using an Anton Paar MCR 302 instrument. The hydrogels were freshly prepared following the previously described method and were scooped on the rheometer plate so that there was no air gap with the cone. Amplitude sweep experiments were performed as a function of strain (g = 0.01-100%) at a fixed angular frequency, w = 1 rad/s to determine the linear viscoelastic region. The storage modulus (G′) and loss modulus (G″) were plotted against strain (g) and crossover point was obtained from the plot. Frequency sweep experiments were done as a function of angular frequency (1–200 rad/s) at a fixed strain of 0.1%

and higher strain of 1% at 25 °C, and the storage modulus (G′) and loss modulus (G″) were plotted against angular frequency (w). The thixotropic behavior of the **P2** hydrogel was determined using a continuous time sweep oscillatory experiment where the gel network was destructed by application of a continuous strain of 0.1−50%. After the complete destruction of the gel denoted by G″ > G′, gel recovery was observed at a constant strain of 0.1%. The whole process was repeated to confirm the reversibility of the restoration process.

6.2.3. Microscopy

SEM imaging was performed using a FEI Quanta 200 (Quanta^{TM}, USA) electron microscope equipped with a tungsten gun operating at 5 kV. All three samples (**P1**, **P2** and **P3**) were analyzed through negative staining under Transmission Electron Microscope (TEM) to visualize the morphology, distribution and homogeneity of hydrogels. Briefly, carbon coated Cu grids (EM grid, 300 mesh, Electron Microscopy Sciences) were glow discharged using PELCO easiGlow glow discharge cleaning system at 20 mA current, for 30 seconds. Initially, 4 μL of sample (10 mg/ml) was applied onto the freshly glow discharged grid and incubated on the grid for 30 sec. Excess buffer was blotted and negative staining was performed using 1% uranyl acetate (Uranyl Acetate 98%, ACS Reagent, Polysciences, Inc.). The grids were stained and blotted gently from the side to remove excess staining solution. The grids were checked at room temperature using a 120 kV Talos L120C electron microscope equipped with a CETA CMOS camera. Data was collected at 120 kV using CETA CMOS camera at magnifications of 2,500-57,000x. AFM imaging was performed using the tapping mode through the MFP-3D of Asylum Research, Oxford Instruments. Confocal imaging was taken with a 63× objective in oil immersion using Leica TCSSP8 confocal microscope and the LAS AF Version 2.1.0 built-in 4316 software, Leica Microsystems GmbH, Germany.

6.2.4. Fluorescence spectroscopy

Intrinsic fluorescence spectra at different peptide concentrations were measured using Hitachi F-7000 FL spectrometer, with excitation at 280 nm and emission range between 300 and 550 nm. Fluorescence excitation spectra were collected from 200 nm to 400 nm with emission at 460 nm. Scan speed was kept at 240 nm/s for each measurement. Thioflavin T (ThT) fluorescence kinetics were performed using BMG LABTECH POLARstar Omega spectrometer in a 96 well plate at room temperature.

6.2.5. Circular Dichroism

Near-UV CD measurements were taken on a JASCO J-1500 CD spectrometer using a 0.1 cm path length cell with a slit width of 2 nm. For each spectrum, three readings were taken with a scan speed of 100 nm min^{-1}, and the average was considered. Smoothing and buffer subtraction were done to process raw data, as per the manufacturer's recommendation.

6.2.6. FTIR spectroscopy

FTIR spectra were collected using a PerkinElmer 100 spectrometer at room temperature. The FTIR spectra of lyophilized hydrogels or supramolecular aggregates were measured using the conventional KBr method. A total 64 number of scans were taken in the spectral range of 1800−1400 cm^{-1} with a spectral resolution of 4 cm^{-1}. Processing and deconvolution of the spectra were acquired using Origin software.

6.2.7. XRD

Data was collected using an X-ray diffractometer RIGAKU smart lab-II with Cu k$_\alpha$ radiation with a wavelength of 0.154 nm and operating power of 9 kW. Sample at 10 mg/ml was spread on a glass slide as a film and allowed to air dry prior to data collection.

6.2.8. NMR

All NMR experiments were carried out on a 500 MHz Bruker spectrometer equipped with RT probe at 25 °C. Two-dimensional ^{1}H-^{1}H total correlation spectroscopy (2D TOCSY) and two-dimensional ^{1}H-^{1}H Nuclear Overhauser SpectroscopY (2D NOESY) were recorded for the peptides in 100 % DMSO-d$_6$, and 90% DMSO-d$_6$ at 298 K, with a mixing time of 80 ms and 500 ms, respectively. All NMR spectra were processed using Topspin^{TM} 4.0.6 (Bruker software suite).

DOSY spectra were obtained for all peptides at 0.5 mg/ml concentration dissolved in different DMSO-d$_6$ / D$_2$O ratios at 298 K. The diffusion time (Δ) was 150 ms. The pulse field gradient length (δ) was adjusted to 1.5 ms in order to obtain 5% residual signal with the maximum gradient strength. The gradient strength was incremented in 16 steps from 2% to 95% of its maximum value in a linear ramp. All DOSY spectra were processed using Bruker topspin 4.0.6 and Bruker dynamics center 2.8 software. Solid state NMR experiments were performed at Bruker spectrometers at B$_0$ field of 800 and 500 MHz, respectively, employing 1.3 mm H/C/N triple resonance probes.

6.2.9. Cryo-EM Sample preparation

Freshly prepared samples (10 mg/ml) were checked by Negative staining under TEM prior to cryo-EM sample preparation. For cryo-EM sample preparation, Quantifoil R1.2/1.3 300 mesh copper grids (Electron Microscopy Sciences) were glow discharged for 90 seconds at 20mA using PELCO easiGlow glow discharge unit with similar parameters as mentioned previously and 3μl of hydrogel samples (10 mg/ml) were added to the freshly glow discharged grids, and incubated for 10 seconds. Finally blotting was carried out for 8.5 seconds at 100% humidity with a positive blot force of 25 and then quickly plunged into liquid ethane using FEI Vitrobot Mark IV plunger.

6.2.10. Cryo-EM data processing

Cryo-EM data acquisition was performed using Thermo Scientific^{TM} Talos Arctica Transmission Electron Microscope at 200kV equipped with K2 Summit Direct Electron Detector. Images were collected automatically using Latitude-S automatic data collection software (Gatan Inc) at nominal magnification 42,000x corresponding to pixel size 1.17 Å at specimen level.[15] Total electron dose of 57 e-/Å^2 at the defocus range of -1.25 μm and -2.75 μm. Data was recorded for 8 sec for a total of 20 frames. Around 571, and 693 movies were collected for **P1**, and **P2** hydrogel samples, respectively. The **P3** sample lacked the filament-like morphology (nanotape/ twisted thin long ribbons) and only 10-12 cryo-EM images were collected.

Data processing was carried out using RELION 3.1.2.[16] Initially, beam-induced motion correction of the individual movie files was performed using RELION MotionCor2. All the motion-corrected micrographs were manually screened using cisTEM software package[17] and the micrographs with a detected fit resolution less than 8 Å were considered for further processing. Contrast transfer function (CTF) was estimated using CTFFIND 4.1.13.[18] Initially, start and end coordinates of the filaments were manually picked using RELION 3.1 for both the hydrogel samples. Around 10,000 segments were extracted at a box size of 240 pixels and using an overlap of 90% between neighboring segments. Reference-free two-dimensional (2D) classification was performed on the extracted particles for both the datasets, using 25 classes (K=25), a regularization parameter of T=4, an in-plane angular sampling rate of 6o, a tube diameter of 160 Å and a restriction of the translational offsets along the helical axis to one helical rise (initial assumption of 4.75 Å). Best 2D class averages were then selected as template for auto-picking and this approach resulted in 150,068 particles for **P1** hydrogel dataset and 243,514 particles for **P2** hydrogel dataset

respectively. Automatically picked particles were extracted with a larger box size of 480 pixels corresponding to a calibrated pixel size of 1.17 Å. Several rounds of 2D classification were performed as mentioned previously using 50 classes (K=50), and with an increased regularization parameter T=100 to clean both the datasets. Particles from good classes were re-extracted further into increased box size of 720 pixels. Subsequently, 2D classification was performed on 720 pixels box particles to identify filament morphology. Power spectrum of high-resolution 2D class averages were computed in RELION and EMAN[19] to approximate the helical rise values from the selected 2D class averages.

6.2.11. Phase Holographic Imaging

The human intestinal cell line SW-620 (ATCC#CCL-227) was used as an *in vitro* model system to evaluate the effects of peptides on gastrointestinal epithelial cell health and viability.[20] The SW 620 cells were grown in Dulbeccos Modified Eagles Medium (DMEM, Gibco) supplemented with 10% bovine serum (FBS, Gibco) at a temperature of 37 °C and 5% CO_2. When the cells reached a confluency level of 70-80%, peptides; **P1**, **P2** and **P3** at a dosage of 1 μM were administered; control group did not receive any peptide treatment. Cells were monitored for a duration of 72 hours using an innovative live cell imaging system called Holomonitor M4 microscope from Phase Holographic Imaging PHI AB, SE. This label-free microscope allowed us to continuously visualize and measure living cells within a humidified cell culture incubator set at 37 °C and 5% CO_2.[21] The cells remained in their culture plates throughout the experiment. The Holomonitor M4 microscope was programmed to capture phase contrast images every 18 minutes at specific positions using a 20× objective lens, ensuring that around 50-100 cells per field were captured over the course of those three days. To analyze these images effectively we utilized the HoloMonitor App Suite (PHI AB), which allowed us to quantify parameters such, as cell count, average cell volume, and percentage of surface area covered by cells (confluence) over time. The data were normalized to zero and are presented as time-lapse graphs that show changes over time at specific intervals (0.17, 7, 15, 24, 36 and 60 h) after the peptide treatment. Statistical analysis was performed using a T-test to compare the groups treated with the peptide to the control groups. This analysis helped determine if there were any differences in cell count, volume and confluence between the two groups.

6.3. Results and Discussion

6.3.1. Peptide designing and hydrogel formation

Nanorod forming self-assembling "T^{55}VYVY^{59}" sequence from the C-terminal SARS CoV E protein motivated us to explore the possibility of hydrogel formation. Inspired by the strong propensity of Fmoc-protected short peptides to self-assemble as a result of π-π stacking interactions between the fluorenyl moieties, we modified the pentapeptide to develop Fmoc-TVYVY. By further rearranging the amino acid residues, we aimed to discover the gelation propensity, understand the molecular mechanism underlying hydrogel formation and to that the role of sequence distribution (Figures 6.1). Here, we adopted the solvent switch method for hydrogel formation. We first dissolved the pentapeptide derivatives at a high concentration (100 mg/ml) in DMSO and then diluted in either 20 mM phosphate buffer (pH 7.4) or in water to trigger hydrogelation. Notably, Fmoc-TVYVY (**P1**) peptide exhibited thermo-responsive gelation. The formation of self-supporting hydrogel was observed within 5 min of incubation at high temperatures (60-80 °C). In contrast, Fmoc-TVVYY (**P2**) demonstrated instantaneous self-
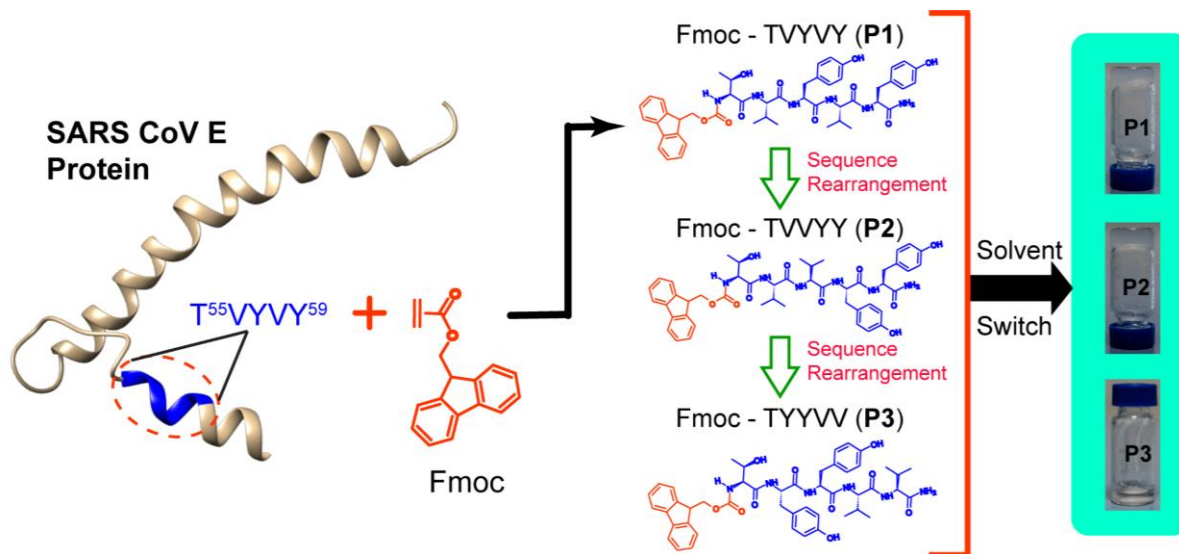
Figure 6.1. Structural Design of Fmoc-Pentapeptides from the SARS-CoV E Protein. A schematic representation illustrating the design of Fmoc-pentapeptides derived from the C-terminal SARS-CoV E protein is presented. The Fmoc group is attached to the N-terminal of the TVYVY sequence, followed by sequence rearrangements leading to the formation of three sequence isomers. The Fmoc-modified peptides exhibit distinct nanoarchitectures upon solvent switch, culminating in the development of hydrogels with unique properties.

supporting hydrogel formation at room temperature, and showed exceptional stability even at high temperatures (checked up to 80 °C). Remarkably, the hydrogel formed by **P2** exhibited extraordinary thixotropic properties for a long period of time after development. Surprisingly, the Fmoc-TYYVV (**P3**) peptide, despite having the same amino acid residues, showed completely different behavior (Figures 6.1). Unlike **P1** and **P2**, which formed self-supporting gels with high water content (~99% (w/v)), **P3** did not form hydrogel under the tested conditions. Thus, a rearrangement in the molecular architecture of the gel forming building blocks may have profound impact on the resulting self-assembled materials. Since **P1** forms thermo-responsive hydrogel that requires high temperatures to establish self-supporting networks, while **P2** assembles quickly at ambient temperature, it suggests that neighboring Tyr residues in **P2** promote stronger aromatic connections, thereby accelerate fiber production and hydrogel assembly. However, alternating Tyr and Val as in P1 requires thermal energy to align and stack due to weaker and more transitory interactions. Rearrangement of the same amino acids eliminates gelation in **P3**, demonstrating sequence selectivity for assembly, particularly the key role of the terminal Tyr residues.

6.3.2. Rheological characterization

The mechanical properties of the hydrogels were examined by carrying out the oscillatory rheological experiments. In rheology, the storage modulus (G′) and loss modulus (G″) are two important parameters associated with viscoelasticity; storage modulus depicts the ability of a deformed material to restore its native state whereas loss modulus indicates the flow behavior of the material under applied stress.[22] Here, hydrogels were prepared at 1 wt%, and the linear viscoelastic region was determined through amplitude/strain sweep experiments within a strain range of 0.01-100%. As depicted in Figure 6.2, hydrogel formation was confirmed for both **P1** and **P2**, as the storage modulus exceeded loss modulus (G′ > G″).[23] Moreover, dynamic strain sweep showed a wide linear viscoelastic region for both **P1**, and **P2** hydrogels, indicating stable gel formation (Figure 6.2A, C). The crossover point (g_c), at which G′ becomes equal to G″, was further determined through the amplitude sweep experiment. For **P1**, G′ and G″ values were ~12259 Pa and ~2280 Pa, respectively, at 0.01% strain (Figure 6.2A). With an increase in the angular strain, the G′ value started to decrease after 0.2% strain and became lower than G″ after g_c = 7.8% (Figure 6.2A). This is the crossover point of **P1** hydrogel, which indicates that the transformation from gel into solution after this point and the value of the G′ as well as G″ at the point was ~1098 Pa. Interestingly, the amplitude sweep analysis for **P2** hydrogel revealed a much higher g_c of ~22.6%
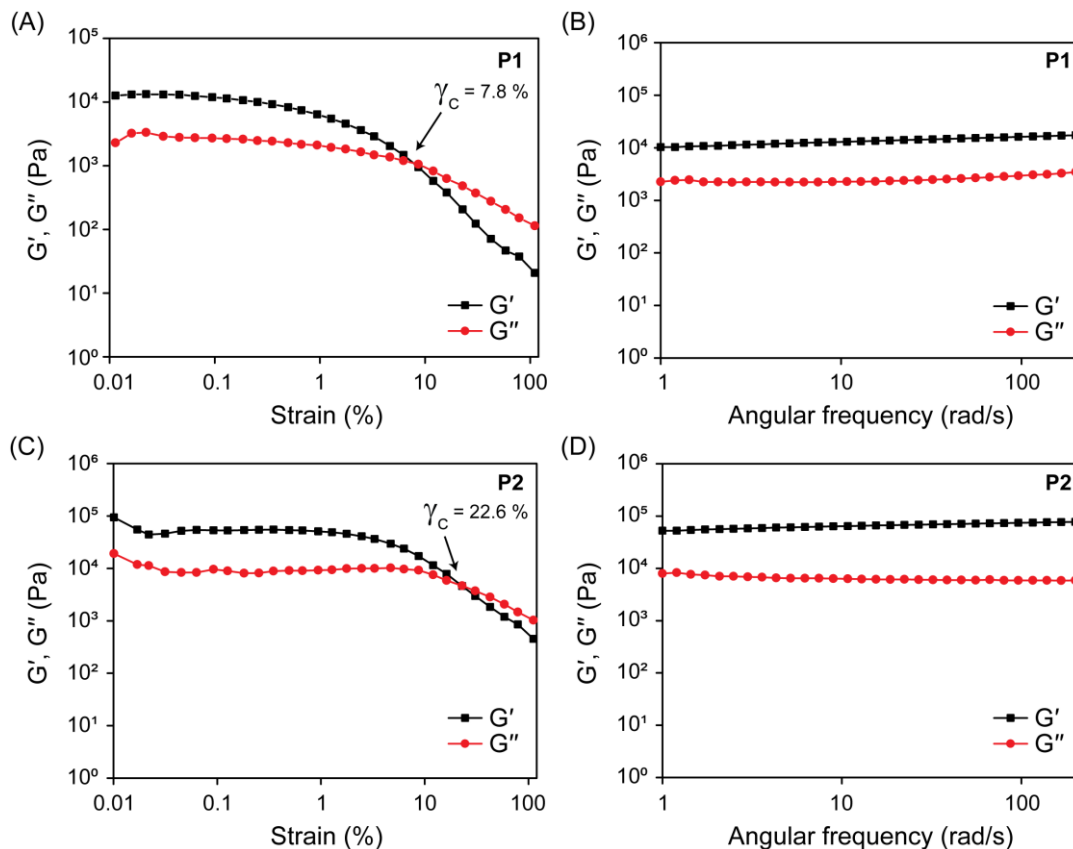
Figure 6.2. Rheological characterization of pentapeptide hydrogels. Rheological strain sweep analyses of (A) **P1**, and (C) **P2** at 1 wt% concentration showing the storage modulus (G') and loss modulus (G"). Rheological frequency sweep experiments for hydrogel (B) **P1**, and (D) **P2** at 1 wt% concentration showing the storage modulus (G') and loss modulus (G").

strain and the value of G' as well as G" at g_c was ~4620 Pa (Figure 6.2C). Therefore, gel-to-sol crossover took place at higher strength for **P2** hydrogel and thus a much higher strain is required to break the gel network for **P2** hydrogel.

Frequency sweep analysis for **P1** and **P2** hydrogels was performed at the linear viscoelastic region (at 0.1% strain) from the amplitude sweep, using a frequency range of 1-200 rad/s. For the hydrogel **P1**, the value of G' varied from ~10300 Pa at 1 rad/s to ~17300 Pa at 200 rad/s and the value of G" varied from ~2250 Pa at 1 rad/s to ~3450 Pa at 200 rad/s (Figure 6.2B). Similarly, for hydrogel **P2**, the value of G' varied from ~52500 Pa at 1 rad/s to ~77600 Pa at 200 rad/s and the value of G" varied from ~8300 Pa at 1 rad/s to ~5890 Pa at 200 rad/s (Figure 6.2D). Therefore, within the linear viscoelastic region, both hydrogels exhibited a G' in the order of 10^4 Pa, with G' always greater than G", indicating significant mechanical strength. Moreover, rheological

measurements clearly depict a higher mechanical strength for **P2**, as obtained from comparing the G′ values and the strain at g_c.

Loss or damping factor (tan δ), a ratio between the moduli (G″/G′), is another crucial parameter for assessing the strength of colloidal forces within the self-assembled networks of soft materials.[24] Usually, a liquid is considered ideally viscous if tan δ > 100, while a solid material is called ideally elastic when tan δ < 0.01, with lower tan δ value indicating the presence of strong interactions. Our experimental observation revealed that the tan δ value for **P1** varied from 0.17-0.23 and for **P2**, it varied from 0.07-0.15. Therefore, a lower tan δ (< 1) observed for both the hydrogels indicates the presence of strong colloidal forces within the self-assembled network and depicts the viscoelastic property of the materials.

Again, frequency sweep experiments were performed for both the hydrogels at higher strain value of 1% to check the properties of the gels at higher strain. It was observed that at higher strain, the value of G′ varied from ~7560 Pa at 1 rad/s to ~5620 Pa at 200 rad/s and the value of G″ varied from ~1750 Pa at 1 rad/s to ~4670 Pa at 200 rad/s, for the hydrogel **P1** (Appendix VI, Figure S6.2A). Similarly, for hydrogel **P2**, the value of G′ varied from ~47800 Pa at 1 rad/s to ~26300 Pa at 200 rad/s and the value of G″ varied from ~6720 Pa at 1 rad/s to ~10300 Pa at 200 rad/s (Appendix VI, Figure S6.2B). The value of damping factor (tan d) varied from 0.3-0.8 for hydrogel **P1** and 0.26-0.45 for hydrogel **P2**. Therefore, with increasing strain, mechanical strength of both the hydrogel decreased. As crossover point for hydrogel **P2** was greater than hydrogel **P1**, therefore mechanical strength of hydrogel **P2** was significantly higher than hydrogel **P1** at higher strain of 1%. Time-sweep oscillatory measurements were performed for **P2** hydrogel, which confirmed its thixotropic property (Appendix VI, Figure S6.3). The applied angular frequency was kept constant at 1 rad/s throughout the experiment and 0.1 and 50% strain values were repeatedly applied at definite intervals. During the first 250 s interval of 0.1% strain, G′ values (~90000 Pa) were greater than G″ values (~10000 Pa) which indicates the distinct gel characteristics (Figure S3). At the next interval, strain was rapidly enhanced to 50% and maintained for 250 s. The G′ value sharply decreased, and it became ~120 Pa which is lower than G″ values (~180 Pa) indicating the dissipation of the gel network and gel-to-sol transition. Again, at the next interval, the applied strain was rapidly decreased to 0.1%, and this constant strain was maintained for 500 s. At this interval, the G′ value further increased (~5100 Pa to 7100 Pa) and it became greater than
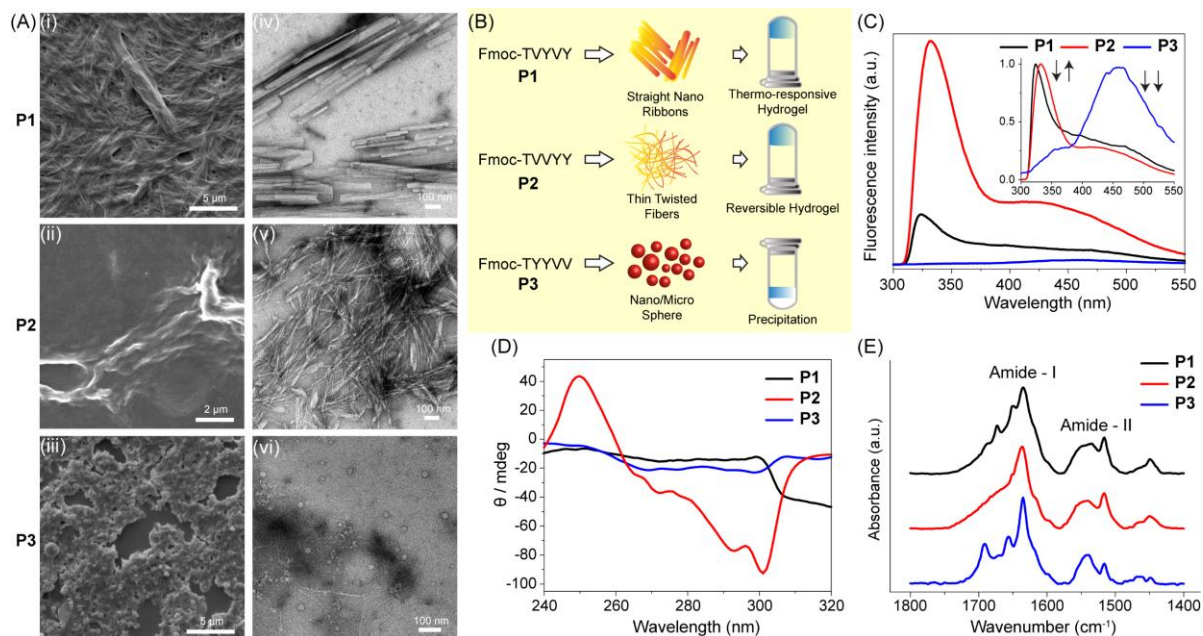
Figure 6.3. Microscopy images of Fmoc-TVYVY, Fmoc-TVVYY, and Fmoc-TYYVV showing different nanostructures. (A) SEM images of (i) **P1**, (ii) **P2**, and (iii) **P3** peptide taken at 1wt% concentration after air drying. Negatively stained TEM images of (iv) **P1**, (v) **P2**, and (vi) **P3** peptide nanostructures taken at 1 wt% concentration. (B) Schematic illustration of self-assembled nanostructures formed by **P1**, **P2**, and **P3** suggested from microscopy. (C) Intrinsic fluorescence spectra of **P1**, **P2**, and **P3** taken at 1wt% concentration with excitation wavelength of 280 nm. Inset shows normalized spectra where arrows at 330 nm represents antiparallel and at 460 nm represents parallel arrangements of fluorenyl moieties. (D) Near-UV CD spectra of **P1**, **P2**, and **P3** taken at 1wt% concentration showing induced chirality upon supramolecule formation. (E) FTIR spectra of **P1**, **P2**, and **P3** taken at 1wt% concentration indicating predominantly β-sheet conformation. All spectra are color coded.

the values of G″ (~700 to 1000 Pa) indicating the restoration of the gel character. The whole process was repeated twice to confirm the reversibility of the restoration process. Although the mechanical rigidity was not completely restored after decreasing the strain, **P2** hydrogel was able to repeatedly retain its mechanical strength even after multiple high strain cycles.

6.3.3. Nanofiber morphology

Upon confirming the formation of hydrogels, we examined the morphology and topology of the Fmoc-pentapeptides hydrogels/supramolecular assemblies using scanning electron microscopy (SEM), and negative stain transmission electron microscopy (TEM) (Figure 6.3A(i-vi)). SEM imaging revealed that the **P1** peptide forms ribbon-like structures, which overlap onto

one another and thereby forming a micro-porous network to entrap the water molecules. **P2**, on the other hand formed a highly dense hydrogel with smooth surface (Appendix VI, Figure S6.4). Interestingly, **P3**, despite not forming a self-supporting hydrogel, displayed self-assembled micelle-like aggregates. High-resolution negative stain TEM imaging further provided a detailed information on the nanostructure morphology (Figure 6.3A(iv-vi)). TEM imaging revealed that **P1** peptide forms straight ribbon-like structures with an average width of 45 ± 16 nm. **P2** peptide self-assembled into thin twisted ribbons that leads to formation of dense networks. The average width for these thin twisted fibers were found to be 11 ± 3 nm. **P3**, on the other hand, self-assembled into nanospheres with an average diameter of 20 ± 5 nm, which eventually leads to precipitation. These differences in the morphologies highlight how subtle changes in molecular composition impact self-assembled structures (Figure 6.3B). The wider, straight nanoribbon formed by the **P1** hydrogel network likely enables them to slide past one another when shear forces are applied during rheological testing; such sliding motions provide less resistance, corresponding to the 10-fold lower hydrogel storage modulus (Figure 6.2). In contrast, the thin twisted ribbons of **P2** hydrogel networks are more narrowly spaced with higher density packing. The tighter integration resists sliding motions upon shearing. Instead, the ribbons likely undergo tensegrity-type deformations, similar to tensegrity structures encountering forces at the joints. This tensegrity mechanism confers greater mechanical rigidity correlating with the higher storage modulus.

6.3.4. Spectroscopic characterization of molecular arrangement

In order to compare the molecular arrangement between these peptide variants, we performed fluorescence emission spectroscopy at 1 wt% peptide concentration (Figure 6.3C). We observed that the **P1** peptide, which forms thermo-responsive hydrogel, showed emission maximum at 324 nm and a flat tail at visible region. In contrast, the emission spectrum of **P2** indicated a fluorescence maximum at 332 nm and broad tail centered at around 450 nm. Interestingly, the peptide **P3** did not show sufficient fluorescence emission and underwent sedimentation; giving a comparatively broad emission around 460 nm. It has been observed that the different arrangements of aromatic rings can induce distinct shifts in the emission peaks.[10, 25] It is noteworthy to mention that the emission maximum at around 330 nm is representative of anti-parallel arrangements, whereas the emission maxima at around 460 nm is indicative of parallel arrangements of aromatic fluorenyl moieties (J-aggregates).[7, 26] Thus, our experimental observation suggests that both the peptides **P1** and **P2** has predominantly anti-parallel arrangement

accompanied by weak parallel arrangements. However, **P2** has a slightly more parallel arrangement compared to **P1**. Surprising, pentapeptide **P3** prefers mostly parallel arrangements, which allows nanosphere to form and coalesce and finally sediment. Moreover, variations in the positions of Tyr residues among the respective peptides may lead to differential fluorenyl-Tyr interactions, which are also likely to contribute to a certain degree.

The supramolecule formation of the pentapeptides within the hydrogels/supramolecular assemblies were also investigated using circular dichroism (CD) spectroscopy (Figure 6.3D). The CD analysis of peptide-based supramolecular materials is prone to artifacts, necessitating careful consideration to avoid light scattering effects.[7, 27] Here, a concentration of 10 mg/mL was considered for measuring near-UV CD spectra. The Fmoc group is inherently achiral in nature and remains CD silent when in free solution. However, it exhibits a robust Cotton effect when organized within a supramolecular chiral environment.[28, 29] Due to the π-π staking of aromatic groups, induced supramolecular chirality can be observed in the wavelength range 240-320 nm. Particularly, the negative peak around 300 nm is associated with the π-π* transition of fluorenyl absorption. Absorptions in 250-295 nm range are due to the transfer of chirality to the fluorenyl group as a result of self-assembly. As depicted in Figure 6.3D, all three peptide systems show negative band in the wavelength range of 260-310 nm, associated with fluorenyl absorption. However, in terms of magnitude, **P2** exhibits highest molar ellipticity than other two. Furthermore, the chirality of supramolecular assembly for **P2** was found to be more pronounced and left-handed in nature (as detected by the negative CD absorbance at 302 nm).[28]

We then performed Fourier-transform infrared spectroscopy (FTIR) to further expand our understanding of the secondary structure within the hydrogels (Figure 6.3E). The amide I region of the FTIR absorbance spectra of hydrogels/supramolecular assemblies showed a distinct peak at ~1634 cm^{-1} and a hump peak at ~1690 cm^{-1}, suggesting a β-sheet conformation, possibly in an anti-parallel arrangement as well as a stacked carbamide groups.[30] Amide I bands were further deconvoluted and peaks were assigned to β-sheet, α-helix, 3_{10}-helix/turn, and random coil regions as depicted in Appendix VI, Figure S6.5. The deconvolution of the amide I band from FTIR spectra revealed differential secondary conformation within the peptide variants. Interestingly, the β-sheet conformation was found to be predominant for all three peptides, while different percentage of alpha helix, 3_{10}-helix/turn were observed. Of note, **P3**, which doesn't form hydrogel also adopts

β-sheet conformation. We then performed thin-film X-ray diffraction (XRD) for **P1**, **P2**, and **P3**, which further validated the presence of a β-sheet secondary structure (Appendix VI, Figure S6.6).

6.3.5. Self-assembly mechanism

To check wheather these self-assembled morphologies are also present at low concentration, we performed atomic force microscopy (AFM) imaging for all three peptides at diluted concentration (Figure 6.4A). AFM images indicated an identical structure to that of the gel state, where **P1** showed straight ribbons overlapped onto one another; **P2** exhibited a dense network of thin fibril structures. **P3**, on the other hand, displayed nano-sphere like structures that well resembles the TEM imaging.

A comprehensive understanding of the self-assembly hold significant importance, as it offers key insights into the mechanism of fibril formation. Amyloid-like character of the peptides was first examined using thioflavin-T (ThT) fluorescence assay,[31] where all three peptides displayed rapid self-assembly (Figures 6.4B and Appendix VI, Figure S6.7). Within few minutes of incubation at room temperature, all three-peptide reached saturation without having any observable lag time. Binding of ThT molecule to the peptide aggregates also reflected in the quenching of their intrinsic fluorescence (Appendix VI, Figure S6.8), and visualized in fluorescence confocal microscopy (Appendix VI, Figure S6.9). We next investigated the molecular arrangement of the fluorenyl moieties during self-assembly for these peptides using concentration dependent intrinsic fluorescence spectroscopy (Figure 6.4C). With increase in the peptide concentration, **P1** showed a red shift from 315 nm to 323 nm with profound increase in the fluorescence intensity, suggesting possible excimer formation with an anti-parallel arrangement of the fluorenyl moieties. In contrast, we observed a slight increase in the fluorescence intensity for the maxima centered at 485 nm, representative of parallel arrangements. **P2** exhibited a greater red shift of the fluorescence maxima at 315 nm to 332 nm, with a significant increase in fluorescence intensity at 485 nm. **P3**, on the other hand, demonstrated a distinct behavior in the intrinsic fluorescence with major fluorescence maxima at 485 nm, indicating predominantly parallel arrangements of fluorenyl moieties. Interestingly, the normalized excitation fluorescence spectra of all three peptides for the peak centered at 485 nm indicated variations in the absorption of fluorenyl and tyrosine moieties (Appendix VI, Figure S6.10).
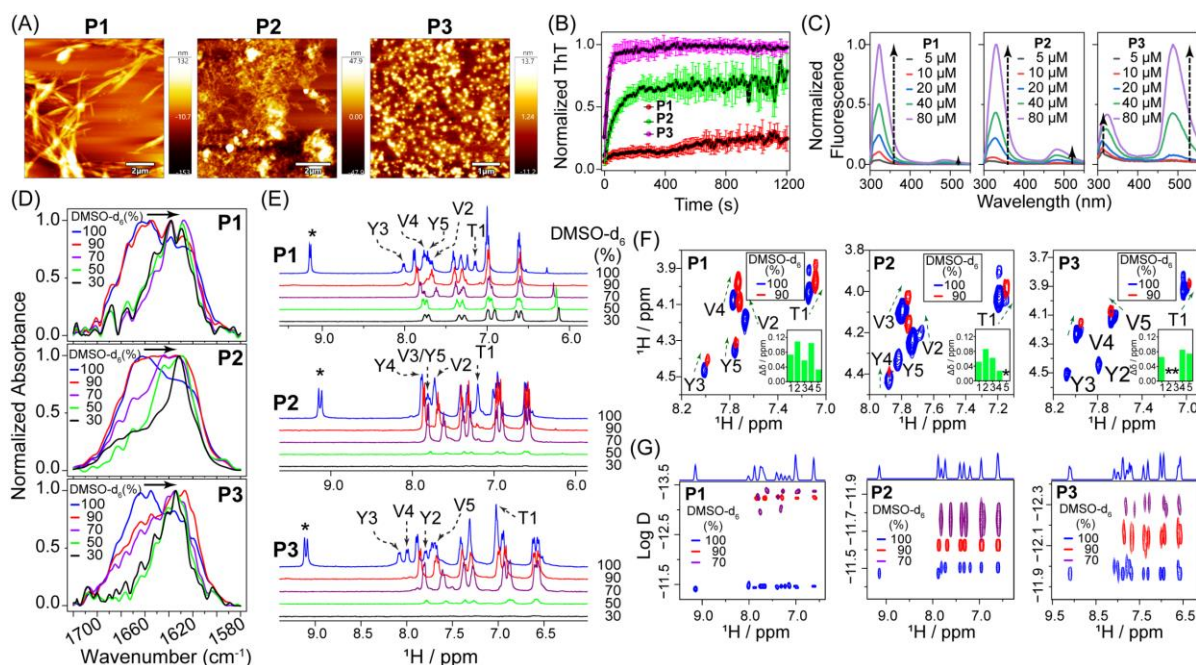
Figure 6.4. Mechanisms of self-assembly. (A) AFM images of **P1**, **P2**, and **P3** at taken at 0.1 wt%, which was diluted from a 1 wt% sample, showing morphological similarities with the TEM image from Figure 1 for respective peptides. (B) ThT fluorescence assay of the peptides suggesting amyloid-like character. (C) Concentration-dependent intrinsic fluorescence spectra of **P1**, **P2**, and **P3** indicating differential molecular arrangements during self-assembly. (D) FTIR spectra of **P1**, **P2**, and **P3** at different DMSO-d_6 percentages showing structural transition from 3_{10}-helix to β-sheet. (E) 1D-^{1}H NMR spectra of **P1**, **P2**, and **P3** at different DMSO-d_6 percentages showing both line broadening and chemical shift changes upon water exposure. The asterisk (*) marks highlight the immediate broadening of proton peak associated with Fmoc group for all three peptides. (F) 2D TOCSY NMR spectra of **P1**, **P2**, and **P3** at 100 % DMSO-d_6 (blue), and 90 % DMSO-d_6 (red) highlighting chemical shift perturbation associated with respective amino acid residues. Inset shows the bar plot of chemical shift perturbation (CSP) for each peptide. (G) The pseudo 2D DOSY spectra of 0.5 mg/mL **P1**, **P2**, and **P3** at different DMSO-d_6 percentages (100 %= blue, 90 %=red, and 70 %= purple). All experiments were performed at 298 K.

We next compared the fluorescence emission spectra between gel and solution state. The emission spectrum of the peptides in sol phase (in 100% DMSO) revealed a fluorescence maximum at ~318 nm, suggesting monomeric state. Changes in the emission spectra for peptides at gel/aggregate state (10 mg/ml) resulted from an increase in intermolecular interactions and self-assembly (Appendix VI, Figure S6.11A). The red shift in the fluorescence maxima clearly indicated the possible existence of a fluorenyl excimer species.

To understand the molecular mechanism of self-assembly leading to gelation, we used various biophysical techniques at different DMSO: water ratio. We first performed FTIR spectroscopy both a high and low concentration and in presence of different DMSO percentages. At 100% DMSO the peptides remain at monomeric condition (both at high and low concentration) under which the peptide adopts predominantly 3_{10}-helix conformation (FTIR absorbance maximum at 1663 cm^{-1}); whereas at 30% DMSO, β-sheet structures were most abundant (FTIR absorbance maximum at 1634 cm^{-1}) (Appendix VI, Figure S6.11B). This transition from 3_{10}-helix to β-sheet conformation was distinctly observed at a low peptide concentration (Figure 6.4D). This gradual transition in the peptide secondary conformation clearly indicates the influence of water molecules in the self-assembly.

In order to get an atomic resolution insight of the self-assembly process we utilized 1D ^{1}H NMR under similar conditions. Each amino acid residues in the 1D NMR spectra for individual peptides were assigned from 2D ^{1}H-^{1}H total correlation spectroscopy (TOCSY) in combination with nuclear Overhauser effect spectroscopy (NOESY) experiments (Appendix VI, Figures S6.12-14). With increase in the water content, we observed both decrease in the NMR signal intensity and chemical shift perturbations (CSPs) in the amide proton peaks for all three peptides, thereby suggesting conformational changes and self-assembly (Figure 6.4E). Interestingly, for all three peptides, the proton peak associated with the Fmoc group (near 9.1 ppm) were found to be completely broadened upon addition of 10 % water, suggesting the immediate involvements of the Fmoc group in the self-assembly process. 2D TOCSY NMR spectra at 100 %, and 90 % DMSO-d_6 further highlighted the involvement of individual amino acid residues in the self-assembly and to that the role of water molecules (Figure 6.4F). Interestingly, we found that Tyr residues showed predominantly intensity decrease as a result of π-stacking, whereas Val residues showed significant CSPs suggesting their involvement in conformational transitions. Temperature co-efficient calculated from the temperature-dependent 1D NMR further revealed that the 3_{10}-helix structures in the monomeric state are possibly stabilized by hydrogen bonding, particularly by the Tyr residues (Appendix VI, Figure S6.15).

Furthermore, we conducted diffusion ordered spectroscopy (DOSY) on the selected peptides at various DMSO-d_6 percentages. By comparing the pseudo 2D DOSY NMR spectra at different DMSO-d_6 percentages, it becomes evident that all three peptides exhibit changes in their

diffusion rate due to aggregation (Figure 6.4G).[4] In the absence of the water, **P1** showed a diffusion coefficient of -11.46 log (m^{2}s^{-1}). Upon addition of 10 % D$_2$O, the diffusion coefficient decreased to -13.23 log (m^{2}s^{-1}), which further decreased to -13.38 log (m^{2}s^{-1}) at 70 % DMSO-d$_6$. Similarly, at 100 % DMSO-d$_6$, peptide **P2** showed a diffusion coefficient of -11.50 log (m^{2}s^{-1}). With increase in the water content the diffusion coefficient was found to gradually decrease; At 90% DMSO-d$_6$ the diffusion coefficient was -11.62 log (m^{2}s^{-1}), and at 70 % DMSO-d$_6$ it was -11.76 log (m^{2}s^{-1}). Similarly, **P3** exhibited a diffusion coefficient of -11.96 log (m^{2}s^{-1}) at 100 % DMSO-d$_6$, which gradually decreased to -12.14 log (m^{2}s^{-1}) at 90 % DMSO and -12.30 log (m^{2}s^{-1}) at 70 % DMSO. Thus, the diffusion coefficient of **P1** indicated 1.91 points while **P2** and **P3** showed a 0.26, and 0.34 points change, respectively in diffusion by the addition of water. These effects prompted us to conclude that all three peptides were involved in self-assembly. However, **P1** aggregates, having lowest diffusion constant among all, were much larger in size when compared with the other two peptide variants (**P2** and **P3**), corroborating with the microscopy data.

6.3.6. Cryo-EM-based ultrastructural analysis

While most of these studies were performed at room temperature, we wanted to explore more to understand the ultra-structure of **P1**, **P2**, and **P3** at near-native physiological conditions. Thus, single-particle cryo-EM was employed to elucidate the ultra-structure of these three peptides. We observed thick, flat, straight ribbon-like structure for **P1** with an average diameter ranging from 8 nm to 40 nm at cryogenic conditions, which is closely related to our negative staining TEM and AFM data (Figures 6.5A and Appendix VI, Figure S6.16). However, negative staining images showed that the diameter of **P1** hydrogel is slightly higher (almost by 5 nm); one possibility is that the hydrogel's dehydration and flattening effect during negative staining made it appear as a thicker filament than cryo-EM images. We also performed cryo-EM reference-free 2D classifications of thin (smaller diameter) filaments to understand the arrangement of the **P1** peptide. Reference free 2D class averages showed that most of the thin filaments were within about 7-13 nm diameter, and peptides were parallelly assembled to adopt the ribbon-like structure (Figure 6.5A, Appendix VI, Figure S6.16). However, the thick filaments were overlapped with each other, and thus, thick filaments were avoided for 2D classification calculation. Moreover, we did not visualize any spiral or twist morphology in ribbon-like filamentous structures. Additionally, we calculated the distance between two individual peptides using the EMAN and RELION layer
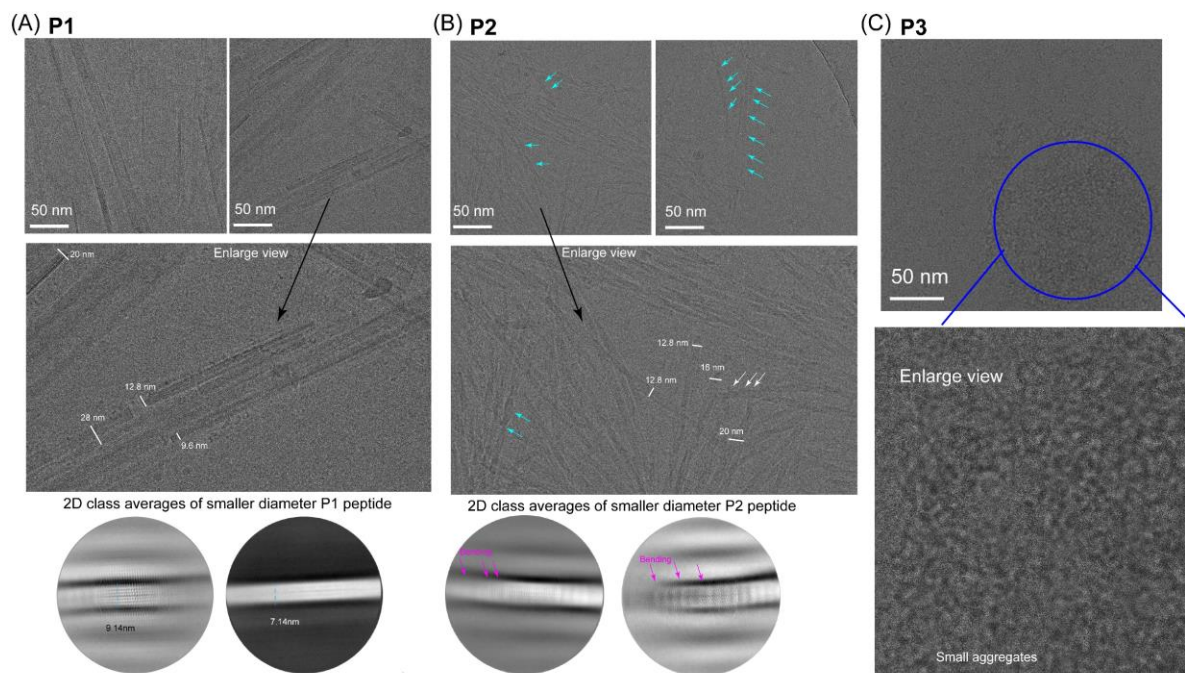
Figure 6.5. Cryo-EM visualization and 2D classification of P1, P2, and P3. (A) Cryo-EM images of **P1** of two different areas show thick flat straight ribbon-like structure with an average diameter varied from 8 nm to 40 nm. 2D class averages show a parallel arrangement of peptides, which maintain a similar distance between individual peptides. No spiral or twist is observed between the peptide assembly. (B) **P2** peptide forms a comparatively thin spiral and twisted ribbons-like structure, which forms a dense network-like structure. The diameter of ribbons is more homogeneous than **P1**. 2D class averages show the parallel arrangement of peptides, which maintain similar distances between individual peptides. No spiral or twist is observed between the peptide assembly. However, 2D class averages indicate peptides are more closely packed than **P1**. (C) Cryo-EM image of **P3** showing self-assembled micelle-like aggregates.

line profile, demonstrating that the distance between individual peptides was ~ 4.58 - 4.82Å (Appendix VI, Figure S6.17A-B). However, due to the low resolution of 2D class averages and noisy layer lines, we were unable to pinpoint the exact distance between the peptides. From 2D class averages of cryo-EM images, 2D averages of thin and thick filaments and raw particles clearly showed extremely heterogeneous filamentous assembly of **P1** peptides (Figures 6.5A, Appendix VI, S6.16A-D and S6.17A-B). Furthermore, **P2** and **P3** were characterized using cryo-EM (Figure 6.5B-C). The cryo-EM images and 2D class averages indicate that the **P2** peptide was assembled as thin twisted filaments, which formed a mesh-like structure (Figure 6.5B). Most of the filament's diameter was within the range of ~6-20 nm (probable diameter) with a bending and

twist within the **P2** filament. This bending and twisting were also visible in 2D class averages (Figures 6.5B, Appendix VI, Figure S6.19 and S6.18A-B). Furthermore, like the **P1** peptide, we calculated the distance between the two individual peptides using the EMAN and RELION layer line profile, and surprisingly, it indicated a very similar distance between the individual peptides, which assembled parallelly with an average inter-peptide distance of ~4.84 Å (Appendix VI, Figure S6.18A-B). We then calculated the inter-peptide distances of several other class averages, which indicates that inter-peptide distance is in between ~4.84 Å; this strongly suggests that the **P2** peptide is more homogeneous than **P1**. This homogeneous assembly of **P2** was also observed in our cryo-EM data, individual particles, and 2D class averages. **P3,** on the other hand, appeared as self-assembled micelle-like aggregates at cryogenic conditions (Figure 6.5C). We were unable to calculate any 2D class averages of these micelle-like aggregates.

Our cryo-EM results, together with negative stain TEM and AFM experiments suggest that drying has no significant role in altering the structure of these **P1**, **P2**, and **P3** hydrogels/assemblies. Furthermore, based on our above observations, we proposed that the pentapeptides **P1** and **P2** form filamentous nanofiber structures, where **P2** is more twisted and homogeneous in diameter.

Next, to understand structural information of **P2**, two-dimensional ^{1}H-^{13}C cross polarization (CP) experiment was performed at a magnetic field corresponding to 500 MHz ^{1}H Larmor frequency with 15 kHz MAS frequency (Appendix VI, Figure S6.20). Broad signals were observed in the aliphatic region after 50 k scans (green trace), suggesting the heterogeneity in the sample.[32] Dipolar coupling-based coherence transfer suggests that the sample is rigid in nature (^{1}H-^{13}C order parameters are close to 1).[2] This was confirmed by scalar coupling based INEPT experiments employing at 55 kHz MAS (B$_0$ field corresponding to 800 MHz ^{1}H Larmor frequency). Apart from a sharp feature originating from DMSO, there are no other ^{13}C peaks originating from the hydrogel. ^{13}C 1D spectrum under the same condition recorded with direct excitation also shows DMSO resonance only. We were able to record CP based ^{1}H-^{13}C correlation at 55 kHz MAS (under low power proton decoupling). The spectrum only features the methyl resonances, where the intensity is proportional to the proton density. However, heterogeneity is also visible from the number of methyl cross peaks. Collectively, no structural information was obtained either from CryoEM or solid-state NMR due to the heterogeneity of the sample.

6.3.7. Phase Holographic Imaging
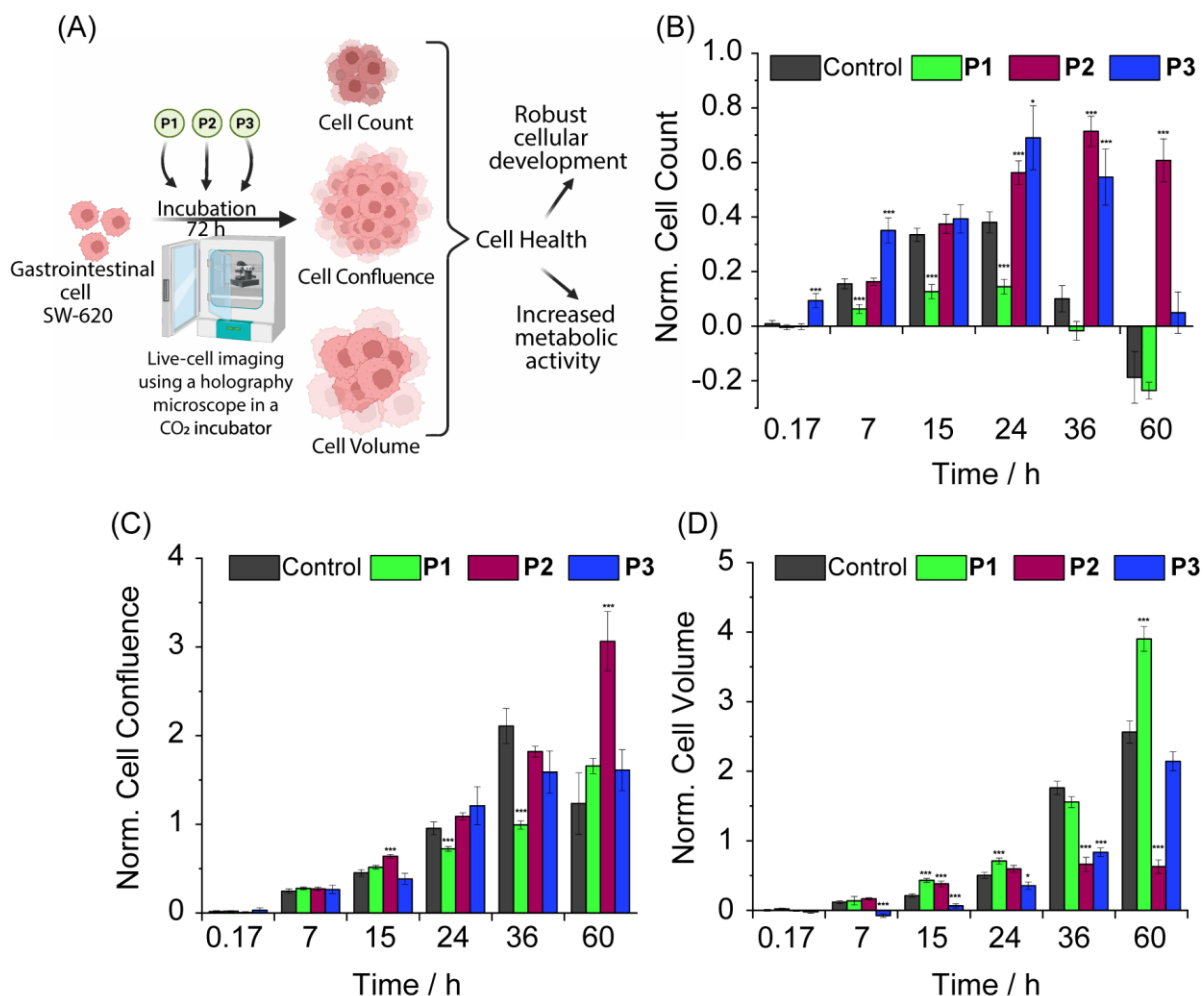
Figure 6.5. Impact of peptides P1, P2, and P3 on the health and growth characteristics of intestinal epithelial SW620 cells over time. (A) Schematic representation of the characterization of peptide impact on gastrointestinal cell SW-620: The figure illustrates the setup for studying the effects of peptides (**P1**, **P2** and **P3**), on SW-620 cells. The cells were cultured in DMEM medium supplemented with serum. Peptides were administered when the cell confluence reached 70-80% alongside a control group. The responses of the cells were observed using a Holomonitor M4 holography microscope, which captured phase contrast images. Analysis of cell count, volume and confluence was performed over a duration of 72 h. (B) Time-lapse depiction of the effect of peptides on SW620 cell count. The average normalized cell counts over the specified intervals are shown as bars in graph. (C) Time-lapse visualization of the effect of peptides on SW620 cell confluence are shown as bars in graph. (D) Time-lapse illustration of peptides' effect on SW620 cell volume over the specified intervals. Statistical significance was determined using a T-test, comparing the effects of each peptide at 0.17, 7, 15, 24, 36, and 60-hour time points to their respective controls. A value of $p<0.05$ was considered statistically significant, ***$p < 0.0001$.

Encouraged by previous studies which showed peptide hydrogels can promote cell growth and viability,[33] we have investigated if **P1**, **P2**, and **P3** hydrogels/supramolecular assemblies could exhibit similar bifunctionality to support mammalian cell health. Using a label-free holographic microscope (HoloMonitor M4) inside an incubator,[34] we visualized cell growth dynamics of human intestinal cells SW620 treated with **P1**, **P2**, and **P3** or untreated (Figure 6.6A, Appendix VI, Figure S6.21). Analyzing impacts on cell counts gave insight into peptide effects on cell viability and growth.[35] Early on at 0.17 h, **P3** significantly boosted counts to 0.093±0.02 versus 0.009±0.01 in controls (p=0.004). By 7 h, **P1** had suppressed counts to 0.062±0.01 compared to 0.15±0.01 in controls (p=0.0004). At 24 h, **P2** and **P3** increased counts to 0.56±0.04 (p=0.002) and 0.69±0.11 (p=0.01) respectively, versus 0.38±0.03 in controls. **P2** and **P3** continued stimulating growth at 36 h with counts of 0.71±0.05 (p<0.00001) and 0.54±0.10 (p=0.0003) versus 0.10±0.04 for controls. Finally at 60 h, **P2** markedly boosted counts to 0.60±0.07 compared to -0.18±0.09 in controls (p<0.00001) (Figure 6.6B). These observations suggest that **P2** is consistently elevating, **P3** early elevating, and **P1** suppressing cell counts over time.

Cell confluence is an important parameter which displays the cell growth and migration capabilities.[36] Peptides did not affect confluence prior to 15 h. At 24 h, **P1** decreased confluence to 0.72±0.02 (p=0.005), whereas **P2** increased it to 1.08±0.03 (p=0.010), compared to 0.95±0.07 in controls. **P1** decreased considerably to 0.99±0.04 (p<0.00001) from 2.10±0.19 in controls after 36 h. At 60 h, **P2** dramatically increased confluence to 3.06±0.33 vs to 1.23±0.34 in controls (p=0.001) (Figure 6.6C). These results suggest that **P2** persistently increased, **P1** decreased, and **P3** altered confluence over time, indicating that intricate peptide affects cell growth and migration.

Cell volume reveals the metabolism and health status of cells.[37] Peptides did not affect volume until 15 h, except for **P3**, lowering it at 7 h (p<0.000001) compared to controls. After 15 h, **P1** and **P2** increased volume to 0.43±0.02 (p<0.000001) and 0.37±0.04 (p=0.0010), but **P3** decreased volume to 0.06±0.03 (p=0.0005) compared to 0.21±0.02 in controls. **P1** later increased while **P2** and **P3** decreased volume compared to controls. At 60 h, **P1** increased volume to 3.90±0.17 (p<0.00001) whereas **P2** dropped it to 0.62±0.09 (p<0.000001) compared to 2.5±0.16 in controls (Figure 6.6D). These results suggest that **P1** elevated, and **P2** and **P3** decreased cell volume with time, indicating varying peptide effects on cell health and metabolism.

Our research indicates that peptides **P1**, **P2**, and **P3** have an impact on cell health. Our findings demonstrate that the number of cells and their density increased over time when exposed to **P2** suggesting its ability to promote cell growth. On the other hand, while **P1** reduced cell quantity and increased volume both **P2** and **P3** caused volume reductions at specific intervals indicating potential metabolic changes. Overall, our label free holography microscopy imaging technique effectively showed the effects of **P2** on cell health throughout a span of 70 h. These findings show that this novel holography microscopy-based method is a better way to get time-lapse data than static imaging methods that need to be fixed or endpoint assays like MTT.

6.4. Conclusion

In summary, we have demonstrated the designing strategy and the development of Fmoc-modified pentapeptide derivatives from the C-terminal SARS CoV E protein. We explored the relationship between peptide sequence and the gelation propensity by utilizing various spectroscopic techniques, which verified the π-π staking into β-sheet structure. Depending on the peptide sequence distribution, different degrees of anti-parallel or parallel arrangements of fluorenyl moieties were evident in the fluorescence spectra, which corresponded to the different morphologies of the self-assembled structures within the hydrogels. SEM, TEM, and AFM indicated that the **P1** hydrogels were formed from high aspect-ratio straight nanoribbons. In contrast, **P2** hydrogels had more entangled and interconnected thin twisted ribbon-like structures, resulting in more stable hydrogels. **P3**, on the other hand, has parallel arrangement into nanosphere structures, resulting in sedimentation. Moreover, these nanostructured materials exhibit varied impact on the human intestinal cell health and metabolism, necessitating further investigations. Therefore, just by changing the sequence distribution, we have unlocked the development of a wide variety of functional nanomaterials. Due to their viral origin, peptides derived from SARS CoV E protein may hold inherent ability to interact specifically with human cells, making them suitable in targeted drug delivery systems or therapeutic applications, especially for coronavirus-related diseases or other associated disorders.

6.5. Appendix VI
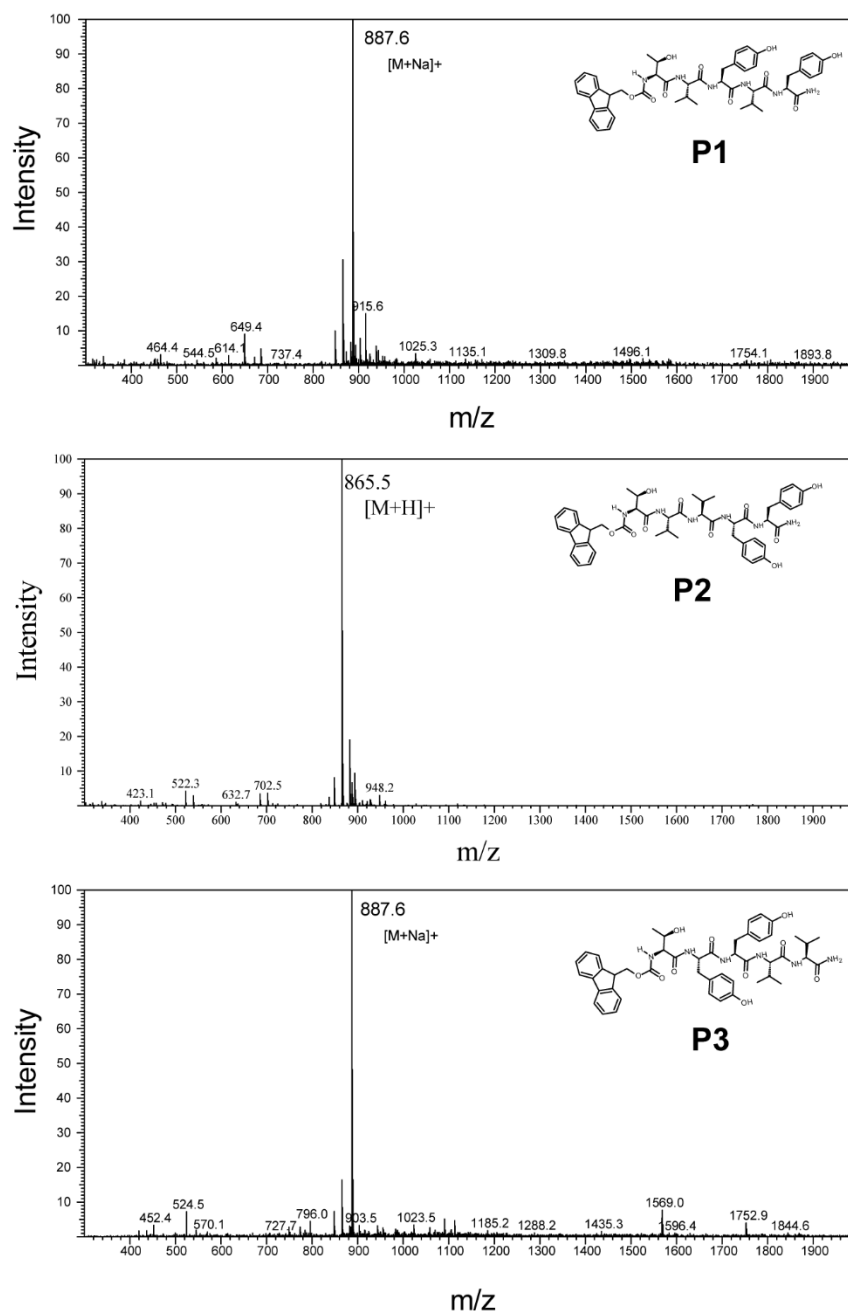
Figure S6.1. Mass spectrum of peptide **P1**, **P2**, and **P3**.
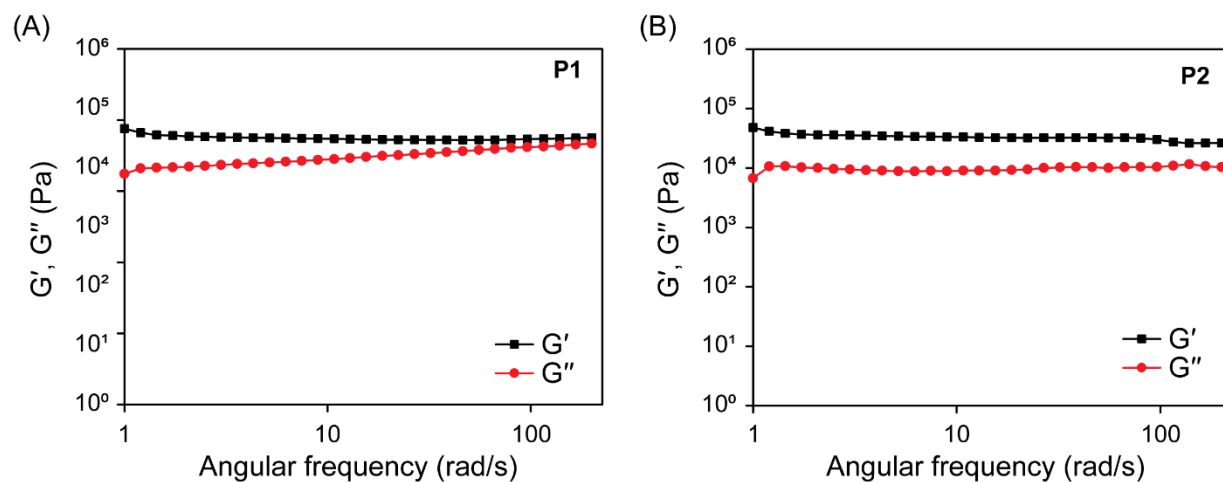
Figure S6.2. Frequency sweep experiments for hydrogel (A) **P1** and hydrogel (B) **P2** at higher strain of 1%.
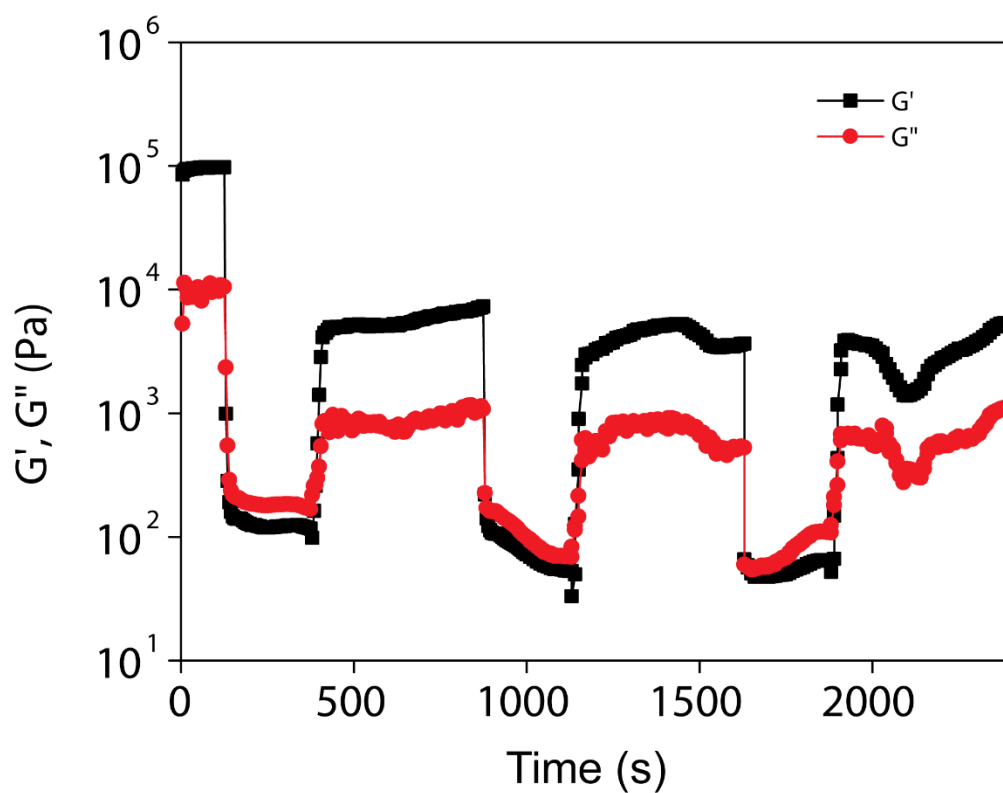
Figure S6.3. Thixotropic behavior of **P2** hydrogel.
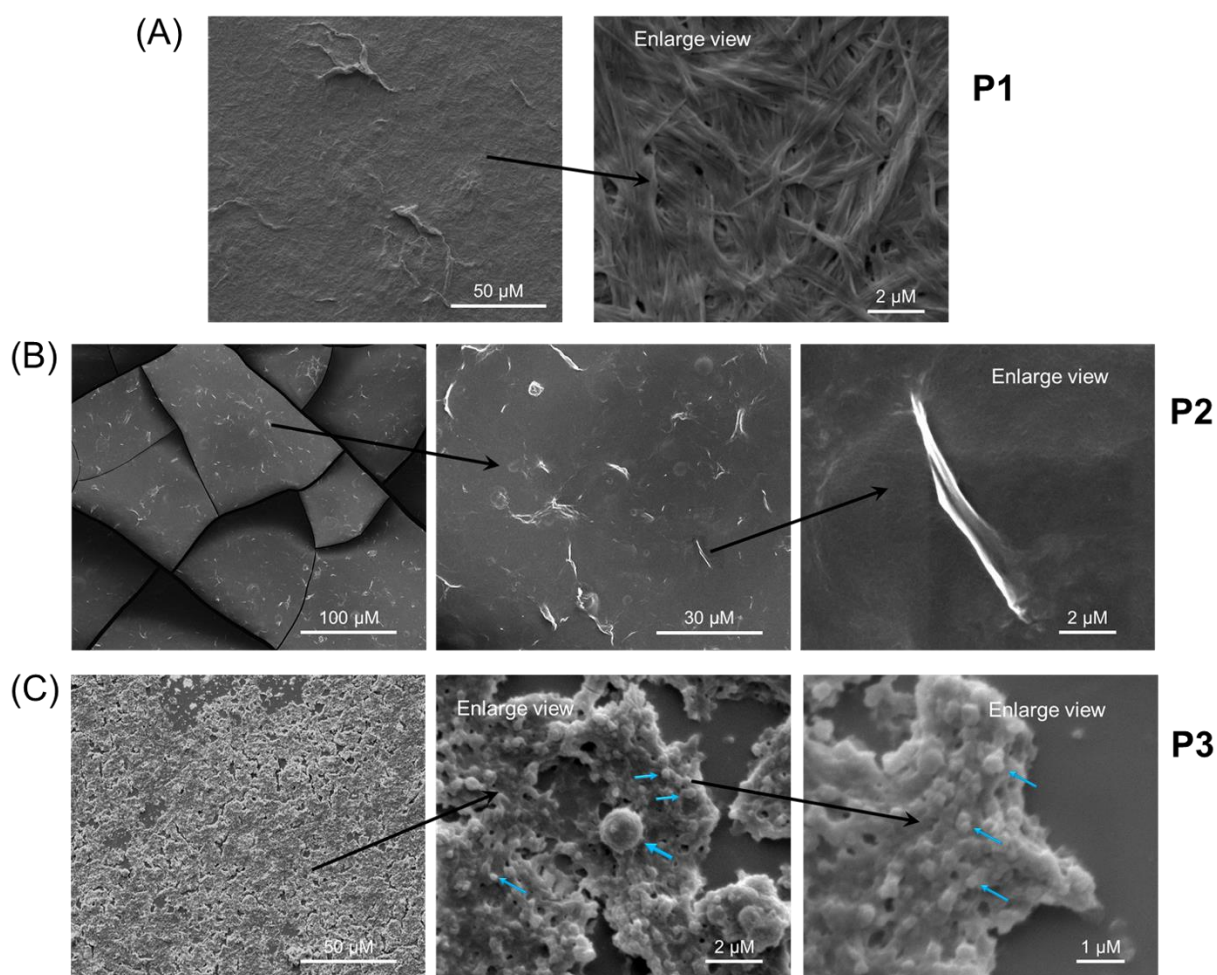
Figure S6.4. SEM images of air dried (A) **P1**, (B) **P2** hydrogels, and (C) **P3** aggregates at different magnifications, showing distinct self-assembled morphology.
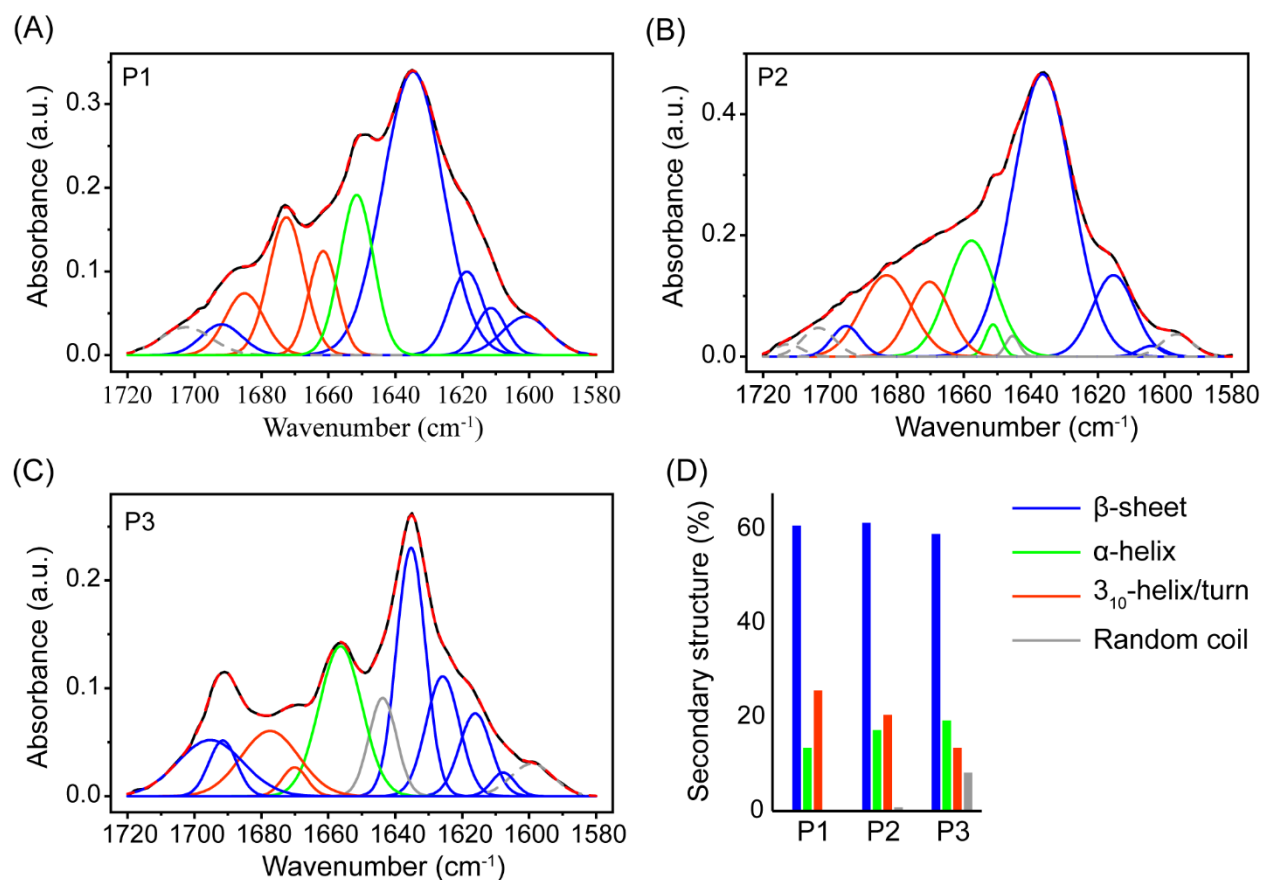
Figure S6.5. Deconvolution of the amide I region in FTIR spectra for (A) **P1**, (B) **P2**, and (C) **P3** peptides. (D) Computed percentage of secondary structure for **P1**, **P2**, and **P3** based on the deconvolution analysis.
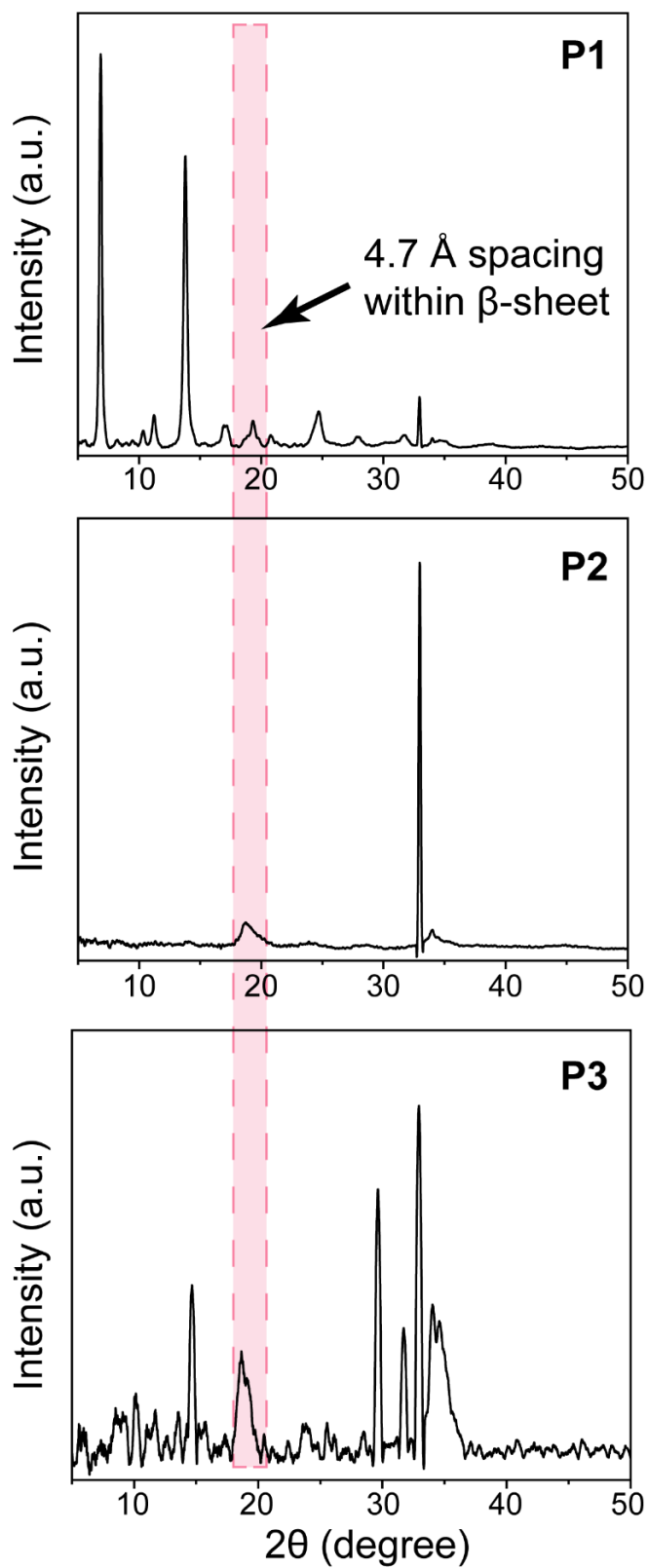
Figure S6.6. Thin film XRD profile of **P1**, **P2**, and **P3** indicating presence of β-sheet secondary structure.
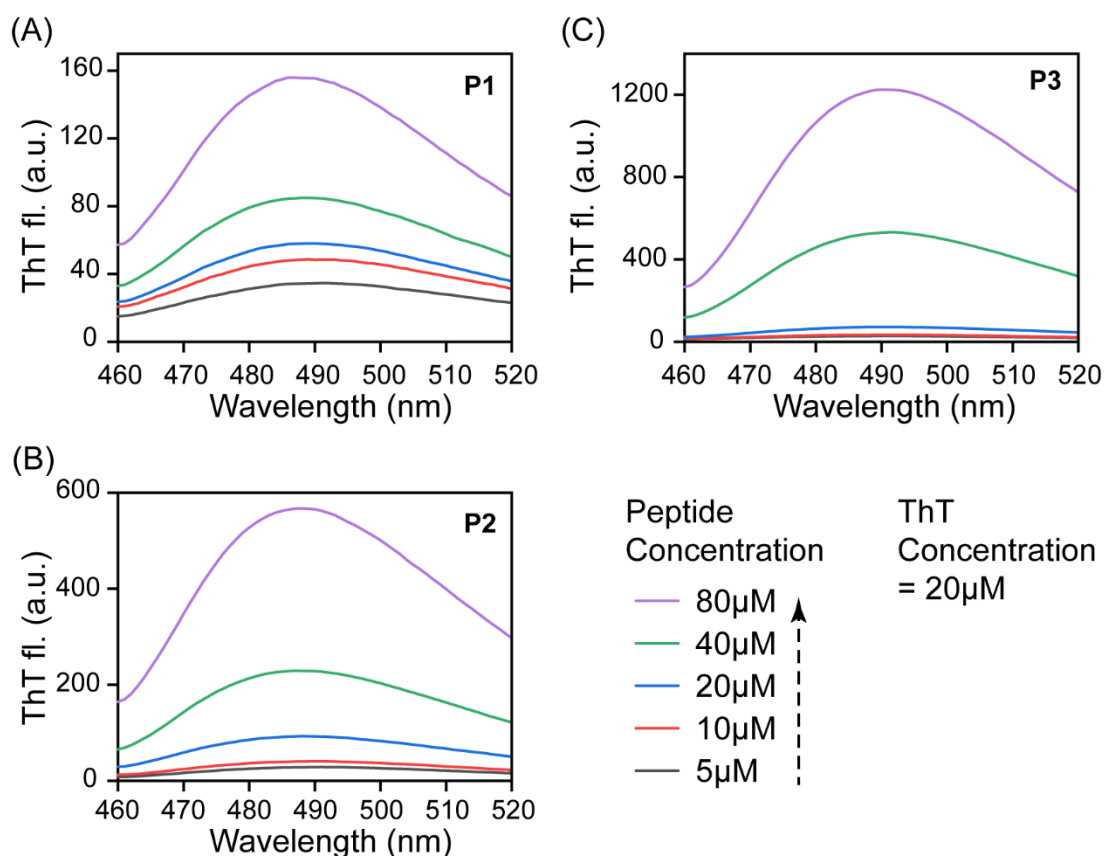
Figure S6.7. Concentration-dependent ThT fluorescence assay of (A) **P1**, (B) **P2**, and (C) **P3** displaying differential increase in the ThT intensity as a function of concentration.
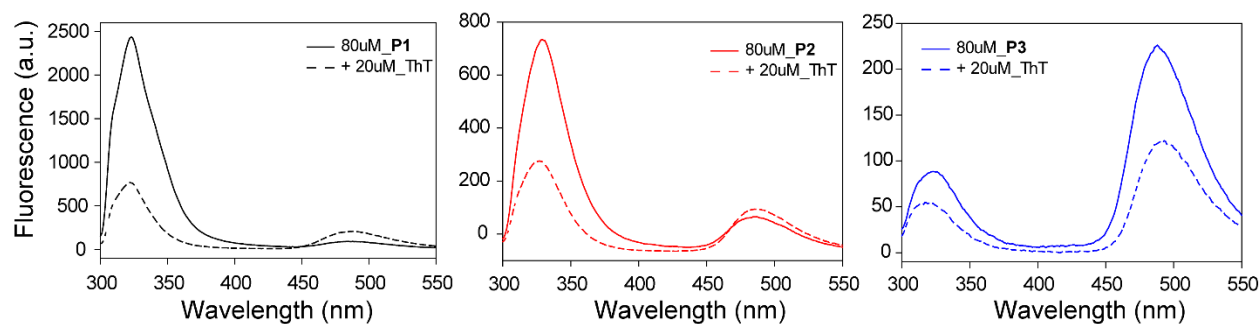
Figure S6.8. Differential quenching of intrinsic fluorescence by ThT. **P1**, and **P2** indicated significant decrease in the intrinsic fluorescence intensity at 323 and 330 nm, respectively, and slight increase at 485 nm. **P3**, on the other hand, showed decrease in both peaks at 330 nm and 485 nm.
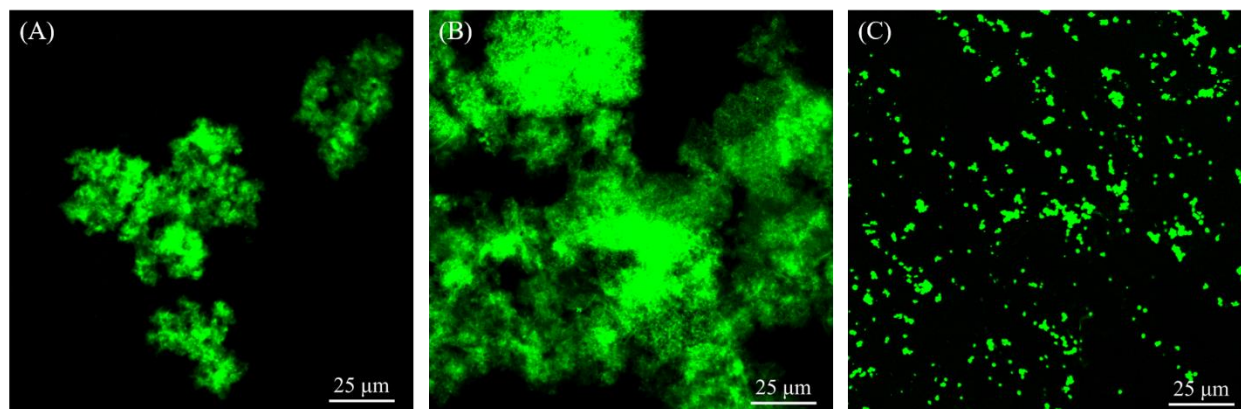
Figure S6.9. Confocal microscopy images of (A) **P1**, (B) **P2**, and (C) **P3** displaying ThT-bound amyloid-like aggregates.
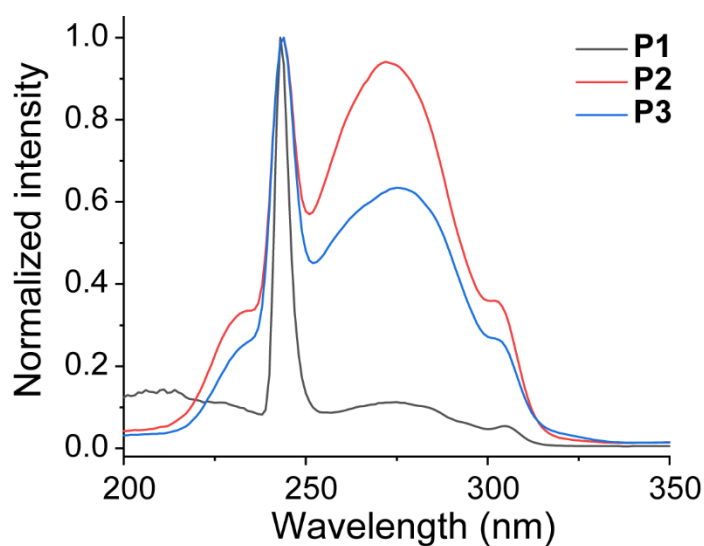
Figure S6.10. Normalized excitation spectra of the 485 nm peak of **P1** (black), **P2** (red), and **P3** (blue) indicates corresponding differential fluorenyl and tyrosine absorption.
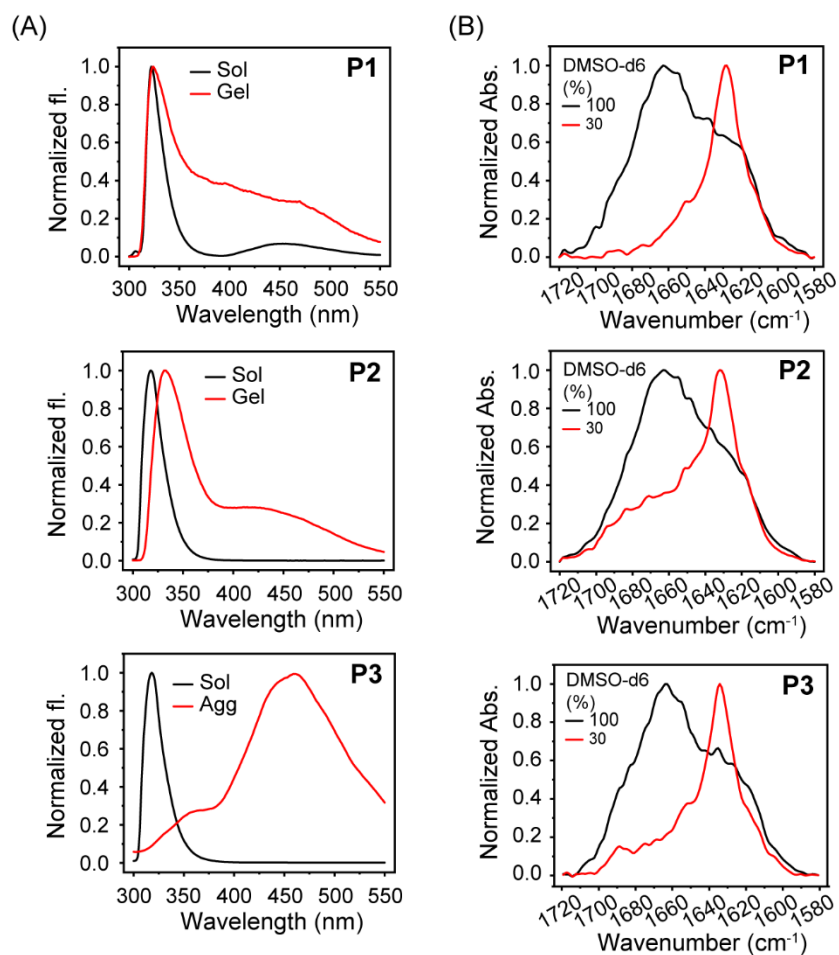
Figure S6.11. (A) Intrinsic fluorescence spectra of **P1**, **P2**, and **P3** at solution and gel/aggregate phase. (B) FTIR spectra of **P1**, **P2**, and **P3** at solution and gel/aggregate phase.
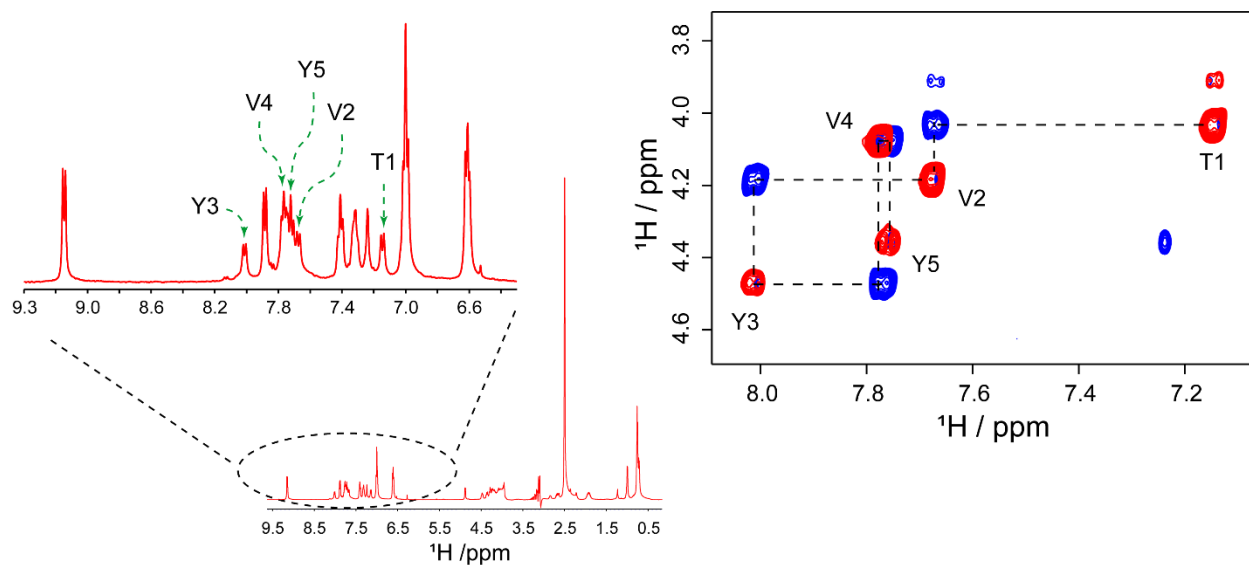
Figure S6.12. 1D ^{1}H NMR spectra of **P1** highlighting the amide region. Amino acid residues were assigned from 2D TOCSY and NOESY NMR spectra and pointed in the 1D spectra.
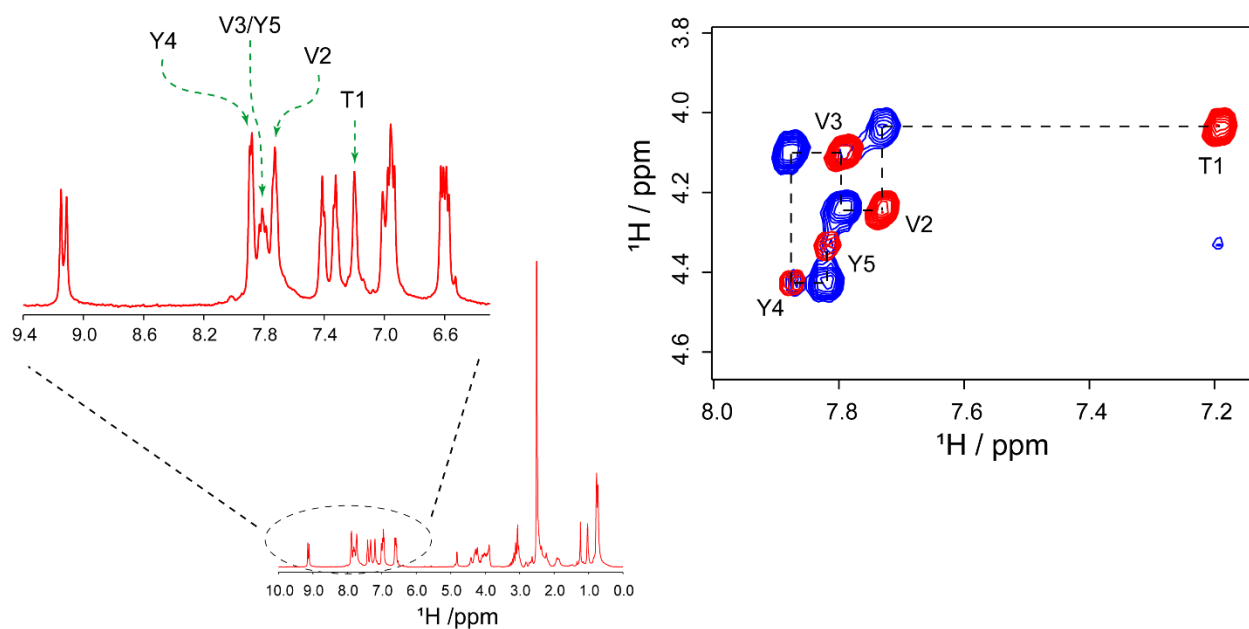
Figure S6.13. 1D ^{1}H NMR spectra of **P2** highlighting the amide region. Amino acid residues were assigned from 2D TOCSY and NOESY NMR spectra and pointed in the 1D spectra.
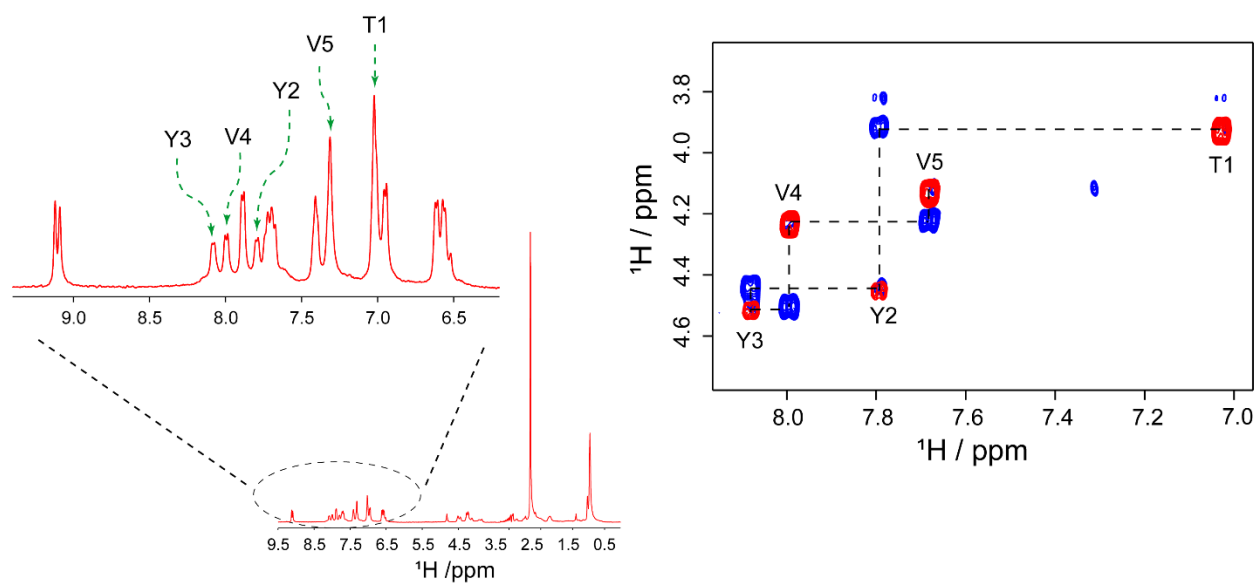
Figure S6.14. 1D ^{1}H NMR spectra of **P3** highlighting the amide region. Amino acid residues were assigned from 2D TOCSY and NOESY NMR spectra and pointed in the 1D spectra.
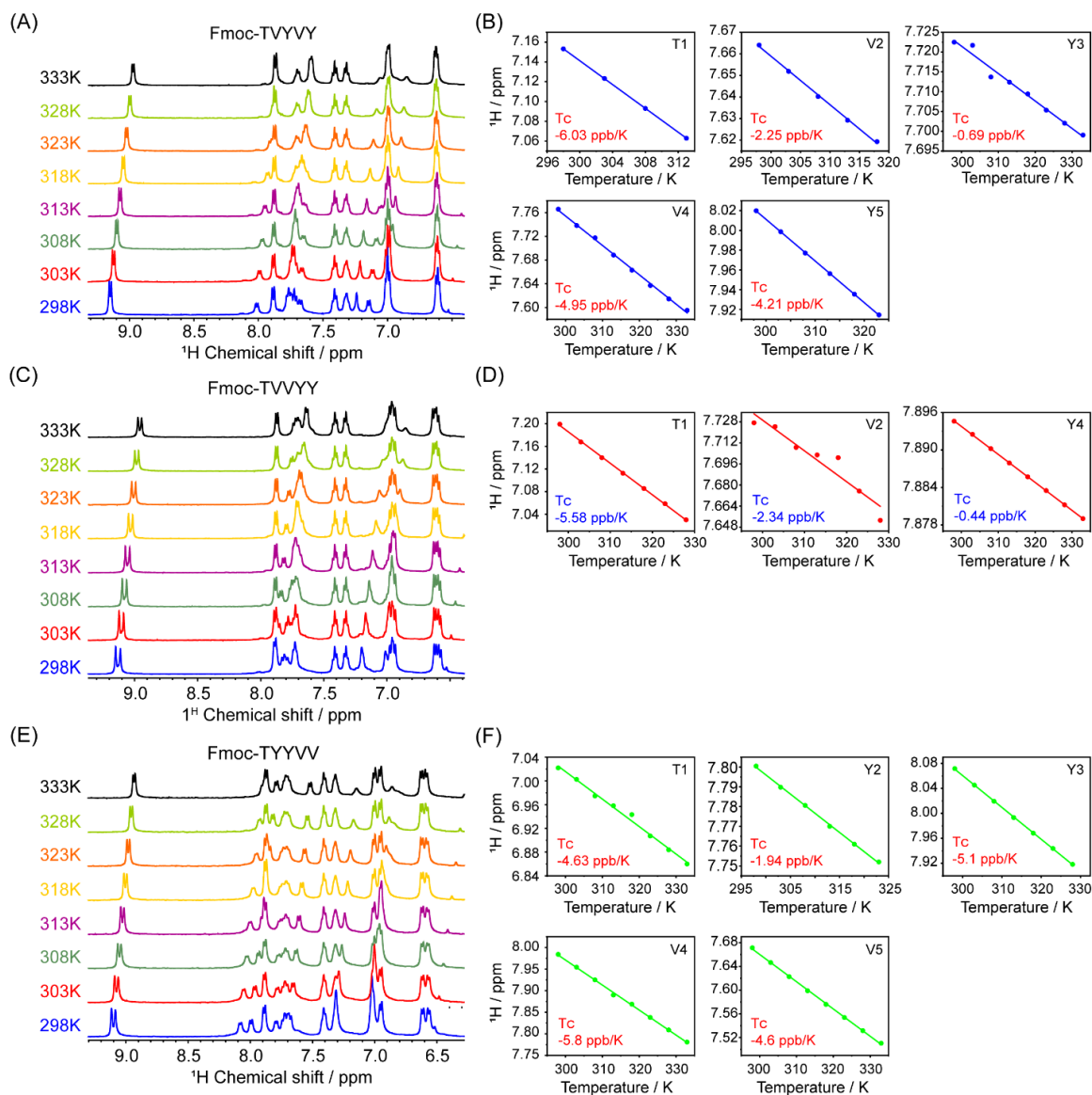
Figure S6.15. Temperature-dependent NMR spectroscopy showing changes in the amide proton chemical shift of (A) Fmoc-TVYVY, (C) Fmoc-TVVYY, and (E) Fmoc-TYYVV at different temperature in 100 % DMSO-d_6. Temperature coefficients of the amino acid residues of (B) Fmoc-TVYVY, (D) Fmoc-TVVYY, and (F) Fmoc-TYYVV calculated from temperature-dependent 1D ^{1}H NMR.

Figure S6.16. Raw particles and reference-free 2D class averages of **P1**: A-C. Representative raw particles showed at different diameters. All the filaments were assembled as thick, flat, straight ribbon-like structures. Thin filaments (C) were considered for 2D class averages calculation. D. Reference-free 2D class averages of **P1** peptide.
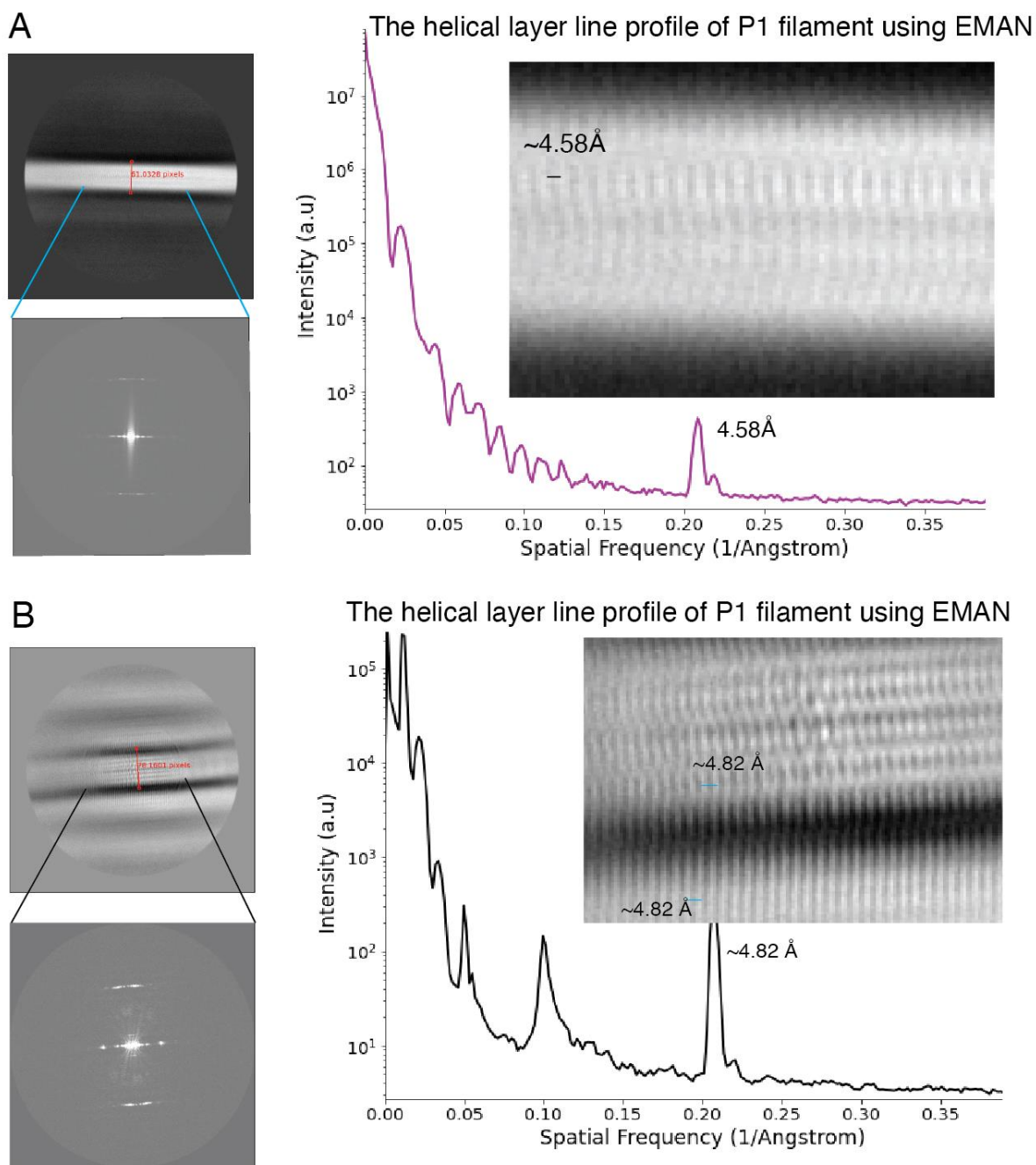
Figure S6.17. Helical layer line profile of **P1** filament using EMAN. A. Best 2D class average selected to calculate the layer line and from layer line profile showed the distance between inter-peptide, which is close to ~4.58 Å. B. Another best 2D class average selected to calculate the layer line and the layer line profile showed the distance between inter-peptides, which is close to ~4.82 Å.
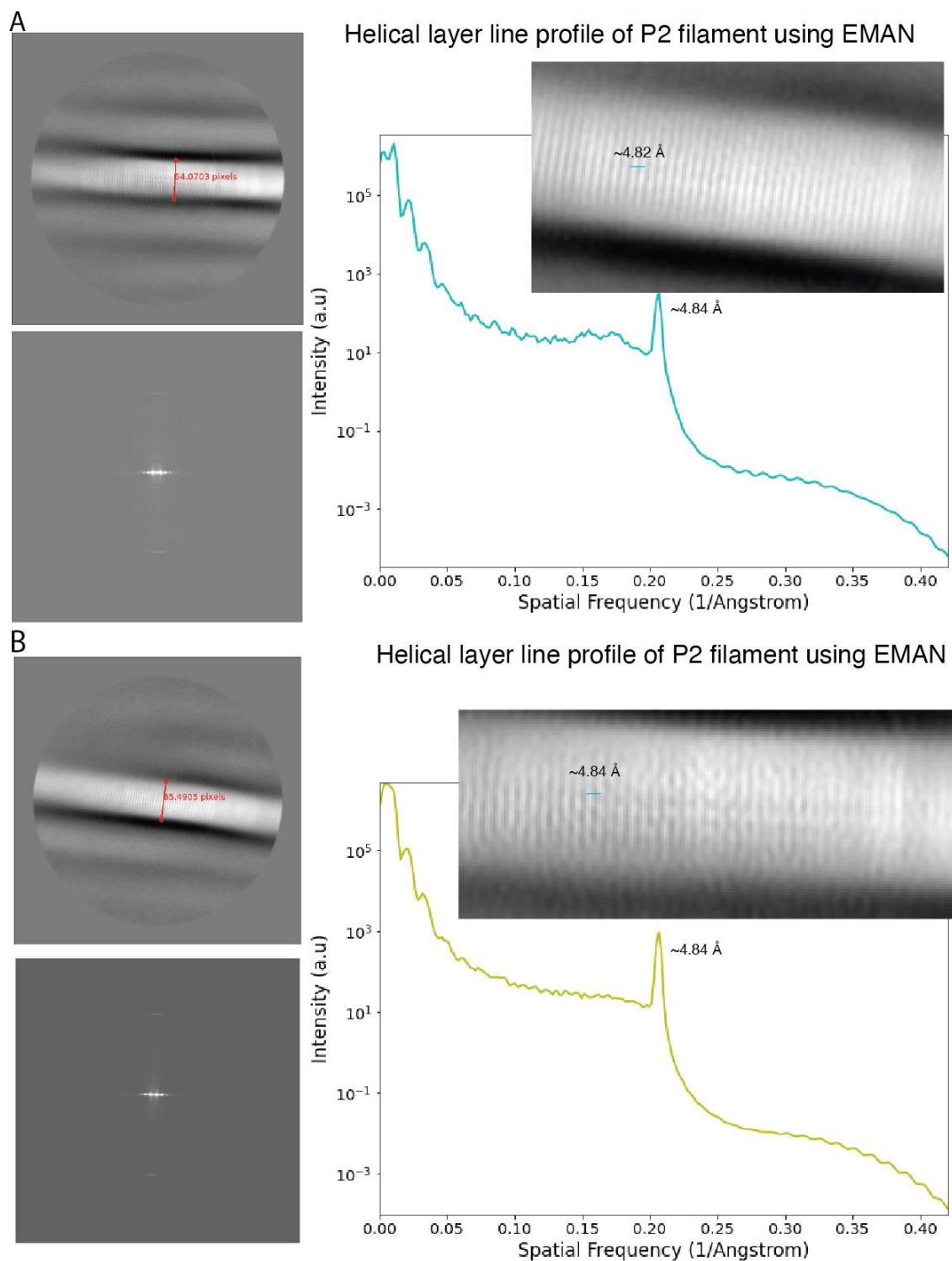
Figure S6.18. Helical layer line profile of **P2** filament using EMAN. A-B. Two best 2D class averages selected to calculate the layer line and the layer line profile showed the distance between inter-peptides, which is close to ~4.84 Å.

2D class averages of Fmoc-TVVYY
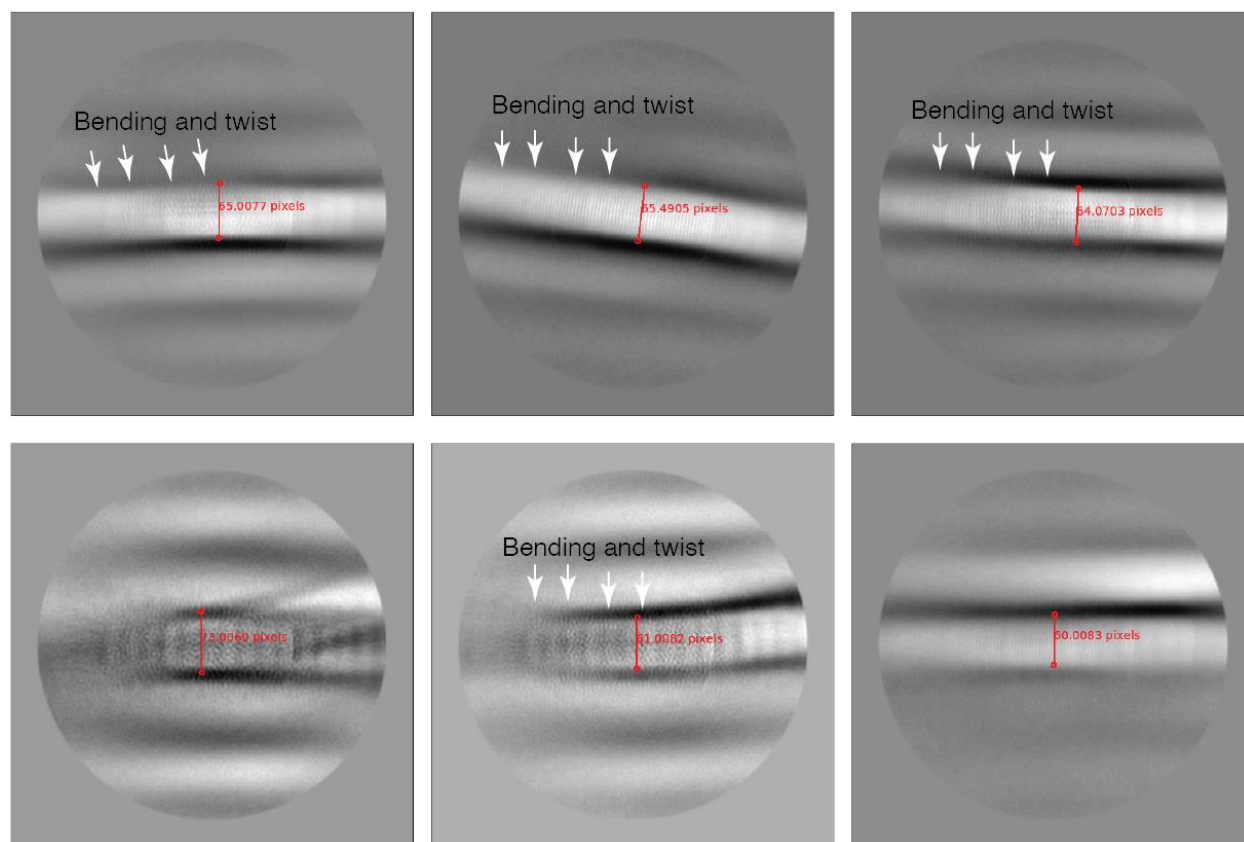
Figure S6.19. Reference-free 2D class averages of **P2** peptide and over all diameters of the **P1** peptides are within the range of 7-9 nm. Only straight isolated comparatively thin filaments were considered for 2D class averages calculation and thus, diameter of **P2** peptide is smaller than raw images and negative stain images.
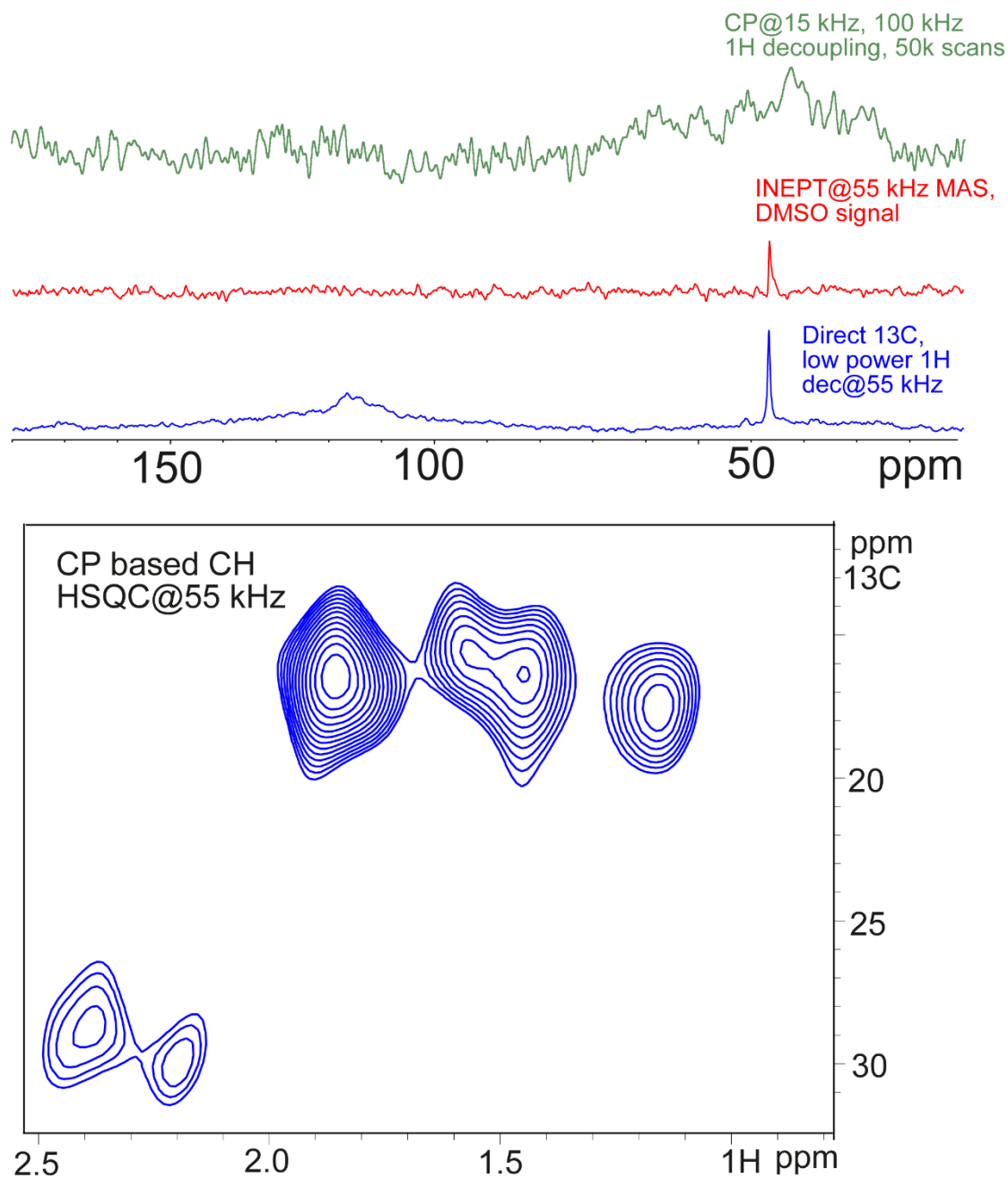
Figure S6.20. From the CP 1D (green) and signals in the methyl group region of 2D, there are inhomogeneities in the spectra. There is no mobile region, suggested by the direct excitation and INEPT spectra. The sharp peak in 13C is due to DMSO. The hump (upper panel, blue), is due to probe background.
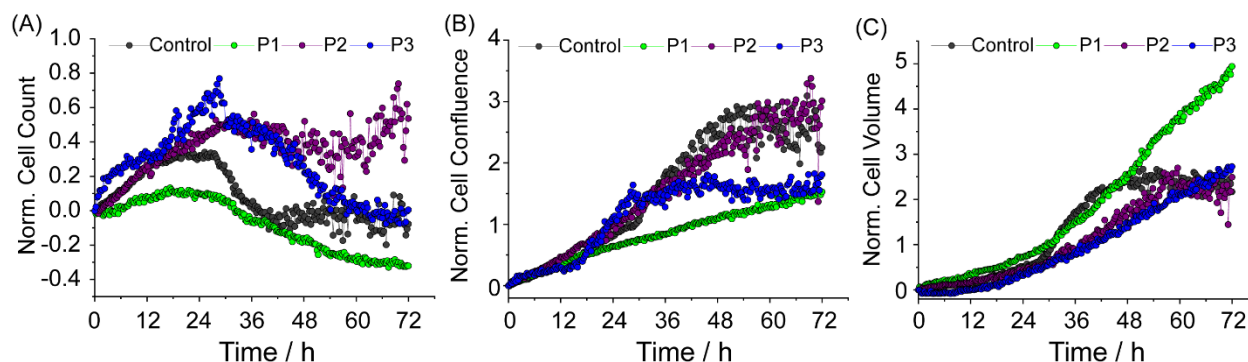
Figure S6.21. Impact of peptides P1, P2, and P3 on the health and growth characteristics of intestinal epithelial SW620 cells over time. The state-of-the-art label-free live cell holography imaging was utilized to quantify cell count, confluence, and volume every 15 minutes over 72 hours following peptide treatment. (A) Time-lapse depiction of the effect of peptides on SW620 cell count illustrates the average normalized cell count over the specified intervals. (B) Time-lapse visualization of the effect of peptides on SW620 cell confluence. (C) Time-lapse illustration of peptides' effect on SW620 cell volume over the specified intervals.

6.6. References

[1] N. Habibi, N. Kamaly, A. Memic, H. Shafiee, *Nano Today* **2016**, 11, 41; Y. Loo, M. Goktas, A. B. Tekinay, M. O. Guler, C. A. Hauser, A. Mitraki, *Adv Healthc Mater* **2015**, 4, 2557; R. de la Rica, C. Pejoux, H. Matsui, *Adv Funct Mater* **2011**, 21, 1018; G. B. Qi, Y. J. Gao, L. Wang, H. Wang, *Adv Mater* **2018**, 30, e1703444; J. Lu, X. Wang, *Adv Exp Med Biol* **2018**, 1064, 297.

[2] S. Jekhmane, M. Prachar, R. Pugliese, F. Fontana, J. Medeiros-Silva, F. Gelain, M. Weingarth, *Angew Chem Int Ed Engl* **2019**, 58, 16943.

[3] G. Fichman, E. Gazit, *Acta Biomater* **2014**, 10, 1671; A. Levin, T. A. Hakala, L. Schnaider, G. J. Bernardes, E. Gazit, T. P. Knowles, *Nature Reviews Chemistry* **2020**, 4, 615.

[4] P. W. Frederix, G. G. Scott, Y. M. Abul-Haija, D. Kalafatovic, C. G. Pappas, N. Javid, N. T. Hunt, R. V. Ulijn, T. Tuttle, *Nat Chem* **2015**, 7, 30.

[5] N. Brown, J. Lei, C. Zhan, L. J. W. Shimon, L. Adler-Abramovich, G. Wei, E. Gazit, *ACS Nano* **2018**, 12, 3253; V. Jayawarna, M. Ali, T. A. Jowitt, A. F. Miller, A. Saiani, J. E. Gough, R. V. Ulijn, *Advanced materials* **2006**, 18, 611; R. Orbach, L. Adler-Abramovich, S. Zigerson, I. Mironi-Harpaz, D. Seliktar, E. Gazit, *Biomacromolecules* **2009**, 10, 2646.

[6] Y. Xie, X. Wang, R. Huang, W. Qi, Y. Wang, R. Su, Z. He, *Langmuir* **2015**, 31, 2885; C. Chen, D. Wu, W. Fu, Z. Li, *Biomacromolecules* **2013**, 14, 2494; X. D. Xu, Y. Jin, Y. Liu, X. Z. Zhang, R. X. Zhuo, *Colloids Surf B Biointerfaces* **2010**, 81, 329.

[7] A. M. Smith, R. J. Williams, C. Tang, P. Coppo, R. F. Collins, M. L. Turner, A. Saiani, R. V. Ulijn, *Advanced materials* **2008**, 20, 37.

[8] T. N. Tikhonova, N. N. Rovnyagina, Z. A. Arnon, B. P. Yakimov, Y. M. Efremov, D. Cohen-Gerassi, M. Halperin-Sternfeld, N. V. Kosheleva, V. P. Drachev, A. A. Svistunov, P. S. Timashev, L. Adler-Abramovich, E. A. Shirshin, *Angew Chem Int Ed Engl* **2021**, 60, 25339; K. Ryan, J. Beirne, G. Redmond, J. I. Kilpatrick, J. Guyonnet, N. V. Buchete, A. L. Kholkin, B. J. Rodriguez, *ACS Appl Mater Interfaces* **2015**, 7, 12702.

[9] J. D. Tang, C. Mura, K. J. Lampe, *J Am Chem Soc* **2019**, 141, 4886; D. E. Clarke, C. D. J. Parmenter, O. A. Scherman, *Angew Chem Int Ed Engl* **2018**, 57, 7709; A. D. Martin, J. P. Wojciechowski, E. Y. Du,

A. Rawal, H. Stefen, C. G. Au, L. Hou, C. G. Cranfield, T. Fath, L. M. Ittner, P. Thordarson, *Chem Sci* **2019**, 11, 1375; S. H. Hiew, H. Mohanram, L. Ning, J. Guo, A. Sánchez-Ferrer, X. Shi, K. Pervushin, Y. Mu, R. Mezzenga, A. Miserez, *Adv Sci (Weinh)* **2019**, 6, 1901173.

[10] M. Ma, Y. Kuang, Y. Gao, Y. Zhang, P. Gao, B. Xu, *J Am Chem Soc* **2010**, 132, 2719.

[11] A. Ghosh, D. Bhattacharyya, A. Bhunia, *Biochim Biophys Acta Biomembr* **2018**, 1860, 335.

[12] Y. Li, W. Surya, S. Claudine, J. Torres, *J Biol Chem* **2014**, 289, 12535.

[13] T. R. Ruch, C. E. Machamer, *Viruses* **2012**, 4, 363.

[14] A. Ghosh, A. S. Pithadia, J. Bhat, S. Bera, A. Midya, C. A. Fierke, A. Ramamoorthy, A. Bhunia, *Biochemistry* **2015**, 54, 2249.

[15] A. Kumar, S. P, S. Gulati, S. Dutta, *J Vis Exp* **2021**.

[16] S. H. Scheres, *J Struct Biol* **2012**, 180, 519.

[17] T. Grant, A. Rohou, N. Grigorieff, *Elife* **2018**, 7.

[18] A. Rohou, N. Grigorieff, *J Struct Biol* **2015**, 192, 216.

[19] G. Tang, L. Peng, P. R. Baldwin, D. S. Mann, W. Jiang, I. Rees, S. J. Ludtke, *J Struct Biol* **2007**, 157, 38.

[20] R. H. Dosh, A. Essa, N. Jordan-Mahy, C. Sammon, C. L. Le Maitre, *Acta Biomater* **2017**, 62, 128.

[21] A. Mölder, M. Sebesta, M. Gustafsson, L. Gisselson, A. G. Wingren, K. Alm, *J Microsc* **2008**, 232, 240.

[22] A. H. Khan, S. Pal, A. K. Ghosh, P. K. Das, *ACS Applied Engineering Materials* **2023**.

[23] Z. Zheng, J. Wu, M. Liu, H. Wang, C. Li, M. J. Rodriguez, G. Li, X. Wang, D. L. Kaplan, *Adv Healthc Mater* **2018**, 7, e1701026.

[24] S. Marullo, A. Meli, N. T. Dintcheva, G. Infurna, C. Rizzo, F. D'Anna, *Chempluschem* **2020**, 85, 301.

[25] Q. Li, Z. Li, *Adv Sci (Weinh)* **2017**, 4, 1600484.

[26] C. Tang, R. V. Ulijn, A. Saiani, *Langmuir* **2011**, 27, 14438.

[27] G. Gottarelli, S. Lena, S. Masiero, S. Pieraccini, G. P. Spada, *Chirality* **2008**, 20, 471.

[28] N. Javid, S. Roy, M. Zelzer, Z. Yang, J. Sefcik, R. V. Ulijn, *Biomacromolecules* **2013**, 14, 4368.

[29] A. R. Hirst, S. Roy, M. Arora, A. K. Das, N. Hodson, P. Murray, S. Marshall, N. Javid, J. Sefcik, J. Boekhoven, J. H. van Esch, S. Santabarbara, N. T. Hunt, R. V. Ulijn, *Nat Chem* **2010**, 2, 1089.

[30] S. Fleming, S. Debnath, P. W. Frederix, T. Tuttle, R. V. Ulijn, *Chem Commun (Camb)* **2013**, 49, 10587.

[31] D. Sarkar, I. Chakraborty, M. Condorelli, B. Ghosh, T. Mass, M. Weingarth, A. K. Mandal, C. La Rosa, V. Subramanian, A. Bhunia, *ChemMedChem* **2020**, 15, 293.

[32] E. Burakova, S. K. Vasa, R. Linser, *J Biomol NMR* **2022**, 76, 197.

[33] S. R. Caliari, J. A. Burdick, *Nat Methods* **2016**, 13, 405; Q. Li, G. Qi, D. Lutter, W. Beard, C. R. S. Souza, M. A. Highland, W. Wu, P. Li, Y. Zhang, A. Atala, X. Sun, *Biomolecules* **2022**, 12; R. Binaymotlagh, L. Chronopoulou, C. Palocci, *J Funct Biomater* **2023**, 14; P. Worthington, D. J. Pochan, S. A. Langhans, *Front Oncol* **2015**, 5, 92.

[34] M. Sebesta, P. J. Egelberg, A. Langberg, J.-H. Lindskov, K. Alm, B. Janicke, presented at *Quantitative phase imaging II*, **2016**.

[35] T. Boontheekul, H. J. Kong, S. X. Hsiong, Y. C. Huang, L. Mahadevan, H. Vandenburgh, D. J. Mooney, *Faraday Discuss* **2008**, 139, 53.

[36] F. Ulrich, C. P. Heisenberg, *Traffic* **2009**, 10, 811.

[37] F. Lang, M. Ritter, H. Völkl, D. Häussinger, *Ren Physiol Biochem* **1993**, 16, 48.

Summary and future outlook

The primary focus of my thesis has been the investigation of the kinetic and structural features of peptide self-assembly, particularly in relation to amyloid aggregation and functional materials. Therefore, comprehensive understanding of self-assembling peptide sequences, which has emerged as a fascinating area of research for the interdisciplinary scientific community, is essential. Our studies involving various biophysical, spectroscopy and microscopy techniques, enabled us to gain insights into the sequence dependence of peptide self-assembly linked to both pathogenesis, and design and development of functional materials.

The first part of the thesis aims to provide a comprehensive understanding of peptide self-assembly and explores the roles of various extrinsic and intrinsic factors in the amyloidogenesis of amyloid beta (Aβ) and human islet amyloid polypeptide (hIAPP). First, it explores the role of a conserved GxxxG motif in the amyloidogenesis of Aβ associated with Alzheimer's disease (AD). Results from this research offer novel insights into the regulatory role of this motif, particularly the G33 and G37 residues, in fibrillation and membrane-mediated oligomerization of Aβ. Furthermore, using nanodiscs as a near-native membrane environment, we observe the formation of comparatively stable oligomers with distinct conformations, both from the native Aβ40 and other minor states of free Aβ40 oligomers. Similarly, hIAPP, another amyloidogenic peptide associated with type 2 diabetes, is examined. We observed that the C-terminal hIAPP fragment, which also contains similar SxxxG/GxxxS motif, leads to structurally distinct oligomers under the influence of extrinsic factors. Moreover, these oligomers can significantly accelerate the aggregation of hIAPP; however, they potentially reduce the presence of toxic aggregate species. Thus, they act as a scavenger of toxic oligomers, potentially opening a new avenue for therapeutic interventions.

This thesis further explores the potential of SVD analysis in revealing hidden patterns and dominant modes of interactions associated with the complex process of amyloidogenesis. It also verifies the applicability of SVD analysis across a diverse range of amyloidogenesis processes, and offers model-free global kinetic information with greater precision. Lastly, we shift our focus towards the other side of peptide self-assembly, i.e., the development of functional biomaterials. We have designed short pentapeptides based on a self-assembling sequence from the C-terminal

SARS CoV E protein. The relationship between peptide sequence arrangement and molecular assembly structure, and how these have influenced the mechanical properties of the hydrogel, has also been demonstrated. Moreover, these supramolecular assemblies with tunable morphology and mechanical properties, are suitable for tissue engineering, injectable delivery, and 3D bio-printing applications.

Our studies on the significance of the GxxxG and related motifs serves as a step forward in developing targeted therapy. Although it offers an intriguing possibility for AD treatments, targeting the GxxxG motif within Aβ presents significant challenges. The ubiquity of the GxxxG motif across transmembrane proteins signifies that disrupting GxxxG-mediated interactions could inadvertently perturb normal protein-protein interactions, potentially yielding unintended off-target effects. Furthermore, the structural polymorphism inherent to this motif complicates the design of effective inhibitors. These intricacies are compounded by the presence of other pivotal motifs within Aβ and the dynamic, adaptable nature of its oligomerization process. With the continuous advancement of technology and development of nanodiscs like molecules, it could be possible to achieve both amyloid inhibition and intricate structure determination. Furthermore, as we gain better understanding of how specific sequences drive peptide self-assembly, we are likely to narrow the gap between disease mechanisms and functional amyloids.
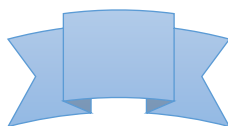
Peer-reviewed publications

Self-assembly and Neurotoxicity of Amyloid-beta (21-40) Peptide fragment: The regulatory Role of GxxxG Motifs

Dibakar Sarkar,[a] Ipsita Chakraborty,[a] Marcello Condorelli,[b] Baijayanti Ghosh,[c] Thorben Maass,[d] Markus Weingarth,[d] Atin K Mandal,[c] Carmelo La Rosa,*[b] Vivekanandan Subramanian,*[e] Anirban Bhunia*[a]

[a]   Mr. Dibakar Sarkar, Dr. Ipsita Chakraborty, Dr. Anirban Bhunia*
        Department of Biophysics
        Bose Institute
        P-1/12 CIT Scheme VII (M), Kolkata 700054, India
        E-mail: bhunia@jcbose.ac.in
[b]   Mr. Marcello Condorelli, Prof. Carmelo La Rosa*
        Department of Chemical Sciences
        University of Catania
        95125 Catania, Italy
        E-mail: clarosa@unict.it
[c]   Miss Baijayanti Ghosh, Dr. Atin K. Mandal
        Division of Molecular Medicine
        Bose Institute
        P-1/12 CIT Scheme VII (M), Kolkata 700054, India
[d]   Mr. Thorben Mass, Dr. Markus Weingarth
        Department of Chemistry
        Utrecht University
        Padualaan 8, 3584 Utrecht, The Netherlands
[e]   Dr. Vivekanandan Subramanian*
        College of Pharmacy
        Univeristy of Kentucky
        Lexington, KY 40536-0596, USA
        E-mail: vivek.nmr@uky.edu

Abstract: The three GxxxG repeating motifs from the C-terminal region of amyloid-beta (Aβ) peptide play a significant role in regulating the aggregation kinetics of the peptide. Mutation of these glycine residues to leucine greatly accelerates the fibrillation process but generates a varied toxicity profile. Using an array of biophysical techniques, we demonstrated the uniqueness of the composite glycine residues in these structural repeats. We have employed solvent relaxation NMR technique to display the role played by the surrounding water molecules in determining the corresponding aggregation pathway. Notably, the conformational changes induced by the Gly^{33} and Gly^{37} mutation result in a significantly reduced toxicity in a neuronal cell line. Our results indicate that the G^{33}xxxG^{37} is the primary motif responsible for Aβ neurotoxicity, hence provide a direct structure-function correlation. Targeting this motif, therefore, can be a promising strategy to prevent neuronal cell death associated with Alzheimer's and other related diseases, such as type II diabetes and Parkinson's.

Introduction

The self-association of Amyloid-beta (Aβ) peptides has been known to be the central event in Alzheimer's Disease (AD) pathogenesis.[1, 2] Despite several decades of research on the relationship between Aβ and AD, researchers are still skeptical about the structure-toxicity correlation. Although the recent evidences on Aβ neurotoxicity have shifted the focus towards the toxic oligomers,[3] fibrils which have long been considered as the cause of disease pathogenesis and cannot be ruled out as evidences pertaining to them are still coming along.[4, 5] A deeper understanding of the molecular mechanisms and pathways underlying Aβ self-aggregation remains a great challenge to current science. Over the years, independent studies have identified the central (K16-G25) and the C-terminal region (K28-G37) play a vital role in Aβ self-assembly.[2, 5, 6] Several of these studies have often highlighted a significance of the GxxxG repeating motif from the C-terminus.[7, 8] The GxxxG motif is a frequently occurring sequence in trans-membrane proteins and some soluble proteins that contain at least one α-helix.[9] The four residue separation aligns the Gly residues in a GxxxG motif to lie on one face of the helix, and has been reported to stabilize the helix-helix association and the folded state of proteins.[9, 10] The lack of side chain in Gly allows the two helices to come into close proximity, and the dimer is thought to be stabilized by van der Waals interactions.[11] The β-branched amino acids such as Ile, Val, and Thr that frequently occurs at the neighbouring positions, facilitates Gly to acts as a molecular notch that further strengthens the helix-helix interactions.[11] It has also been reported that AxxxG has a similar effect to the GxxxG motif.[9] Studies have shown that Gly→Leu mutation in these motifs affect amyloid precursor protein dimerization, processing, and subsequent Aβ production.[8] These motifs were suggested to have significant impact on β-sheet formation and the associated neurotoxicity.[7] Before converting into β-sheet, Aβ adopts an antiparallel β-hairpin structure at the G^{33}LMVG^{37} region.[12] Thus, mutation in this segment could favor oligomerization, and subsequent fibrillation. A comprehensive understanding of the system is necessary for a possible structure-function correlation of Aβ pathogenesis. However, the mechanistic insight into this segment-specific aggregation resulting in the structured/unstructured aggregates remains elusive.

Comparison of Synthetic Neuronal Model Membrane Mimics in Amyloid Aggregation at Atomic Resolution

Swapna Bera, Nilanjan Gayen, Sk. Abdul Mohid, Dipita Bhattacharyya, Janarthanan Krishnamoorthy, Dibakar Sarkar, Jihye Choi, Nirakar Sahoo, Atin K. Mandal, DongKuk Lee, and Anirban Bhunia*

Read Online

ACCESS | Metrics & More | Article Recommendations | Supporting Information

ABSTRACT: Alzheimer's disease (AD) is a severe neurodegenerative disorder caused by abnormal accumulation of toxic amyloid plaques of the amyloid-beta (Aβ) or the tau proteins in the brain. The plaque deposition leading to the collapse of the cellular integrity is responsible for a myriad of surface phenomena acting at the neuronal lipid interface. Recent years have witnessed dysfunction of the blood−brain barriers (BBB) associated with AD. Several studies support the idea that BBB acts as a platform for the formation of misfolded Aβ peptide, promoting oligomerization and fibrillation, compromising the overall integrity of the central nervous system. While the amyloid plaque deposition has been known to be responsible for the collapse of the BBB membrane integrity, the causal effect relationship between BBB and Aβ amyloidogenesis remains unclear. In this study, we have used physiologically relevant synthetic model membrane systems to gain atomic insight into the functional aspects of the lipid interface. Here, we have used a minimalist BBB mimic, POPC/POPG/cholesterol/GM1, to compare with the native BBB (total lipid brain extract (TLBE)), to understand the molecular events occurring in the membrane-induced Aβ_{40} amyloid aggregation. Our study showed that the two membrane models accelerated the Aβ_{40} aggregation kinetics with differential secondary structural transitions of the peptide. The observed structural transitions are defined by the lipid compositions, which in turn undermines the differences in lipid surface phenomena, leading to peptide induced cellular toxicity in the neuronal membrane.

KEYWORDS: Amyloid beta, blood−brain barrier, total brain lipid extract, NMR, relaxation, fluorescence, protein aggregation
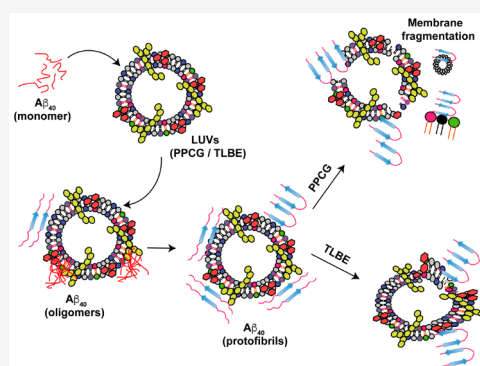
INTRODUCTION

Alzheimer's disease (AD) is considered to be one of the top ten leading causes of death worldwide.[1] According to a recent survey on AD, more than 46.8 million people from all over the world have become the victim of this deadly disease.[2] AD, like the other progressive neurodegenerative disorders, such as Parkinson's, and Huntington's Disease, is caused by accumulation of misfolded proteins in the brain tissue, which ultimately drives the pathogenesis. As per the "Amyloid cascade hypothesis", under nonidyllic environment, pathological amyloid precursor protein (APP; a large transmembrane receptor protein) processing by a group of enzymes (β- and γ-secretase) yields the aggregation-prone 40/42 residues long amyloid-beta peptides (Aβ_{40}/Aβ_{42}), which are unable to fold correctly (Figure 1A).[3] The cell's quality control machinery professionally eliminates most of the peptides;[4,5] nevertheless, these amyloids somehow evade the system and undergo rapid deposition in the form of insoluble, neurotoxic amyloid plaques (nanoscale aggregates of Aβ along with hyperphosphorylated tau proteins), in several regions of the cerebral neutrophils and vasculature.

Several studies have provided evidence for the membrane surfaces to serve as an important scaffold for the aggregation

pathway.[6] This indicates the functional involvement of the peptide−lipid interface in the progressive neurodegeneration associated with AD. This functional interface is very crucial for targeted therapeutic intervention and to carry out fundamental research to identify the peptide−lipid interacting domains at atomic resolution. Numerous research studies have been performed to gain a greater understanding of the mechanism of membrane-mediated amyloidogenesis and the resultant neurotoxicity.[6−8] However, the diversity of the membrane components and the different proportions of individual lipids in the natural membranes associated with the brain have been a big hurdle in the progress of most lipid−peptide interaction studies. Native membrane's complexity has restricted the construction of even a simplified in-vitro model to study the complex phenomenon associated with Aβ amyloidogenesis
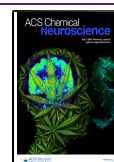
Solvent Relaxation NMR: A Tool for Real-Time Monitoring Water Dynamics in Protein Aggregation Landscape

Ipsita Chakraborty,[⊥] Rajiv K. Kar,[⊥] Dibakar Sarkar, Sourav Kumar, Nakul C. Maiti, Atin Kumar Mandal, and Anirban Bhunia*

Cite This: *ACS Chem. Neurosci.* 2021, 12, 2903−2916

Read Online

ACCESS | 📊 Metrics & More | 📰 Article Recommendations | 🆘 Supporting Information

ABSTRACT: Solvent dynamics strongly induce the fibrillation of an amyloidogenic system. Probing the solvation mechanism is crucial as it enables us to predict different proteins' functionalities, such as the aggregation propensity, structural flexibility, and toxicity. This work shows that a straightforward NMR method in conjunction with phenomenological models gives a global and qualitative picture of water dynamics at different concentrations and temperatures. Here, we study amyloid system Aβ40 and its fragment AV20 (A21-V40) and G37L (mutation at Gly37 → Leu of AV20), having different aggregation and toxic properties. The independent validation of this method is elucidated using all-atom classical MD simulation. These two state-of-the-art techniques are pivotal in linking the effect of solvent environment in the near hydration-shell to their aggregation nature. The time-dependent modulation in solvent dynamics probed with the NMR solvent relaxation method can be further adopted to gain insight into amyloidogenesis and link with their toxicity profiles.

KEYWORDS: Amyloidogenesis, solvent relaxation, amyloid beta, classical simulation, toxicity, hydration-dynamics
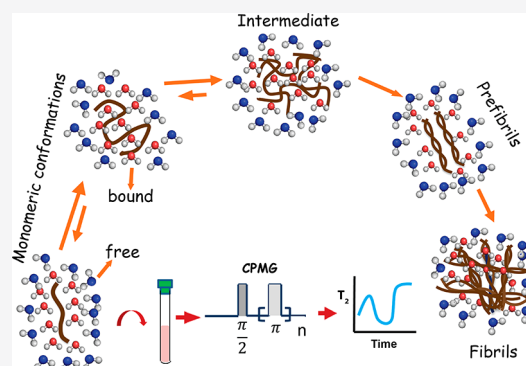
1. INTRODUCTION

Solvent dynamics play a crucial role in governing the structural and functional architecture of biomolecules.[1] The impact of solvent in physical behavior is mediated through system energetics; however, the exact role remains an unsolved puzzle. Water, being a major solvent component, controls the dynamics, conformation, and stability (referred to as a structure−function relationship).[2,3] Proteins are evolutionarily edited biological polymers known to undergo intramolecular and intermolecular phase transitions.[4] Their structural evolutions are critical to the functionality of many intrinsically disordered proteins (IDPs).[5] In particular, the conformational transitions induced by the interplay between protein and water drive the macro-systemic changes. In the early phase, proteins are in monomeric conformation and impart strong interaction with solvent water through the hydrophilic segments.[4,6,7] The synergistic effect between protein intermolecular interactions and solvation leads to structural perturbation, which in turn exposes the hydrophobic region and decreases the solvent accessible surface area.[8] Successively, the propensity toward aggregation leads to fibrillation through different intermediate-stages.[9] This includes the formation of protein-rich droplets, protofibril, and fibril induced by time-dependent changes in solvent−solute interaction.[6,10] The solvent's motional behavior depends on the aggregation pathway, chemical nature, and architecture of the macromolecular systems to be observed (at

different intermediate stages) and thus varies from system to system.

High-resolution NMR spectroscopy offers several compelling experimental tools to probe protein−water interactions. Most of these experiments are involved in probing the interface from the protein side, such as phase modulated CLEAN chemical EXchange spectroscopy (CLEANEx), hydrogen/deuterium (H/D) exchange, and intermolecular $^1H−^1H$ nuclear Overhauser effects (NOEs),[11−15] whereas the rest only monitor the water. The most common tool that belongs to this class is the magnetic relaxation dispersion (MRD) experiment on the quadrupolar nuclei, i.e., ^2H and ^{17}O of the water pool.[13,16,17] Further, it is also possible to monitor water exchange by measuring the line width of ^{17}O water resonance of external water.[18] Nevertheless, these NMR techniques have drawbacks that restrict us from the real-time monitoring dynamics of water. First, these experiments are technically complicated and have a longer experimental time (of the order of ∼h). Thus, the parameters extracted by these methods are time-averaged properties of the solvent−solute system. Second,

Chemical Science

EDGE ARTICLE

Check for updates
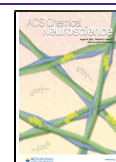
All publication charges for this article have been paid for by the Royal Society of Chemistry

An explicitly designed paratope of amyloid-β prevents neuronal apoptosis *in vitro* and hippocampal damage in rat brain†

Ashim Paul, [a] Sourav Kumar, [b] Sujan Kalita, [a] Sourav Kalita, [a] Dibakar Sarkar, [c] Anirban Bhunia, [c] Anupam Bandyopadhyay, [d] Amal Chandra Mondal *[be] and Bhubaneswar Mandal *[a]

Synthetic antibodies hold great promise in combating diseases, diagnosis, and a wide range of biomedical applications. However, designing a therapeutically amenable, synthetic antibody that can arrest the aggregation of amyloid-β (Aβ) remains challenging. Here, we report a flexible, hairpin-like synthetic paratope (**SP1**, ~2 kDa), which prevents the aggregation of Aβ monomers and reverses the preformed amyloid fibril to a non-toxic species. Structural and biophysical studies further allowed dissecting the mode and affinity of molecular recognition events between **SP1** and Aβ. Subsequently, **SP1** reduces Aβ-induced neurotoxicity, neuronal apoptosis, and ROS-mediated oxidative damage in human neuroblastoma cells (SH-SY5Y). The non-toxic nature of **SP1** and its ability to ameliorate hippocampal neurodegeneration in a rat model of AD demonstrate its therapeutic potential. This paratope engineering module could readily implement discoveries of cost-effective molecular probes to nurture the basic principles of protein misfolding, thus combating related diseases.

Introduction

The deposition of amyloid fibrils has consequences with numerous protein-misfolding diseases, including Alzheimer's, Parkinson's, and Huntington's disease, Prion diseases, and type-2 diabetes.[1,2] The detailed molecular mechanism of Alzheimer's disease (AD) is not intelligible yet. However, growing shreds of evidence suggest that the aggregation of amyloid-β peptide (Aβ) from native non-toxic monomers to highly toxic amyloid fibrils in the extracellular space and formation of neurofibrillary tangles (NFTs) in neurons are the principal hallmarks for the pathogenesis of AD.[3,4] In the past two decades, numerous strategies have been exercised to find a cure for AD.[5] These strategies involve metal chelators, nanoparticles, the amyloidogenic core region (KLVFF)[6–8] or other fragments of the Aβ peptide,[9,10] chemical chaperones,[11,12] peptide-based

inhibitors,[13–16] small molecules,[5,17] and conformation-selective antibodies.[18–21] Antibody-based drug design is the most intriguing as antibodies engulf and eliminate the toxic Aβ species. Besides, antibodies have demonstrated the scope and potential of immunotherapy. Nevertheless, they are associated with severe adverse effects such as Fc-mediated pro-inflammatory immune responses. Recently, affibodies[22–26] have shown prevention of the self-aggregation of Aβ by encapsulating the Aβ peptide and reducing pro-inflammatory immune responses, which led to a novel therapeutic approach against AD.[18–27] Among the mentioned strategies, a rationally designed, short peptide from a self-aggregation site of Aβ showed promising results even in clinical trials with superior bioavailability and less toxicity.[5,28]

Here, we aimed to construct an explicitly designed synthetic paratope inspired by a peptide fragment of Aβ that could potentially be a clinical candidate for targeting Aβ. A paratope is a part of an antibody known to recognize the epitope region of an antigen selectively.[18–21] The knowledge from prior investigations by our group and numerous reports has empowered us to construct a flexible, parallel β-hairpin-like synthetic paratope (**SP1**, Fig. 1a and b). The size of the designed **SP1** is smaller than that of any existing antibody and affibody. We explored its efficiency in binding to Aβ using various spectroscopic techniques. The atomic-scale mechanistic study by NMR dissected the recognition mechanism. We show that **SP1** remarkably disaggregates the preformed Aβ aggregates and potentially dissolves Aβ plaques through different *in vitro* studies. Besides, **SP1** reduces Aβ40 induced cytotoxicity, oxidative stress-mediated apoptotic events, and

aLaboratory of Peptide and Amyloid Research, Department of Chemistry, Indian Institute of Technology Guwahati (IITG), North Guwahati, Assam-781039, India. E-mail: bmandal@iitg.ac.in

bNeuroscience Research Unit, Department of Physiology, Raja Peary Mohan College, Hooghly, Uttarpara, West Bengal-712258, India. E-mail: acmondal@mail.jnu.ac.in

cBiomolecular NMR and Drug Design Laboratory, Department of Biophysics, Bose Institute, P-1/12 CIT Scheme VII (M), Kolkata 700054, India

dPeptide Engineering Laboratory, Department of Chemistry, Indian Institute of Technology, Ropar, Punjab-140001, India

eLaboratory of Cellular & Molecular Neurobiology, School of Life Sciences, Jawaharlal Nehru University, New Delhi-110 067, India

† Electronic supplementary information (ESI) available. See DOI: 10.1039/d0sc04379f

Mechanistic insight into functionally different human islet polypeptide (hIAPP) amyloid: the intrinsic role of the C-terminal structural motifs†

Dibakar Sarkar,[a] Narayan Chandra Maity,[b] Gourav Shome, [ID][c] Kyriakos Gabriel Varnava,[d] Vijayalekshmi Sarojini, [ID][d] Subramanian Vivekanandan,[e] Nirakar Sahoo,[f] Sourav Kumar,[a] Atin Kumar Mandal,[c] Ranjit Biswas [ID][b] and Anirban Bhunia [ID] *[a]

Targeting amyloidosis requires high-resolution insight into the underlying mechanisms of amyloid aggregation. The sequence-specific intrinsic properties of a peptide or protein largely govern the amyloidogenic propensity. Thus, it is essential to delineate the structural motifs that define the subsequent downstream amyloidogenic cascade of events. Additionally, it is important to understand the role played by extrinsic factors, such as temperature or sample agitation, in modulating the overall energy barrier that prompts divergent nucleation events. Consequently, these changes can affect the fibrillation kinetics, resulting in structurally and functionally distinct amyloidogenic conformers associated with disease pathogenesis. Here, we have focused on human Islet Polypeptide (hIAPP) amyloidogenesis for the full-length peptide along with its N- and C-terminal fragments, under different temperatures and sample agitation conditions. This helped us to gain a comprehensive understanding of the intrinsic role of specific functional epitopes in the primary structure of the peptide that regulates amyloidogenesis and subsequent cytotoxicity. Intriguingly, our study involving an array of biophysical experiments and *ex vivo* data suggests a direct influence of external changes on the C-terminal fibrillating sequence. Furthermore, the observations indicate a possible collaborative role of this segment in nucleating hIAPP amyloidogenesis in a physiological scenario, thus making it a potential target for future therapeutic interventions.

[a] *Department of Biophysics, Bose Institute, EN 80, Sector V, Kolkata 700 091, India. E-mail: bhunia@jcbose.ac.in, anirbanbhunia@gmail.com*

[b] *Chemical, Biological and Macromolecular Sciences, S. N. Bose National Centre for Basic Sciences, Sector-III, Salt Lake, Kolkata 700106, India*

[c] *Division of Molecular Medicine, Bose Institute, EN 80, Sector V, Kolkata 700 091, India*

[d] *School of Chemical Sciences, The University of Auckland, Private Bag 92019, Auckland, New Zealand*

[e] *College of Pharmacy, University of Kentucky, Lexington, KY 40536-0596, USA*

[f] *Department of Biology, University of Texas Rio Grande Valley, Edinburg, Texas, 78539, USA*

1. Introduction

Protein misfolding and subsequent amyloid formation is allied with the pathology of a wide range of human diseases, including Alzheimer's, Parkinson's, type-2 diabetes, Huntington's disease, *etc.*[1–5] Human islet amyloid polypeptide (hIAPP) is a 37-residue peptide implicated in type-2 diabetes resulting from aggregation under certain conditions.[6,7] With regards to the growing prevalence of diabetes worldwide, it is increasingly important to gain mechanistic insight into hIAPP amyloidosis.[8–13] For a comprehensive understanding of the mechanism of hIAPP aggregation, it is imperative to consider the aggregation-prone domains within the hIAPP sequence. Over the years, emphasis has been given to discovering the residues crucial for hIAPP fibrillation. For example, the N-terminal hIAPP$_{8-16}$ fragment has been found to form fibrils with similar properties to hIAPP where Phe15 is required for stabilizing an on-pathway α-helical dimer.[14,15] Recent studies have revealed a crucial region spanning the residue stretch, L$_{12}$ANFLVH$_{18}$ associated with hIAPP aggregation.[14,16] Despite the fact that this segment

Chapter 4: Structural Insights Into the Amyloidogenic Aβ and Tau Species in Alzheimer's disease Pathophysiology: Defining Functional Motifs for Therapeutic Interventions 📘❓

By Dibakar Sarkar ; Anirban Bhunia

Ⓒ Get permissions	❝❞ Cite	⤳ Share ⌄

The misfolding and subsequent amyloidogenic aggregation of the Amyloid β (Aβ) peptide and Tau protein has been recognized as the major hallmark in Alzheimer's disease pathophysiology. Therefore, understanding the molecular architecture of amyloid fibrils under various conditions is essential for developing therapeutic interventions. Over the decades, several parallel studies around the globe have been focusing on defining novel therapeutic target motifs. However, the highly dynamic attributes of the functional intermediates have stymied much of the progress in gaining crucial structural information. Nevertheless, high-resolution solid- and solution-state NMR spectroscopy have served as an indispensable means to gain essential insight into the structure-function correlation prompting innumerable studies to define newer therapeutic strategies. In this chapter, we have mainly focused on the structural characteristics of Aβ and Tau aggregates as obtained mostly from the NMR perspective. Further, careful experimental planning could guide us to uncover the complex stages of amyloid aggregation, focusing on transient intermediates. This would, in turn, reveal efficient target motifs for effective therapeutic interventions.

Article

GxxxG Motif Stabilize Ion-Channel like Pores through Cα—H···O Interaction in Aβ (1-40)

Carola Rando [1], Giuseppe Grasso [1], Dibakar Sarkar [2], Michele Francesco Maria Sciacca [3], Lorena Maria Cucci [1], Alessia Cosentino [1], Giuseppe Forte [4], Martina Pannuzzo [5], Cristina Satriano [1], Anirban Bhunia [2] and Carmelo La Rosa [1,*]

1   Dipartimento di Scienze Chimiche, Università degli Studi di Catania, Viale A. Doria 6, 95125 Catania, Italy
2   Department of Biophysics Bose Institute, Unified Academic Campus, Bidhan Nagar, EN 80, Kolkata 700091, India
3   Consiglio Nazionale delle Ricerche, Istituto di Cristallografia, 95121 Catania, Italy
4   Dipartimento di Scienze del Farmaco e della Salute, Università degli Studi di Catania, Viale A. Doria 6, 95125 Catania, Italy
5   Laboratory of Nanotechnology for Precision Medicine, Fondazione Istituto Italiano di Tecnologia, Via Morego 30, 16163 Genoa, Italy
*   Correspondence: clarosa@unict.it

Abstract: Aβ (1-40) can transfer from the aqueous phase to the bilayer and thus form stable ion-channel-like pores where the protein has alpha-helical conformation. The stability of the pores is due to the presence of the GXXXG motif. It has been reported that these ion-channel-like pores are stabilized by a Cα—H···O hydrogen bond that is established between a glycine of the GXXXG sequence of an alpha-helix and another amino acid of a vicinal alpha-helix. However, conflicting data are reported in the literature. Some authors have suggested that hydrogen bonding does not have a stabilizing function. Here we synthesized pentapeptides having a GXXXG motif to explore its role in pore stability. We used molecular dynamics simulations, quantum mechanics, and experimental biophysical techniques to determine whether hydrogen bonding was formed and had a stabilizing function in ion-channel-like structures. Starting from our previous molecular dynamics data, molecular quantum mechanics simulations, and ATR data showed that a stable ion-channel-like pore formed and a band centered at 2910 cm^{-1} was attributed to the interaction between Gly 7 of an alpha-helix and Asp 23 of a vicinal alpha-helix.

Keywords: Aβ; ion-channel-like; pore; membrane; toxicity; FTIR-ATR; quantum mechanics; AFM; hydrogen bond

1. Introduction

Protein misfolding and assembly are complex, intertwined processes resulting in the development of a heterogeneous population of aggregates closely related to many chronic pathological conditions, including type 2 diabetes mellitus (T2DM) [1], Parkinson's disease (PD) [2], and Alzheimer's disease (AD) [3]. Proteins associated with these diseases are called intrinsically disordered proteins (IDPs) because they do not have a well-defined tertiary structure but explore a large conformational space ensemble [4]. IDPs can also cause membrane damage, which is crucial in the pathogenesis of protein-misfolding diseases. To develop effective drug candidates against these diseases, a comprehensive understanding of the molecular mechanism by which IDPs disrupt the membrane is imperative. Based on biophysical data, three models of the so-called amyloid cascade hypothesis that are compatible with membrane damage have been developed [5]. From a kinetic point-of-view, in the first stage, the generation of a stable transmembrane ion-channel-like pores was detected (poration mechanism), and sequentially, membrane destabilization via a "carpet model" or phospholipid removal from the bilayer by a detergent-like mechanism [6]. In addition, a molecular mechanism that describes the transfer of IDPs from the aqueous phase

Delineating the Role of GxxxG Motif in Amyloidogenesis: A New Perspective in Targeting Amyloid-Beta Mediated AD Pathogenesis

Dibakar Sarkar and Anirban Bhunia*

Cite This: https://doi.org/10.1021/acsbiomedchemau.3c00055

Read Online

ACCESS | Metrics & More | Article Recommendations

ABSTRACT: The pursuit of a novel structural motif that can shed light on the key functional attributes is a primary focus in the study of protein folding disorders. Decades of research on Alzheimer's disease (AD) have centered on the Amyloid β (Aβ) pathway, highlighting its significance in understanding the disorder. The diversity in the Aβ pathway and the possible silent tracks which are yet to discover, makes it exceedingly intimidating to the interdisciplinary scientific community. Over the course of AD research, Aβ has consistently been at the forefront of scientific inquiry and discussion. In this review, we epitomize the role of a potential structural motif (GxxxG motif) that may provide a new horizon to the Aβ conflict. We emphasize on how comprehensive understanding of this motif from a structure−function perspective may pave the way for designing novel therapeutics intervention in AD and related diseases.
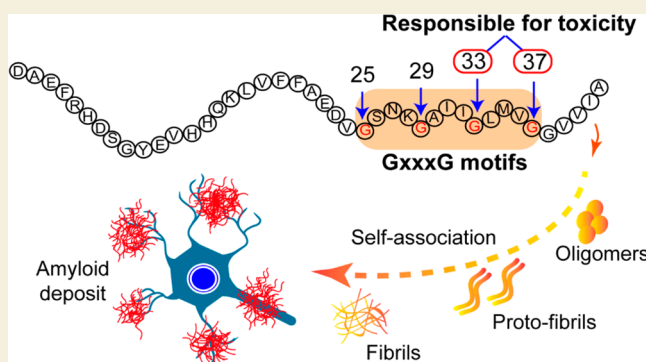
INTRODUCTION

Alzheimer's disease (AD) is a severe neurodegenerative disorder, characterized by progressive impairment of cognitive function and memory loss. To date, there are over 45.0 million AD cases worldwide, enlisting it as the fifth most prevalent cause of death on a global scale and the number is growing at an alarming rate.[1] By 2050, the number of individuals with dementia is expected to cross over 120 million.[2] On top of that, the emotional and financial burden on patients, their families, and communities are enormous. Although over 25 amyloid-forming proteins have been identified and linked to various severe diseases, AD stands out as the most important of them.[3] This distinction arises from its extensive prevalence within the aging population, highlighting its prominence as a significant global health concern. The landscape of AD and dementia-related mortality is intricate, with numerous confounding factors contributing to the overall picture, including age, gender, advanced disease severity, and comorbid conditions such as diabetes, hypertension, coronary artery disease, and cerebrovascular disease. Comprehending the intricate interplay between disease severity and mortality is indispensable for predicting long-term outcomes and evaluating the effectiveness of novel therapeutic interventions. Given the extended timeframes involved, assessing these long-term effects often presents challenges within the framework of randomized controlled trials. As of now, the accumulation of amyloid-beta (Aβ) peptide into extracellular amyloid plaques is considered to be the distinct morphological hallmark of AD.[4−8] However, the in-depth molecular mechanism of Aβ pathway driving AD pathogenesis is still unclear. Over the years, significant findings on the proteolytic processing of amyloid precursor protein (APP),[9−12] potential evidence of highly toxic transient Aβ oligomers,[13−19] and presence of high degree of polymorphism[20−24] in fibril structures have created an intricate scenario.

In this rapidly evolving landscape, the conserved GxxxG motifs present in the C-terminus of Aβ appears to be a noteworthy target. Here, we present a systematic and cross-disciplinary state-of-the art update of the translational research based on biophysical, structural, and cellular data that substantiate the crucial role of well-designed GxxxG motifs in the biological spectrum of Aβ40/42. We provide a comprehensive and evidence-based overview of recent developments in the understanding of the regulatory role played by the GxxxG motif at different temporal scales. Lastly,

Contents lists available at ScienceDirect

Biophysical Chemistry

journal homepage: www.elsevier.com/locate/biophyschem

Application of singular value decomposition analysis: Insights into the complex mechanisms of amyloidogenesis

Dibakar Sarkar [a], Sudipto Saha [b], Janarthanan Krishnamoorthy [c,*], Anirban Bhunia [a,*]

[a] Department of Chemical Sciences, Bose Institute, Unified Academic Campus, Salt Lake, Sector V, Kolkata 700 091, India
[b] Department of Biological Sciences, Bose Institute, Unified Academic Campus, Salt Lake, Sector V, Kolkata 700 091, India
[c] School of Biomedical Engineering, Jimma Institute of Technology, Jimma University, Ethiopia

ARTICLE INFO

ABSTRACT

Amyloidogenesis, with its multifaceted nature spanning from peptide self-assembly to membrane-mediated structural transitions, presents a significant challenge for the interdisciplinary scientific community. Here, we emphasize on how Singular Value Decomposition (SVD) can be employed to reveal hidden patterns and dominant modes of interaction that govern the complex process of amyloidogenesis. We first utilize SVD analysis on Circular Dichroism (CD) spectral datasets to identify the intermediate structural species emerging during peptide-membrane interactions and to determine binding constants more precisely than conventional methods. We investigate the monomer loss kinetics associated with peptide self-assembly using Nuclear Magnetic Resonance (NMR) dataset and determine the global kinetic parameters through SVD. Furthermore, we explore the seeded growth of amyloid fibrils by analyzing a time-dependent NMR dataset, shedding light on the kinetic intricacies of this process. Our analysis uncovers two distinct states in the aggregation of Aβ40 and pinpoints key residues responsible for this seeded growth. To strengthen our findings and enhance their robustness, we validate those using simulated data, thereby highlighting the physical interpretations derived from SVD. Overall, SVD analysis offers a model-free, global kinetic perspective, enabling the selection of optimal kinetic models. This study not only contributes valuable insights into the dynamics but also highlights the versatility of SVD in unravelling complex processes of amyloidogenesis.

1. Introduction

Protein misfolding and subsequent amyloid accumulation is associated with a variety of human disorders, including Alzheimer's, Parkinson's, and type 2 diabetes, among others. [1–6] Understanding the mechanisms that underlie amyloidogenesis is of utmost significance, [7] given the increasing prevalence of these disorders and their profound impact on human health. [8] Typically, the process of amyloidogenesis involves an array of steps that results in the self-association of unfolded or partially folded protein/peptides, which eventually leads to the development of β-sheet rich mature fibrils. [9,10] Initially, during lag phase, the monomers undergo conformational transitions that give rise to oligomeric intermediates. These short-lived structures rapidly evolve into proto-fibrillar species during an exponential growth phase, eventually giving rise to well-defined fibrillar structures. Another key aspect to this multifaceted disorders is the process of seeded growth, where pre-existing aggregates catalyze the assembly of new fibrils. [11,12] This

process not only underscores how aggregates act as templates but also highlights their ability in propagating pathological protein assembly. [13] The interplay between different amyloid proteins or their fragments are equally significant, which shapes the diverse landscapes of amyloid disorders, from structural diversity to complex aggregation pathways. [14–16] Additionally, amyloidogenic peptide's ability to interact with cellular membranes has also created significant attention as a pivotal step in the progression of amyloidosis. [17–19] While recent experimental findings have shifted the focus towards the crucial role played the oligomeric intermediates in cellular toxicity, the effect of lipid bilayer in this regard is quite diverse. Depending on the lipid compositions, cell membrane can accelerate or modulates aggregation rate and results in structural polymorphism. However, the intrinsic ability of toxic oligomers in disrupting lipid bilayer or in forming ion-channel-like pores that eventually leads to cellular dysfunction appears to be most striking. [20] Nonetheless, the intricate interplay between processes like self-assembly, cross-assembly, seeded growth, and

---

* Corresponding authors.
  E-mail addresses: jana.jk2006@gmail.com (J. Krishnamoorthy), bhunia@jcbose.ac.in (A. Bhunia).